

---

Electronic Theses and Dissertations, 2004-2019

---

2014

## Rhenium, osmium and iridium diborides by mechanochemistry: Synthesis, structure, thermal stability and mechanical properties

Zhilin Xie  
*University of Central Florida*

 Part of the [Engineering Commons](#)

Find similar works at: <https://stars.library.ucf.edu/etd>

University of Central Florida Libraries <http://library.ucf.edu>

This Doctoral Dissertation (Open Access) is brought to you for free and open access by STARS. It has been accepted for inclusion in Electronic Theses and Dissertations, 2004-2019 by an authorized administrator of STARS. For more information, please contact [STARS@ucf.edu](mailto:STARS@ucf.edu).

---

### STARS Citation

Xie, Zhilin, "Rhenium, osmium and iridium diborides by mechanochemistry: Synthesis, structure, thermal stability and mechanical properties" (2014). *Electronic Theses and Dissertations, 2004-2019*. 736.  
<https://stars.library.ucf.edu/etd/736>

RHENIUM, OSMIUM AND IRIDIUM DIBORIDES BY  
MECHANOCHEMISTRY: SYNTHESIS, STRUCTURE, THERMAL  
STABILITY AND MECHANICAL PROPERTIES

by

ZHILIN XIE

B.S. China University of Petroleum, 2010

M.S. University of Central Florida, 2012

A dissertation submitted in partial fulfillment of the requirements  
for the degree of Doctor of Philosophy  
in the Department of Mechanical and Aerospace Engineering  
in the College of Engineering and Computer Science  
at the University of Central Florida  
Orlando, Florida

Fall Term  
2014

Major Professors: Nina Orlovskaya and Richard Blair

©2014 Zhilin Xie

## ABSTRACT

Borides are implemented in a range of industrial applications due to their unique mechanical, electrical, thermal and catalytic properties. In particular, transition metal diborides are of special interest. In the recent years, borides of rhenium (Re), osmium (Os) and iridium (Ir) have been studied as for their ultra-hardness and superior stiffness. In this dissertation, a mechanochemical method is introduced to produce rhenium diboride ( $\text{ReB}_2$ ) powder, a novel hexagonal osmium diboride ( $h\text{-OsB}_2$ ), and iridium boride powders. Densification by Spark Plasma Sintering (SPS), thermal stability and mechanical properties of  $h\text{-OsB}_2$  were also studied.

$\text{ReB}_2$  was recently reported to exhibit high hardness and low compressibility, which both are strong functions of its stoichiometry, namely Re to B ratio. Most of the techniques used for  $\text{ReB}_2$  synthesis reported 1:2.5 Re to B ratio because of the loss of the B during high temperature synthesis. However, as a result of B excess, the amorphous boron, located along the grain boundaries of polycrystalline  $\text{ReB}_2$ , would degrade the  $\text{ReB}_2$  properties. Therefore, techniques which could allow synthesizing the stoichiometric  $\text{ReB}_2$  preferably at room temperature are in high demand.  $\text{ReB}_2$  powder was synthesized at low temperature using mechanochemical route by milling elemental crystalline Re and amorphous B powders in the SPEX 8000 high energy ball mill for 80 hours. The formation of boron and perrhenic acids are also reported after  $\text{ReB}_2$  powder was exposed to the moist air environment for a twelve month period of time.

Hexagonal osmium diboride ( $h\text{-OsB}_2$ ), a theoretically predicted high-pressure phase, has been synthesized for the first time by a mechanochemical method, i.e., high energy ball milling. X-ray diffraction (XRD) indicated the formation of  $h\text{-OsB}_2$  after 2.5 hours of milling, and the



reaction reaches equilibrium after 18 hours of milling. The lattice parameters of the  $h$ -OsB<sub>2</sub> are  $a=2.916\text{\AA}$  and  $c=7.376\text{\AA}$ , with a  $P63/mmc$  space group. Transmission electron microscopy confirmed the appearance of the  $h$ -OsB<sub>2</sub> phase. The thermal stability of  $h$ -OsB<sub>2</sub> powder was studied by heating under argon up to 876 °C and cooling *in vacuo* down to -225 °C. The oxidation mechanism of  $h$ -OsB<sub>2</sub> has also been proposed. The hexagonal phase partially converted to the orthorhombic phase (20 wt.%) after spark plasma sintering of  $h$ -OsB<sub>2</sub> at 1500°C and 50MPa for 5 minutes. Hardness and Young's modulus of the  $h$ -OsB<sub>2</sub> were measured to be  $31 \pm 9$  GPa and  $574 \pm 112$  GPa, respectively by nanoindentation method.

Prior to this research a number of compounds have been prepared in Ir-B system with lower than 2 boron stoichiometry, and no IrB<sub>2</sub> phases have been synthesized experimentally. In this dissertation, three new iridium boride phases, ReB<sub>2</sub>-type IrB<sub>2</sub>, AlB<sub>2</sub>-type IrB<sub>2</sub> and IrB have been synthesized with a similar mechanochemical method. The formation of these three phases has been confirmed by both X-ray diffraction (XRD) and transmission electron microscope (TEM) after 30 hours of ball milling and 48 hours of annealing. The IrB<sub>2</sub> phases have hexagonal crystal structures and the new IrB phase has an orthorhombic crystal structure. The segregation of iridium from iridium borides' lattices has also been studied by high resolution TEM.

*Dedicated to my grandparents, Shuijin Xie and Meihua Liu,  
my parents, Haiping Xie and Lihui Deng  
for their love and support.*

## ACKNOWLEDGMENTS

I would like to thank my advisor, Professor Nina Orlovskaya, for her guidance and support in the past four and half years. Prof. Orlovskaya has taught me a significant amount of knowledge and a variety of experimental skills. I believe what I learned from her in these years will help me succeed in my future career. I express my deepest gratitude to Prof. Orlovskaya for all the time and efforts she has put into guiding me through my research. Thanks to my co-advisor, Professor Richard Blair. He is very patient and kind. It is always comfortable to work with him. Without his ideas in the discovery of the new hexagonal phase of OsB<sub>2</sub>, Chapters 3 to 7 in this dissertation may not exist. Thanks to Dr. Linan An, Dr. Jan Gou and Dr. Seetha Raghavan for serving on my committee and for their valuable critique and suggestions.

I acknowledge the scientists, Yan Chen, David Cullen and Andrew Payzant, from Oak Ridge National Laboratory. Dr. Chen helped me during my whole PhD study even after he graduated. I feel lucky that I had such a good labmate who used to sit beside me. I am very grateful for his help! Thanks to Dr. Cullen and Dr. Panyzant for treating me good in my every visit to Oak Ridge National Laboratory. Both of them are very knowledgeable and helpful. Without them, I would not be able to complete my dissertation decently. Also, I would like to thank the 11-BM staff in the Advanced Photon Source at the Argonne National Laboratory, who helped with synchrotron X-ray diffraction for my samples, which played a very important role in my first publication. Thanks to Huili Gao and Prof. Miladin Radovic, who helped sinter the OsB<sub>2</sub> sample with spark plasma sintering. Thanks to Dr. Mykola Lugovy who helped me analyze the great amount of nanoindentation data. Thanks to other collaborators: Thomas Graule, Jakob

Kuebler, Martin Mueller and Andreas Mortensen, who also contributed to this work.

I thank my labmates, Amjad Aman, Richard Stadelmann, Anthony Terracciano, Manuel Robayo, Jonathan Torres, Maximo Navarro and Billy Huges. Amjad and I joined Dr. Orlovskaya's research group in the same year. Although we work on very different research projects, but we always share our good and bad experience. It is also very enjoyable to play tennis with him. Richard is very helpful and enthusiastic to almost everything. He checks if everybody is doing OK several times a day, to make sure that no one is too depressed. He is also the one who organizes people to have lunch together, made our lunch break the best time of the day. He has the funniest ring tone and likes playing rock music in the lab. Without Richard our life would be a lot worse! Anthony is very smart and brave, never afraid of fire and explosions. Thank him for going to gym with me in the past two years, otherwise I would not be able to bench press my bodyweight. Thanks to Jonathan and Maximo for their encouragement, especially when I was preparing my PhD qualifying exams. I would also like to thank Dr. Blair's students. Restrepo has solid understanding of mechanochemistry and he always shares his helpful experience and ideas. Jacob helped me start my work on solid state chemistry. He is so nice that he is always ready to help. I can never forget that Restrepo and Jacob saved me from the nitric acid accident. Thanks to Nash, a cool guy, for letting me use his hydrogen tank, and also for organizing all the interesting events.

I especially thank my family, whose love and support helped me overcome many difficulties. My parents sacrificed a lot for my brother, sister and myself. Without their strong support, we would not have received good education. I cannot expect more from them. Thanks to my brother and sister who showed me good examples for being a good student since I was in

elementary school. I miss my grandparents; all I have done was trying not to disappoint them. I wish I can spend more time with them in the future. Finally, thanks to my girlfriend, Janicely Serrano, for her love and care. She is a person who can appreciate my weird sense of humor. I cannot forget the encouragement that she gave me when I was frustrated and depressed.

The work in Chapter 2, “Mechanochemical synthesis of  $\text{ReB}_2$  powder”, was previously published by Nina Orlovskaya, Zhilin Xie, Mikhail Klimov, Helge Heinrich, David Restrepo, Richard Blair and Challapalli Suryanarayana in *Journal of Materials Research*, Volume 26, Issue 21 (2011) pp. 2772-2779 Copyright © 2011 Materials Research Society. Reprinted with the permission of Cambridge University Press. The work was supported by National Science Foundation project DMR-0748364 “CAREER: Hard and tough boron rich ceramic laminates designed to contain thermal residual stresses.”

The work in Chapter 3, “Novel high pressure hexagonal  $\text{OsB}_2$  by mechanochemistry”, was previously published by Zhilin Xie, Moritz Graule, Nina Orlovskaya, E. Andrew Payzant, David A. Cullen, and Richard G. Blair in *Journal of Solid State Chemistry*, Volume 215, (2014) pp. 16-21 Copyright © 2014 Elsevier Inc. Reprinted with the permission of Elsevier. The work was supported by NSF project DMR - 0748364. High and low temperature X-ray diffraction studies were supported by Center for Nanophase Material Sciences, Oak Ridge National Laboratory; STEM studies were supported by Oak Ridge National Laboratory’s Shared Research Equipment (ShaRE) User Program, which is sponsored by the Office of Basic Energy Sciences, U.S. Department of Energy. We gratefully acknowledge use of WebEMAPS for generating simulated diffraction patterns, available online at <http://emaps.mrl.uiuc.edu/>. We acknowledge Prof. Miladin Radovic and Mr. Huili Gao, Texas A&M University, College Station, Texas for

the help with SPS, and Dr. Yan Chen, Spallation Neutron Source, Oak Ridge National Laboratory, Oak Ridge, Tennessee for the help with Rietveld refinement. Use of the Advanced Photon Source was supported by the U.S. Department of Energy, Office of Science, Office of Basic Energy Sciences, under Contract No. DE-AC02-06CH11357.

The work in Chapter 4, “Thermal stability of hexagonal OsB<sub>2</sub> under argon atmosphere”, was previously published by Zhilin Xie, Richard G. Blair, Nina Orlovskaya, David A. Cullen and E. Andrew Payzant in *Journal of Solid State Chemistry*, Volume 219, (2014) pp. 210-219 Copyright © 2014 Elsevier Inc. Reprinted with the permission of Elsevier. This work was supported by NSF projects DMR - 0748364. High and low temperature X-ray diffraction studies and electron microscopy were supported by Center for Nanophase Material Sciences, which is sponsored at Oak Ridge National Laboratory by the Scientific User Facilities Division, Office of Basic Energy Sciences, U.S. Department of Energy. The authors also wish to thank Ceradyne, Inc. for the donation the crystalline <sup>11</sup>B powder.

The work in Chapter 5, “Hexagonal OsB<sub>2</sub> reduction upon heating in H<sub>2</sub> containing environment”, was previously published by Zhilin Xie, Richard G. Blair, Nina Orlovskaya and E. Andrew Payzant in *Advances in Applied Ceramics*, (2014) Copyright © 2014. Reprinted with the permission of Maney Publishing. This work was supported by NSF project DMR - 0748364. High-temperature X-ray diffraction studies were supported by Center for Nanophase Materials Sciences, which is sponsored at Oak Ridge National Laboratory by the Scientific User Facilities Division, Office of Basic Energy Sciences, U.S. Department of Energy.

The work in Chapter 6 and Chapter 8 was supported by NSF project DMR - 0748364. Electron microscopy was supported by Center for Nanophase Material Sciences, which is

sponsored at Oak Ridge National Laboratory by the Scientific User Facilities Division, Office of Basic Energy Sciences, U.S. Department of Energy.

The work in Chapter 7 was supported by NSF project DMR – 0748364. The bulk of electron microscopy work was performed as part of a user project supported by ORNL's Center for Nanophase Materials Sciences (CNMS), which is a DOE Office of Science User Facility. M.M.'s and N.O.'s work at EPFL, which included nanoindentation experiments, was supported by the European Research Council under the European Union's Seventh Framework Programme (FP/2007-2013) / ERC Advanced Grant Agreement No. 291085 and N.O.'s work at Empa was supported by the Swiss National Science Foundation, International Short Visit, IZK0Z2\_154379. The authors would also like to thank Prof. A. Mortensen, EPFL for his valuable suggestions and revisions of the manuscript.

## TABLE OF CONTENTS

LIST OF FIGURES .....	xiii
LIST OF TABLES .....	xix
CHAPTER 1: INTRODUCTION AND LITERATURE REVIEW .....	1
1.1 Rhenium Diboride.....	5
1.1.1 Synthesis of ReB <sub>2</sub> .....	6
1.1.2 Crystal structure of ReB <sub>2</sub> .....	9
1.1.3 Stability of ReB <sub>2</sub> .....	11
1.1.4 Properties of ReB <sub>2</sub> .....	12
1.2 Osmium Diboride.....	19
1.2.1 Synthesis of OsB <sub>2</sub> .....	20
1.2.2 Crystal structures of OsB <sub>2</sub> and phase transformation .....	22
1.2.3 Properties of OsB <sub>2</sub> .....	25
1.2.4 Other osmium borides.....	29
1.3 Iridium Borides .....	31
1.4 Other important transition metal borides .....	35
1.5 Correlation between hardness and elastic constants .....	38
1.6 Mechanochemistry .....	41
1.6.1 Overview of Mechanochemistry .....	41
1.6.2 High energy ball milling .....	45
1.6.3 Mechanics in Mechanochemistry .....	55
CHAPTER 2: MECHANOCHEMICAL SYNTHESIS OF ReB <sub>2</sub> POWDER .....	61
2.1 Introduction.....	61
2.2 Experimental .....	65
2.2.1 Phase Analysis .....	65
2.2.2 Microscopy .....	66
2.2.3 Compositional Analysis .....	66
2.2.4 Micro-Raman Spectroscopy.....	66
2.3 Results and discussion .....	67
2.3.1 Microscopies .....	69
2.3.2 SIMS .....	71
2.3.3 Raman spectroscopy .....	74
2.3.4 Reaction of powder ReB <sub>2</sub> with O <sub>2</sub> and H <sub>2</sub> O .....	76
2.4 Conclusion .....	77
CHAPTER 3: NOVEL HIGH PRESSURE HEXAGONAL OsB <sub>2</sub> BY MECHANOCHEMISTRY .....	79
3.1 Introduction.....	79
3.2 Experimental .....	83
3.3 Results and discussion .....	84
3.4 Conclusion .....	93
CHAPTER 4: THERMAL STABILITY OF HEXAGONAL OsB <sub>2</sub> UNDER ARGON ATMOSPHERE.....	94



4.1 Introduction.....	94
4.2 Experimental.....	96
4.3 Results.....	98
4.3.1 Phase composition of OsB <sub>2</sub> powder after mechanochemical synthesis at room temperature .....	98
4.3.2 High temperature stability and phase composition of hexagonal OsB <sub>2</sub> under Ar .....	103
4.3.3 Phase composition of OsB <sub>2</sub> powder after mechanochemical synthesis at room temperature .....	105
4.3.4 Low temperature stability of hexagonal OsB <sub>2</sub> <i>in vacuo</i> .....	112
4.4 Discussion.....	114
4.5 Conclusion .....	116
CHAPTER 5: HEXAGONAL OsB <sub>2</sub> REDUCTION UPON HEATING IN H <sub>2</sub> CONTAINING ENVIRONMENT .....	118
5.1 Introduction.....	118
5.2 Experimental.....	120
5.3 Results and discussion .....	121
5.4 Conclusions.....	130
CHAPTER 6: THERMAL ANALYSIS OF HEXAGONAL OsB <sub>2</sub> .....	131
6.1 Introduction.....	131
6.2 Experimental.....	133
6.3 Results and Discussion .....	134
6.4 Conclusions.....	143
CHAPTER 7: HEXAGONAL OsB <sub>2</sub> : SINTERING, MICROSTRUCTURE AND MECHANICAL PROPERTIES .....	144
7.1 Introduction.....	144
7.2 Experimental.....	147
7.3 Results and discussion .....	149
7.3.1 SPS of OsB <sub>2</sub> .....	149
7.3.2 Microstructure of sintered OsB <sub>2</sub> .....	151
7.3.3 Mechanical behavior of OsB <sub>2</sub> .....	161
7.4 Conclusions.....	172
CHAPTER 8: SYNTHESIS OF NEW IrB <sub>2</sub> PHASES AND Ir SEGREGATION AT HIGH TEMPERATURE .....	174
8.1 Introduction.....	174
8.2 Experimental.....	178
8.3 Results and Discussion .....	179
8.4 Conclusions.....	196
CHAPTER 9: CONCLUSIONS AND FUTURE WORK.....	198
APPENDIX A: COPYRIGHT PERMISSION LETTERS .....	204
APPENDIX B: TRANSMISSION ELECTRON MICROGRAPHS.....	217
LIST OF REFERENCES .....	233

## LIST OF FIGURES

Figure 1: Bulk moduli of the elements. Note that the modulus scale is logarithmic. (data from [19]). Reprinted from International Journal of Refractory Metals and Hard Materials, 24, J.J. Gilman, R.W. Cumberland and R.B. Kaner, Design of hard crystals, 1-5, [10] Copyright (2006), with permission from Elsevier. ....	3
Figure 2: The phase diagram of the Re-B system. [82] Reprinted from Journal of Alloys and Compounds, 252, Shigeki Otani, Takashi Aizawa and Yoshio Ishizawa, Preparation of ReB <sub>2</sub> single crystals by the floating zone method, 19-21, [73] Copyright (1997), with permission from Elsevier. ....	8
Figure 3. Schematic presentation of the ReB <sub>2</sub> unit cells. B atoms — small blue spheres; Os atoms — big yellow spheres. ....	10
Figure 4: H <sub>V</sub> of ReB <sub>2</sub> plotted as a function of load (A), and a scratch on the surface of a natural diamond parallel to the (100) plane created by an ingot of ReB <sub>2</sub> (B). From H.-Y. Chung, M. B. Weinberger, J. B. Levine, A. Kavner, J.-M. Yang, S. H. Tolbert and Kaner, Richard B., "Synthesis of Ultra-Incompressible Superhard Rhenium Diboride at Ambient Pressure," Science, vol. 316, pp. 436-439, 2007. [52] Reprinted with permission from AAAS. ....	14
Figure 5: The phase diagram of the Os-B system. Springer and the original publisher / Journal of Thermal Analysis and Calorimetry, 76, 2004, 975-983, Phase diagram investigation and thermodynamic study of Os-B system, L. Stuparević and D. Živković, Figure 7, original copyright notice is given to the publication in which the material was originally published, by adding; with kind permission from Springer Science and Business Media, [117]. ....	22
Figure 6: The three predicted crystal structures of OsB <sub>2</sub> : RuB <sub>2</sub> -type (orthorhombic) (A); ReB <sub>2</sub> -type (hexagonal-I) (B); AlB <sub>2</sub> -type (hexagonal-II) (C). ....	23
Figure 7: Measured hardness values of orthorhombic OsB <sub>2</sub> from different papers: <i>a</i> [29], <i>b</i> [32] and <i>c</i> [121]. ....	27
Figure 8: The phase diagram of the Ir-B system. [141, 142] Reprinted from Journal of the Less Common Metals, 82, H. Ipser and P. Rogl, Constitution diagrams of the binary systems Pd-B and Ir-B, 363, Copyright (1981), with permission from Elsevier. ....	32
Figure 9: The crystal structure of WB <sub>4</sub> (A) and the top view of crystal structure (B). [34] .....	36
Figure 10: Correlation of hardness and bond strength for the osmium compounds. Reprinted from Journal of Physics and Chemistry of Solids, 69, Miao Zhang, Mei Wang, Tian Cui, Yanming Ma, Yingli Niu and Guangtian Zou, Electronic structure, phase stability, and hardness of the osmium borides, carbides, nitrides, and oxides: First-principles calculations, 2096–2102, Copyright (2008), with permission from Elsevier. [131] .....	40
Figure 11: Publications about mechanochemistry as function of time. [176] .....	42
Figure 12: <i>In situ</i> X-ray diffraction with real-time monitoring the mechanochemical process. Reprinted by permission from Macmillan Publishers Ltd: Nature Chemistry [188], copyright (2012). ....	44
Figure 13: A schematic of the working mechanism of high energy ball milling. ....	45
Figure 14: A SPEX 8000D Mixer/Mill (a), and WC milling vial and media (b). ....	48
Figure 15: A Fritsch planetary mill (A) and a schematic showing its working mechanism (B). [178]. ....	49

Figure 16: An attritor (A) and the structure of rotating arms on a shaft in the attrition ball mill (B). .....	49
Figure 17: EDEM simulation of ball milling using WC balls and vials with a SPEX ball mill... 54	54
Figure 18: Schematic illustration of structural changes in a shear band: 1, half space; 2, shear band with displacement; 3, layer with structural changes. Reprinted by permission from Taylor & Francis Group LLC - Books, [194], copyright (2003).....	59
Figure 19: Diagram of a chemical reaction in a thin layer. Reprinted by permission from Taylor & Francis Group LLC - Books, [194], copyright (2003).....	59
Figure 20: (a) X-ray diffraction patterns of Re powder, (b) B powder and (c) ReB <sub>2</sub> mechanically alloyed powders after 30, 50, and 80 hours of milling. The observed broad peak at ~18° 2 $\theta$ in (b) is a common peak seen for amorphous materials. ....	68
Figure 21: SEM micrograph of ReB <sub>2</sub> powders after ball milling for 80 hours.....	70
Figure 22: (a) TEM micrograph of a particle of ReB <sub>2</sub> powder after 80 hours of milling, (b) Electron diffraction of ReB <sub>2</sub> particle, (c) TEM micrograph of ReB <sub>2</sub> lattice fringes. ....	70
Figure 23: Distribution maps of (a) Boron, (b) Rhenium, (c) Tungsten in a ReB <sub>2</sub> particle. ....	71
Figure 24: Negative secondary ion mass spectrometry of ReB <sub>2</sub> powders after 0.5h (a, d); 40h (b, e); and 80h (c, f) milling time. ....	72
Figure 25: Positive second ion mass spectrometry of ReB <sub>2</sub> powders after 0.5h (a); 40h (b); and 80h (c) milling time. ....	73
Figure 26: Raman spectra of mechanically alloyed ReB <sub>2</sub> powders after 80 hours of ball milling. ....	75
Figure 27: X-ray diffraction patterns of ReB <sub>2</sub> powder after 1 year storage in the plastic bag without any protective atmosphere. ....	77
Figure 28: Sealed vacuum quartz ampule with sample pellet loaded in a boron nitride crucible. 84	84
Figure 29: The OsB <sub>2</sub> XRD pattern from a conventional laboratory X-ray diffractometer. After mechanochemical synthesis, the hexagonal OsB <sub>2</sub> powder was annealed <i>in vacuo</i> at 1050 °C for 6days. The unindexed peak around d-spacing=2.5Å (▲) may be due to Os <sub>2</sub> B <sub>3</sub> . ....	86
Figure 30: Synchrotron XRD pattern of OsB <sub>2</sub> after SPS consisting of 80wt% hexagonal and 20wt% orthorhombic phases. No other phases, such as WC, Os <sub>2</sub> B <sub>3</sub> or crystalline B were found. ....	88
Figure 31: The crystal structure of hexagonal OsB <sub>2</sub> . Osmium atoms are the larger gray spheres, and boron atoms are the smaller black spheres. ....	88
Figure 32: The <i>a</i> and <i>c</i> lattice parameters of hexagonal OsB <sub>2</sub> along with the volume of the unit cell in the -225°C to 875°C temperature range. ....	90
Figure 33: A SEM micrograph (a) and EDS (b) of OsB <sub>2</sub> powder after 18 hours of milling. ....	91
Figure 34: HAADF-STEM images of OsB <sub>2</sub> powder (a,b), individual OsB <sub>2</sub> nanocrystallites (c,d) with corresponding fast Fourier transforms (e,g) and simulated diffraction patterns (f,h).....	92
Figure 35: The XRD diffractogram, TEM and SEM images of mechanochemically synthesized OsB <sub>2</sub> (A, B and C) powder at room temperature before heating experiment and Os <sub>2</sub> B <sub>3</sub> (D, E and F) produced by ball milling Os and crystalline <sup>11</sup> B mixture for 54h. More TEM images of OsB <sub>2</sub> and Os <sub>2</sub> B <sub>3</sub> are shown in Appendix B from Figure 88 to Figure 92. ....	100
Figure 36: The XRD diffractogram, SEM and bright-field STEM images of osmium metal (A, B and C), amorphous and crystalline boron (D, E and F) and crystalline <sup>11</sup> B (G, H and I). More	

TEM images of Os, amorphous and crystalline boron, and $^{11}\text{B}$ are shown in Appendix B from Figure 82 to Figure 87.....	102
Figure 37: The <i>in situ</i> high-temperature XRD contour plot (A) and XRD patterns (B) of <i>h</i> -OsB <sub>2</sub> upon heating and cooling under an argon atmosphere.....	104
Figure 38: The weight percentage of OsB <sub>2</sub> (◆ or ◇), Os <sub>2</sub> B <sub>3</sub> (■ or □), OsB (Δ) and Os (● or ○) as function of temperature upon heating (filled symbol) and cooling (open symbol) under an argon atmosphere.....	104
Figure 39: An expanded view (A) of the dash-line box in Figure 37A and the corresponding XRD patterns (B) at 876 °C and 826 °C upon cooling.....	105
Figure 40: The lattice parameters <i>a</i> (A), <i>c</i> (B) and unit cell volume <i>V</i> (C) of OsB <sub>2</sub> together with CTCE of <i>a</i> (D), <i>c</i> (E) and <i>V</i> (F) as function of temperature upon heating (■) and cooling(□) under an argon atmosphere.....	107
Figure 41: The lattice parameters <i>a</i> (A), <i>c</i> (B) and unit cell volume <i>V</i> (C) of Os as function of temperature upon heating (■) and cooling (□) under an argon atmosphere.....	108
Figure 42: Density of <i>h</i> -OsB <sub>2</sub> as function of temperature upon heating (■) and cooling (□) under an argon atmosphere.....	110
Figure 43: The lattice parameters <i>a</i> (A), <i>c</i> (B) and the unit cell volume <i>V</i> (C) of <i>h</i> -OsB <sub>2</sub> as function of temperature upon cooling (■) and heating (□) <i>in vacuo</i> .....	113
Figure 44: <i>In situ</i> high-temperature XRD contour plot (A) and XRD patterns (B) of <i>h</i> -OsB <sub>2</sub> upon heating and cooling under 4 vol% H <sub>2</sub> /Ar reforming gas atmosphere.....	122
Figure 45: Weight percentage of OsB <sub>2</sub> (◆), Os <sub>2</sub> B <sub>3</sub> (▲) and Os (●) as function of temperature upon heating under 4 vol% H <sub>2</sub> /Ar reforming gas atmosphere.....	124
Figure 46: Lattice parameter <i>a</i> (A), <i>c</i> (B) and unit cell volume <i>V</i> (C) of OsB <sub>2</sub> together with CTCEs of <i>a</i> (D), <i>c</i> (E) and <i>V</i> (F) as function of temperature upon heating under 4 vol% H <sub>2</sub> /Ar reforming gas atmosphere.....	125
Figure 47: Lattice parameter <i>a</i> , <i>c</i> and unit cell volume <i>V</i> of Os as function of temperature upon heating (A, B, C) and cooling (D, E, F) under 4 vol% H <sub>2</sub> /Ar reforming gas atmosphere.....	126
Figure 48: The schematic of the steps of OsB <sub>2</sub> reduction to metallic Os upon heating in H <sub>2</sub> and O <sub>2</sub> containing environment.....	129
Figure 49: A schematic of O <sub>2</sub> interactions with OsB <sub>2</sub> lattice at different temperature upon heating in Ar where a minor presence of oxygen.....	132
Figure 50: Positive secondary ion mass spectroscopy (A, B and C) and negative secondary ion mass spectroscopy (D).....	135
Figure 51: The thermogravimetric analysis and differential scanning calorimetry (A) and the mass spectra of off-gas (B).....	137
Figure 52: <i>In situ</i> high temperature TEM micrographs of hexagonal OsB <sub>2</sub> at 25°C (A), 300°C (B), 700°C (C) and 900°C (D).....	139
Figure 53: Lattice fringes and average grain area as function of temperature and grain area distribution of OsB <sub>2</sub> at 25°C (A), 300 °C (B) 700°C (C) and 900 °C (D).....	140
Figure 54: <i>In situ</i> high temperature TEM micrographs of hexagonal OsB <sub>2</sub> at 25°C (A), 300°C (B), 700°C (C) and 900°C (D).....	141

Figure 55: <i>In situ</i> high temperature TEM micrographs of hexagonal OsB <sub>2</sub> at 25°C (A), 300°C (B), 700°C (C) and 900°C (D). More <i>in situ</i> high temperature TEM micrographs are shown in Appendix B from Figure 93 to Figure 97. ....	142
Figure 56: An image of the sintered OsB <sub>2</sub> sample during FIB milling (TEM sample preparation). .....	149
Figure 57: A sintering regime used for densification of hexagonal OsB <sub>2</sub> powder. Both temperature, pressure, and shrinkage data were collected during spark plasma sintering as a function of time. ....	153
Figure 58: The OsB <sub>2</sub> sample after spark plasma sintering (left), and a US quarter coin (right) for comparison of the sizes. ....	153
Figure 59: X-ray diffraction pattern of sintered OsB <sub>2</sub> ceramics (A), along with a phase composition map (B) and corresponding EBSD map (C) where the phase content (A and B) as well as crystallographic orientation of each individual OsB <sub>2</sub> grain could be identified (C). ....	154
Figure 60: Microstructure of OsB <sub>2</sub> after SPS (A). The optical micrograph shows a nonhomogeneous densification. (B) TEM micrograph of OsB <sub>2</sub> where the grains are clearly visible but also quite a high numbers of pores are also present. (C) SEM micrograph of OsB <sub>2</sub> polished surface taken using InLens detector and (D) the SEM micrograph of the same OsB <sub>2</sub> surface as in (C) but produced using backscattered ESB detector. ....	155
Figure 61: Grain size distribution of OsB <sub>2</sub> ceramics after SPS calculated from the results presented in Figure 59C, Figure 60B and D. The average grain size is equal to 0.56µm thus the produced OsB <sub>2</sub> is a submicron ceramics. ....	155
Figure 62: TEM micrographs of hexagonal (A) and orthorhombic (D) OsB <sub>2</sub> grains with the corresponding electron diffraction patterns (B and E, respectively), along with their high resolution images and the corresponding FFT patterns (C and F). ....	156
Figure 63: SEM micrograph of the polished OsB <sub>2</sub> ceramics with corresponding EDS spectra collected at two different areas on the surface. The area 1 highlighted within dark field (a pore), enriched in B while no Os can be detected, while the area 2 highlighted at the surface of OsB <sub>2</sub> ceramics surrounding the pore is enriched in Os. ....	158
Figure 64: SEM micrograph of the polished surface of OsB <sub>2</sub> ceramics after sintering with corresponding distribution of Os (B), B (C), and O (D) elements collected as EDS maps. ....	159
Figure 65: TEM image of the material present within a pore in OsB <sub>2</sub> sample after sintering (A); the corresponding electron diffraction pattern of the area highlighted with a dashed circle (B); TEM micrograph of the material located in a different pore (C); along with higher resolution image of the selected location with a pore highlighted with a dashed rectangle (D). ....	160
Figure 66: SEM micrograph of the two impressions produced by nanoindentation of polished OsB <sub>2</sub> surface with a spherical indenter with a load of 8 mN. ....	164
Figure 67: Load–displacement (A) and recalculated indentation stress – indentation strain (B) diagrams produced by nanoindentation of polished OsB <sub>2</sub> surface where “pop-in” events were present during the loading portion of the load-displacement curve. ....	169
Figure 68: Load – displacement (A) and recalculated indentation stress – indentation strain (B) diagrams produced by nanoindentation of polished OsB <sub>2</sub> surface where no pop-in event was present during loading or unloading portions of the load-displacement curve. ....	170
Figure 69: The scanning probe micrographs of the OsB <sub>2</sub> surfaces before (A, D) and after (B, C, E and F) indentation. ....	171

Figure 70: Mechanism of high energy ball milling (A) and maximum axial and shear stresses present during mechanochemical synthesis of Os-B compound as a function of contact area (B).	176
Figure 71: XRD pattern (A), SEM (B) micrographs of raw iridium powder.	180
Figure 72: XRD pattern (A), SEM (B) and TEM (C) micrographs of raw boron powder.	181
Figure 73: XRD patterns of Ir and B powder mixture at different milling time.	183
Figure 74: TEM of the Ir and B mixture after 90 hours of ball milling.	185
Figure 75: SEM (A) and EDS (B) of Ir and B powder mixture after 90 hours of ball milling.	187
Figure 76: Schematic of oxidation of higher iridium borides to lower borides: $\text{ReB}_2$ -type $\text{IrB}_2$ (A), $\text{AlB}_2$ -type $\text{IrB}_2$ (B), $\text{IrB}_{1.35}$ (C) and $\text{IrB}_{1.1}$ (D). The larger yellow spheres are iridium atoms, and the smaller blue or pink spheres are boron atoms. The boron vacancies can only exist at the blue sphere sites.	188
Figure 77: XRD patterns of Ir and B powder mixture after 30 hours of ball milling and 48 hours of annealing (A), and 90 hours of ball milling and 72 hours of annealing (B).	190
Figure 78: TEM of the Ir and B mixture after 90 hours of ball milling and 72 hours of annealing.	192
Figure 79: STEM images of the Ir and B mixture after 90 hours of ball milling and 72 hours of annealing. (A), (C) and (E) are bright field micrographs; (B), (D) and (F) are high angle annular dark field micrograph.	193
Figure 80: High resolution STEM bright field micrographs showing the identified locations of individual Ir atoms. (A) is an expanded view of the area highlighted with a box in Fig 9 (A); (B) is an expanded view of the area highlighted with a box in Fig 9 (C).	194
Figure 81: Ir atoms segregation along the disordered defective domain out of $\text{IrB}_2$ lattice after annealing at $1050\text{ }^\circ\text{C}$ for 72 hours. Bright field high resolution STEM micrograph (A); high angle annular dark field STEM micrograph (B); magnified image of lattice fringes (C) of the area selected in (A); magnified image of triplets of Ir atoms (D) of the area selected in (B); the marked locations of Ir atoms where the central atom of the each triplet located inside of the lattice fringe (E). The magnification is identical for (C), (D) and (E) images	195
Figure 82: Bright field (A, C and E) and dark field (B, D and F) STEM images of pure Os metal.	217
Figure 83: Bright field (A, C and E) and dark field (B, D and F) STEM images of pure Os metal.	218
Figure 84: Bright field (A, C and E) and dark field (B, D and F) STEM images of pure Os metal.	219
Figure 85: Bright field (A, C and E) and dark field (B, D and F) STEM images of amorphous and crystalline boron.	220
Figure 86: Bright field (A, C and E) and dark field (B, D and F) STEM images of crystalline $^{11}\text{B}$ .	221
Figure 87: Bright field (A and C) and dark field (B and D) STEM images of crystalline $^{11}\text{B}$ .	222
Figure 88: Bright field (A, C and E) and dark field (B, D and F) STEM images of hexagonal $\text{OsB}_2$ .	223
Figure 89: Bright field (A, C and E) and dark field (B, D and F) STEM images of hexagonal $\text{OsB}_2$ .	224

Figure 90: Bright field (A, C and E) and dark field (B, D and F) STEM images of hexagonal OsB <sub>2</sub> . .....	225
Figure 91: Bright field (A, C and E) and dark field (B, D and F) STEM images of Os <sub>2</sub> B <sub>3</sub> . .....	226
Figure 92: Bright field (A, C and E) and dark field (B, D and F) STEM images of Os <sub>2</sub> B <sub>3</sub> . .....	227
Figure 93: High temperature TEM images of <i>h</i> -OsB <sub>2</sub> particles at different temperature.....	228
Figure 94: High temperature TEM images of <i>h</i> -OsB <sub>2</sub> particles at different temperature.....	229
Figure 95: High temperature TEM images of <i>h</i> -OsB <sub>2</sub> particles at different temperature.....	230
Figure 96: High temperature TEM images of <i>h</i> -OsB <sub>2</sub> particles at different temperature.....	231
Figure 97: High temperature TEM images of <i>h</i> -OsB <sub>2</sub> particles at different temperature.....	232

## LIST OF TABLES

Table 1: Characteristic reactions in the Ir-B system according to the Ipsier and Rogl [141, 142]. Reprinted from Journal of the Less Common Metals, 82, H. Ipsier and P. Rogl, Constitution diagrams of the binary systems Pd-B and Ir-B, 363, Copyright (1981), with permission from Elsevier. ....	33
Table 2: Specifications of SPEX tungsten carbide vial. ....	46
Table 3: Lattice parameters of the synthesized ReB <sub>2</sub> after mechanical alloying for 30, 50 and 80 hours. ....	69
Table 4: Intensity ratio of impurities to boron SIMS peaks. ....	74
Table 5: The lattice parameters of hexagonal OsB <sub>2</sub> . ....	87
Table 6: Reaction information and ball milling parameters. ....	97
Table 7: Lattice parameters of Os-B compounds. ....	99
Table 8: CTEs of Os metal in <i>a</i> , <i>c</i> and <i>V</i> upon heating and cooling under an argon atmosphere. ....	111
Table 9: CTEs of Os metal in <i>a</i> , <i>c</i> and <i>V</i> upon heating and cooling under 4 vol% H <sub>2</sub> /Ar reforming gas atmosphere. ....	124
Table 10: Crystal structures and lattice parameters of iridium borides. ....	189



## CHAPTER 1: INTRODUCTION AND LITERATURE REVIEW

Stiff, incompressible and superhard materials are of great importance and interest for science, technology and industrial applications. [1, 2] They can be used as abrasives and where wear and oxidation resistance are important design parameters. Modern materials science and engineering places a significant emphasis on the rational design and synthesis of new materials possessing superior mechanical and functional properties. Novel superhard materials with hardness higher than 40 GPa are one of the focal points of such materials' development [3-9]. The methodology and criteria used in searching for these materials were described in a series of publications [10, 11]. It was postulated that the structural stability, such as elastic stiffness, resistance to plastic deformation as well as resistance to structural changes, is a measure of the material's hardness [12]. The chemical bonding between individual atoms determines hardness, the bond strength determines the elastic stiffness, and the mobility of dislocations determines the plastic deformation of materials. For the elastic stiffness, both resistance of bonds to stretching and bending are important. The resistance to stretching is measured by the elastic bulk modulus and resistance to bending is measured by shear modulus. [10] To have high stiffness, both bulk and shear moduli have to be maximized. Resistance to plastic deformation should also be high for the material to be hard, as the plasticity is determined by the dislocation mobility, which should be suppressed as much as possible.

It has been found that the three dimensional covalent network formed by tetrahedrally bonded  $sp^3$  carbon atoms brings extremely high hardness to diamond. [13] *c*-BN also has very

symmetric covalent bonding structure similar to diamond. Thus, a three-dimensional network with strong bonds is required for a material to be superhard. A quest of challenging mechanical properties of diamond is always present, and a number of different strategies to search for the ultra-hard and ultra-stiff solids are employed and reported [13]. The strategies to design compounds with high elastic stiffness are also outlined in [12]. The measures of stiffness of the material are (1) bulk modulus, which is resistance to the volume change of the material, and (2) shear modulus, which is a resistance to shape change [14-16]. From known materials, diamond has the highest bulk modulus and it was postulated that it is unlikely that a material with a lower bulk modulus than that of diamond can have higher hardness. [10, 12]. One of the new approaches to design superhard and ultra-incompressible materials has been reported by Kaner *et al.* [13], by combining metals that have a high bulk modulus with small, covalent bond-forming atoms. The compounds with high bulk modulus have been screened in [12] and it was identified that among the first 94 chemical elements in the periodic table, osmium (Os) and carbon (C) provide the highest values of bulk moduli – 462 GPa [17] and 443 GPa [12, 14, 18], respectively (Figure 1), with rhodium (Rh) – 380 GPa [19], and iridium (Ir) – 383 GPa [19], rhenium (Re) – 370 GPa [19], following very closely to C and Os values. Ruthenium (Ru) – 348 GPa [19], tungsten (W) – 308 GPa [19], platinum (Pt) – 282.7 GPa [20], molybdenum (Mo) – 259.77 GPa [21], gold (Au) – 220 GPa [22], and tantalum (Ta) – 189.72 GPa [23] are the next elements with high bulk moduli [12]. There is a direct correlation between the reported bulk moduli of different materials and their valence-electron volumetric density (VED) [12, 24]. The VED is determined by the number of valence electrons divided by the unit cell volume, and C and Os elements have the highest VED values reported [10, 12].

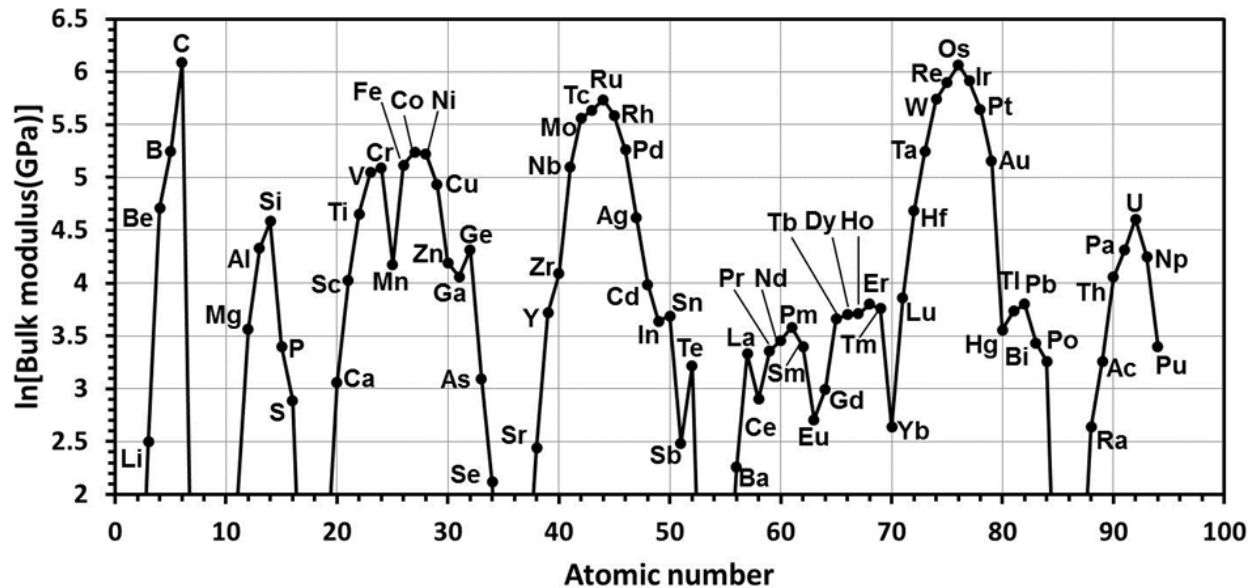


Figure 1: Bulk moduli of the elements. Note that the modulus scale is logarithmic. (data from [19]). Reprinted from International Journal of Refractory Metals and Hard Materials, 24, J.J. Gilman, R.W. Cumberland and R.B. Kaner, Design of hard crystals, 1-5, [10] Copyright (2006), with permission from Elsevier.

In addition to the bulk modulus, the shear modulus is another key property of material determining its hardness. It is an even more important property than the bulk modulus as the shear strain at an indentation can reach up to 100% or more, while the volumetric strain can only approach 20% for covalent compounds and is much less for metals [10]. Here again diamond has the highest shear modulus, namely 580 GPa (octahedral plane), with 210 GPa for Ir following next; however, Ir is only about half as stiff as diamond [12, 19]. First principles calculations have shown that Os may be stiffer ( $C_{44}=256$  GPa) than Ir in shear [25].

While diamond exhibits both high bulk modulus and high hardness, Os has low hardness – 3.9 GPa, which is still the highest hardness reported for the metallic materials. The low hardness of Os indicates low ability of the metal to resist plastic deformation, while the elastic stiffness of the compound is high. A high ductility is determined by the movements of

dislocations, which is responsible for plastic deformation and low hardness of the material. The dislocation mobility is determined by viscosity associated with conduction electrons, phonons, or both and the mobility can be suppressed by the presence of the barriers to impede the movements of the core of dislocations. [11] In case of simple metals, where bonding is not directional, non-localized and a “sea” of the electrons is present, the barriers are low and dislocations move easily compromising the resistance of material to plastic deformation [12, 24]. It was realized that the crystal structures of simple metals do not have significant static barriers to dislocation motions [11, 24]. Thus, in order to improve the resistance to plastic deformation, the barriers to prevent or limit the dislocation movement should be very local to the scale of the dislocation core. Therefore, local chemical bonding will lead to a low mobility of the dislocations, improved resistance to plastic deformation, and, as a result, increased hardness.

In the past decade, there has been a significant interest in the transition metal boride, nitride, and carbide compounds and the number of papers published on the synthesis and properties of these materials explored in the past 3 to 5 years [1, 26-50]. While carbides and oxides of some transition metals formed highly incompressible materials such as  $\text{RuO}_2$  [51] and WC, borides of transition metals are more likely to form high hardness materials such as  $\text{ReB}_2$  [52] and  $\text{OsB}_2$  [13, 53]. Extensive resources have been dedicated to the synthesis and study of  $\text{OsB}_2$ ,  $\text{ReB}_2$ ,  $\text{RuB}_2$ ,  $\text{IrB}_{1.1}$ ,  $\text{WB}_4$ ,  $\text{CrB}_4$ ,  $\text{Os}_{1-x}\text{Ru}_x\text{B}_2$ ,  $\text{Re}_x\text{W}_{1-x}\text{B}_4$  and other transition metal borides. [52-57].  $\text{OsB}_2$  and  $\text{ReB}_2$  have received special attention, as they were reported to have high valence-electron density due to presence of Os and Re ions in the lattice while, at the same time, ultra-incompressibility and high stiffness arising from the high degree of B-B and Os(Re)-B bond covalency [4, 8, 58]. Unlike  $\text{ReB}_2$  and  $\text{OsB}_2$ , iridium borides have never been reported with

integer iridium to boron ratio. Thus, it is worthwhile to investigate new synthetic routes to borides such as IrB<sub>2</sub>. Herein is a comprehensive review of transition metal borides focusing on Re-B, Os-B and Ir-B systems.

### 1.1 Rhenium Diboride

Rhenium diboride (ReB<sub>2</sub>) was first synthesized by Placa *et al.* more than 50 years ago, [59] but its interesting mechanical properties were revealed only recently. It was reported that ReB<sub>2</sub> has a hardness of 48 GPa when the applied load is 0.49 N [52], which means the ReB<sub>2</sub> has the highest hardness among all the transition metal diborides. ReB<sub>2</sub> is an ultra-incompressible material with bulk modulus in the range of 334 GPa to 371 GPa. [52, 60-65] The high shear modulus of ReB<sub>2</sub> ( $G=276$  GPa [64]) makes it suitable for applications in abrasive tools and wear resistant coatings. The metallic property of ReB<sub>2</sub> as a hard material is also very interesting while most of other hard materials are semiconductor or insulator. This new superhard ceramic attracted lots attention in the scientific community but brought controversy as well. Dubrovinskaia *et al.* [66] suggested that the hardness of ReB<sub>2</sub> was overestimated since the indentation size effect exists in the reported load range. Also, Chung *et al.* reported that the ReB<sub>2</sub> is able to scratch polished diamond [52, 67], but it was not reproduced by Otani *et al.* [68] In another report, much lower hardness (22 GPa) was reported when ReB<sub>2</sub> was synthesized under high temperature and high pressure, [69] although it was explained that excess boron used in the synthesis should be responsible for the degradation of mechanical properties. [70] Regardless of

the controversy, it is accepted that  $\text{ReB}_2$  is a hard and incompressible material. The discovery of its excellent mechanical properties is a great success for the new paradigm of designing superhard materials. This section will serve as a review on the rhenium boride system but mainly focus on the  $\text{ReB}_2$ .

### 1.1.1 Synthesis of $\text{ReB}_2$

$\text{ReB}_2$  was first synthesized in 1962 by heating elemental Re and B powders with molar ratio of 1:2 under vacuum at 1200 °C or under helium flow at 1500 °C [59].  $\text{ReB}_2$  has also been synthesized with other methods such as spark plasma sintering (SPS) [70, 71], pulsed laser deposition (PLD) [45], arc melting [52, 64, 69, 70], zone melting [72] and optical floating methods [73]. Polycrystalline  $\text{ReB}_2$  was synthesized in a DS6×8MN cubic press at 5 GPa and 1600°C for 60 minutes. [61] In order to measure the intrinsic properties of  $\text{ReB}_2$ , single crystals were grown using an aluminum flux at 1400°C [46], which was the first synthesis of superhard material by flux crystal growth under ambient pressure.  $\text{ReB}_2$  single crystal tends to preferentially grow along the (001) direction [46], which agrees with the results reported using an optical floating zone (FZ) furnace [73].  $\text{ReB}_2$  films with thickness of 0.3µm were prepared by Latini *et al.* [45] using pulsed laser deposition technique. Hexagonal platelets of  $\text{ReB}_2$  crystals were also prepared using  $(\text{B}_3\text{H}_8)\text{Re}(\text{CO})_4$  molecular precursor through the confined-plume chemical deposition technique. [74] In most of the high-temperature syntheses of  $\text{ReB}_2$ , excess boron was used to compensate for boron loss during high-temperature sintering [45, 61, 63, 64, 69]. 1:2.5 molar ratio between Re to B was generally used in their syntheses. However, excess

boron located along grain boundaries of polycrystalline  $\text{ReB}_2$  can degrade the  $\text{ReB}_2$  properties. Thus, a method does not involve the boron loss issue (or does not require excess boron) is desired for the synthesis of phase pure  $\text{ReB}_2$ .

The formation of  $\text{ReB}_2$  was studied using density functional calculations, which regards B atom incorporation into a Re lattice and occupation of interstitial sites. [75] Crystal structure of  $\text{ReB}_2$  and  $\text{ReB}_3$  were studied based on this model. [75] Other rhenium borides, such as  $\text{Re}_2\text{B}$ ,  $\text{Re}_3\text{B}$ ,  $\text{Re}_7\text{B}_3$  and  $\text{ReB}_3$ , were also successfully synthesized. [71, 76-81]  $\text{Re}_2\text{B}$  was only reported by Neshpor *et al.* [76] in 1958, with no further reports.  $\text{Re}_3\text{B}$ ,  $\text{Re}_7\text{B}_3$  and  $\text{ReB}_3$  were found in arc melted rhenium and boron powders [77]. Unfortunately, no details about the experimental procedures, such as molar ratio of Re to B and arc melting times, were provided. The appearance of different phases is very likely due to inhomogeneous arc melting:  $\text{Re}_3\text{B}$  and  $\text{Re}_7\text{B}_3$  formed at Re rich region, while  $\text{ReB}_3$  formed at boron-rich region. Impurities such as  $\text{Re}_3\text{B}_7$  and  $\text{Re}_7\text{B}_3$  were also observed during the synthesis using SPS technique [71]. In addition to  $\text{Re}_7\text{B}_3$ ,  $\text{Re}_3\text{B}$  and  $\text{ReB}_3$  were also observed as byproducts in [78] while the authors were preparing Re and  $\text{YB}_6$  alloys. It shows that the stoichiometry of Re-B compounds is dependent on the ratio of raw Re and  $\text{YB}_6$  ratio, which confirmed that inhomogeneous mixed Re and B powders can result in formation of other Re-B compounds as byproducts. Atomic ratio between B and Re in Re-B compounds increases with increasing amounts of B input.  $\text{Re}_7\text{B}_3$  was also observed as an impurity when the floating zone method was used for  $\text{ReB}_2$  synthesis. [73] This was due to excess Re metal in the molten zone from the Re rod that was used for the synthesis.  $\text{Re}_3\text{B}$  was synthesized again in 1996, by arc melting constituents under argon, annealing at 1070 K for 280 hours in an evacuated sealed quartz tube and quenching into cold water. [79] A series of rhenium

borides including  $\text{Re}_3\text{B}$  were obtained under high pressure and high temperature (10 GPa, 1800°C) sintering and quenching with the use of nanocrystalline rhenium and amorphous boron precursors. [80] The Re-B phase diagram was reported by Portnoi *et al.* [82] and is shown in Figure 2.  $\text{Re}_3\text{B}$ ,  $\text{Re}_7\text{B}_3$  and  $\text{ReB}_2$  were also observed when Re and B powders were loaded to diamond anvil cell (DAC) for *in situ* X-ray diffraction analysis at different temperature and pressure. [81] Since the B to Re atomic ratio is very low in  $\text{Re}_3\text{B}$ ,  $\text{Re}_2\text{B}$  or  $\text{Re}_7\text{B}_3$ , there are less B-B or Re-B covalent bonds exist in their unit cell compared to the higher borides of rhenium. Thus,  $\text{Re}_2\text{B}$ ,  $\text{Re}_3\text{B}$  and  $\text{Re}_7\text{B}_3$  are not likely to possess high hardness. That is why  $\text{ReB}_2$  attracted the most attention among all the Re-B compounds. As of yet, phase pure  $\text{ReB}_3$  has not been synthesized.  $\text{ReB}_3$  may have higher hardness than  $\text{ReB}_2$ , and thus it is meaningful to synthesize phase pure  $\text{ReB}_3$  and study its mechanical properties.

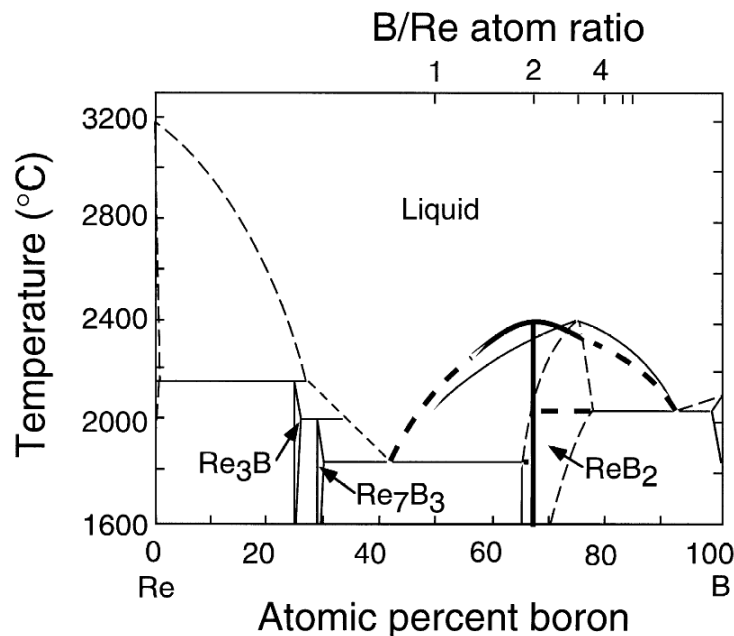


Figure 2: The phase diagram of the Re-B system. [82] Reprinted from Journal of Alloys and Compounds, 252, Shigeki Otani, Takashi Aizawa and Yoshio Ishizawa, Preparation of  $\text{ReB}_2$  single crystals by the floating zone method, 19-21, [73] Copyright (1997), with permission from Elsevier.



Another higher rhenium boride,  $\text{ReB}_4$ , has not yet been prepared and its properties have been studied using computational methods such as local density approximation (LDA) and generalized gradient approximation (GGA). [34] It was predicted that  $\text{ReB}_4$  would be another superhard material. The electronic densities of states and electronic localization function analysis confirmed that  $\text{ReB}_4$  possesses strong B–B and Re–B bonding. [83] However, this phase is still awaiting synthesis. Soto *et al.* modeled the formation of  $\text{ReB}_x$  ( $x$  from 0 to 3) using solid state reaction with density functional theory. It was proposed that boron atoms are more likely to occupy interstitial sites of the parent metal (Re). [75] Structural and magnetic properties were also studied computationally by assuming small rhenium boride clusters exist in  $\text{Re}_m\text{B}_n$  ( $m=1-3$ ,  $n=1-3m$ ). [84]

### 1.1.2 Crystal structure of $\text{ReB}_2$

$\text{ReB}_2$  possesses hexagonal crystal structure in the space group  $P6_3/mmc$ , No.194 [59], with  $a$  ranging from 2.897 Å to 2.9035 Å and  $c$  from 7.472 Å to 7.485 Å [45, 46, 52, 59, 61, 64, 69-73] depending on the synthesis methods described in the previous section. The hexagonal structure is the only rhenium diboride structure that has been synthesized. Neutron diffraction studies indicated that the two Re atoms occupy the sites  $(1/3, 2/3, 1/4)$  and  $(1/3, 2/3, 3/4)$ , and the four B atoms occupy the sites  $(2/3, 1/3, 0.048)$ ,  $(1/3, 2/3, 0.548)$ ,  $(2/3, 1/3, 0.452)$  and  $(1/3, 2/3, 0.952)$ . [56, 85] The  $\text{ReB}_2$  unit cells are shown in Figure 3. The hexagonal structure consists of alternating layers of hexagonally arranged rhenium and boron. Boron forms infinite sheets consisting of 6-member rings in a chair configuration. The chair configuration allows close

packing of the layers. The shortest and longest B–B bond lengths are 1.820 Å and 3.025 Å, respectively; while the shortest and longest Re–B bond lengths are 2.227 Å and 2.257 Å, respectively. [85] Preferred orientation in the (002) direction was observed when a ReB<sub>2</sub> film was prepared by pulsed laser deposition. [45] The Re lattice expands 5% when B is incorporated into interstitial sites of Re, forming ReB<sub>2</sub> [52], which results in the shortest metal–metal bonds among all the transition metal diborides [86]. First principles calculations show that ReB<sub>2</sub> has stronger directional bonding between ions than other transition metal borides or nitrides. [87] ReB<sub>2</sub> has covalent-like Re–B bonds due to hybridization of Re–5d and B–2p states. However, there is also some ionic character with electron transfer from rhenium to boron atom and the obvious metallic characters. [88]

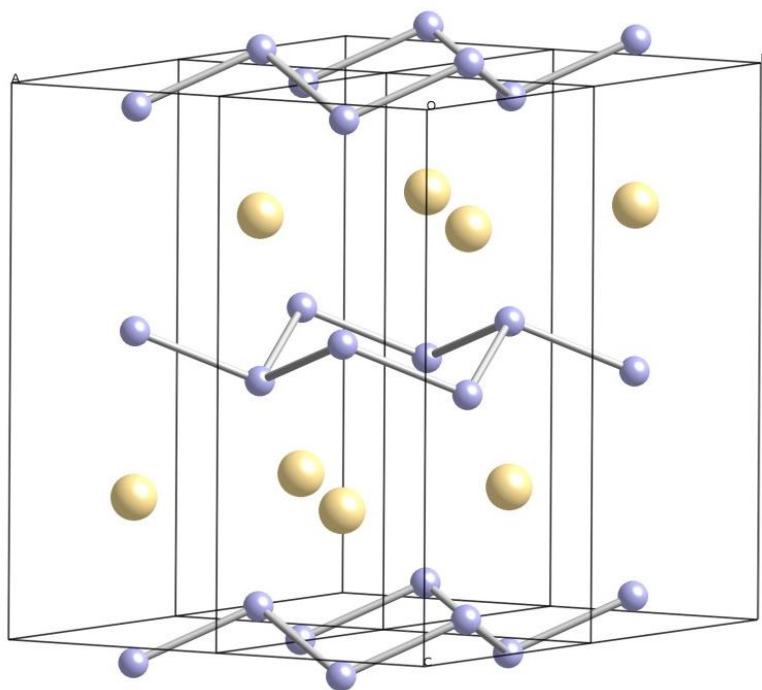


Figure 3. Schematic presentation of the ReB<sub>2</sub> unit cells. B atoms — small blue spheres; Re atoms — big yellow spheres.

### 1.1.3 Stability of ReB<sub>2</sub>

First principles calculations have shown that ReB<sub>2</sub> is stable in both hexagonal and orthorhombic structures, but the hexagonal structure is more stable than the orthorhombic structure. [87, 89] An appearance of a pseudogap around the Fermi level helps increase the stability of the hexagonal structure of ReB<sub>2</sub>. [87] Among all the Re–B compounds, ReB<sub>2</sub>, Re<sub>2</sub>B<sub>3</sub>, ReB, Re<sub>2</sub>B and Re<sub>7</sub>B<sub>3</sub> were predicted to be mechanically stable based on density functional theory. [90] A different calculation, also based on density functional theory, shows that the boron to rhenium molar ratios of 2:1 and 4:3 have the highest stability among all the Re–B compounds. [84]

#### (1) High temperature stability of ReB<sub>2</sub>

The thermal stability and oxidation resistance of ReB<sub>2</sub> single crystal and powder was studied in dry air up to 1000°C with thermogravimetric analysis. [46] Unlike some other transition metal borides [91, 92], ReB<sub>2</sub> exhibits weight loss at high temperature in air. Weight losses happened at 800°C for ReB<sub>2</sub> single crystal and 600°C for ReB<sub>2</sub> powder due to formation of volatile ReO<sub>3</sub>. [46] Total of 1.5% and 50% of weight losses were observed to ReB<sub>2</sub> single crystal and powder, respectively, by the end of the run. [46] The phase stability of ReB<sub>2</sub> was studied at 2000 K with laser heating diamond anvil cell conjunction with synchrotron X-ray diffraction, which shows that no phase transformation was observed. [60] However, during the *in situ* high-temperature XRD studies in [61], ReB<sub>2</sub> XRD peaks completely disappeared at 700°C. The authors suggested that a phase transition occurred in between 600°C and 700°C. It was also

reported that rhenium borides have low oxidation resistance in air [82], suggests that these materials should be stored in inert atmosphere.

## (2) High pressure stability of ReB<sub>2</sub>

A high-pressure phase transition from the traditional *P6/mmc* hexagonal structure to MoB<sub>2</sub>-type structure was predicted to occur at 272 GPa according to first principles calculations by Zhong *et al.* [88] Pressure-induced structural transformations of rhenium borides were studied using density-functional theory, which shows that ReB<sub>2</sub> and Re<sub>3</sub>B were the most stable phases among all the Re–B compounds at high-pressure (up to 90 GPa). [90] The high-pressure stability of ReB<sub>2</sub> was investigated by *in situ* measurements performed during the compression of ReB<sub>2</sub> powders. These experiments indicated that ReB<sub>2</sub> is stable at least up to 41.8 GPa without phase transformation. [61] The phase stability of ReB<sub>2</sub> was also studied under pressures up to 30 GPa with diamond anvil cell experiments in conjunction with synchrotron X-ray diffraction. No phase transformation was observed other than changes of lattice parameters. [93] Even if both pressure and temperature were applied up to 7.5 GPa and 1100K, respectively, still no phase transformation was observed, proving the high stability of hexagonal ReB<sub>2</sub>. [60]

### 1.1.4 Properties of ReB<sub>2</sub>

#### (1) Hardness and strength

The hardness of ReB<sub>2</sub> was predicted to be 46 GPa by density functional theory. [85] Strong B–B and Re–B bonds play critical roles to its high hardness according to electronic and phonon analyses. [85] The calculations show that ReB<sub>2</sub> has its highest hardness of 50.3 GPa

along the  $c$  crystallographic axis. [94] It was also stated that hardness is mainly determined by transversely oriented bonds. [94] Numerical estimations of Vickers Microhardness for rhenium borides, carbides and nitrides indicate that adding additional small atoms may or may not increase its hardness. [95]

Microindentation was performed on a polished  $\text{ReB}_2$  ingot. [52] The average hardness was measured to be  $30.1 \pm 1.3$  GPa with loading of 4.9N and  $48.0 \pm 5.6$  GPa with loading of 0.49N. The maximum hardness was reported to be 55.5 GPa under 0.49 N of load. [52] The distribution of the hardness values versus indentation load is shown in Figure 4A. In another report, a maximum hardness of  $49.9 \pm 4.6$  GPa under a 0.49 N load was reported for a  $\text{ReB}_2$  film prepared by pulsed laser deposition. [45] The (002) plane of  $\text{ReB}_2$  shows the highest hardness of  $40.5 \pm 2.4$  GPa at low load when measured with microindentation on  $\text{ReB}_2$  single crystals. [46] Nanoindentation on the (002) plane of  $\text{ReB}_2$  gives a lower hardness of  $36.4 \pm 0.2$  GPa. [46]  $\text{ReB}_2$  was shown to scratch the face of natural diamond parallel to (100) plane [52] (Figure 4B), but it was not reproduced [68]. The  $\text{ReB}_2$  single crystals have shown lower hardness than polycrystalline  $\text{ReB}_2$  samples due to grain boundaries in the polycrystalline sample, which inhibit crack growth. [46, 96, 97] Flux-grown  $\text{ReB}_2$  crystal [46] shows a lower hardness than that of the  $\text{ReB}_2$  crystal produced by tri-arc or zone melting [46, 52, 72, 98]. This is due to the higher boron deficiency in flux-grown  $\text{ReB}_2$  crystals, which leads to the reduction of the number of B–B and Re–B bonds. [46] There are more boron vacancies in the flux-grown  $\text{ReB}_2$  crystals as corroborated by the smaller lattice parameters of the flux-grown  $\text{ReB}_2$  crystal when compared to the  $\text{ReB}_2$  prepared by tri-arc or zone melting methods. [70, 72] In order to develop a route that produces the highest hardness, different molar ratios of Re : B and pressure – temperature – time

of sintering conditions were tried by Qin *et al.* [69]. It was reported that preparation under 5 GPa and 1600 °C for 60 min with Re and B mixed with a molar ratio of 1:2.5 produced the best results. [69] However, the synthesized rhenium diboride still showed a very low Vickers hardness of only 20 GPa, which is far from superhard. [69] The excess boron used by Qin *et al.* in their synthesis may be responsible for the low measured hardness according to [70]. Vickers microhardness values of ReB<sub>2</sub> produced by spark plasma sintering at 20 MPa and 1600 °C for 34.5 min are in the range of 20.7–31.1 GPa depending on indentation load, and the fracture toughness was measured to be  $7.36 \pm 0.69 \text{ MPa}\cdot\text{m}^{1/2}$ . [71] Hardness of ReB<sub>2</sub> single crystal in (10 $\bar{1}$ 0) and (0001) planes at high temperature were measured by Otani *et al.* [68] A relatively high hardness was maintained at 1000°C with  $H_v = 14.3 \pm 0.6 \text{ GPa}$  in the (10 $\bar{1}$ 0) plane and  $H_v = 19.8 \pm 1.4 \text{ GPa}$  in the (0001) plane. [68] It is interesting to note that the melting point of ReB<sub>2</sub> is lower than other refractory borides such as TaB<sub>2</sub>, HfB<sub>2</sub> or ZrB<sub>2</sub>, but it has the highest hardness at 1000°C. [68]

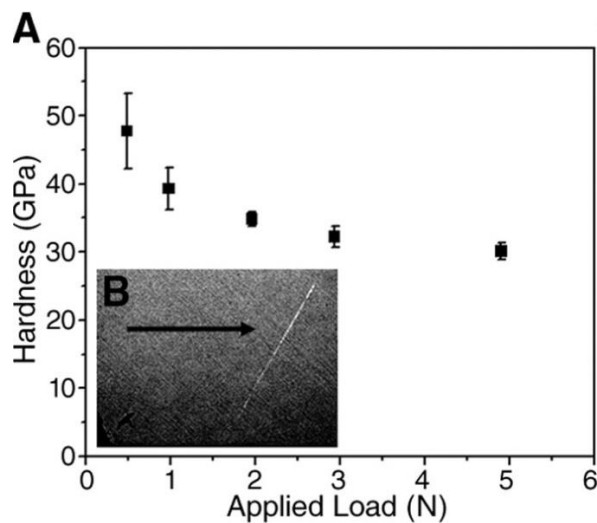


Figure 4:  $H_v$  of ReB<sub>2</sub> plotted as a function of load (A), and a scratch on the surface of a natural diamond parallel to the (100) plane created by an ingot of ReB<sub>2</sub> (B). From H.-Y. Chung, M. B. Weinberger, J. B. Levine, A. Kavner, J.-M. Yang, S. H. Tolbert and Kaner, Richard B.,

"Synthesis of Ultra-Incompressible Superhard Rhenium Diboride at Ambient Pressure," *Science*, vol. 316, pp. 436-439, 2007. [52] Reprinted with permission from AAAS.

The simulated Young's modulus of OsB<sub>2</sub> was reported to be between 642 and 725 GPa depending on the computational method. [40, 87, 99, 100] The shear modulus of ReB<sub>2</sub> was reported to be in the range of 289.4 to 310 GPa. [40, 87, 99-101] A high shear strength, 35.3 GPa, was predicted for ReB<sub>2</sub> from first principles calculations on the indentation strength of ReB<sub>2</sub> [102], which suggests that ReB<sub>2</sub> is suitable for applications in abrasive tools and wear resistant coatings. [102] ReB<sub>2</sub> possesses highly anisotropic elastic constants with the ratio  $E_{33}/E_{11}$  equal to 1.57, [70] and it is known that significant elastic anisotropy can induce microcracks easily [100, 103]. Thus, it is disadvantageous for use as an abrasive tool or wear resistant material. The anisotropic indentation modulus of ReB<sub>2</sub> was measured to be  $675 \pm 7$  GPa in the (002) plane and significantly lower ( $510 \pm 13$  GPa) for the perpendicular plane using nanoindentation. [46] The elastic moduli of ReB<sub>2</sub> increases as temperature decreases from room temperature towards 0 K. [104] The Poisson's ratios  $\nu_{13}$  and  $\nu_{31}$  are very low, indicating that B-B and B-Re bonds in the *c*-axis direction are very strong. [104]

## (2) Compressibility

In the past decade, many theoretical calculations [40, 87, 100, 101, 105] and experimental studies have been performed on the incompressibility of ReB<sub>2</sub>. [52, 60-65]. Both LDA and GGA calculations have shown that ReB<sub>2</sub> has a high bulk modulus comparable to diamond. [106] The bulk modulus of ReB<sub>2</sub> was predicted to be 350 GPa by density-functional theory. [85] *Ab initio* plane-wave pseudo potential density functional theory [101] also predicts that ReB<sub>2</sub> should be a low-compressible material with a bulk modulus of 359.9 GPa. Hexagonal ReB<sub>2</sub> shows anisotropy in compressibility with larger compressibility in the *c* direction than other directions.

[101] The shear modulus was calculated to be 298.2 GPa, which is about 54.1% and 70.1% of the shear modulus of diamond and superhard *c*-BN, respectively. [101] The bulk and shear moduli of ReB<sub>2</sub> were reported to be 356 GPa and 293 GPa, respectively using first-principles plane-wave basis pseudopotential calculations. [40] *Ab initio* density functional theory (DFT) calculations by Zhang *et al.* indicated that ReB<sub>2</sub> has a high bulk modulus of 347.7 GPa and relatively low shear modulus of 273.5 GPa. [107] The low ratio of shear to bulk moduli indicates that ReB<sub>2</sub> is intrinsically brittle. [107] In summary, theoretical predictions of the bulk modulus of ReB<sub>2</sub> range from 335 to 377 GPa [40, 87, 100, 101, 105], showing very good agreement with experimental studies that the measured bulk modulus of ReB<sub>2</sub> to be in the range of 334 GPa to 371 GPa [52, 60-65].

The compressibility of ReB<sub>2</sub> was studied by *in situ* compression of ReB<sub>2</sub> powder up to 41.8 GPa [61]. Both *a* and *c* lattice parameters show nonlinear dependence on pressure [61], which is different from previously reports indicating a linear dependent relationship [52, 60]. The compressibility of ReB<sub>2</sub> was also studied with *in situ* high-pressure X-ray diffraction under quasi-hydrostatically pressure up to 30 GPa in a diamond anvil cell, from which the bulk modulus was calculated to be 360 GPa. [52] The same bulk modulus value was obtained in an angular dispersive high-pressure X-ray diffraction study by Pellicer-Porres *et al.* at pressures up to 25 GPa. [63] Anisotropic compressibility was found in the *a* and *c* axes of ReB<sub>2</sub> with the *c* direction less compressible than the *a* direction. This resulted from greater electronic repulsion along the *c* direction while atoms are all perfectly aligned along *c* direction. [52] The bulk modulus of ReB<sub>2</sub> at standard temperature and pressure (STP) was found to be 334 ± 23 GPa by synchrotron X-ray diffraction analysis, which shows good agreement with other reported values.



[60] The compressibility of ReB<sub>2</sub> was studied under pressures up to 30 GPa in a diamond anvil cell and analyzed using synchrotron X-ray diffraction. [93] Anisotropic expansion was observed [93], which is consistent with the theoretical results [101]. The anisotropic and nonhomogeneous compressibility are due to the difference of the Re–B and B–B bonds, and also between nonequivalent Re–B bonds. [1, 63] Compressibility in the *a* and *c* lattice parameters are  $1 \times 10^{-3}$  GPa<sup>-1</sup> and  $6.2 \times 10^{-4}$  GPa<sup>-1</sup>, respectively. [63] The elastic moduli of polycrystalline ReB<sub>2</sub> were measured as a function of temperature (5–325K) using resonant ultrasound spectroscopy (RUS), it was found that ReB<sub>2</sub> has high bulk (317 GPa) and shear moduli (276 GPa) at room temperature, and the moduli increase with decreasing temperature with softening below 50K. [64] The shear modulus of ReB<sub>2</sub> was reported to be  $223 \pm 11$  GPa by surface Brillouin spectroscopy (SBS) [65]

The complete elastic modulus tensor of ReB<sub>2</sub> was measured using resonant ultrasound spectroscopy by Levine *et al*, [70] which shows that the moduli are highly dependent on the morphology of samples and also affected by presence of excess boron. [70] The lattice vibrational properties of ReB<sub>2</sub> were examined in a diamond anvil cell at pressures up to 8 GPa using Raman spectroscopy, which shows that both the B–B and Re–B bonds play an important role supporting the applied load and the bonds along the *c*-axis tend to take greater loads. [108] Since the B to Re atomic ratio is very low in Re<sub>3</sub>B, Re<sub>2</sub>B or Re<sub>7</sub>B<sub>3</sub>, there are less B–B or Re–B bonds in their unit cells compared to the higher borides. Thus, Re<sub>2</sub>B, Re<sub>3</sub>B and Re<sub>7</sub>B<sub>3</sub> are not likely to possess high hardness or incompressibility. However, Re<sub>7</sub>B<sub>3</sub> has been reported to have even higher incompressibility ( $B = 483$  GPa) than ReB<sub>2</sub> ( $B \approx 360$  GPa). [81]

### (3) Thermal expansion

The thermal expansion and heat capacities of  $\text{ReB}_2$  within the temperature range of 0 to 2000K, were calculated by first-principles calculations with the plane-wave pseudopotential density functional theory method. [109] The calculations indicated that high temperatures lead to a larger heat capacity, and a larger coefficient of thermal expansion at a constant pressure. [109] The Debye temperature at ambient temperature of  $\text{ReB}_2$  was reported to be 731K [70], which is slightly lower than the calculated value, 744K, by first-principles plane wave pseudopotential calculations. [109] Calculations also show that the coefficient of thermal expansion of  $\text{ReB}_2$  should be highly isotropic and the volumetric CTE is about 3 times that of the linear CTE. [109] The volumetric coefficient of thermal expansion of  $\text{ReB}_2$  was calculated to be  $1.4 \times 10^{-6} \text{ K}^{-1}$  at 1000 K [109] and is in good agreement with the measured value [85] of  $1.95 \times 10^{-6} \text{ K}^{-1}$ . The coefficient of thermal expansion is more sensitive to temperature rather than pressure. [109] The higher the temperature, the slower the thermal expansion coefficient increases. [109]

The thermal expansion behavior of  $\text{ReB}_2$  was studied [60, 61, 85]. Polycrystalline  $\text{ReB}_2$  powder was heated up to 1000°C and the coefficients of thermal expansion (CTEs) of  $a$ ,  $c$  and unit cell volume for  $\text{ReB}_2$  were measured to be  $8.5(5) \times 10^{-6} \text{ }^\circ\text{C}^{-1}$ ,  $8.1(5) \times 10^{-6} \text{ }^\circ\text{C}^{-1}$  and  $2.5(1) \times 10^{-5} \text{ }^\circ\text{C}^{-1}$ , respectively. [61] A thermal expansion study by Zhou *et al.* [85] was performed up to about 1750K and the reported CTEs for the lattice parameters of  $a$  and  $c$  are  $6.5 \times 10^{-6} \text{ K}^{-1}$ . Both investigations shows that CTEs along the  $a$  and  $c$  crystallographic directions are almost identical, which agrees with the calculated results that  $\text{ReB}_2$  has isotropic thermal expansion. In [60] the thermal equation was given as Equation 1.1 where  $\alpha$  is volumetric CTE and  $T$  is temperature.

$$\alpha = 1.33 \times 10^{-5} + 1.48 \times 10^{-8}T \quad (1.1)$$

The thermal expansion of ReB<sub>2</sub> was also studied at 2000 K by laser heating a diamond anvil cell in conjunction with synchrotron X-ray diffraction. It was found that ReB<sub>2</sub> is thermally isotropic and mechanically anisotropic. [93] The temperature dependence of the  $c/a$  ratio is as low as 10<sup>-6</sup> K<sup>-1</sup>, while the pressure dependence is about 9×10<sup>-4</sup> GPa<sup>-1</sup>, which means expansion is more affected by pressure rather than by temperature. [93] In addition, the melting point of ReB<sub>2</sub> was reported as 2400 °C in [68] and 1830 °C in [82].

#### (4) Other properties

The band structure, according to the first principles calculations, of ReB<sub>2</sub> indicates that it is a metallic conductor. [87] The resistivity of ReB<sub>2</sub> at room temperature was measured to be 45±15μΩ [46], which agrees well with the theoretical calculations [87, 100]. Levine *et al.* reported that ReB<sub>2</sub> does not show superconductivity until cooled down to 2.0K [46], while Strukova *et al.* reported  $T_c$  of ReB<sub>2</sub> is in the range of 4.5 to 6.3K and Re<sub>3</sub>B has superconductivity at  $T_c=4.7$ K [110]. The measured standard enthalpy of formation of ReB<sub>2</sub> is -18.4 kJ/g·atom by calorimetry. [111]

### 1.2 Osmium Diboride

Osmium diboride (OsB<sub>2</sub>) is another hard and ultra-incompressible material with hardness of 37 GPa [29] and a bulk modulus of 365-395 GPa [53]. The high hardness is due to the existence of short and strong B–B and Os–B bonds in the unique structure. The Os–B bonds have high covalent character because of the hybridization between the Os–5d and B–2p states.

The formation of orthorhombic OsB<sub>2</sub> is considered as boron atoms incorporated into hexagonal Os (parent metal) and a distortion of the unit cell to a body centered orthorhombic structure. [53] Similar to ReB<sub>2</sub>, OsB<sub>2</sub> also shows metallic character. There are three structures predicted for OsB<sub>2</sub>: orthorhombic, ReB<sub>2</sub>-type hexagonal and AlB<sub>2</sub>-type hexagonal structures. [112] First principles calculations predicted a high-pressure phase transformation from orthorhombic to ReB<sub>2</sub>-type hexagonal structure was predicted at 2.5 GPa [112] or 10.8 GPa [113], but no phase transformation was observed even at pressures up to 32 GPa [53]. The orthorhombic structure was the only structure that synthesized before the work by Xie *et al.*, in which a ReB<sub>2</sub>-type hexagonal OsB<sub>2</sub> was successfully synthesized for the first time.

### 1.2.1 Synthesis of OsB<sub>2</sub>

In 1961, Kempter *et al.* [114] claimed to have synthesized a hexagonal OsB<sub>2</sub> phase, but the reported lattice parameters are identical to those of OsB<sub>1.1</sub> (JC-PDS 030-0879 reported in 1978) suggesting that the phase actually produced was OsB<sub>1.1</sub>. Meanwhile, there was an unknown phase observed by Kempter *et al.* after heating 1Os : 2B, 2Os : 5B or 1Os : 3B mixtures above 1300°C. [114, 115] By heating finely divided elements at 1300°C for 6 hours followed by arc melting, the unknown phase was finally determined as orthorhombic OsB<sub>2</sub> in 1962, and this is the first synthesis of OsB<sub>2</sub>. [115] The crystal structure and stoichiometry of OsB<sub>2</sub> was confirmed again later in 1963 by Aronsson *et al.* and more accurate lattice parameters were reported. [116]

Two different methods were used to synthesize OsB<sub>2</sub> by Cumberland *et al.* [53]: 1) the self-propagating reaction of OsCl<sub>3</sub> and MgB<sub>2</sub> mixtures with molar ratio of 2:3 and 2) heating a mixture of osmium and boron powders with molar ratio of 1:5 at 1000°C for 3 days. Arc melting elemental powders under argon protective environment was also used to synthesize OsB<sub>2</sub>. [29] The phase diagram of Os–B system determined by metallographic investigations is presented in Figure 5. [117] The melting point of orthorhombic OsB<sub>2</sub> is 1870 ± 20°C, and the solid solubility of B in Os was found to be less than 0.5 at% B. [117] The molar ratio and composition of elemental powders are very important for the synthesis of pure OsB<sub>2</sub>. It was very difficult to homogenize the arc melted OsB<sub>2</sub> samples by annealing even at temperatures up to 1740°C for as long as 48h. [117] Thus, re-melting after arc melting was usually performed to ensure homogeneity of the OsB<sub>2</sub> product. [118] Well-formed orthorhombic OsB<sub>2</sub> single crystals with flat facets have been grown using a Cu-B eutectic flux at 1450°C. [119] The dimensions of the single crystals are about 0.27×0.18×0.15 mm<sup>3</sup>. [119]

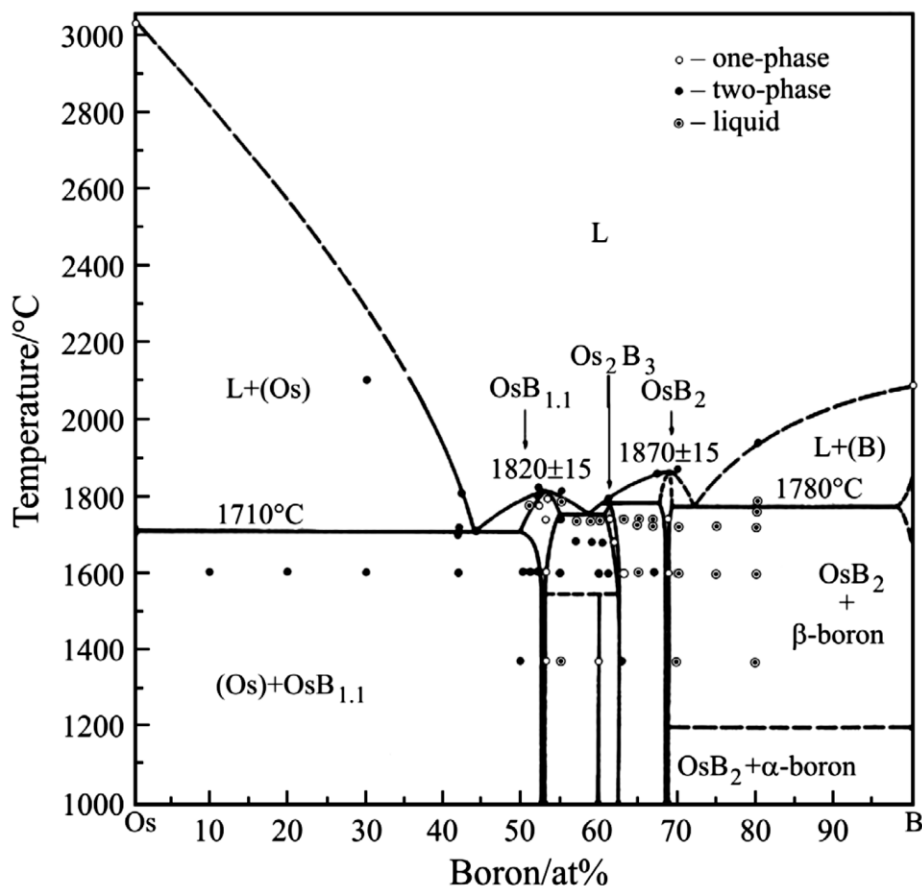


Figure 5: The phase diagram of the Os-B system. Springer and the original publisher / Journal of Thermal Analysis and Calorimetry, 76, 2004, 975-983, Phase diagram investigation and thermodynamic study of Os-B system, L. Stuparević and D. Živković, Figure 7, original copyright notice is given to the publication in which the material was originally published, by adding; with kind permission from Springer Science and Business Media, [117].

### 1.2.2 Crystal structures of OsB<sub>2</sub> and phase transformation

Based on the neutron diffraction analysis, orthorhombic OsB<sub>2</sub> belongs to the space group *Pmmn*, No.59, with  $a = 4.685\text{\AA}$ ,  $b = 2.873\text{\AA}$  and  $c = 4.077\text{\AA}$ . [56] Orthorhombic OsB<sub>2</sub> has layered structure as shown in Figure 6A. The boron atoms form boat-like six member rings and the Os

atom arrangement is in corrugated hexagonal sheets. [56] The Os–B distances, very important parameters that affect mechanical properties of the  $\text{OsB}_2$ , are 2.172(2) Å and 2.293(3) Å, and the B–B distances are 1.820(2) Å and 1.899(2) Å. [56] The two Os atom positions are (0.25, 0.25,  $z$ ) and (0.75, 0.75,  $\bar{z}$ ) with  $z = 0.1545$ . The four B atom positions are ( $x$ , 0.25,  $z$ ), ( $\bar{x}+0.5$ , 0.25,  $z$ ), ( $\bar{x}$ , 0.75,  $\bar{z}$ ) and ( $x+0.5$ , 0.75,  $\bar{z}$ ) with  $x = 0.0557$  and  $z = 0.6325$ . [56]

Before the work reported by Xie *et al.*, the orthorhombic structure was the only  $\text{OsB}_2$  structure that had been experimentally observed. However,  $\text{OsB}_2$  can potentially adopt three structures: orthorhombic (Figure 6A),  $\text{ReB}_2$ -type hexagonal (Figure 6B) and  $\text{AlB}_2$ -type hexagonal (Figure 6C). These structures were predicted by Chen *et al.* based on the first-principles theory (local density approximation). [112] The  $\text{ReB}_2$ -type (hexagonal-I) structure is in space group  $P6_3/mmc$  (*hP6*, No. 194) with lattice parameters  $a = 2.900$  Å and  $c = 7.478$  Å. The  $\text{AlB}_2$ -type (hexagonal-II) structure is in space group  $P6/mmm$  (*hP3*, No.191) with lattice parameters  $a = 3.005$  Å and  $c = 3.253$  Å. By comparing the heats of formation of the three structures, the orthorhombic structure is the most stable structure followed by the hexagonal-I and then the hexagonal-II structures.

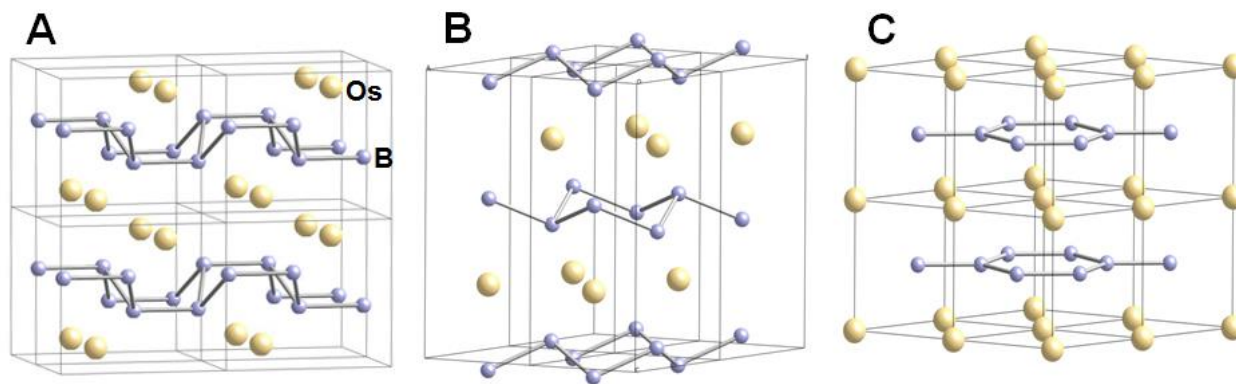


Figure 6: The three predicted crystal structures of  $\text{OsB}_2$ :  $\text{RuB}_2$ -type (orthorhombic) (A);  $\text{ReB}_2$ -type (hexagonal-I) (B);  $\text{AlB}_2$ -type (hexagonal-II) (C).

Calculations also have shown that the transformation from orthorhombic to hexagonal-I structure can occur at pressures as low as a 2.5 GPa. [112] The pressure induced phase transformation of orthorhombic OsB<sub>2</sub> to hexagonal-I type OsB<sub>2</sub> was also studied by Ren *et al.* [113] Their enthalpy calculations, using GGA simulation, indicated that the phase transition from orthorhombic to hexagonal-I structure of OsB<sub>2</sub> happens at 10.8 GPa. Although both theoretical studies predicted that phase transitions, orthorhombic OsB<sub>2</sub> exhibits a very small anisotropic volume compressibility when subjected to pressure up to 32 GPa, in a high-pressure diamond anvil cell. No phase changes were observed during hydrostatic compression [53]. Calculations also indicated that the phase transformation from orthorhombic to hexagonal is not affected by temperature, which means that the transformation can be purely pressure induced. [113] Both orthorhombic and hexagonal-I type OsB<sub>2</sub> are mechanically stable and the later has a higher bulk modulus, which means the hexagonal structure of OsB<sub>2</sub> is less compressible than the orthorhombic structure. [113] The ReB<sub>2</sub>-type hexagonal structure of OsB<sub>2</sub> shows the lowest compressibility along the *c* axis and it is comparable to diamond. [112] It is also important to note that the shear elastic constant  $C_{44}$  of hexagonal OsB<sub>2</sub> (209 GPa) is much larger than that of orthorhombic structure (80 GPa), which suggests that the hexagonal structure has greater resistance in shear deformation in the (100) plane. [113]

While *oP*<sub>6</sub>-type orthorhombic OsB<sub>2</sub> has received the most attention, *oP*<sub>12</sub>-type orthorhombic OsB<sub>2</sub> was also predicted to be thermodynamically and mechanically stable. [120] The B–B bonds in the *oP*<sub>6</sub>-type structure are in layers and the lengths are almost equivalent (1.80 Å and 1.875 Å), but the B–B bonds in the *oP*<sub>6</sub>-type structure are split to alternative long (1.815 Å) and short (1.684 Å) chains. [120] The calculated average hardness and Young's modulus of the



$oP_{12}$ -type OsB<sub>2</sub> were 24.3 GPa and 471.1 GPa, respectively. The  $oP_{12}$ -type OsB<sub>2</sub> has a hardness slightly higher than that of the  $oP_6$ -type OsB<sub>2</sub> (22.8 GPa). The bulk modulus and shear modulus for the  $oP_{12}$ -type OsB<sub>2</sub> were calculated to be 315.9 GPa and 188.2 GPa, respectively, and for  $oP_6$ -type OsB<sub>2</sub> are 339 GPa and 187 GPa, respectively. In addition, the  $oP_{12}$ -type OsB<sub>2</sub> is predicted to be a semiconductor. [120]

### 1.2.3 Properties of OsB<sub>2</sub>

#### (1) Hardness and strength

The hardness of orthorhombic OsB<sub>2</sub> along the  $b$  and  $c$  crystallographic axes are 42.1 GPa and 45.5 GPa, respectively, based on the calculations by Šimůnek *et al.* [94] However, the hardness along the  $a$  direction was calculated to be only 25.6 GPa. A computational investigation (density functional theory) on the hardness of OsB<sub>2</sub>, indicated that additional boron results in an increase in the valence electron density and the formation of covalent bonds, which increases the hardness. [121] Covalent Os–B bonds in OsB<sub>2</sub> contribute to the high hardness of OsB<sub>2</sub> because the highly directional bonding is needed to withstand both elastic and plastic deformations. [122]

The first report of the hardness of orthorhombic OsB<sub>2</sub> shows that OsB<sub>2</sub> powder is able to scratch sapphire window, which means the OsB<sub>2</sub> has a hardness at least higher than 20 GPa. [53] Using microindentation, the average Vickers hardness of orthorhombic OsB<sub>2</sub> was measured to be approximately 37 GPa when the applied load is lowered to 0.245N. [29] The average nanoindentation hardness is  $21.6 \pm 3.0$  GPa at the maximum applied load of 0.49 N. [29] At the same time, an indentation size effect was observed; the hardness of OsB<sub>2</sub> increased significantly

when the applied load was decreased. In addition to the indentation size effect, the hardness on the grain along the  $\langle 100 \rangle$  direction is much higher than that along the  $\langle 001 \rangle$  direction. [29] The different measured hardness values along  $\langle 100 \rangle$  and  $\langle 001 \rangle$  may be from the anisotropy of the OsB<sub>2</sub> crystal structure itself because B–B bonds (1.80 Å) exist in  $\langle 100 \rangle$  direction are shorter and stronger than B–B bonds (4.10 Å) in  $\langle 001 \rangle$  direction, which results in stronger resistance to dislocation in the  $\langle 100 \rangle$  direction. [29] Microhardness measurements of OsB<sub>2</sub> were also performed on the (001) plane. A Vickers hardness ( $H_v=36$  GPa) was reported with an applied load of 0.6-0.8N, and decreased to 30 GPa when the load increased to 1N. [121] In order to compare the reported hardness values of orthorhombic OsB<sub>2</sub>, all the hardness values of orthorhombic OsB<sub>2</sub> from experimental studies are plotted in Figure 7. By studying the electronic and structural properties of orthorhombic OsB<sub>2</sub> using first principles calculation with local density approximation, it was concluded that Os–B bonds have strong covalent character and that the high hardness of OsB<sub>2</sub> is due to the covalent bonding between osmium 5d states and boron 2p states in the orthorhombic structure. [58] First principles calculations by Ji *et al.* indicated that the elastic properties of OsB<sub>2</sub> are more anisotropic than other Os–B phases. [123] The ideal tensile strength of OsB<sub>2</sub> was calculated to be higher than 20 GPa by first principles calculations. [124] However, the shear strength of OsB<sub>2</sub> ranges from 9.1 GPa to 26.9 GPa, which suggest a high anisotropy in shear strength. [124]

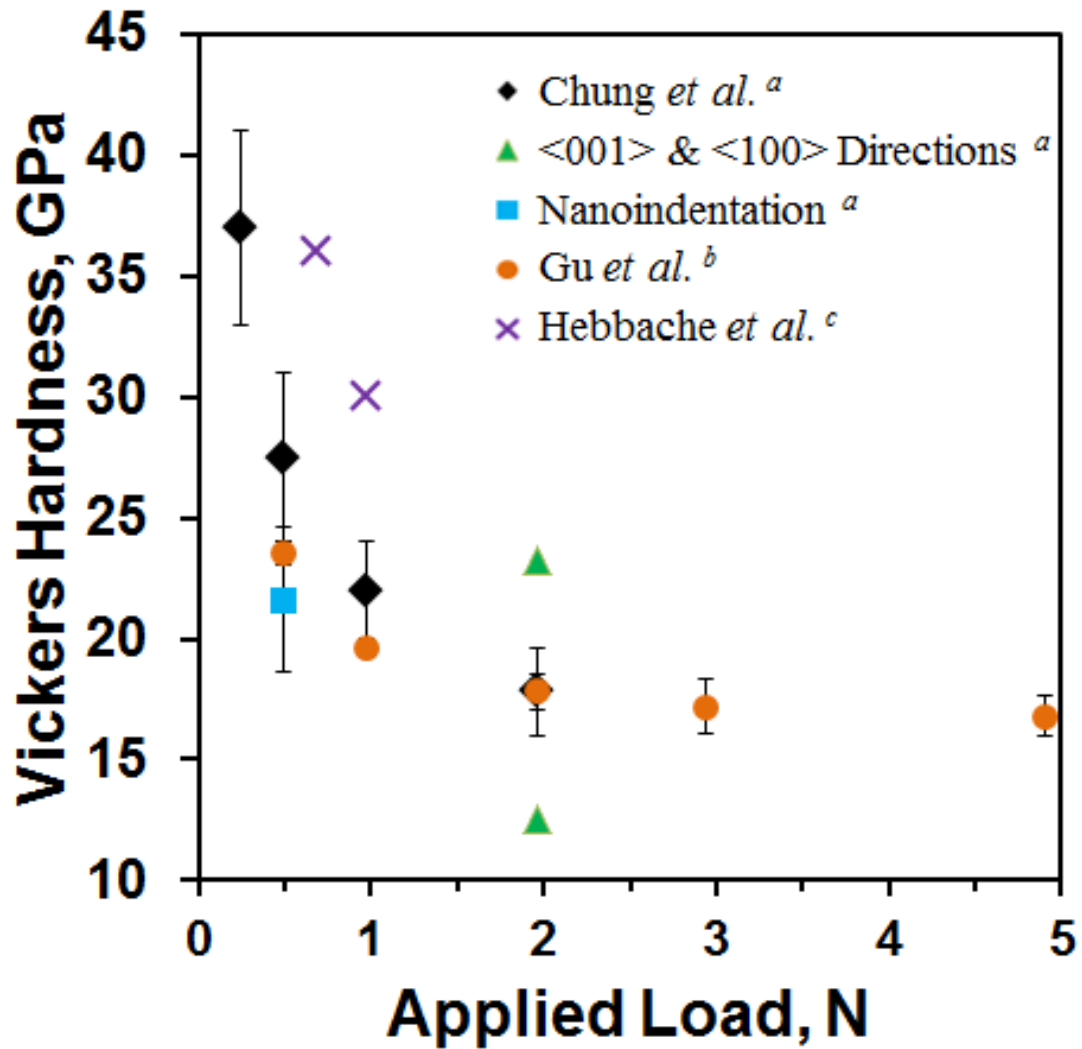


Figure 7: Measured hardness values of orthorhombic OsB<sub>2</sub> from different papers: *a* [29], *b* [32] and *c* [121].

The Young's modulus of orthorhombic OsB<sub>2</sub> was measured to be  $410 \pm 35$  GPa by Chung *et al.* [29] using nanoindentation with Oliver and Pharr method [125] and the values agree with LDA and GGA calculations in [126]. The (101) lattice plane shows the largest strain while the (001) lattice plane shows the smallest strain, as measured by radial diffraction in a diamond anvil cell under high pressure. [127] It was also determined that larger strain along the *a* axis than the *b* and *c* axes, which means that the *a* axis supports the largest differential stress. [127]

The yield strength of orthorhombic OsB<sub>2</sub> was calculated to be 11 GPa under a hydrostatic pressure of 27.5 GPa. [127] The interpreted value of the hardness of OsB<sub>2</sub> along *a* axis shows the highest hardness to be 25.6 GPa, which is different from the prediction that hardness in *c* axis is the highest. [94] Although OsB<sub>2</sub> was reported to have a high hardness and may be used as abrasive material, ideal strength calculation indicates that it is susceptible to failure in certain direction under shear stresses as low as 9.1 GPa. [124] This is due to the highly anisotropic Os–Os (001) layers contains no B–Os and B–B bonds. [124]

## (2) Compressibility

Using local density approximation, the bulk modulus of orthorhombic OsB<sub>2</sub> was calculated to be 364.87 GPa. [58] In another study, it was reported that the calculated bulk modulus with and without spin-orbit coupling are 364 and 365 GPa, respectively. [122] Hou *et al.* reported the structural parameters, elastic constants, and electronic structures of OsB<sub>2</sub>, which revealed that the *c* crystallographic direction is the least compressible. [128] Bulk moduli were reported to be 336.1 GPa and 303.45 GPa by LDA and GGA calculations, respectively. [128] It was also concluded that the strong covalent Os–B bonding and B–B bonding play an important role in the incompressibility and hardness of OsB<sub>2</sub>. [128] The compressibility of orthorhombic OsB<sub>2</sub> was measured using high-pressure X-ray diffraction in a diamond anvil cell at pressures up to 32 GPa, which gives a resulting bulk modulus of 365-395 GPa depending on the fitting parameters. [53] Unit cell volume and axes of OsB<sub>2</sub> decrease with increasing pressure linearly. [53] An anisotropic compression of axes was observed and the *b* direction of OsB<sub>2</sub> crystal is the most compressible, while the *c* direction is the least compressible [53], which is in agreement with calculated results [128]. The anisotropic of the compressibility of the crystallographic axes

can be explained by the different types of arrangements of atoms between the *a-b* plane and the *c* direction where strong repulsive forces exist under pressure since atoms are all perfectly aligned along the *c* direction. [53]

### (3) Other properties

While most of the known hard materials are either insulators or semiconductors, OsB<sub>2</sub> is a metallic conductor that may be useful for special situations that require high hardness, stiffness and conductivity. [122] Similar to ReB<sub>2</sub>, there is a mixture of metallic, covalent and ionic bonding in the orthorhombic OsB<sub>2</sub>. [126, 128] The ionic character of OsB<sub>2</sub> is originated from the charge transfer from Os cation to B according to the charge density distribution analysis. [126] Additionally, orthorhombic OsB<sub>2</sub> was reported to be a superconductor at temperature below 2.1 K. [118, 119] By comparing the measured transition temperature for OsB<sub>1.9</sub> and OsB<sub>2.1</sub> (both have  $T_c = 2.1\text{K}$ ), one can see that transition temperature of OsB<sub>2</sub> does not have a strong dependence on boron stoichiometry. [118] The resistivity of orthorhombic OsB<sub>2</sub> decreases when the temperature decreases from 293K to 50K in both OsB<sub>2</sub> single crystal and polycrystalline sample. [119]

#### 1.2.4 Other osmium borides

During the synthesis of OsB<sub>2</sub>, other Os–B phases such as OsB<sub>1.1</sub> and Os<sub>2</sub>B<sub>3</sub> were observed. [53, 114, 117, 121] The melting point of OsB<sub>1.1</sub> is 1820±15°C, which is 50°C lower than that of the orthorhombic OsB<sub>2</sub>. [117] Single-phase crystalline OsB powder with a WC-type hexagonal structure was synthesized at a moderate temperature (900°C) using liquid tin as a flux.

[129] Four different structures (WC, NaCl, CsCl or ZnS type) for osmium monoboride (OsB) were studied using first principles methods, none of them are superhard and it was suggested that the weak Os–B bonding is responsible for the low hardness. [130, 131] All the 4 potential OsB structures are mechanically stable [130] but the hexagonal WC-type is the most stable. [126, 131] The bulk modulus of OsB was reported to be  $453 \pm 6$  GPa, which is close to that of diamond. [32] OsB also has metallic characters and a phase transition from a  $c/a < 1$  to a  $c/a > 1$  was predicted at 31 GPa. [132] The coefficient of thermal expansion of OsB was calculated to be  $1.67 \times 10^{-5}/\text{K}$  and  $2.01 \times 10^{-5}/\text{K}$  by LDA and GGA, respectively. [133] While the OsB<sub>2</sub> shows great anisotropy in elastic constants, OsB shows small elastic anisotropy. [132]

In section 1.1.4, it was mentioned that, adding additional small atoms may or may not increase the hardness of rhenium borides, carbides and nitrides. [95] However, it was noticed that hardness of osmium borides increases with boron content increasing. [123] Two borides, Os<sub>2</sub>B<sub>5</sub> and OsB<sub>3</sub>, are predicted to have higher hardness (34.4 GPa and 36.9 GPa, respectively) than the synthesized OsB<sub>2</sub>. This result is awaiting experimental verification. [123] Another higher boride, osmium tetraboride (OsB<sub>4</sub>), may have very interesting properties, but has not been synthesized. The hardness of OsB<sub>4</sub> with WB<sub>4</sub>-type hexagonal structure ( $P6_3/mmc$ ) was reported to be 46.2 GPa and 48.5 GPa based on the GGA and LDA calculations, respectively. [34] The ground state of OsB<sub>4</sub> was reported to be with an orthorhombic  $Pmnm$  structure. [134] The orthorhombic  $Pmnm$  OsB<sub>4</sub> has a high shear modulus of 218 GPa and hardness of 28 GPa according to the first principles calculations by Zhang *et al.* [134] The bulk modulus of orthorhombic OsB<sub>4</sub> was calculated to be 294 GPa [134], which is not as high as that of OsB<sub>2</sub>

(348 GPa) [32]. The Young's modulus of orthorhombic OsB<sub>4</sub> was reported to be 524 GPa [134], which is higher than that of OsB<sub>2</sub> (410 ± 35 GPa) [29].

### 1.3 Iridium Borides

While transition metal borides such as RuB<sub>2</sub>, ReB<sub>2</sub> and OsB<sub>2</sub> all have “ideal” structural formulas with integer ratios between the transition metal and boron, iridium borides with an ideal structural formula have never been reported. Aronsson *et al.* conducted the first experiments on the Ir–B system in 1960. [77] By utilizing arc melting, the first iridium boride was synthesized with a stoichiometry of approximately IrB<sub>~1.1</sub> and it is isomorphous to ThSi<sub>2</sub> (C<sub>c</sub>-type). The lattice parameters of IrB<sub>~1.1</sub> are  $a=2.81\text{Å}$  and  $c=10.26\text{Å}$ . [77] After a more comprehensive characterization of the powder prepared by arc melting, an iridium boride with a higher boron content IrB<sub>1.5</sub> was found. It adopts the C2/m monoclinic structure with  $a=10.523\text{Å}$ ,  $b=2.910\text{Å}$ ,  $c=6.099\text{Å}$  and  $\beta=91^\circ$ . [135] IrB<sub>1.35</sub> was also synthesized by arc melting. [116] IrB<sub>1.35</sub> has a C2/m monoclinic structure with  $a=10.525\text{Å}$ ,  $b=2.910\text{Å}$ ,  $c=6.099\text{Å}$  and  $\beta=91^\circ 4'$ . [116] Additionally, IrB<sub>1.1</sub>, IrB<sub>1.35</sub> and IrB<sub>1.5</sub>, IrB<sub>0.9</sub> were synthesized by heating mixtures of Ir and B at 1200 °C followed by quenching. [136] At temperatures higher than 1200°C, IrB<sub>0.9</sub> with WC-type structure is the most stable. [136] The lattice parameters of the boron rich and metal rich phases of IrB<sub>~1.35</sub> were compared, showing that boron rich IrB<sub>~1.35</sub> has larger unit cell parameters. [137] Although IrB<sub>2</sub> was not experimentally synthesized, it is important to know that Mo<sub>0.3</sub>Ir<sub>0.7</sub>B<sub>2</sub> was synthesized by heating powder mixture at 900–1200°C in an argon atmosphere. [138] The Mo<sub>0.3</sub>Ir<sub>0.7</sub>B<sub>2</sub> has a hexagonal structure with lattice parameters of  $a= 2.92\text{Å}$  and  $b= 7.48\text{Å}$ . [138]

Since the crystal structure and lattice parameters are very similar to that of  $\text{ReB}_2$ , the crystal structure of the  $\text{Mo}_{0.3}\text{Ir}_{0.7}\text{B}_2$  can be regarded as all Re atoms in  $\text{ReB}_2$  randomly are replaced by 30% Mo and 70% Ir atoms. The  $\text{ReB}_2$ -type of  $\text{IrB}_2$  may not be stable, but the addition of 30 at% Mo stabilizes the  $\text{ReB}_2$ -type structure. This may explain why pure  $\text{IrB}_2$  has not been synthesized.

Based on the known liquidus and solidus lines from the phase diagram and calculation procedures by Rao and Belton *et al.* [139, 140], compositions of Ir-B system at higher temperature, 2800, 2900 and 3000K were also determined by Živković *et al.* [141] The phase diagram of the Ir-B system is shown in Figure 8, and the characteristic reactions, compositions and temperatures are presented in Table 1 [141]

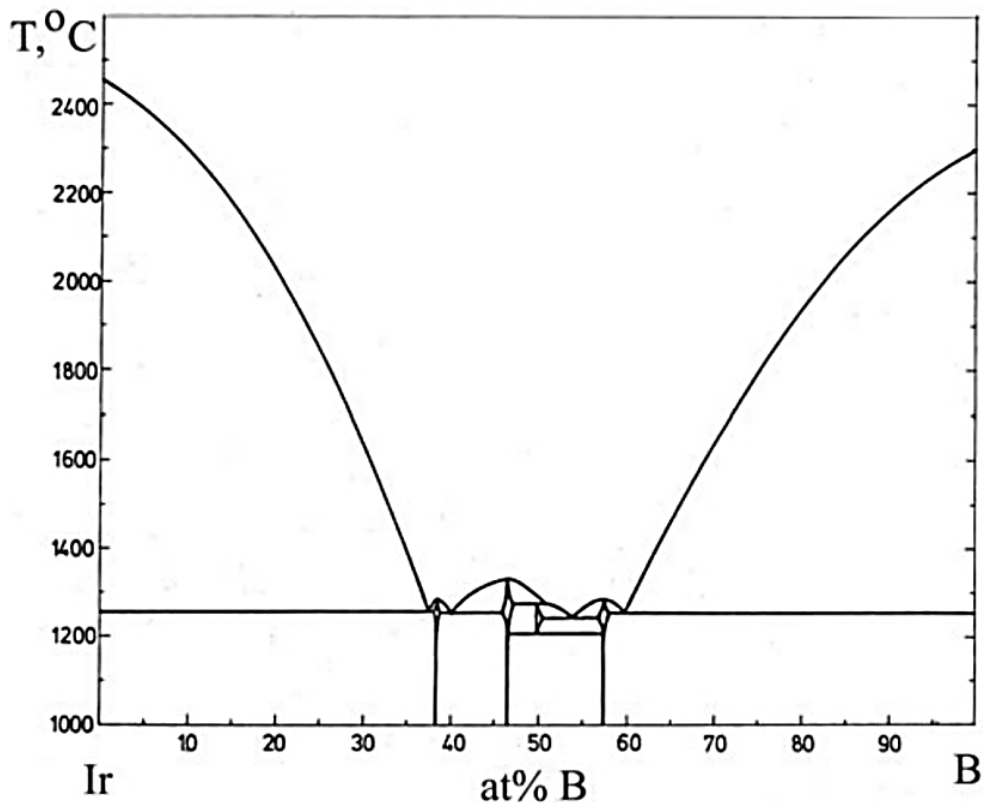


Figure 8: The phase diagram of the Ir-B system. [141, 142] Reprinted from Journal of the Less Common Metals, 82, H. Ipsier and P. Rogl, Constitution diagrams of the binary systems Pd-B and Ir-B, 363, Copyright (1981), with permission from Elsevier.



Table 1: Characteristic reactions in the Ir-B system according to the Ipser and Rogl [141, 142]. Reprinted from Journal of the Less Common Metals, 82, H. Ipser and P. Rogl, Constitution diagrams of the binary systems Pd-B and Ir-B, 363, Copyright (1981), with permission from Elsevier.

Temperature, °C	Reaction	B-content (at%)	Type of reaction
1259 ± 4	$L \rightarrow Ir + IrB_{0.7}$	37.5	eutectic
1287 ± 4	$L \rightarrow IrB_{0.7}$	38.5	congr.melt.
1258 ± 4	$L \rightarrow IrB_{0.7} + IrB_{0.9}$	40.0	eutectic
1333 ± 4	$L \rightarrow IrB_{0.9}$	46.5	congr.melt.
1274 ± 0	$L + IrB_{0.9} \rightarrow IrB$	50.0	peritectic
1209 ± 3	$IrB \rightarrow IrB_{0.9} + IrB_{1.35}$	50.0	eutectoid
1248 ± 3	$L \rightarrow IrB + IrB_{1.35}$	54.0	eutectic
1287 ± 5	$L \rightarrow IrB_{1.35}$	57.5	congr.melt.
1255 ± 0	$L \rightarrow IrB_{1.35} + B$	60.0	eutectic

The electronic transition spectrum of iridium monoboride (IrB) was recorded and analyzed using a laser vaporization/reaction free jet expansion source and laser induced fluorescence spectroscopy by Pang *et al.* [143] In Pang's report, the synthesis of IrB was performed using iridium rod and 0.5% B<sub>2</sub>H<sub>6</sub> in argon flow. [143] However, there was no phase analysis reported, thus, the stoichiometry, purity and composition of the "IrB" are questionable especially when no iridium boride with an integer Ir to B ratio was ever reported. Pure IrB<sub>1.35</sub> was synthesized using iridium and crystalline boron elemental powders with a molar ratio of 1:1.5, melted with electron beam gun under high vacuum. [144] The refined structure data confirmed that the IrB<sub>1.35</sub> has a monoclinic crystal structure (space group *C2/m*, No. 12) with  $a=10.523 \text{ \AA}$ ,  $b=2.898 \text{ \AA}$ ,  $c=6.100 \text{ \AA}$  and  $\beta=91^\circ 143'$ . [144] The microindentation hardness of IrB<sub>1.35</sub> was reported to be as high as  $49.8 \pm 6.0 \text{ GPa}$  under the load of 0.49N [144], which is much higher than another reported value ( $13.8 \pm 0.8 \text{ GPa}$ ) in [137]. The unexpected high hardness shows that the correlations between hardness and shear or bulk moduli needs further

investigation. [144] A 0.4  $\mu\text{m}$  thick  $\text{IrB}_{1.1}$  film was prepared by pulsed laser deposition on iridium and crystalline boron mixture with molar ratio of 1:1.5. [57] The  $\text{IrB}_{1.1}$  has tetragonal structure (space group  $I41/amd$ , No. 141) with  $a=b=2.819 \text{ \AA}$  and  $c=10.321 \text{ \AA}$  and a slight preferred orientation along the [004] direction. The microindentation hardness of  $\text{IrB}_{1.1}$  was reported to be  $43 \pm 5 \text{ GPa}$ . [57]

The hardness of  $\text{IrB}_2$  was predicted to be about 35 GPa by *ab initio* density-functional theory approach. [145] The orthorhombic  $Pmnm$  structure is the most stable structure for  $\text{IrB}_2$  with lattice parameters  $a= 3.152 \text{ \AA}$ ,  $b= 4.548 \text{ \AA}$  and  $c= 4.042 \text{ \AA}$ . The Ir and B atoms occupy the Wyckoff 2a (0, 0, 0.66392) and 4e (0.5, 0.30067, 0.85033) sites, respectively. [4] This structure is the same as the orthorhombic  $\text{OsB}_2$  structure, but the lattice parameters are different. Similar to  $\text{ReB}_2$  and  $\text{OsB}_2$ , theoretical calculation indicates that  $\text{IrB}_2$  should possess metallic character. [146]  $\text{IrB}_2$  with an orthorhombic  $Pmnm$  structure has a bulk modulus of 300 and 276 GPa by the LDA and GGA calculations, respectively. [4, 146] The hardness of  $\text{IrB}_2$  with a  $Pmnm$  structure was predicted to be 14.97 GPa, which is lower than that of the  $\text{IrB}_2$  with  $P63/mmc$  structure (26.65 GPa). [146] The correlation between hardness and  $C_{44}$  indicates that  $C_{44}$  may be a better hardness predictor for transition metal diborides. [43, 146] The stability of  $\text{WB}_2$ -type,  $\text{AlB}_2$ -type,  $\text{OsB}_2$ -type, and  $\text{ReB}_2$ -type of  $\text{IrB}_2$  increase with pressure and no phase transition were predicted using enthalpy calculations. [4]

$\text{IrB}$  is elastically stable with a hexagonal  $P6_3/mmc$  structure. [146] According to the first principles calculations, the bulk modulus of  $\text{IrB}$  is higher than that of the  $\text{IrB}_2$ , which are 346 GPa and 309 GPa, respectively, by LDA and GGA calculations. [146] The calculated hardness of  $\text{IrB}$  is 12.36 GPa. [146] Another  $\text{IrB}$  with orthorhombic crystal structure in the space group

*Pnma* was reported to be dynamically and elastically stable according to the first-principles calculations. [4] A high-pressure phase transition of IrB from the *Pnma* to an anti-NiAs phases was predicted to occur at 5 GPa. [4]

#### 1.4 Other important transition metal borides

The superhardness of  $WB_4$  was reported only recently in 2011 [54] even though the material was synthesized in 1966 [147]. While  $WB_2$  has an  $AlB_2$ -type hexagonal structure in space group *P6/mmm* (*hP3*, No. 191) with  $a=3.02\text{\AA}$ ,  $c=3.05\text{\AA}$  [148],  $WB_4$  also has a hexagonal structure but in space group *P63/mmc* with  $a=5.200\text{\AA}$ ,  $c=6.340\text{\AA}$ . [147] The crystal structure of  $WB_4$  is shown in Figure 9. It was believed that, with higher boron content, a higher hardness would be achieved for transition metal borides. In the case of tungsten borides, this has been verified since the  $WB_2$  has a hardness of only  $\sim 20$  GPa [149] but  $WB_4$  has hardness of  $43.3 \pm 2.9$  GPa when the applied load is 0.49N. [54] As a superhard material, the advantage of  $WB_4$  is that tungsten metal is most cost effective than other transition metals such as Re, Os, Ru, etc. Synthesis of phase pure  $WB_4$  is difficult because the  $WB_4$  is not a thermodynamically favorable material when the B:W molar ratio is lower than 12:1 according to the phase diagram [54, 147]. In addition to the high hardness,  $WB_4$  shows a bulk modulus of 339 GPa [54] or  $304 \pm 10$  GPa [32] measured by high-pressure X-ray diffractions. The boride is stable in air up to  $400^\circ\text{C}$ , which is lower than that of  $ReB_2$  crystals ( $800^\circ\text{C}$ ). [54]

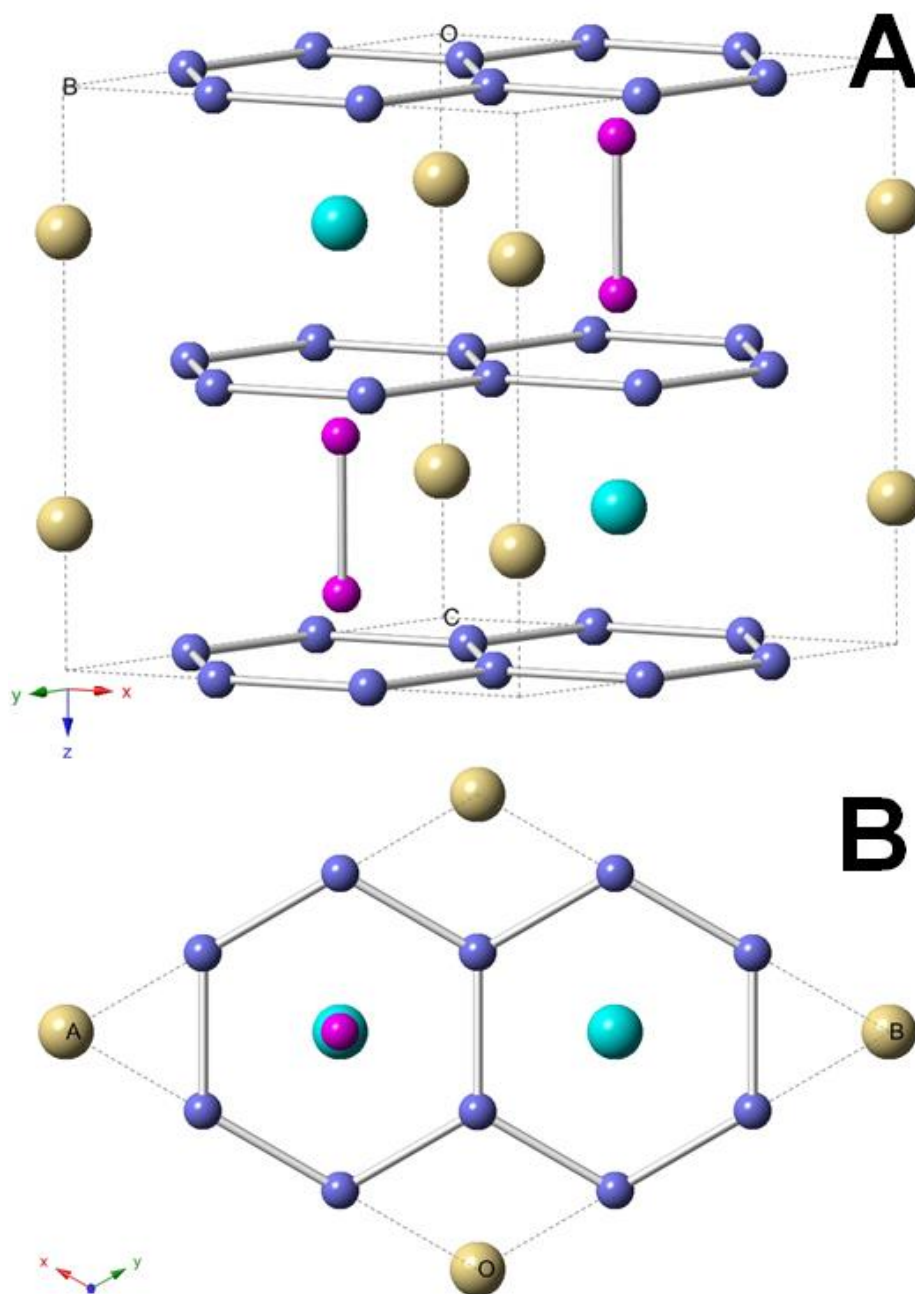


Figure 9: The crystal structure of  $WB_4$  (A) and the top view of crystal structure (B). [34]

The majority of hexagonal transition metal diborides ( $TMB_2$ ) crystallize in  $AlB_2$ -type structure (TM=Ti, Zr, Hf, V, Nb, Mo, W, Cr, Ta, Ag and Au). [1, 150] As shown in Figure 6C, the  $AlB_2$ -type structure contains alternating layers of transition metal atoms and boron atoms,

and the boron atoms are in the same plane. However, the ReB<sub>2</sub>-type structure has puckered hexagonal rings of boron atoms in every boron layer, which results in shorter TM-B bonds (TM stands for transition metal atoms). This is one of the most important reasons that ReB<sub>2</sub> has remarkably higher hardness when compared to other transition metal borides. Thus, looking for transition metal borides with this unique ReB<sub>2</sub>-type structure is of great importance. This is similar to *c*-BN which mimics the structure of diamond. [150, 151]

Although there is only another binary transition metal boride, TcB<sub>2</sub>, that adopts a ReB<sub>2</sub>-type structure, seven borides with mixed metals (Mo<sub>0.3</sub>Ru<sub>0.7</sub>B<sub>2</sub>, Mo<sub>0.3</sub>Os<sub>0.7</sub>B<sub>2</sub>, W<sub>0.3</sub>Ru<sub>0.7</sub>B<sub>2</sub>, W<sub>0.3</sub>Os<sub>0.7</sub>B<sub>2</sub>, V<sub>0.4</sub>Os<sub>0.6</sub>B<sub>2</sub>, Mo<sub>0.6</sub>Ir<sub>0.4</sub>B<sub>2</sub> and W<sub>0.56</sub>Ir<sub>0.44</sub>B<sub>2</sub>) were reported to crystallize in the ReB<sub>2</sub>-type structure. [138, 150, 152, 153] Mixed metal diborides may be another source of superhard materials because the mixed metals are barriers to the movement of dislocations. [13] For example, the hexagonal ReB<sub>2</sub>-type Os<sub>0.5</sub>W<sub>0.5</sub>B<sub>2</sub> synthesized by Gu *et al.* [32] was reported to have a hardness of 40.4 GPa, which is much higher than that of OsB<sub>2</sub>. [13] The hardness of Re<sub>*x*</sub>W<sub>1-*x*</sub>B<sub>4</sub> increased to 50 GPa when 1 at.% Re was added to the parent WB<sub>4</sub> structure. [54] Elastic moduli values decrease when the ReB<sub>2</sub> is modified to Re<sub>0.5</sub>Ir<sub>0.5</sub>B<sub>2</sub> due to the occupation of anti-bonding states. [154] In contrast, the elastic moduli values increase when OsB<sub>2</sub> is modified to Os<sub>0.5</sub>W<sub>0.5</sub>B<sub>2</sub>. [154] The shear modulus is more sensitive to the metal mixing because of the bonding changes, but bulk modulus does not change much by mixing metals because the value of bulk modulus is more dependent on valence electron densities rather than on bond strength. [154] From Lin's computational results, transition metal mixed diborides with a hexagonal structure are generally more stable than those with an orthorhombic structure. [154] Although the orthorhombic Os<sub>1-*x*</sub>Ru<sub>*x*</sub>B<sub>2</sub> synthesized by Weinberger *et al.* shows a hardness decreases with Ru

content increasing ( $x$  from 0 to 1), it was explained that the Ru–B bonds are weaker than that of the Os–B bonds, which decreases the hardness of  $\text{Os}_{1-x}\text{Ru}_x\text{B}_2$  with increasing Ru content increasing. [55]

### 1.5 Correlation between hardness and elastic constants

The indentation method is usually used to test the hardness of materials. However, it is easily affected by loading and unloading speed, load level, anisotropy of materials, method of measurements, defects in sample, and any other factors. [1] The indentation size effect is well known in that the measured hardness increases with decreased indentation load. The indentation size effect was observed in almost all indentation tests of transition metal borides. It was explained that the high values of indentation hardness at low loads are because of the materials' high elastic moduli. [155] However, hardness is related to the plastic deformation. Thus, the low-load indentation hardness values from materials' elastic regime are not the true hardness. The “absolute” hardness of materials is very difficult to measure, making it difficult to develop microscopic theory of hardness. [1] In order to predict new superhard materials, the correlations between hardness and other physical parameters are very important. [150] It was suggested that a hard material should satisfy three conditions, (1) resist volume decrease under load, (2) resist deformation from the direction of applied load and (3) resist plastic deformation. [1, 3, 31] In the report by Veprek *et al.* [155], it was pointed out that high shear strength is also necessary for intrinsic superhard materials.

It has been proved that high incompressibility does not imply high hardness because bulk modulus is used to evaluate elastic strength while hardness is for plastic strength. [94, 150] By observing the correlation between hardness and bulk moduli of various osmium borides, carbides, nitrides and oxides, it was also confirmed that there is no obvious correlation between hardness and bulk modulus [131]. However, a strong linear correlation between hardness and shear modulus was observed in three transition metal borides,  $\text{RuB}_2$ ,  $\text{OsB}_2$  and  $\text{ReB}_2$ . [98] In comparison, the correlation between hardness and bulk modulus was not obvious. [98] In other reports [2, 10, 156, 157], the shear modulus was also regarded as a better indicator of hardness. It also has been established that hardness versus shear modulus shows better correlation than the hardness versus bulk modulus for the selected materials. [3, 150]

Another good example is that Os metal has the highest bulk modulus (396–462 GPa) among all the metals [17, 158-160] but it has a hardness as low as 4 GPa [32]. The bulk modulus is governed by electron concentration while the hardness is determined by elastic and plastic properties, which are dependent on structures. [32, 130] A high shear modulus, very important for achieving a high hardness, allows the material to resist deformation in directions other than that of the applied load. This can explain why Os possesses a high bulk modulus but low hardness. [32] Also, it explains the relatively high bulk modulus and low hardness of  $\text{OsB}$ , and a relatively low bulk modulus but high hardness for  $\text{WB}_4$ . [32] Compared to higher borides,  $\text{OsB}$  has a high electron concentration due to its low boron content, which maintained the high bulk modulus of Os, but there is no direct B–B bonding in  $\text{OsB}$  also due to the low boron content. [32] It is the opposite for the  $\text{WB}_4$ . By comparing with other transition metal borides, Gu *et al.* concluded that the higher the boron content, the higher the hardness but lower the bulk modulus

and *vice versa*. [32] While the higher borides are difficult to synthesize, and the intermediate borides compromise between bulk modulus and hardness, materials such as  $\text{ReB}_2$ ,  $\text{OsB}_2$  and  $\text{Os}_{0.5}\text{W}_{0.5}\text{B}_2$  may be more promising to be used as abrasive materials. [32] The correlation of hardness and bond strength of osmium compounds is presented in Figure 10, which shows a very linear relationship between hardness and bond strength.

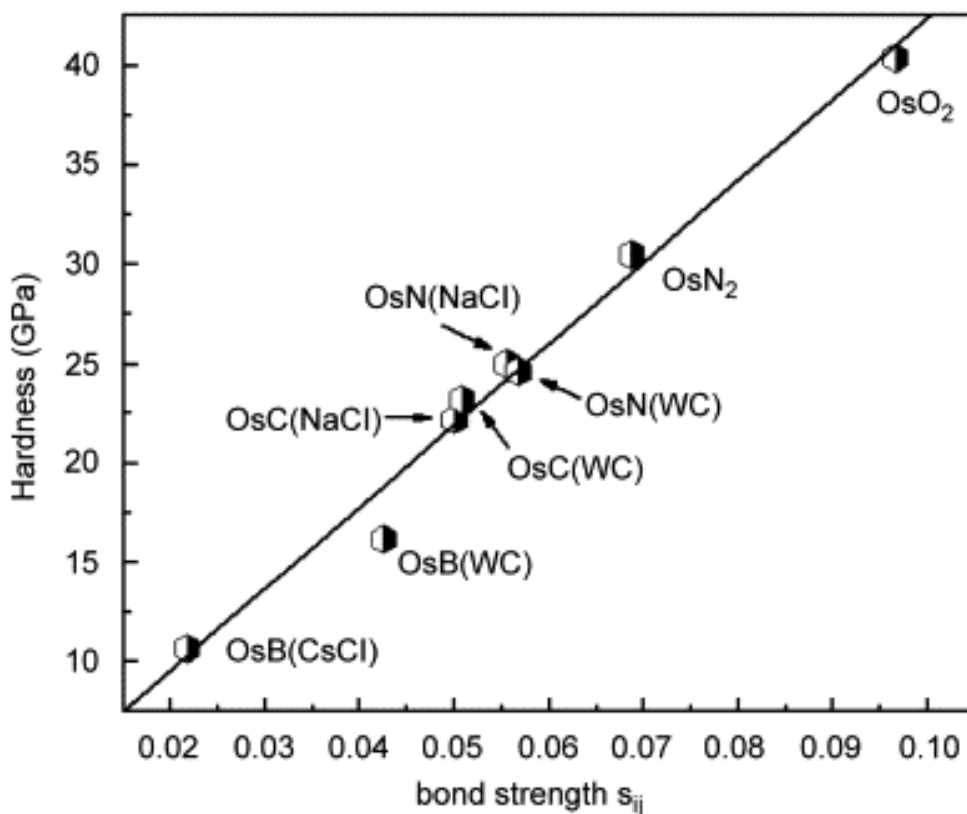


Figure 10: Correlation of hardness and bond strength for the osmium compounds. Reprinted from Journal of Physics and Chemistry of Solids, 69, Miao Zhang, Mei Wang, Tian Cui, Yanming Ma, Yingli Niu and Guangtian Zou, Electronic structure, phase stability, and hardness of the osmium borides, carbides, nitrides, and oxides: First-principles calculations, 2096–2102, Copyright (2008), with permission from Elsevier. [131]



## 1.6 Mechanochemistry

### 1.6.1 Overview of Mechanochemistry

Mechanochemistry is chemical reactions and phase transformations induced by mechanical energy, such as by ball milling. Mechanochemistry is a subject of solid state chemistry where intra-molecular bonds are broken by mechanical forces. [161] Solids are different from gases and liquids, in that they can support shear strain. [162] Thus mechanical forces can trigger chemical reactions. Surface energies increase through the process of attrition. This increased surface energy effectively lowers the energy needed to initiate a chemical reaction and the low diffusion distances allow synthesis to occur at or near room temperatures.

The first experimental study involving mechanochemistry was performed as early as the 4th century BC that quicksilver (mercury) was extracted by grinding cinnabarite (HgS) in a copper mortar with presence of vinegar. [163] Carey Lea, the father of mechanochemistry [164], was the first scientist mentioned that heat and mechanical forces can introduce different reactions for the same materials in his publications during 1892-1894. [165-168] However, Boldyrev suggested that the mechanochemical phenomena may be observed even earlier by Michael Faraday in 1827. [168-170] He also performed mechanochemical experiments to produce silver from AgCl with metals such as Zn and Cu in a set of mortar and pestle. [168, 171] Mechanochemistry was not considered a mainstream approach in the past, until recently, more and more publications involved this topic. [171] Figure 11 shows the publication number of papers that is related to mechanochemistry per year versus time, where a clear exponential growth trend can be seen. There are a few reasons suggested that mechanochemical method

will become a popular research approach in the future: (1) Mechanochemical method is more energetically efficient while compared to traditional high-temperature solid-state synthesis methods requiring extended high temperature heating during solid-state chemical reactions. (2) The mechanochemical synthesis (mechanosynthesis) represents scalable technologies that can be used to produce bulk quantities of polymers, alloys and ceramic materials. For example, the shaker mill can produce a minimum of 2 grams of powder while the pebble mill can produce more than 1000 kg. [172] (3) It is able to synthesize new nanoscale and non-equilibrium phases. For example, solid solution of Fe-Cu system can be obtained only by mechanochemical method. [173-175] (4) Most of the mechanochemical syntheses do not require solvents, which reduced the production of waste and consumption of fossil derived materials. It is more sustainable compare to other methods that depend on solvents. [171]

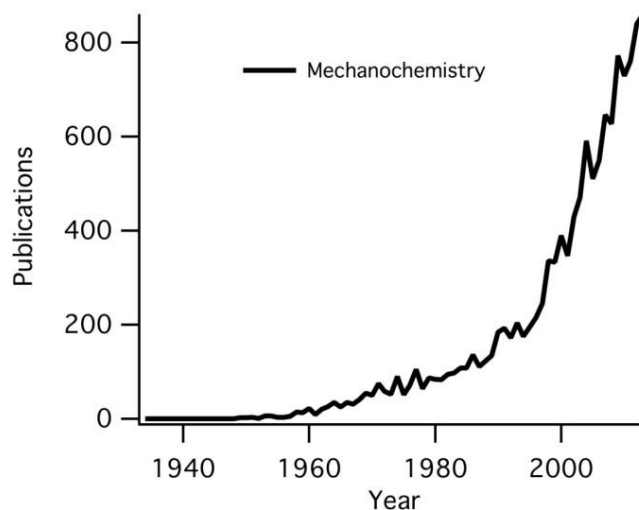


Figure 11: Publications about mechanochemistry as function of time. [176]

The mechanism of the mechanochemistry or mechanosynthesis is still not very clear and remained controversial. Many theories and models [171, 177] were proposed, but they all have

their own limitations. The major difficulties are: First of all, there are a variety of different types of chemical reactions, which cannot be easily explained by a single model or theory; secondly, there is not a way to directly observe the ongoing mechanochemical reactions at microscopic, molecular or even atomic level. [171] The hot spot theory suggests that the local friction heat plays an important role while surfaces slide on each other, which causes not only plastic deformation of the materials, but also brings local temperature up to 1000 °C in a very short period of time about  $10^{-3}$ ~ $10^{-4}$  seconds. [171] The magma-plasma model considers only normal impacts, which can increase the local temperature to higher than  $10^4$  °C. [177] Localized friction heating may provide the required thermal energy to complete synthesis of new phases. The localized high pressure, high shear events occur without dramatic temperature rises as heat is mostly provided by the reaction enthalpies and most reactions involving pure elements to form a compound are enthalpically favored.

Mechanochemistry has been used to produce variety of materials. Mechanical alloying was used to produce high performance alloys for aerospace applications in 1960s. [178] Mechanochemistry is also used for synthesis or activation of ceramic materials. [179-181] The recent research on polymer mechanochemistry shows a promising future for this method to be applied in polymer synthesis. [182] Brantley *et al.* [183] reported the selective scission of covalent bonds during mechanochemical process. Besides, mechanical forces are able to stabilize reactive intermediates, which provided chances to obtain different kinds of transformations. [183] Many solvent free mechanochemical reactions between fullerenes were investigated with both high energy and low energy ball milling by Wang *et al.* [184] It was reported that some fullerene derivatives can only be obtained by solvent free high-speed vibration milling. [184]

Guo *et al* reported the prospective applications and mechanisms in pollution remediation and waste management. [185] In addition, mechanochemical technologies can also recycle materials that are difficult to be recycled by traditional methods, such as waste plastics and rubbers. [185]

Recently, an *in situ* XRD instrument has been invented by Halasz1 *et al.* [186, 187], which allows a real-time monitoring of the mechanochemical milling reactions with time resolution in seconds. The high-energy and high penetrating X-rays were used as source, and a ball mill was customized to couple with the X-ray diffractometer as shown in Figure 12. [186] It is believed that this technique can be very helpful for the understanding of the ball milling process because the intermediate products can be observed. For example, organic pharmaceutical cocrystals have been mechanochemically synthesized with this technique and the intermediate cocrystallization of nicotinamide and suberic acid were observed with XRD. [187]

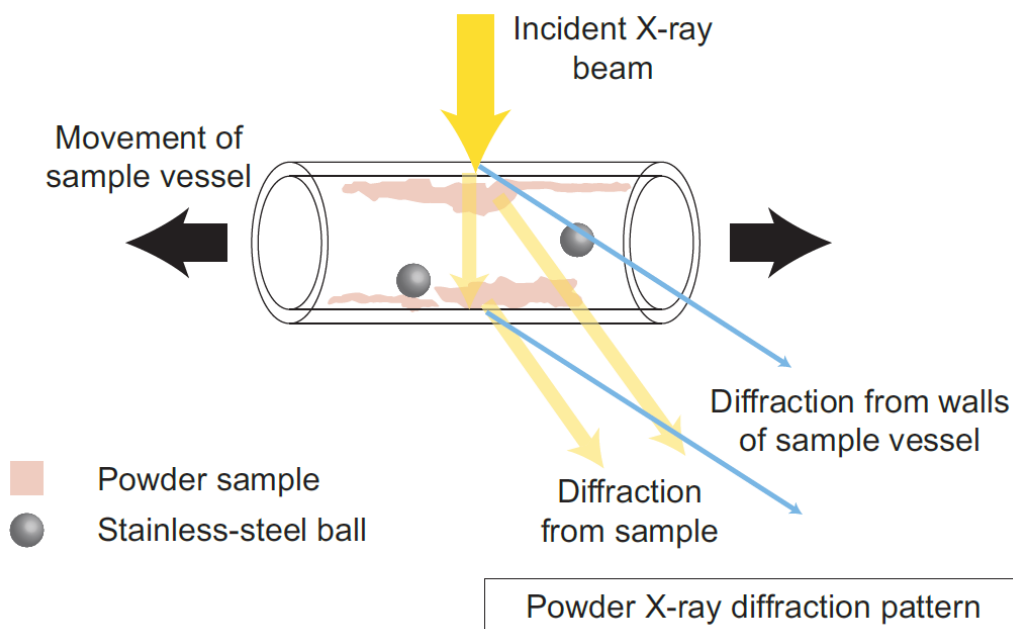


Figure 12: *In situ* X-ray diffraction with real-time monitoring the mechanochemical process. Reprinted by permission from Macmillan Publishers Ltd: Nature Chemistry [188], copyright (2012).

## 1.6.2 High energy ball milling

Ball milling is a widely used technique as a part of mechanochemical synthesis techniques. Ball milling was originally used to produce nickel- and iron-base superalloys for applications in the aerospace industry in 1966. [178] Later it was discovered that it is capable to synthesize a variety of equilibrium and non-equilibrium phases, such as metastable phases, quasicrystalline phases, solid solutions, amorphous alloys and nanostructures. [178] It accelerates the kinetics of chemical reactions by creating fresh interfaces between reacting phases by dynamic fracturing, deformation and cold welding of the solid particles. [189] The schematic of ball milling mechanism is shown in Figure 13.

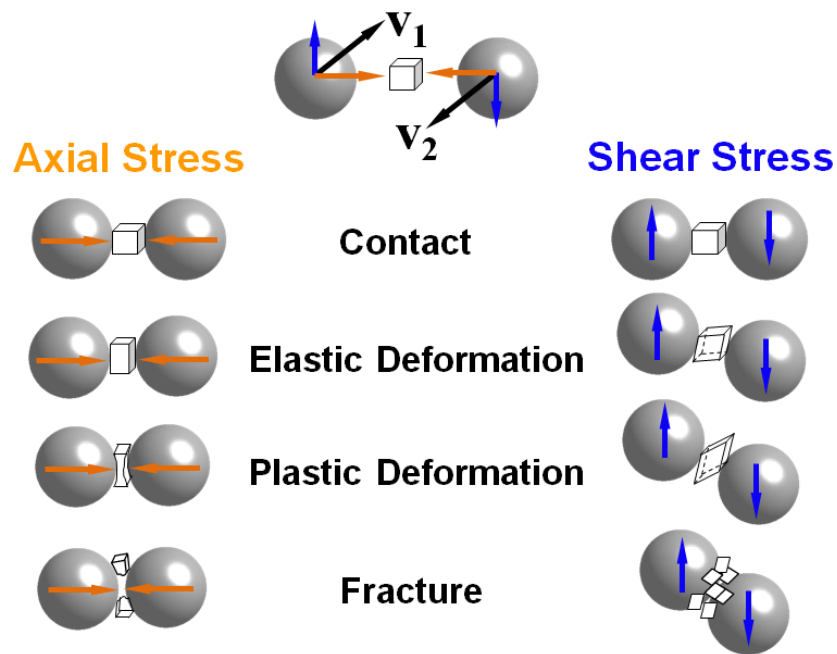


Figure 13: A schematic of the working mechanism of high energy ball milling.

There are many different milling technologies including planetary mills, shaker mills, attrition mills and pebble mills. [172] Shaker mills are the most commonly used mills for

laboratory investigations. A typical SPEX 8000D Mixer/Mill with a tungsten carbide (WC) milling vial and milling media are shown in Figure 14, which are manufactured by SPEX CertPrep, Metuchen, NJ. The specifications of the vial are listed in Table 2. The mill motor works at 1425 RPM (at 50Hz) and allow the vial to move 5.9cm back-and-forth, and 2.5cm side-to-side, which provided very high speed (5m/s) for the balls to move in the vial and thus provided very high impact forces. This type of mill is considered as high energy ball mill. The SPEX CertPrep also provides a variety of different vial materials, such as hardened steel, zirconia, tungsten carbide, alumina, plastic, etc.

Table 2: Specifications of SPEX tungsten carbide vial.

Diameter	2.25 in
Height	2.5 in
Volume	55mL
Sample Capacity - Grinding	3 - 10 mL
Sample Capacity - Mixing	25 mL
Typical Sample Size	10 g
Durability	Long wearing
Hardness	Mohs 8.5+ ; Knoop 1400-1800
Major Elements	W, C, Co
Minor Elements	Ta, Ti, Nb
Resistance To Abrasion	High
Slurry Grinding	Yes
Comparative Efficiency	Very High

Planetary ball mills are able to process a few hundred grams of the powder at one time. Its vial movement path is similar to a planet, thus it is called “planetary mill”. The vials also

rotate with their own axis, but opposite of support disk rotation direction, so that the centrifuge forces are counteracted. Thus, the balls and powder in the vials are free to move, brings both friction effect and impact effect. Figure 15 shows a Fritsch planetary mill and a schematic of its working mechanism. Attritor is made of a vertical drum and with a series of impellers in side (Figure 16), which transfers kinetic energy to the balls. Attritors can mill large quantities of powder at one time, in the range of 0.5 to 40 kg. The velocity of milling media is only 0.5 m/s, which is much smaller when compared to SPEX high energy ball mill. The laboratory attritor works 10 times faster than conventional ball mills. [178] Pebble mill, which is also known as roller mill or tumbling mill, is used for industrial applications. It is able to process large quantities of materials on the order of hundreds of pounds. [172] Pebble mills are usually used to reduce particle size to make finer powder materials rather than for chemical reactions due to the low energy impacts. [172] The energy input is lower in attritor and pebble mill when compared to shaker mill, which results in slower movement of milling media. However, it may be more efficient to use attritor or pebble mill when solvent exists. [172]

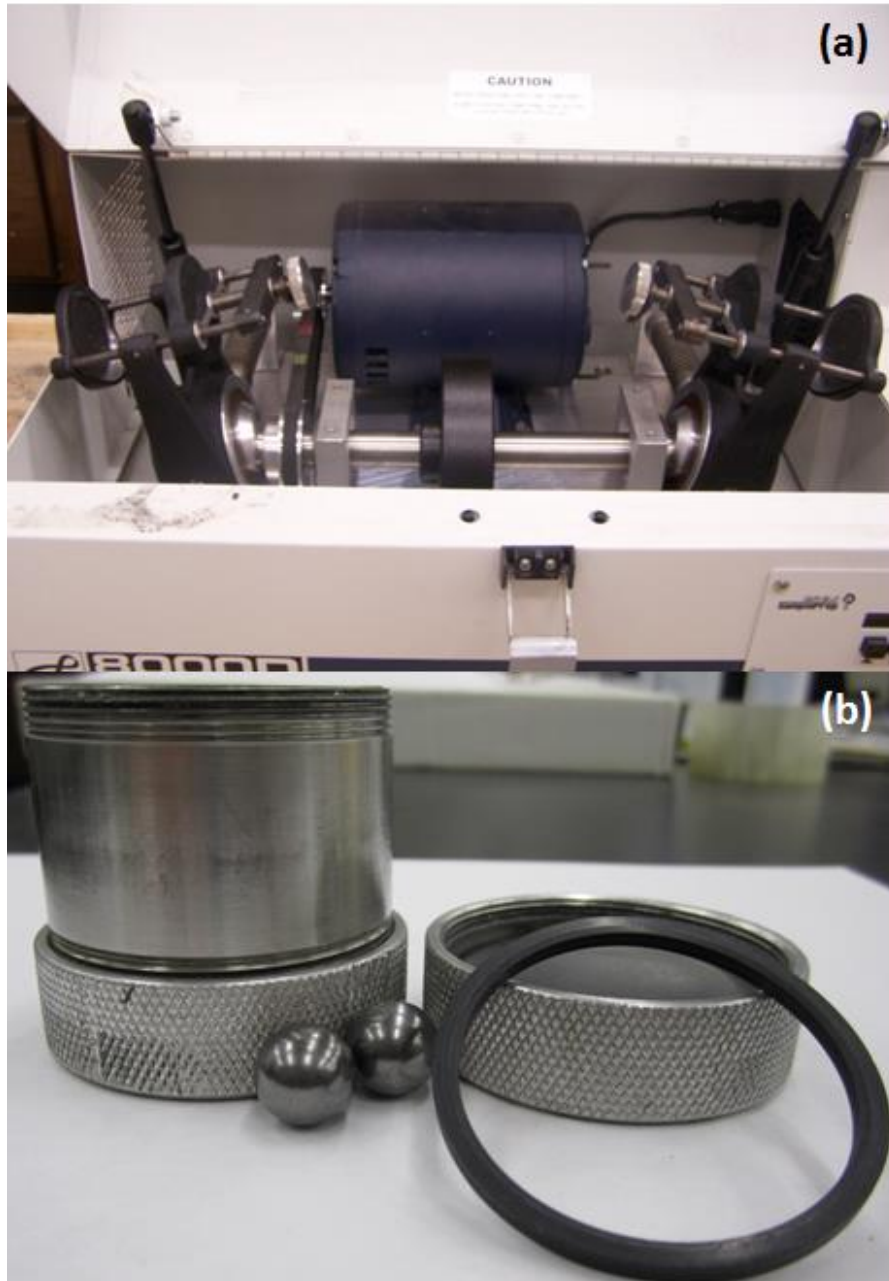


Figure 14: A SPEX 8000D Mixer/Mill (a), and WC milling vial and media (b).



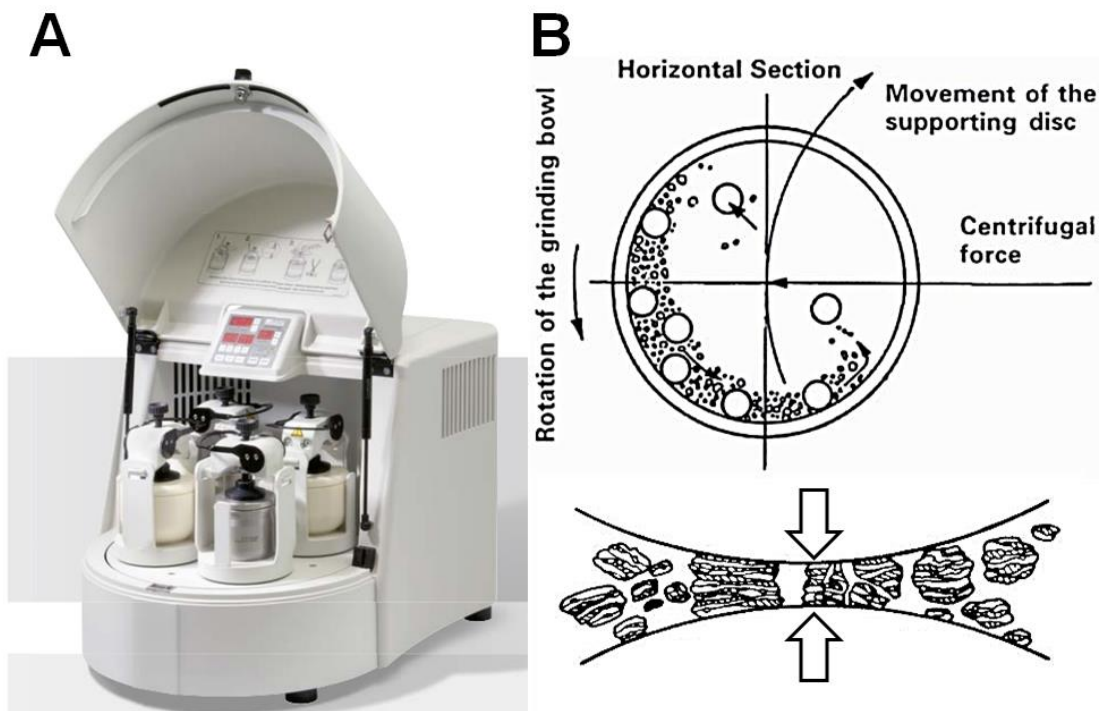


Figure 15: A Fritsch planetary mill (A) and a schematic showing its working mechanism (B). [178]

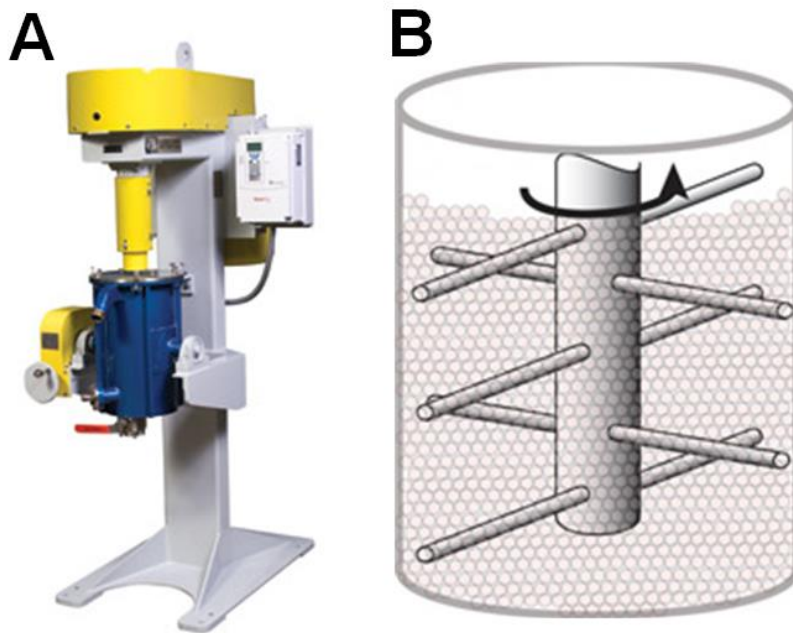


Figure 16: An attritor (A) and the structure of rotating arms on a shaft in the attrition ball mill (B).

The mechanochemical synthesis is a complex process, and there are many variables that may affect the ball milling process. [178] It is important to optimize these parameters to obtain desired products, save milling time and energy, reduce contamination, and reduce the wear of equipment. Here are the important parameters that have great influence to the ball milling:

- Milling container
- Milling medium
- Ball to powder mass ratio
- Milling time
- Milling speed
- Milling atmosphere
- Temperature
- Powder to container volume ratio

It is important to note that not all the parameters are independent to each other.

#### (1) Milling container

When considered that the materials on the container wall can be dislodged and mixed into product powder, it is very important to choose an appropriate container material to avoid the most unwanted contaminations. For example, when it requires a metal free environment to produce the materials, ceramic vials such yttria-stabilized zirconia (YSZ), silicon nitride ( $\text{Si}_3\text{N}_4$ ), sapphire, or hard porcelains are good options. Another factor may affect ball milling is the shape of the vial end caps. There are two types of end caps: flat end and round end. The round end caps can avoid powder accumulation at corners and provide more shear impacts. In the opposite, the flat end design offers stronger and larger counts of normal impacts. It was reported that the

mechanical alloying happened much faster when flat end caps were used. [190]

## (2) Milling medium

Similarly, the materials from milling media are also possible to be chipped off and mixed together with the product powder. Thus, the material of milling medium is normally the same as that of the milling container to reduce the types of contamination. When high density milling medium, such as tungsten carbide or zirconia, is required, the milling medium material will be set first and then determine what vial material to use. The size of milling medium is also very important. The larger size milling medium carries more energy for single impacts. High energy impacts are needed for some mechanochemical reactions, where larger size milling media cannot be replaced by larger number of smaller-size milling media. However, when kinetic energy of milling media is too high, there are higher chances to introduce contamination. In the extreme cases, both vials and milling media can be damaged.

## (3) Ball to powder mass ratio

Appropriate ball to powder mass ratio is required for a successful ball milling process. When the ratio is too low, it takes longer time to finish ball milling. For the purpose of introducing chemical reactions by ball milling, this parameter is even more important because a low ball to powder mass ratio may not provide sufficient energy to activate the reaction. However, when the ball to powder mass ratio is too high, there are higher chances for the powder to be contaminated. It also accelerates the wear damage to vials and balls.

## (4) Milling time

The milling time is dependent on the material of the powder, the type of mill used, milling speed, the ball to powder mass ratio, etc. Before the optimized empirical parameters were

obtained, the powder material in the mill was sampled every certain time until the desired product was obtained. For laboratory mechanochemical synthesis, the newly invented *in situ* X-ray diffractometer may be very helpful to shorten this optimization time while the milling process is real-time monitored.[186] In order to decrease the vials' temperature and reduce wear on the mill's motor, it was suggested that the milling should be interrupted every certain period of time.

#### (5) Milling speed

The faster the mill rotates, the faster the milling media move and thus the higher energy provided to the powder. However, the maximum milling speed does not only depend on the power of the motor, but also depend on the design. When the ball milling rotation is above the critical speed, the balls and powder will not fall down due to the high centrifugal force, which decreases the milling efficiency. Another disadvantage of high speed milling is that the mill produces a lot of heat in a short time, which may damage the vials and the mill itself. Thus, an extra cooling system may be required when a mill is customized for high speed milling.

#### (6) Milling atmosphere

Inert vial atmosphere, such as high-purity argon or helium, is desired when ball milling air-sensitive materials. The loading and unloading of materials are usually carried on in a glovebox. During milling, the particle size is significantly decreased, thus the high surface area to volume ratio will make the powder even more air-sensitive. The gaskets in between the vial body and caps are very critical at this point. Viton gaskets are usually used to keep the vial atmosphere. The SPEX steel vials were very well designed, but their WC carbide vial caps may need more improvement, because while tightening the WC vial caps, the gaskets deform along

twisting direction and cause displacement of the gasket. This may result in an experimental failure that not only the inert vial atmosphere cannot maintain, but also can cause leakage of powder! Also, after long time milling, the vials can become loose due to the intensive vibrations. This may also lead to air leakage. For reactive metal powders such as, Mg or Al, even a small amount of air leakage is not acceptable. Thus, some investigators have tried to put ball mill in a glove box with an inert atmosphere.

#### (7) Temperature

During milling, a part of mechanical energy is converted to chemical energy or to break chemical bonds. The rest of the energy is converted to heat due to friction or impacts. Depending of the types of mill and milling intensity, the amount of heat produced varies, thus the influence of heating to the ball milling process also varies. Heating can facilitate diffusion and lower energy barrier for chemical reaction. However, high temperature can bring thermal stress and fatigue to the vials and thus shorten their life time. In some reactions, low temperature is required in order to obtain intermediate metastable phases, thus, a cooling system is needed.

#### (8) Powder to container volume ratio

The powder to container volume ratio determined how much empty space exists in the vial that allows powder and milling media to move freely. Especially for high energy ball milling, it has to be ensured that the vials are not over filled. Powder to container volume ratio is usually lower than 50%, which means the vial is less than half filled. However, when the powder is too little, the milling media have more chances to collide on each other or on the walls directly, which results in more contamination.

Based on the construction features of a mill and its operational regime, the relation between pressure and shear can vary in a wide range. [191] There have been investigators use software to simulate the ball milling process. The simulations are very helpful to guide the experimental design because it enables to obtain the best milling parameters in a shorter time. Discrete element models of the milling process were generated using EDEM software by Hick *et al.* [192]. It was reported that the SPEX shake mill can produce compressive force of 0.4 to 3 GPa and large shear forces by using steel milling vials and balls. [192] By the similar simulation using EDEM, the shear stress produced during ball milling with WC balls and vials is presented in Figure 17. The red color means the collision produces a shear stress higher than 1000 MPa when the contact area is assumed to be  $1\text{mm}^2$ .

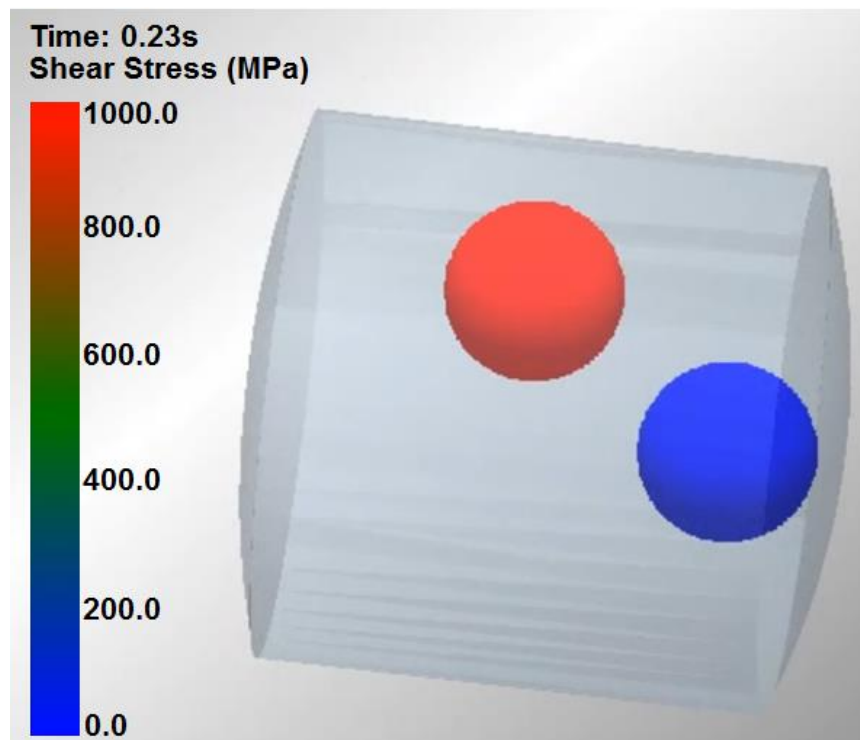


Figure 17: EDEM simulation of ball milling using WC balls and vials with a SPEX ball mill.

### 1.6.3 Mechanics in Mechanochemistry

In the mechanochemical process, shear force is more effective than pure isotropic compression, because shear changes the symmetry of a solid or molecule. [162] The electronic structure of bonds in solids becomes unstable after the breaking of symmetry, which makes the solid tend to have chemical reaction. [162] Large strain created by mechanical forces brings together the highest occupied molecular orbital (HOMO) and the lowest unoccupied molecular orbital (LUMO) to close the gap, which decreased internal stability of the system. [162] The bonding electrons delocalize into the anti-bonding states. Electrons move freely and the activation energy for the reaction becomes zero, thus, reaction happens. [162, 193]

Shear strain induced structural changes were thoroughly studied by Levitas *et al.* [194-198] In order to explain the mechanochemical phenomena, a continuum thermodynamic model of strain-induced nucleation at the tip of a dislocation pile-up has been developed. [196] The model regarded the transformation strain as a spherical tensor. As shown in Figure 18, an infinite rigid-plastic half-space with normal  $\sigma_n$  and shear stresses  $\tau$  on the surface under the plane strain condition, the existence of a region with localized plastic shear deformation was assumed. A diagram of the chemical reactions in a thin layer due to shear strain is shown in Figure 19. The model has also considered the adiabatic heating and the reaction-induced plastic can be such significant that result in heating over 1500°C. [194] It explained how the combination of plastic shear and high pressure can significantly reduce the phase transformation / chemical reaction pressure. It also demonstrated the importance of plastic strain in mechanosynthesis of new phases. [196] Recently, strain-induced chemical reactions were observed experimentally in the

shear band in both Ti–Si and Nb–Si mixtures [199, 200]. The major equations for describing strain-induced phase transformation are listed from Equation 1.1 to Equation 1.17. [194] (Reprinted by permission from Taylor & Francis Group LLC - Books, [194], copyright (2003).)

### 1. Kinematic decomposition

$$\boldsymbol{\varepsilon} = \boldsymbol{\varepsilon}_e + \boldsymbol{\varepsilon}_p + \boldsymbol{\varepsilon}_t \quad (1.1)$$

where  $\boldsymbol{\varepsilon}$ ,  $\boldsymbol{\varepsilon}_e$ ,  $\boldsymbol{\varepsilon}_p$  and  $\boldsymbol{\varepsilon}_t$  are total strain, elastic strain, plastic strain and transformation strain, respectively.

### 2. Constitutive equations

#### 2a. Elasticity law and expression for entropy

$$\mathbf{T} = \frac{\partial \psi(\dots, \xi)}{\partial \boldsymbol{\varepsilon}_e} \quad s = -\frac{\partial \psi(\dots, \xi)}{\partial \theta} \quad (1.2)$$

where  $T$ ,  $s$ ,  $\psi$ ,  $\xi$  and  $\theta$  are stress tensor, entropy, Helmholtz free energy, order parameter, temperature.

#### 2b. Yield condition and plastic flow rule

$$f(\mathbf{T}, \dots, \xi) = 0 \quad \dot{\boldsymbol{\varepsilon}}_p = \mathbf{f}_p(\mathbf{X}_p, \xi) \quad \mathbf{X}_p := \mathbf{T} - \frac{\partial \psi}{\partial \boldsymbol{\varepsilon}_p} \quad (1.3)$$

where  $\mathbf{X}_p$  is dissipative force conjugated to dissipative rate  $\dot{\boldsymbol{\varepsilon}}_p$ .

#### 2c. Evolution equation for internal variables

$$\dot{\mathbf{g}} = \mathbf{f}_g(\mathbf{X}_g, \xi) \quad \mathbf{X}_g := -\frac{\partial \psi}{\partial \mathbf{g}^t} \quad (1.4)$$

where  $\mathbf{X}_g$  is dissipative force conjugated to dissipative rate  $\dot{\mathbf{g}}$  and  $\mathbf{g}$  is set of internal variables.

### 3. Sliding and fracture conditions at the interface

$$\text{If } |\sigma_n| < \sigma_c \text{ or } |\tau| < \tau_s \Rightarrow \dot{\mathbf{u}}^2 - \dot{\mathbf{u}}^1 = \mathbf{0} \quad (\text{coherent interface}) \quad (1.5)$$

$$|\tau| = \tau_s \Rightarrow \dot{\mathbf{u}}_s^2 - \dot{\mathbf{u}}_s^1 \neq \mathbf{0} \quad (\text{semicoherent interface}) \quad (1.6)$$



$$|\sigma_n| = \sigma_c \Rightarrow \dot{\mathbf{u}}^2 - \dot{\mathbf{u}}^1 \neq \mathbf{0} \quad (\sigma_n = \tau = 0) \quad (\text{fracture}) \quad (1.7)$$

where  $\sigma_n$  and  $\sigma_c$  are normal stress and critical normal stress, respectively,  $\tau$  and  $\tau_s$  are shear stress and critical shear stress, respectively,  $\mathbf{u}$  and  $\mathbf{u}_s$  are displacement and tangential displacement, respectively.

#### 4. Local driving force for structural changes

$$X := \int_{\varepsilon_1}^{\varepsilon_2} \mathbf{T} : d\boldsymbol{\varepsilon} - (\psi_2 - \psi_1) - \int_t^{t+\Delta t} (s\dot{\theta} + \mathbf{X}_p : \dot{\boldsymbol{\varepsilon}}_p + \mathbf{X}_g : \dot{\boldsymbol{g}}) dt \quad (1.8)$$

where  $X$  is local driving force for structural changes.

#### 5. Global dissipation rate $D$ and global driving force for the structural changes $X_v$ .

$$D = X_v \dot{\chi} \quad \dot{\chi} := 1/t_s \quad (1.9)$$

$$X_v := \bar{X} V_n = \int_{V_n} X dV_n - \int_{\Sigma_n} \Gamma d\Sigma_n \quad (1.10)$$

where  $X_v$  is generalized driving force for structure change (SC),  $\dot{\chi}$  generalized rate,  $t_s$  is structure change duration and  $\Gamma$  is surface energy per unit area.

#### 6. Time-independent kinetics

##### 6a. SC criterion

$$\bar{X} = K \quad (1.11)$$

where  $K$  is the experimentally determined dissipation increments during the structure change.

##### 6b. Extremum principle for the determination of all known parameters $\mathbf{b}$

$$\bar{X}(\mathbf{b}^*) - K(\mathbf{b}^*) < 0 = \bar{X}(\mathbf{b}) - K(\mathbf{b}) \quad (1.12)$$

where  $\mathbf{b}$  is Burger's vector.

##### 6c. Dissipative threshold $K$

$$K = L\sigma_y\varepsilon_0 \quad (1.13)$$

where  $L$  is the half length of a pill-box nucleus,  $\sigma_y$  is yield stress and  $\varepsilon_0$  is volumetric transformation strain.

6d. Extremum principle for determination of stable solution (global SC criterion)

$$\int_S \int_{\mathbf{u}_1}^{\mathbf{u}_2} \mathbf{p} \cdot d\mathbf{u} dS \Rightarrow \min \quad (\text{particular case at prescribed } \mathbf{u} \text{ at } S). \quad (1.14)$$

where  $\mathbf{p}$  is traction vector.

7. Thermally activated kinetics

7a. SC criterion

$$\bar{X} \geq K^0 \quad (1.15)$$

where  $K^0$  is a thermal threshold for structure change.

7b. Kinetic equation

$$t_s = t_0 \exp\left(-\frac{(\bar{X}-K^0-E_a)V_n N}{R\theta_{ef} n}\right) \text{ at } 0 \leq \bar{X} - K^0 \leq E_a \quad (1.16)$$

where  $E_a$  is activation energy per unit mass when  $X = K^0$ ,  $V_n$  is region undergoing the structure change,  $n$  is number of atoms in volume  $V_n$  which undergo thermal fluctuations,  $N$  is a number of dislocations in a pile-up,  $R$  is radius of the anvil, and  $\theta_{ef}$  is effective temperature.

7c. Principle of the minimum of the transformation time

$$t_s = t_0 \exp\left(-\frac{(\bar{X}(\mathbf{b}^*)-K^0(\mathbf{b}^*)-E_a(\mathbf{b}^*))m_n^* N}{R\theta_{ef}^* n}\right) \rightarrow \min \quad (1.17)$$

where  $m$  is the mass of small transforming particle.

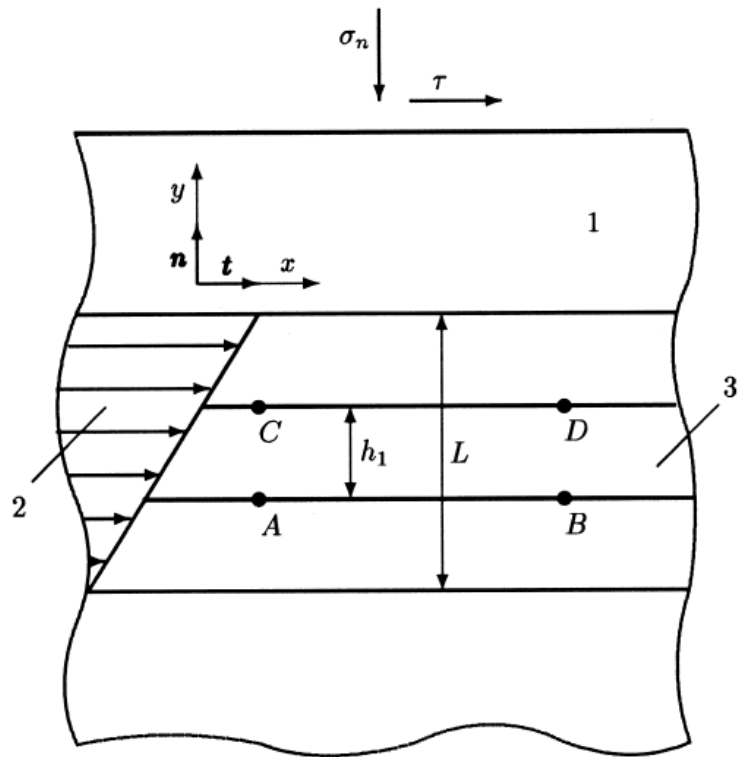


Figure 18: Schematic illustration of structural changes in a shear band: 1, half space; 2, shear band with displacement; 3, layer with structural changes. Reprinted by permission from Taylor & Francis Group LLC - Books, [194], copyright (2003).

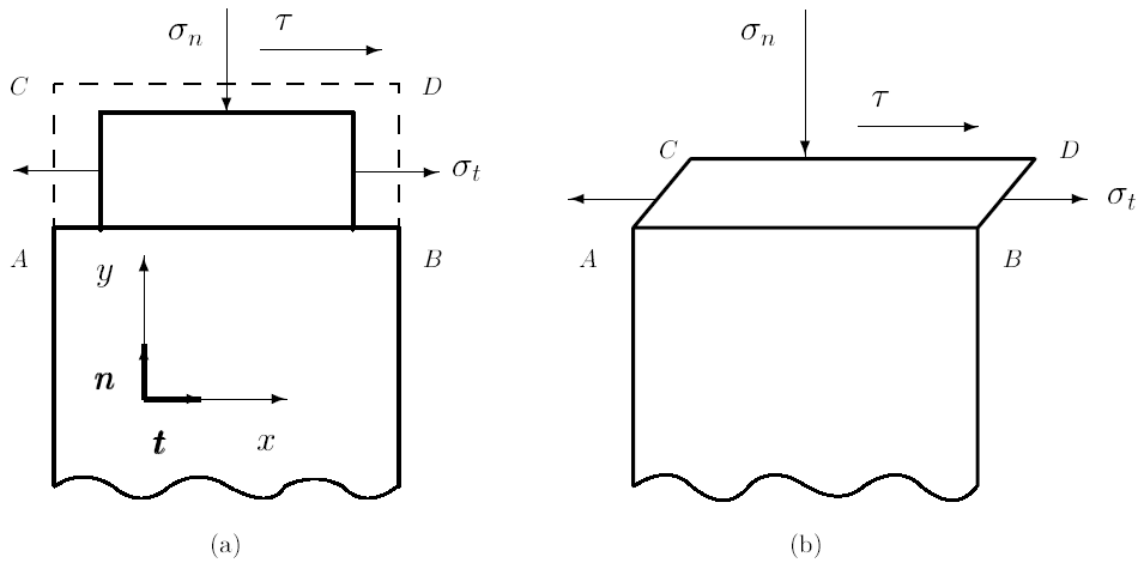


Figure 19: Diagram of a chemical reaction in a thin layer. Reprinted by permission from Taylor & Francis Group LLC - Books, [194], copyright (2003).

Ji *et al.* used rotational diamond anvil cell (RDAC) to study pressure induced phase transformation of nanocrystalline *h*-BN to *w*-BN, where no phase transformation was observed under pure hydrostatic pressure up to 52.8 GPa, but only 6.7 GPa of pressure was required to cause phase transformation under shear. [201] It was explained that the nucleation occurs at the tip of the strain-induced defects where strong pressure and deviatoric stress concentrator exist. [201] Also there is additional plastic flow in disordered grain boundaries due to the smaller grain size in the nanocrystals. [201] This confirmed that the combination of shear stress and high pressure can significantly reduce the phase transformation pressure. [201]

## CHAPTER 2: MECHANOCHEMICAL SYNTHESIS OF ReB<sub>2</sub> POWDER

This work was previously published as “Mechanochemical synthesis of ReB<sub>2</sub> powder” by Nina Orlovskaya, Zhilin Xie, Mikhail Klimov, Helge Heinrich, David Restrepo, Richard Blair and Challapalli Suryanarayana in *Journal of Materials Research*, Volume 26, Issue 21 (2011) pp. 2772-2779 Copyright © 2011 Materials Research Society. Reprinted with the permission of Cambridge University Press. <http://dx.doi.org/10.1557/jmr.2011.249>

### 2.1 Introduction

Rhenium diboride (ReB<sub>2</sub>) is a boron-rich ceramic that has been receiving a lot of attention in the scientific community because of its unusual properties. It has been reported as a superhard material [45, 46, 52] with a hardness of 48 GPa measured at a small applied load (0.5N). It was also reported that it exhibits strong and highly covalent bonding, while a strong hybridization between the Re 5d and B 2p states indicates that Re-B bonds have also prevalent covalent character with some degree of ionic bonding present [40, 85, 99]. Covalent boron-boron bonds are significantly stronger than the covalent Re-B bonds [112], and such difference between the B-B and Re-B bonds, as well as between nonequivalent Re-B bonds is responsible for anisotropic compressibility and rigidity of the structure [202]. The strong directional B-B bonding complimented by Re-B covalent bonds are responsible for the high resistance to elastic and plastic deformations resulting in high shear, bulk, and Young’s moduli, which are indicative of high hardness of the compound [64]. It was also reported that both Re 5d and B 2p states are

at the Fermi level and, hence,  $\text{ReB}_2$  exhibits metallic behavior [46, 107]. There have been numerous discussions in regard to the actual hardness of  $\text{ReB}_2$  which was reported in *Science*<sup>1</sup>. Several reports [66, 68, 69] suggest that the hardness of  $\text{ReB}_2$  was overestimated since it was measured in the region where the indentation size effect (ISE) is known to exist. According to different studies [66, 68, 69] the hardness value for  $\text{ReB}_2$  lies well below the threshold of 40 GPa, and claims of  $\text{ReB}_2$  being a super-hard material cannot be justified. However, evidence was produced [70] that the measured mechanical properties are strongly compositional dependent, where Re to B stoichiometry as well as morphology of the grains play important roles in the mechanical behavior of  $\text{ReB}_2$ . In particular, the presence of excess of amorphous boron along the grain boundaries of spark plasma sintered  $\text{ReB}_2$ , where 1:2.5 Re to B stoichiometric ratio was used to synthesize polycrystalline material, was responsible for the measured lower hardness and Young's modulus values [70]. Another problem, which makes  $\text{ReB}_2$  very difficult material to work with, is that it slowly degrades in the presence of moist air. When  $\text{ReB}_2$  interacts with water in air it becomes covered with a viscous solution within a few months. This property becomes especially serious when high surface area powders are exposed to water vapors in air, which may complicate  $\text{ReB}_2$  implementation in industrial applications.

Although, the stoichiometric compound is  $\text{ReB}_2$ , a phase of highest boron content in the Re-B phase diagram [203], it is difficult to synthesize a stoichiometric phase, and excess boron is usually required to ensure the formation of  $\text{ReB}_2$  due to boron loss during the synthesis. Several approaches are reported on the synthesis of  $\text{ReB}_2$  [45, 46, 52, 56, 59, 64, 68, 69, 71, 72, 74, 202, 203]. In paper [202]  $\text{ReB}_2$  was prepared using the solid state synthesis in an alumina crucible at 1300K for 4 hours in vacuum from elemental B and Re taken in a molar ratio of 2.5:1. It was

reported that the synthesized material contained 5% impurity. Hexagonal platelets  $\text{ReB}_2$  crystals were synthesized using  $(\text{B}_3\text{H}_8)\text{Re}(\text{CO})_4$  molecular precursor through the confined-plume chemical deposition (CPCD) technique [74]. The precursor has a 1:3 Re/B stoichiometry, which mitigated the loss of boron during synthesis. Arc melting of the 1:2.5 ratio of elemental Re and  $^{11}\text{B}$  in Ar atmosphere was used in paper [64] to synthesize a composition of  $\text{ReB}_2$ . Three different techniques, all with some excess of B, were reported to be used for the synthesis of  $\text{ReB}_2$ . Spark Plasma Sintering, tri-arc crystal growing technique, and arc-melting are reported as techniques of choice to produce dense  $\text{ReB}_2$  [70]. Solid state synthesis from Re and B powders in Re/B molar ratio of 1:2.5 under pressure of 5 GPa and high temperature  $1600^\circ\text{C}$  for 60 minutes, followed by quenching to the room temperature at  $100^\circ\text{C}/\text{s}$  was reported in paper [69].  $\text{ReB}_2$  crystals have also been synthesized by arc melting [52], zone melting [72] and optical floating zone furnace synthesis [68] techniques. Thin  $\text{ReB}_2$  films were produced by pulsed laser deposition (PLD) technique using  $\text{ReB}_2$  target, which was prepared by electron beam melting of the mixture of 1:2.5 Re to B powders [45]. While most of the techniques used to synthesize  $\text{ReB}_2$  used excess boron, a few papers [46, 56, 59, 71] utilize a 1:2 stoichiometric ratio for  $\text{ReB}_2$  synthesis. In [59] two methods are reported, where one part of spectroscopically pure Re was heated with two parts of amorphous B. One method was by heating the powder mixture in sealed evacuated silica tubes at  $1200^\circ\text{C}$  for 12 hours and another method was by induction heating under the atmosphere of helium in vitrified alumina crucibles at  $1500^\circ\text{C}$ . Both methods yielded  $\text{ReB}_2$  structure [59]. In [56], the 1:2 mixture of Re to crystalline  $^{11}\text{B}$  powders were pressed into pellets, which were heated in an induction furnace under Ar atmosphere. The pellets were melted at 2600K for one hour. After synthesis,  $\text{ReB}_2$  samples were ground down using a ball mill with

WC milling cups and balls. The 1:2 Re to B ratio was also used for synthesis of  $\text{ReB}_2$ , but with the significant presence of aluminum as the growth medium [46]. The mixture was heated to  $1400^\circ\text{C}$  and held at temperature for 5 hours, it was slowly cooled to  $700^\circ\text{C}$  and then quickly cooled to room temperature. After synthesis, the aluminum flux was dissolved in NaOH, and  $\text{ReB}_2$  crystals were washed with deionized water and dried in air [46]. SPS technique was also used to sinter dense  $\text{ReB}_2$  pellets by using 1:2 Re to B powder mixture [71] but besides the  $\text{ReB}_2$  phase,  $\text{Re}_7\text{B}_3$  phase along with C impurity was also obtained during sintering. All the described techniques, used for the synthesis of  $\text{ReB}_2$ , involved using of high temperatures, sometimes as high as 2600K. Since the vapor pressure of boron is much higher than that of rhenium, it created a problem with the stoichiometry of the  $\text{ReB}_2$  compound. A technique for  $\text{ReB}_2$  synthesis at nominally room temperature would represent a major advance in the material's manufacture. The discussion in the literature inspired us to examine a new synthetic route to  $\text{ReB}_2$  powders. These powders, as well as those of other boron-rich solids are typically not commercially available; therefore, techniques which allow synthesis of boron-rich solids are of high interest, especially if synthesis is performed at room or near room temperatures.

One technique that is highly suitable for producing different powdered materials is through mechanochemical methods [178]. This approach allows synthesis of numerous novel materials and very complex compounds by applying mechanical force to mixtures of elemental powders [191]. It involves repeated cold welding, fracturing, and re-welding of powder particles due to heavy deformation. As a result, the microstructure gets refined and the increased diffusivity (due to creation of a high density of crystalline defects) and reduced diffusion distances (due to refinement of microstructure) allow synthesis to take place at or near room



temperature. In a mechanochemical synthesis, attrition results in the reduction of particle size. This effectively creates micro reaction regimes where frictional heating can supply the activation energy for the production of line compounds from the elements. At this point, the heat of reaction can drive the reaction forward and even result in a self-propagating reaction [204]. This method has been used to produce intermetallic phases, metallic glasses and composites and different borides [178, 205-210]. Here we report the mechanochemical synthesis of  $\text{ReB}_2$  powders.

## 2.2 Experimental

Rhenium metal powder (Cerac Inc, 99.99% pure, -325 mesh,) and boron powder (Alfa Aesar, 99% pure, -325 mesh, amorphous) were used as received. A total of 20 grams of a stoichiometric amount of rhenium and boron powders were loaded into a SPEX tungsten carbide vial with two 12.7mm diameter tungsten carbide balls. The grinding was done by a SPEX 8000 mixer mill for a total of 80 hours.

### 2.2.1 Phase Analysis

Every 5 hours, a small sample was removed for phase analysis by X-ray diffraction (XRD) method. No protective atmosphere was present during the vial opening and collection of small amount of ground powders. A Rigaku D/MAX X-Ray Diffractometer was used to record X-ray diffraction patterns of the powder.

### 2.2.2 Microscopy

The morphology and grain size of the powders were examined using a Scanning Electron Microscope (Zeiss ULTRA-55 FEG SEM). A Transmission Electron Microscope (FEI Technai F30 TEM ) was used to get finer resolution images of the synthesized particles as well as to produce an area map distribution of Re, B, and W elements in the material.

### 2.2.3 Compositional Analysis

Adept 1010 Dynamic SIMS System (Physical Electronics USA) has been used to collect mass spectra for the samples. Cs primary beam of 3kV and 25nA or 50nA was rastered over area  $1000 \times 1000 \mu\text{m}$ . Both negative and positive secondary ions were collected. An auxiliary e-gun was used for charge neutralization.

### 2.2.4 Micro-Raman Spectroscopy

A Renishaw InVia Raman spectrometer was used to study the vibrational spectra of  $\text{ReB}_2$  powders. The Raman spectrometer system is comprised of two lasers (532nm and 785nm) to excite the sample, a single spectrograph fitted with holographic notch filters and a Leica optical microscope rigidly mounted and optically coupled to the spectrometer. The generated laser power was 25mW. Before collecting spectra of  $\text{ReB}_2$ , the spectrometer was calibrated with a Si standard using a Si band position at  $520.3\text{cm}^{-1}$ . The average collection time for a single spectrum

was 300s. Five measurements were performed from different locations of the powder in order to obtain the repeatable data. The 50x objective was used for illumination of the spot of 3-4 $\mu$ m in diameter.

### 2.3 Results and discussion

The synthesis of the desired ReB<sub>2</sub> phase out of elemental Re and B was monitored by powder X-ray diffraction (XRD). The XRD patterns of metallic Re and B amorphous powders used for mechanochemical synthesis of ReB<sub>2</sub> are shown in Figure 20 (a) and (b). Figure 20 (c) shows the X-ray diffraction patterns of ReB<sub>2</sub> powders after different milling times. The quantity of ReB<sub>2</sub> increased with increased milling time. After 5, 10, 15 or even 20h of milling significant amounts of Re metal were still present. After 30 hours of milling a small amount of Re was still evident with the ReB<sub>2</sub> formed. After 50h of ball milling no Re was detected by XRD. The peaks of (002), (100) and (103) ReB<sub>2</sub> planes are sharper and have an increased intensity after 50h in comparison with 30h of milling, which indicates the presence of a more crystalline product. The WC phase was also present due to degradation of the milling media and vial upon contact with the abrasive product. Table 3 lists the lattice parameters of the synthesized ReB<sub>2</sub> after mechanical alloying for 30, 50 and 80h, and lattice parameters of ReB<sub>2</sub> reported in the literature (PDF card # 01-073-1392) are also given for comparison [59]. As one can see from the Table 3, the measured lattice parameters match closely to the reported values. It is also noted that the lattice parameters slightly decrease with increase in mechanical alloying time, while the *c/a* ratio increases with longer mechanical alloying time approaching the reported value.

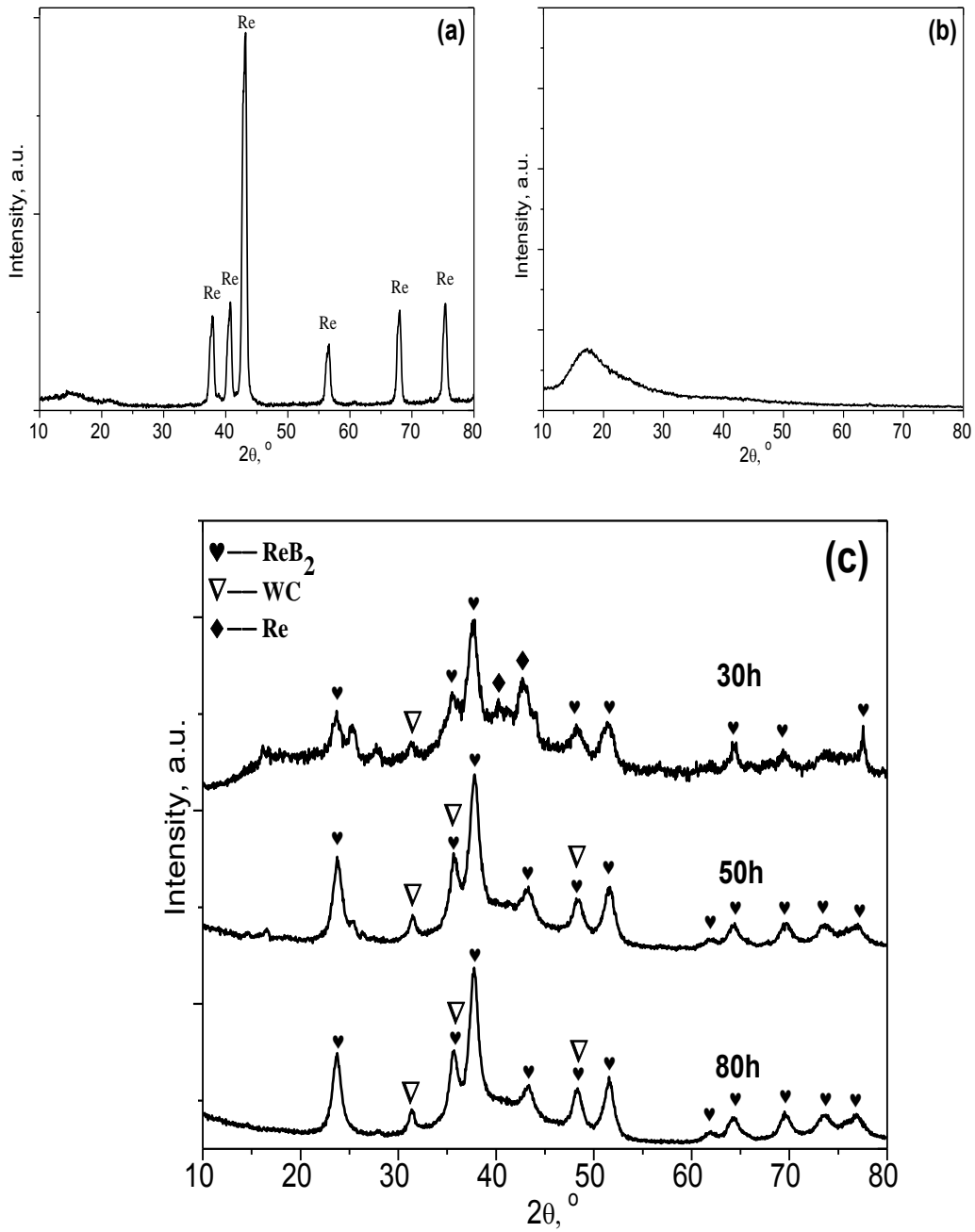


Figure 20: (a) X-ray diffraction patterns of Re powder, (b) B powder and (c) ReB<sub>2</sub> mechanically alloyed powders after 30, 50, and 80 hours of milling. The observed broad peak at ~18° 2θ in (b) is a common peak seen for amorphous materials.

Table 3: Lattice parameters of the synthesized ReB<sub>2</sub> after mechanical alloying for 30, 50 and 80 hours.

Mechanical alloying time (hour)	a (Å)	c (Å)	c/a ratio
30	2.9176	7.5023	2.5714
50	2.9057	7.4867	2.5766
80	2.9018	7.4867	2.5800
PDF#01-073-1392 [59]	2.9000	7.4780	2.5786

### 2.3.1 Microscopies

Figure 21 presents an SEM micrograph of the ReB<sub>2</sub> powders after 80h of milling. It can be seen that a wide particle size distribution is observed. The size of the largest agglomerates is about 1 μm. Along with morphology study of agglomerates by SEM, high resolution characterization of selected particles was performed using TEM. A typical particle of mechanochemically synthesized ReB<sub>2</sub> and its electron diffraction are shown in Figure 22. The particle size is about 60nm wide and 150nm long. It consists of a number of crystallites 5-10nm in diameter agglomerated together. The selected area electron diffraction pattern of the particle shows clearly defined diffraction spots, indicating that the particle is crystalline in nature. The maps of the distribution of Re, B, and W (Figure 23) show that the distribution of B is not homogeneous and a high concentration of boron can be seen in a location at one side of the particle under study. Tungsten was also located on the opposite side of the particle, thus confirming the XRD data of contamination of the ReB<sub>2</sub> by the material used to make the vial and milling media.

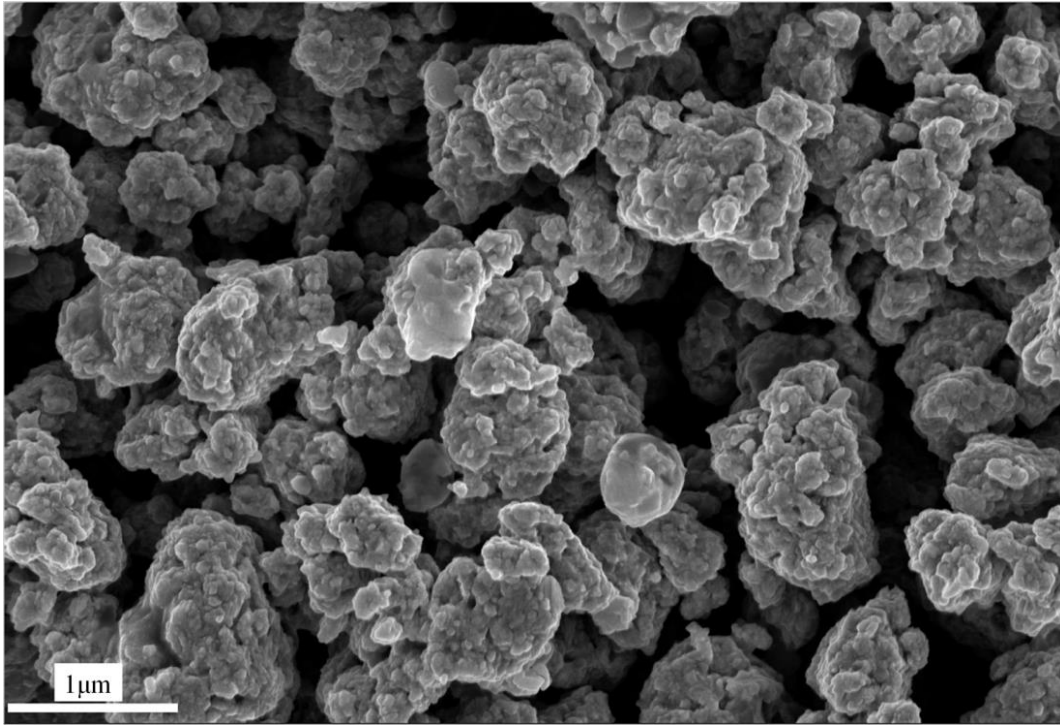


Figure 21: SEM micrograph of ReB<sub>2</sub> powders after ball milling for 80 hours.

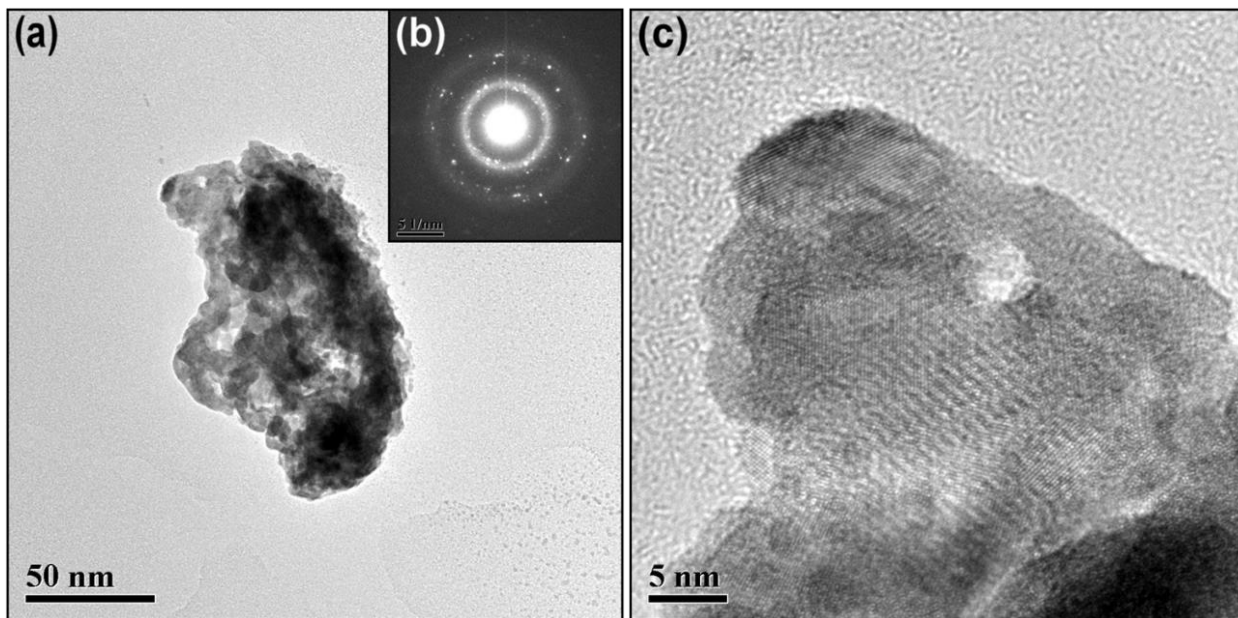


Figure 22: (a) TEM micrograph of a particle of ReB<sub>2</sub> powder after 80 hours of milling, (b) Electron diffraction of ReB<sub>2</sub> particle, (c) TEM micrograph of ReB<sub>2</sub> lattice fringes.

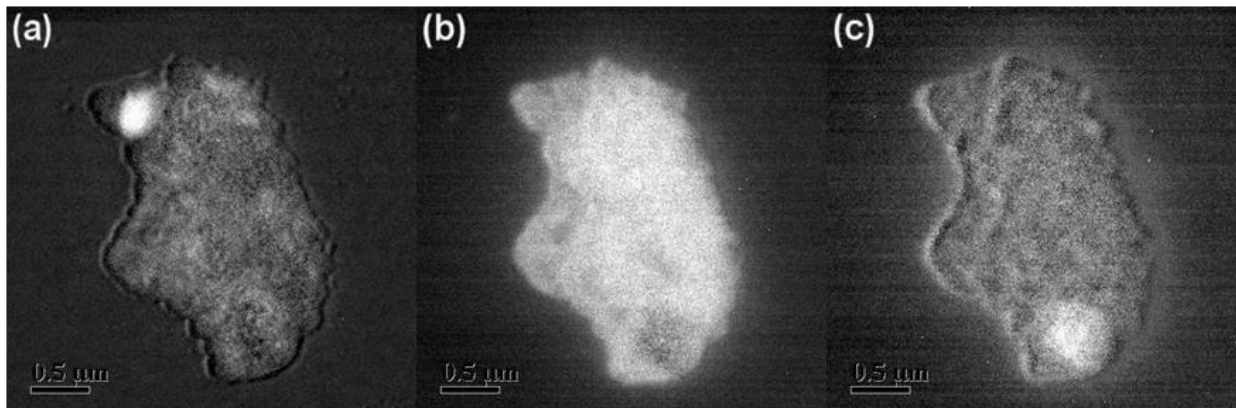


Figure 23: Distribution maps of (a) Boron, (b) Rhenium, (c) Tungsten in a  $\text{ReB}_2$  particle.

### 2.3.2 SIMS

The presence of a number of impurities was also confirmed by SIMS. It can be seen from Figure 24 (a), that oxygen was detected in the mixture after milling for 0.5h since the  $^{16}\text{O}$  peak was present along with other oxygen containing peaks such as  $\text{O+B}$ ,  $\text{O}_2$ , and  $\text{BO}_2$ . The intensity of the  $^{16}\text{O}$  peak increased relative to the intensity of  $^{10,11}\text{B}$  peak as milling time was increased indicating the further O contamination of the powders. The relative intensity of O, BO and  $\text{BO}_2$  peaks over the  $^{10,11}\text{B}$  peak is shown in Table 4 and one can see that the oxygen content increased as milling time increased from 0.5h to 40h reaching a saturation point since the oxygen content did not increase significantly from 40h to 80h of milling. The  $\text{Re+O}$  peak intensity was also compared to the  $\text{Re+B}$  peak intensity for all three milling times. The intensity ratios of these peaks are presented in Table 4 and it is consistent with the increase in oxygen content after milling. Prominent among the other impurities were C, F, and Cl. While it was detected that the carbon content decreased with increased milling time, the F and Cl content increased upon milling for 40h, but decreased after 80h milling. This indicates that the impurities were not

distributed homogeneously in the powder, and the probes that were taken for analysis were not homogeneous; otherwise we should see the increase of the impurities content as time of milling increased.

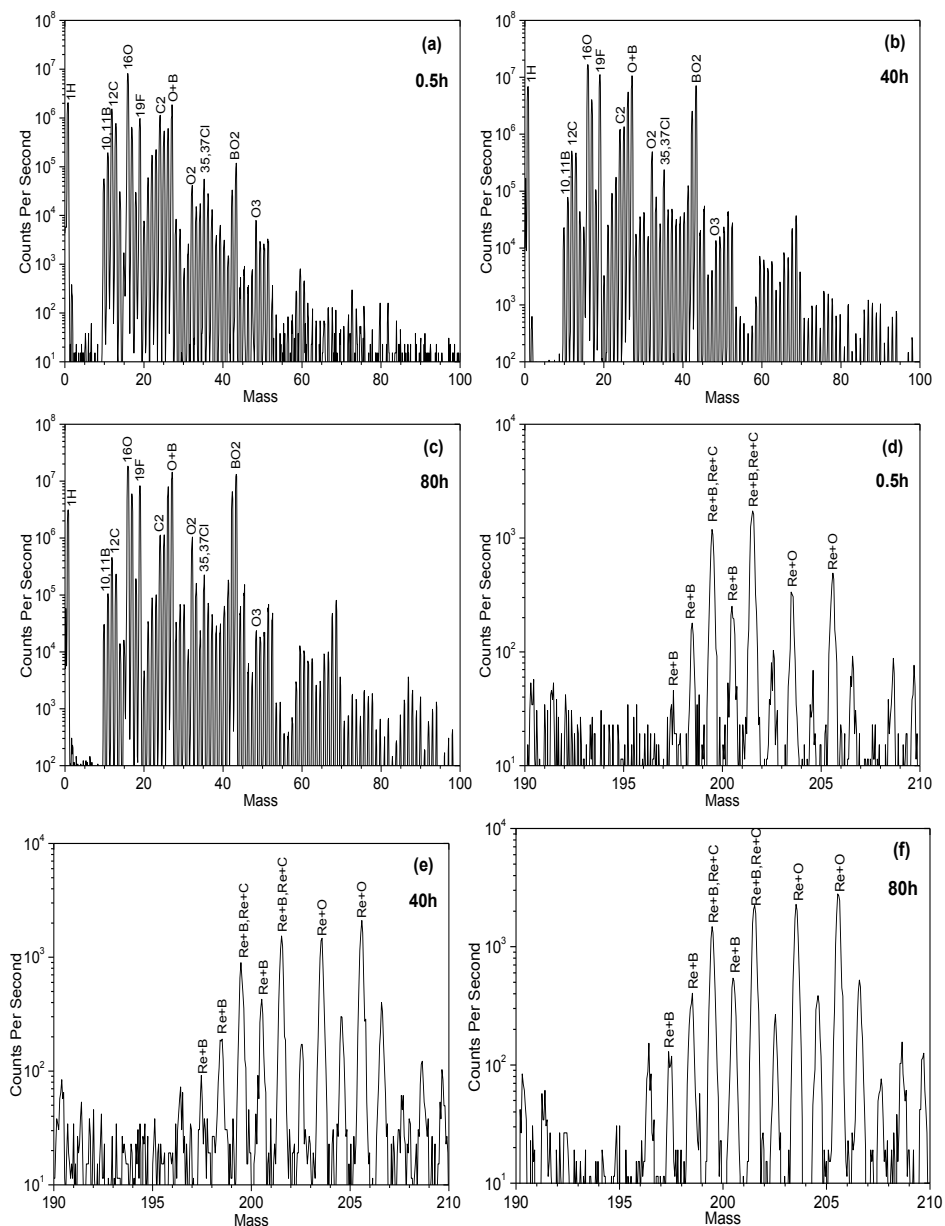


Figure 24: Negative secondary ion mass spectrometry of  $\text{ReB}_2$  powders after 0.5h (a, d); 40h (b, e); and 80h (c, f) milling time.



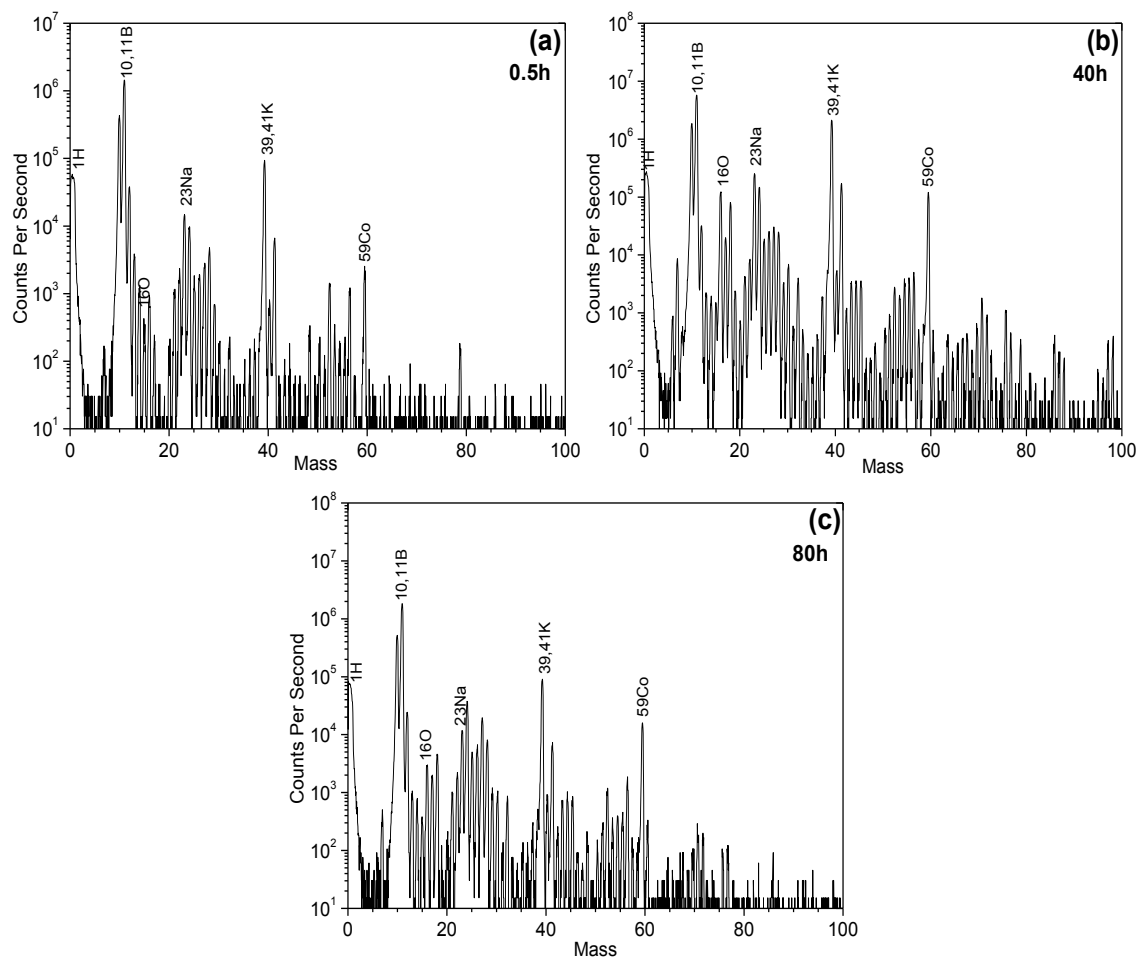


Figure 25: Positive second ion mass spectrometry of  $\text{ReB}_2$  powders after 0.5h (a); 40h (b); and 80h (c) milling time.

Interestingly, hydrogen was detected in the powder after 30 minutes as well as after prolonged milling. The relative intensity of the H peak was the lowest after 30 minutes of milling and increased after longer milling. This could indicate the presence of water in the batch during milling. Positive secondary ions are more sensitive to detect metallic contaminations and they were used to detect metallic impurities present in Figure 25. Both Na and K were detected and their quantity increased upon increase in the milling time. However, their quantity was small after 80h of milling in comparison with 40h of milling time, which could be explained by the

non-homogeneous distribution of the elements in the batch. Co was also detected, as WC alloy contains Co as a soft binder in WC-Co cement composite.

Table 4: Intensity ratio of impurities to boron SIMS peaks.

Intensity Ratio		Time, hour		
		0.5	40	80
Negative secondary ions	$\text{BO}/^{10,11}\text{B}$	9.6900	138.89	136.99
	$\text{BO}_2/^{10,11}\text{B}$	0.9414	91.743	125.00
	$\text{Re+O/Re+B}$	1.9547	4.9285	5.1546
	$^{12}\text{C}/^{10,11}\text{B}$	7.9069	6.5309	4.3346
	$^{19}\text{F}/^{10,11}\text{B}$	5.0478	143.95	78.667
	$^{35,37}\text{Cl}/^{10,11}\text{B}$	0.2895	3.0687	2.1380
	$^1\text{H}/^{10,11}\text{B}$	10.666	89.451	29.868
Positive secondary ions	$^{16}\text{O}/^{10,11}\text{B}$	0.0007	0.0214	0.0016
	$^{39,41}\text{K}/^{10,11}\text{B}$	0.0647	0.3678	0.0496
	$^{59}\text{Co}/^{10,11}\text{B}$	0.0018	0.0208	0.0087
	$^{23}\text{Na}/^{10,11}\text{B}$	0.0102	0.0441	0.0065

### 2.3.3 Raman spectroscopy

Raman spectra of  $\text{ReB}_2$  powders were acquired using two 532nm and 785nm lasers (Figure 26). Factor group analysis of  $\text{ReB}_2$  hexagonal structure results in 2  $E_{1g}$  and 2  $E_{2g}$  Raman active phonon modes, where  $E_{1g}$  and  $E_{2g}$  modes are reported as B-B pair atom vibrations in a-b plane of the unit cell as an “out-of-phase” vibrations with a calculated phonon energy of 85.2 MeV for  $E_{1g}$  mode and 90.4 MeV for  $E_{2g}$  mode 4. In the spectrum collected with IR frequencies, two bands are detected: one at  $190\text{ cm}^{-1}$  and another at  $\sim 786\text{ cm}^{-1}$ . In the spectrum

collected using visible laser, two peaks at  $\sim 228\text{cm}^{-1}$  and  $780\text{ cm}^{-1}$  wave numbers are also detected, but in addition two  $\sim 1400\text{cm}^{-1}$  and  $1580\text{cm}^{-1}$  broad bands are present. These  $1400\text{cm}^{-1}$  and  $1580\text{cm}^{-1}$  bands indicate the presence of carbon, which is explained by contamination of the  $\text{ReB}_2$  powders by milling. Due to the current experimental set up of the notch filter in the Invia spectrometer, only bands with wave numbers higher than  $180\text{ cm}^{-1}$  could be detected.

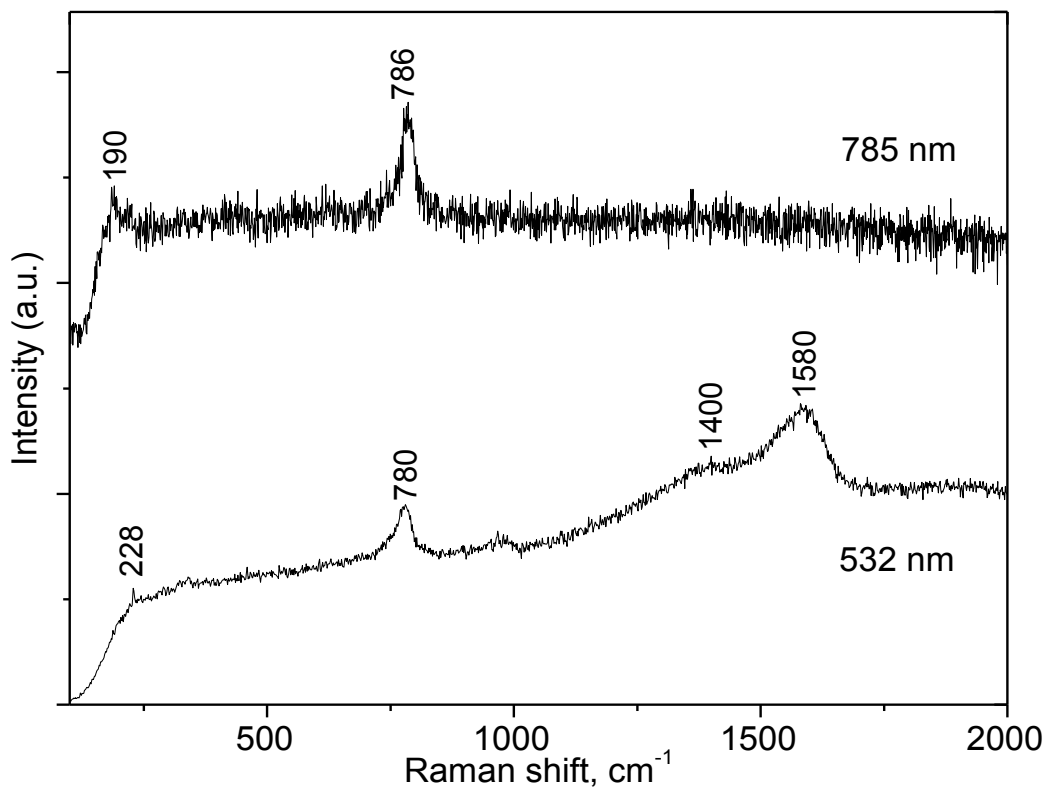
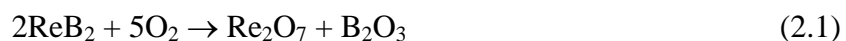


Figure 26: Raman spectra of mechanically alloyed  $\text{ReB}_2$  powders after 80 hours of ball milling.

### 2.3.4 Reaction of powder ReB<sub>2</sub> with O<sub>2</sub> and H<sub>2</sub>O

Upon storing ReB<sub>2</sub> powder in air, packed in the plastic bag; it was found that the powders formed hard agglomerates. The XRD pattern of the long time stored powder is shown in Figure 27. This may be due to a sequential attack by oxygen and water. Initially oxygen may react with the surface of ReB<sub>2</sub> to form Re<sub>2</sub>O<sub>7</sub> and B<sub>2</sub>O<sub>3</sub> (Equation 2.1).



This reaction is thermodynamically favored with a heat of reaction of -1235.3 kJ/mol of ReB<sub>2</sub>. Not only is there a severe lattice mismatch between these oxides and the ReB<sub>2</sub> compound but they quickly react with atmospheric water to form boric acid (Equation 2.2, -629.3 kJ/mol) and perrhenic acid (Equation 2.3, -55.812 kJ/mol).



The net reaction (Equation 2.4) is enthalpically favored by -7.592 kJ/mol. [111, 211]



These acids are hygroscopic and create a liquid layer that allows further degradation of the bulk material. In fact, storage of this material in air while in contact with nylon 6,6 results in holes in the nylon due to acidic degradation. Equation 2.1 through Equation 2.4 suggest that applications of ReB<sub>2</sub> will require exclusion of oxygen or water vapors since the reaction sequence cannot proceed without both. High surface area powders are more susceptible than solid billets.

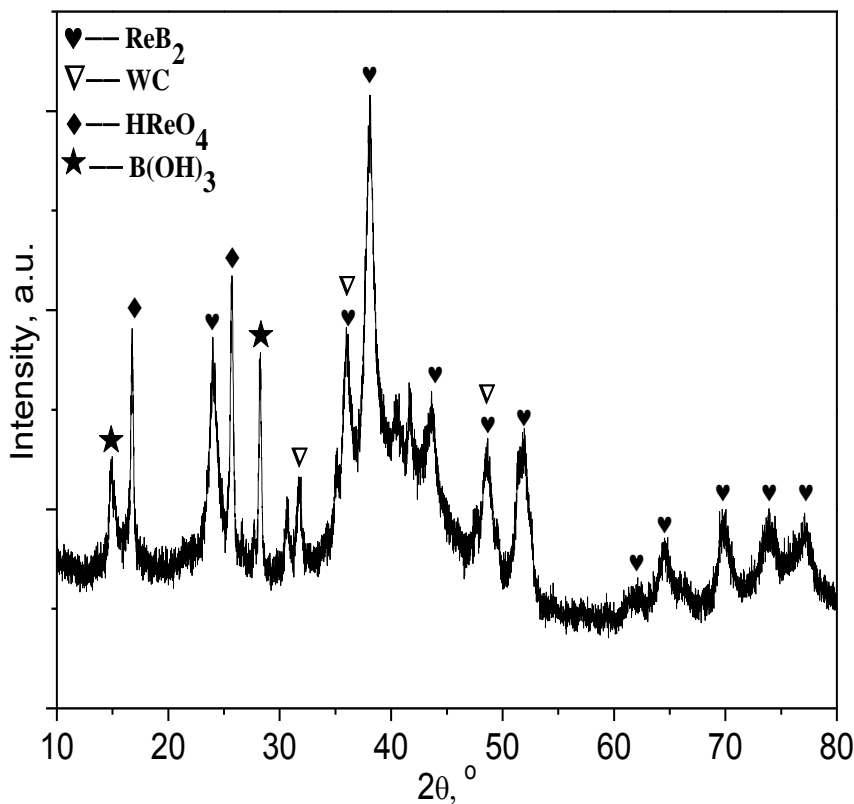


Figure 27: X-ray diffraction patterns of  $\text{ReB}_2$  powder after 1 year storage in the plastic bag without any protective atmosphere.

#### 2.4 Conclusion

We have shown that  $\text{ReB}_2$  powders can be synthesized mechanochemically from elemental crystalline Re and amorphous B powders in the stoichiometric 1:2 ratio. A complete reaction was realized after 70-80 hours of milling in a SPEX-8000 high energy ball mill. By using this approach we have eliminated the need for excess boron reported by others. The synthesized powders were agglomerates of small crystallites as evidenced by SEM. High resolution TEM showed that the material had a clear crystalline structure. The batch became

contaminated both with WC-Co milling media during milling and with oxygen and hydrogen coming from the environment during selection of the intermediate samples for analysis. It is our expectation that powders free of excess of boron will facilitate a thorough understanding of the role composition on the hardness and elastic moduli of  $\text{ReB}_2$  ceramics. This is also a scalable solution that will ultimately allow larger quantities of this potentially useful material to be prepared.

## CHAPTER 3: NOVEL HIGH PRESSURE HEXAGONAL OsB<sub>2</sub> BY MECHANOCHEMISTRY

This work was previously published as “Novel high pressure hexagonal OsB<sub>2</sub> by mechanochemistry” by Zhilin Xie, Moritz Graule, Nina Orlovskaya, E. Andrew Payzant, David A. Cullen, and Richard G. Blair in *Journal of Solid State Chemistry*, Volume 215, (2014) pp. 16-21 Copyright © 2014 Elsevier Inc. Reprinted with the permission of Elsevier. <http://dx.doi.org/10.1016/j.jssc.2014.03.020>

### 3.1 Introduction

In the past decade, extensive work has been done on the synthesis and study of OsB<sub>2</sub>, ReB<sub>2</sub>, RuB<sub>2</sub>, IrB<sub>1.1</sub>, and WB<sub>4</sub> transition metal borides [52-54, 56, 57]. OsB<sub>2</sub> and ReB<sub>2</sub> were reported to have high valence-electron density due to presence of Os and Re ions in the lattice. They also possess ultra-incompressibility and high stiffness that arise from the high degree of B-B and Os(Re)-B bond covalency [52, 58]. It was reported [52] that upon incorporation of B atoms, the Os hexagonal closed packed lattice expands by approximately 10%, forming orthorhombic OsB<sub>2</sub> *Pmmn* (NO. 59, *oP*<sub>6</sub>-type) with lattice parameters  $a=4.684 \text{ \AA}$ ,  $b=2.872 \text{ \AA}$  and  $c=4.076 \text{ \AA}$  [116]. ReB<sub>2</sub>, unlike OsB<sub>2</sub>, crystallizes in the hexagonal *P63/mmc* (NO. 194) structure with lattice parameters  $a=2.9 \text{ \AA}$  and  $c=7.478 \text{ \AA}$  [52]. Incorporation of B into the interstitial tetrahedral site of Re lattice produces a 5% expansion of the lattice when ReB<sub>2</sub> is formed. This smaller expansion results in shorter Re-Re bonds and increased bond strength, which in turn

leads to increased stiffness and improvement of other mechanical properties. Hexagonal  $\text{ReB}_2$  contains strong covalent B-B and Re-B bonds, which also contribute to the superior mechanical properties of the material.

The pressure stability and stress-strain relationship at large structural deformation of  $\text{OsB}_2$  has been studied by applying density functional theory [124]. The ideal critical stress at which a perfect  $\text{OsB}_2$  lattice becomes unstable under tensile or shear deformation was calculated to be 20 GPa in tension and only 9.1 GPa in shear [124]. It has been shown that while interstitial boron atoms enhance tensile strength by forming strong directional covalent bonds with Os atoms, the Os-Os metallic bonds are prone to deform under applied shear stresses, thus greatly reducing the resistance of  $\text{OsB}_2$  to large shear deformation in certain easy-slip directions [124]. Orthorhombic  $\text{OsB}_2$  exhibits very small anisotropic volume compressibility when subjected to pressures up to 32 GPa in a high-pressure diamond anvil cell where no phase changes were observed during hydrostatic compression [53]. It was found that the  $c$ -direction of the orthorhombic lattice is the least compressible and  $b$ -direction of the crystal is the most compressible [29, 94]. Other high-pressure hydrostatic experiments report the stability of this phase up to 34 GPa [32]. It was predicted that hexagonal  $\text{ReB}_2$  might also be transformed to a different metastable phase by applying shear stress, as it has a relatively low ideal shear strength (34 GPa), albeit it is much higher than that of  $\text{OsB}_2$  (9.1 GPa) [212]. Thus, it is not hydrostatic, but rather deviatoric stress which significantly affects both the crystal structure and mechanical properties of  $\text{OsB}_2$  and  $\text{ReB}_2$  components.

While most published work reports the existence of a thermodynamically stable  $oP_6$ -type  $\text{OsB}_2$   $Pm\bar{m}n$  orthorhombic structure [53, 56, 115, 121, 135], other  $\text{OsB}_2$  structures have also been



predicted. Using local density approximation, Hao *et al.* [120] predicted that OsB<sub>2</sub> can adopt an *oP*<sub>12</sub> OsB<sub>2</sub> *Pnma* structure. In addition, two pressure-stabilized hexagonal OsB<sub>2</sub> phases, hexagonal ReB<sub>2</sub>-type *P63/mmc* and hexagonal AlB<sub>2</sub>-type *P6/mmm* structures were predicted to exist by first-principles calculations[112]. These phases have never been reported experimentally. In 1960, Kempter *et al.* [114] claimed to have synthesized a hexagonal OsB<sub>2</sub> phase, but the reported lattice parameters are identical to those of OsB<sub>1.1</sub> (JC-PDS 030-0879 reported in 1978) suggesting that the phase actually produced was OsB<sub>1.1</sub>. Using local density approximation, it was calculated that only 2.5 GPa of pressure is required to transform orthorhombic into a hexagonal ReB<sub>2</sub>-type OsB<sub>2</sub> structure[112]. The phase stability and pressure-induced structural phase transition of OsB<sub>2</sub> was also investigated[113], which predicted an orthorhombic to ReB<sub>2</sub>-type hexagonal phase transition pressure of 10.8 GPa. However, in both of these studies the authors did not specify what type of stress -- uniaxial, hydrostatic or shear -- was required to cause the transition. It was pointed out[113] that hexagonal ReB<sub>2</sub>-type OsB<sub>2</sub> structure is expected to be a stable phase, as no soft mode at any wave vectors of the phonon band structure was found. It was also predicted that the ReB<sub>2</sub>-type hexagonal OsB<sub>2</sub> would have a higher bulk and shear moduli than the phase with an orthorhombic structure. [113]

Mechanochemical syntheses, in a high-energy ball mill, have recently been implemented for the production of boron rich solids [178, 213]. A unique feature of this method is the appearance of plastic flow with strong stress concentrators caused by the shear stress and strain induced by high energy ball milling. This plays a crucial role in facilitating the formation of hard and stiff metastable boron rich solids. The strain-induced synthesis of compounds, utilizes both strong elastic and plastic shear deformations upon milling, leading to the appearance of new

phases by solid-state chemical reactions. This facilitates phase transitions at lower pressure, as well as substituting reversible phase transformations with fully irreversible phase transformations [195]. The strain-controlled kinetics governs the rate of the chemical reactions for new phase formation. Acceleration of chemical reactions is caused by rapid corrugation of reaction interfaces triggered by shear stress driven rearrangement instabilities[214]. It was shown in elegant rotational diamond anvil cell experiments that structural changes do not happen unless plastic shear deformation occurs during hydrostatic compression[215]. While pure hydrostatic or axial pressure does not cause plastic flow, the applied shear stress during mechanochemical synthesis either significantly lowers the barrier or even generates unhindered barrierless growth of the metastable product. High frictional resistance to the radial plastic flow in the particles is created during the numerous impact events by ball milling [195, 216]. In the presence of such friction stress, equal to the yield strength in shear of the material, the impact pressure can easily reach several Mbar in magnitude facilitating chemical processes. It was reported that the rate of solid-state chemical reactions increases by factors of  $10^2$ - $10^5$  when shear deformation is present and some chemical reactions simply cannot occur unless the shear flow is present[217]. It was also proposed that elastic shear strain accelerates chemical reactions by lowering the energy gap between the highest occupied bonding and lowest unoccupied anti-bonding molecular orbital[162, 193]. Here we report the mechanochemical synthesis of hexagonal ReB<sub>2</sub>-type OsB<sub>2</sub> phase, which has been predicted to exist, but has never been experimentally prepared.

### 3.2 Experimental

Osmium metal powder (99.95% pure, Heraeus, South Africa) and boron powder (99% pure, -325 mesh, a mixture of amorphous and crystalline phases, Alfa Aesar) were used for the mechanochemical synthesis of OsB<sub>2</sub>. Enough Os and B powders (molar ratio 1:3) were loaded into a WC vial with two 12.7mm WC balls to produce a ball to powder weight ratio of 2.7:1. The balls and vial used in the milling were covered with OsB<sub>2</sub> product formed from previous milling syntheses. All loading operations were carried out in an argon-filled glovebox. The vials were sealed with Viton gaskets to reduce oxygen contamination during milling. The milling was performed in a SPEX 8000D mixer mill for a total of 20 hours. Every 30 minutes the milling was interrupted and vials were left for 30 minutes without grinding in order to decrease the vials' temperature and reduce wear on the mill's motor. After every two hours of milling, a small amount of sample powder was removed from the vial for X-ray diffraction (XRD) analysis. A Rigaku D/MAX X-Ray Diffractometer with a copper source (Cu K $\alpha$ l =1.5418Å) was used to record the powder XRD patterns. After the hexagonal OsB<sub>2</sub> powder was synthesized, a small quantity was loaded into a fused silica ampule (Figure 28), sealed under vacuum, and annealed up to 6 days at 1050 °C. The synthesized OsB<sub>2</sub> powder was sintered using fast current assisted technique (SPS25–10, Thermal Technologies, CA). The spark plasma sintering (SPS) of the powder packed in the graphite die was performed at 1500°C, 50MPa for 5 minutes. The heating and loading rates employed were 47°C/min and 10MPa/min, respectively. A high resolution powder XRD pattern was collected with synchrotron X-rays ( $\lambda$ =0.4137Å) at the Advanced Photon Source (Beamline 11-BM), Argonne National Laboratory. Refinement of the structure

was performed using the GSAS EXPGUI [218, 219] and HighScore Plus software. For the temperature stability experiment, a PANalytical X'Pert Pro MPD system was used to collect XRD patterns at low temperature (using an Oxford PHENiX stage) and at high temperatures (using an Anton Paar XRK900 reaction chamber). The OsB<sub>2</sub> sample was protected in argon atmosphere during high temperature (25 °C to 875 °C) XRD and *in vacuo* during low temperature (-225 °C to 25 °C) XRD experiments. The morphology and particle size of the powders were examined in a Zeiss ULTRA-55 FEG scanning electron microscope (SEM) equipped with a silicon drift energy dispersive X-ray spectroscopy (EDS) detector capable of detecting low Z elements such as B. A JEOL JEM2200FS aberration-corrected scanning transmission electron microscope (STEM) was used to obtain high-resolution images of the hexagonal OsB<sub>2</sub> nanoparticles.



Figure 28: Sealed vacuum quartz ampule with sample pellet loaded in a boron nitride crucible.

### 3.3 Results and discussion

Figure 29 shows the XRD pattern of the powder after annealing. New ReB<sub>2</sub>-type hexagonal OsB<sub>2</sub> structure started forming after 2.5 hours of milling, as detected by X-ray analysis. Although two hexagonal structures (ReB<sub>2</sub>-type and AlB<sub>2</sub>-type) were predicted for

OsB<sub>2</sub>, only the ReB<sub>2</sub>-type was produced via mechanochemical synthesis, as the stresses required for formation of AlB<sub>2</sub>-type should be higher than those produced during high energy ball milling. The reaction was obviously not complete after 2.5h of milling since elemental Os peaks were prevalent in the diffractogram. After grinding for 6 hours, the intensities of peaks from the hexagonal OsB<sub>2</sub> phase begin to dominate the diffractogram, and after 8 hours of grinding, the amount of crystalline Os metal phase decreased drastically. The Os peaks became almost undetectable after 12 hours of grinding. After 18 hours of grinding, hexagonal OsB<sub>2</sub> became the absolutely major phase. While the contamination of OsB<sub>2</sub> product with WC phase during milling is an issue in the synthesis of a phase pure powder, the low WC ball to raw powder weight ratio and coating of OsB<sub>2</sub> product on balls and vial from previous milling provided a clear pathway to synthesize hexagonal OsB<sub>2</sub> powder where no WC phase was detected by XRD. In order to verify the high-temperature stability of the hexagonal OsB<sub>2</sub> structure as well as to remove strain of the particles introduced during high energy milling and increase crystallinity of the powder, the OsB<sub>2</sub> powder was annealed at 1050 °C *in vacuo* for 6 days. It was determined that after such annealing, the OsB<sub>2</sub> maintained its hexagonal structure and did not transform to the orthorhombic (*Pmnm*, No. 59, *oP*<sub>6</sub> type) phase, which shows the relatively high stability of hexagonal OsB<sub>2</sub> at high temperature *in vacuo*. After annealing, the crystallinity of the OsB<sub>2</sub> phase increased, as one would expect after such high-temperature exposure. Os<sub>2</sub>B<sub>3</sub> phase might also be present as an intermediate product of the Os and B high energy milling, since one extra peak, tentatively belonging to Os<sub>2</sub>B<sub>3</sub>, was found in the XRD pattern of the synthesized powder (Figure 29). While no separate peaks of WC were detected by XRD in synthesized OsB<sub>2</sub> powder, the minute broadening of the OsB<sub>2</sub> peaks at the higher d-spacings might indicate either the

existence of the small separate WC phase or formation of the graded WC-OsB<sub>2</sub> composition of the powder after milling. It is possible that the *hkl*-dependent peak broadening observed in the (103) peak may indicate size/stain anisotropy in the powder, or presence of another phase, or both.

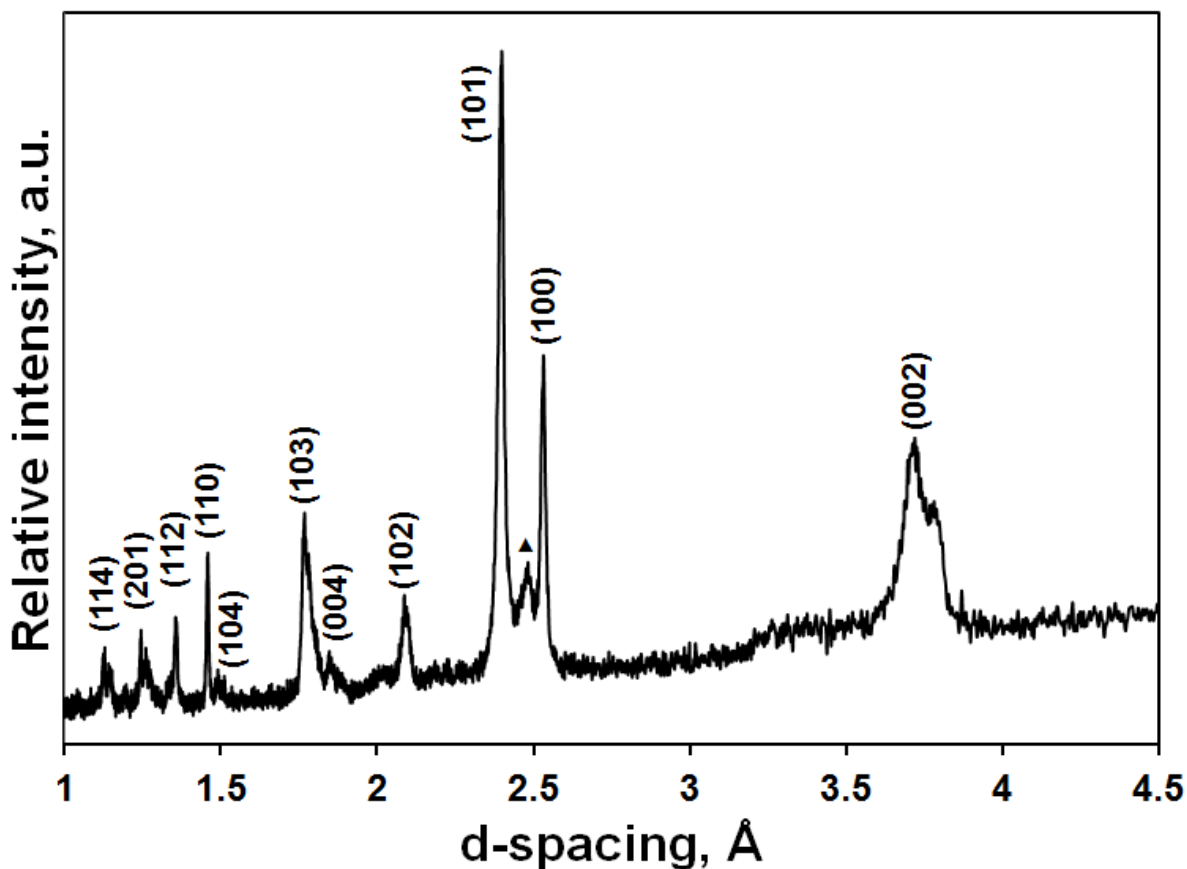


Figure 29: The OsB<sub>2</sub> XRD pattern from a conventional laboratory X-ray diffractometer. After mechanochemical synthesis, the hexagonal OsB<sub>2</sub> powder was annealed *in vacuo* at 1050 °C for 6days. The unindexed peak around d-spacing=2.5Å (▲) may be due to Os<sub>2</sub>B<sub>3</sub>.

While it was impossible to obtain a good fit of the OsB<sub>2</sub> pattern of mechanochemically synthesized powder by Rietveld refinement because of strain present in the lattice and the existence of the extra peak, the sintering of the powder produced a well-defined mixture of two

OsB<sub>2</sub> structures, both hexagonal and orthorhombic phases were present in the sintered sample after SPS. The majority of the structure after SPS was still belonging to the hexagonal OsB<sub>2</sub> lattice (~80wt%), while about 20wt% of the material transformed into orthorhombic phase, thus the 80:20 mixture of hexagonal and orthorhombic phases were produced after SPS. No other phases were detected and all the peaks were identified in XRD pattern (Figure 30). The lattice parameters are reported in Table 5, where lattice parameters of hexagonal ReB<sub>2</sub> are also presented for comparison in addition to the calculated lattice parameters of the predicted hexagonal OsB<sub>2</sub> structure [113]. The schematic presentation of the hexagonal OsB<sub>2</sub> unit cell based on measured lattice parameters is shown in Figure 31. This structure consists of alternating layers of hexagonally arranged osmium and boron. The boron forms infinite sheets consisting of 6-member rings in a chair configuration. In contrast, the boron layers in orthorhombic OsB<sub>2</sub> takes on a boat configuration [56]. The chair configuration allows closer packing of the layers. The hexagonal phase consists of boron layers 3.725 Å apart while the orthorhombic phase has these layers 4.073 Å apart. As a result the hexagonal phase has a density of 12.91 g/cm<sup>3</sup> and the orthorhombic phase has a slightly lower density of 12.83 g/cm<sup>3</sup>.

Table 5: The lattice parameters of hexagonal OsB<sub>2</sub>.

Lattice parameters	<i>a</i> (Å)	<i>c</i> (Å)	<i>c/a</i> ratio
Mechanochemically Synthesized OsB <sub>2</sub>	2.916	7.376	2.53
ReB <sub>2</sub> PDF#01-073-1392 [59]	2.900	7.478	2.58
Calculation data (GGA) of OsB <sub>2</sub> [113]	2.941	7.338	2.50

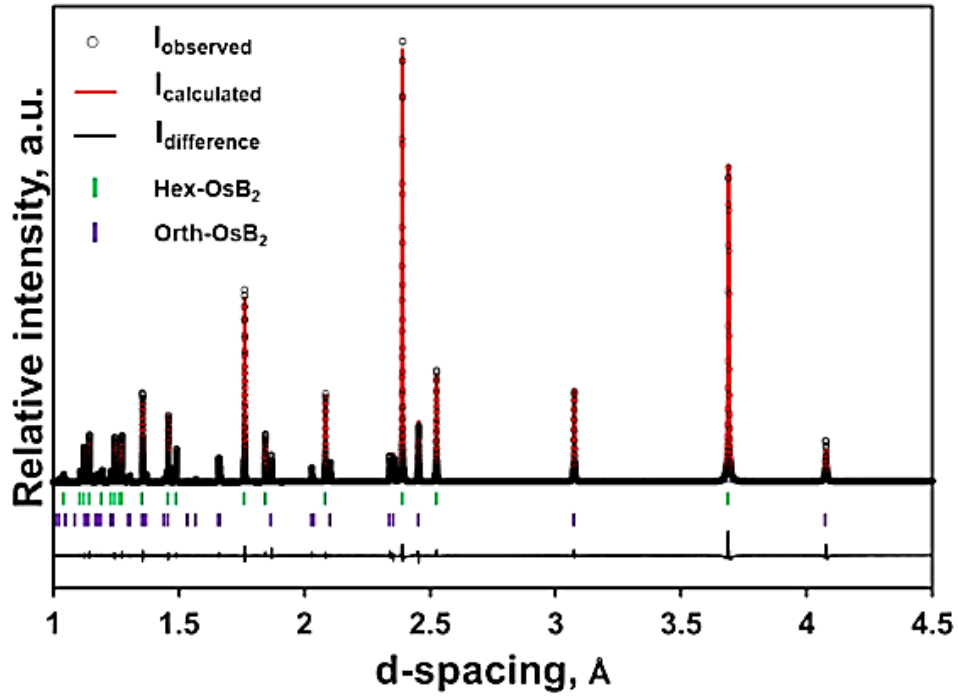


Figure 30: Synchrotron XRD pattern of  $\text{OsB}_2$  after SPS consisting of 80wt% hexagonal and 20wt% orthorhombic phases. No other phases, such as WC,  $\text{Os}_2\text{B}_3$  or crystalline B were found.

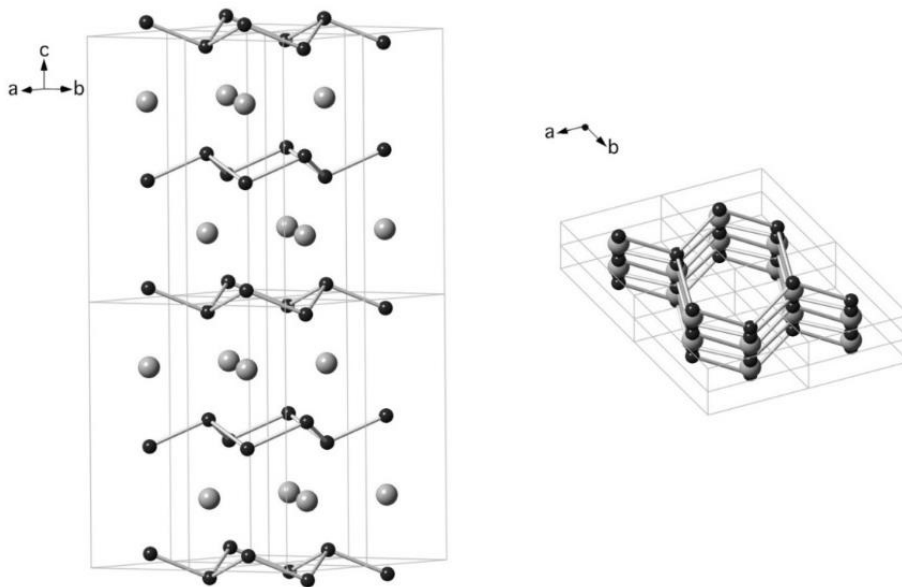


Figure 31: The crystal structure of hexagonal  $\text{OsB}_2$ . Osmium atoms are the larger gray spheres, and boron atoms are the smaller black spheres.



In order to further investigate the phase stability of hexagonal OsB<sub>2</sub>, the powder was both heated in the temperature range of 25°C to 875°C under argon protective environment and cooled down from 25°C to -225°C *in vacuo* while *in situ* XRD measurement were simultaneously performed. The lattice parameters along with the hexagonal OsB<sub>2</sub> unit cell volume were calculated as a function of temperature using the obtained data. A change in *a* and *c* lattice parameters and unit cell volume of hexagonal OsB<sub>2</sub> as a function of temperature is presented in Figure 32. It was determined that the hexagonal OsB<sub>2</sub> structure is stable within the entire -225 °C to 875 °C temperature range both upon cooling and heating and the increase of *a* and *c* lattice parameters with increasing temperature was confirmed. While there is a clear trend for an increase in the lattice parameters as the temperature rises, the *a* lattice parameter shows a decrease in the 300°C to 500°C temperature range, indicating a negative thermal expansion of the material in this crystallographic direction.

The particle size and morphology of the agglomerates of mechanochemically synthesized hexagonal OsB<sub>2</sub> powder was investigated by SEM. The irregular shape of the agglomerates as well as the wide agglomerate size distribution is seen in the SEM image of the powder ground for 18 hours (Figure 33). Most of the agglomerates are smaller than 10 μm, although some of the agglomerates exceed 30 μm in effective diameter. EDS analysis confirmed the presence of Os, B, C as well as some oxygen. A peak for tungsten (from tungsten carbide) is present in the EDS spectrum, but no peaks for tungsten carbide were evident in the XRD pattern.

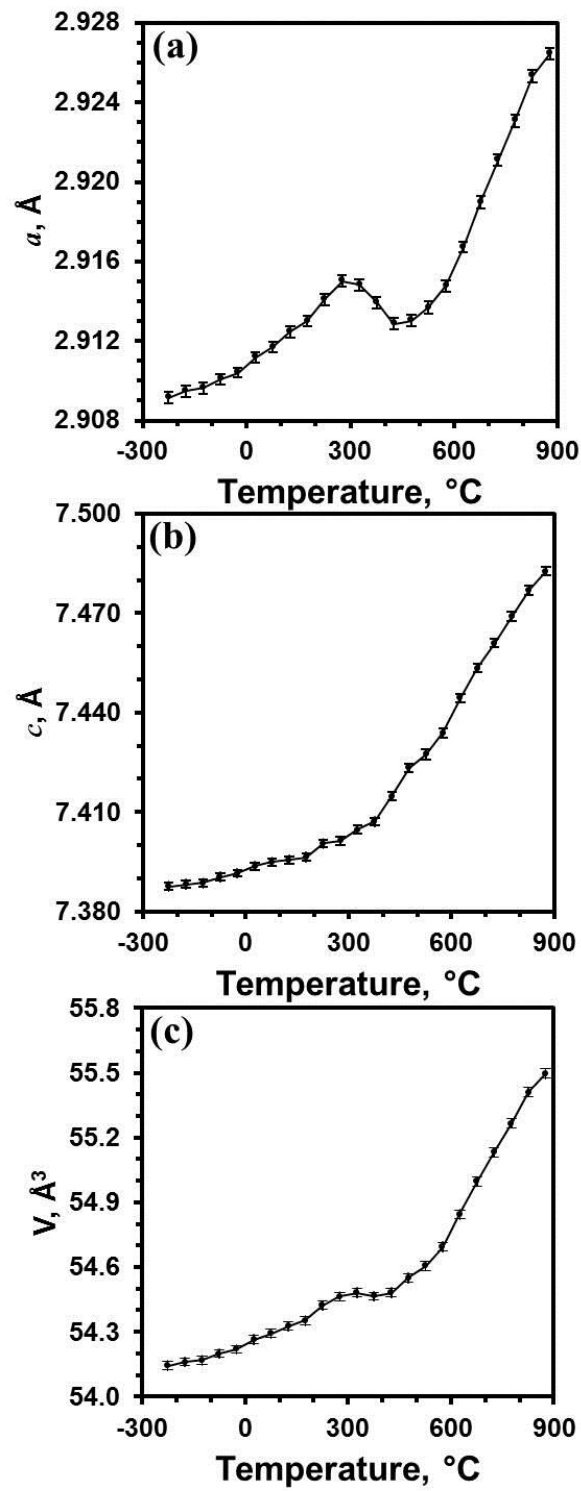


Figure 32: The  $a$  and  $c$  lattice parameters of hexagonal  $\text{OsB}_2$  along with the volume of the unit cell in the  $-225^{\circ}\text{C}$  to  $875^{\circ}\text{C}$  temperature range.

Aberration-corrected scanning transmission electron microscopy (STEM) was also used to study the atomic arrangement of the hexagonal  $\text{OsB}_2$  powder. Characteristic high-angle annular dark-field (HAADF) images of  $\text{OsB}_2$  particles are presented in Figure 34. By sonicating the powder in methanol for 1 min, the larger agglomerated particles were broken down into smaller aggregates of 100-500 nm in size, as shown in Figure 34a. These aggregates were made up of nanocrystallites ranging in size from 1 to 10 nm (Figure 34b). High-resolution STEM images of  $\text{OsB}_2$  nanocrystallites aligned along the major zone axes are presented in Figure 34c-d, with the corresponding fast Fourier transform (FFT) presented and simulated diffraction patterns in Figure 34e-h. Figure 34c presents  $\text{OsB}_2$  nanocrystallites aligned along the  $[001]$  direction, and Figure 34d presents other  $\text{OsB}_2$  nanocrystallites aligned along the  $[100]$  direction. Diffractograms of both particles match those of hexagonal  $\text{OsB}_2$  phase.

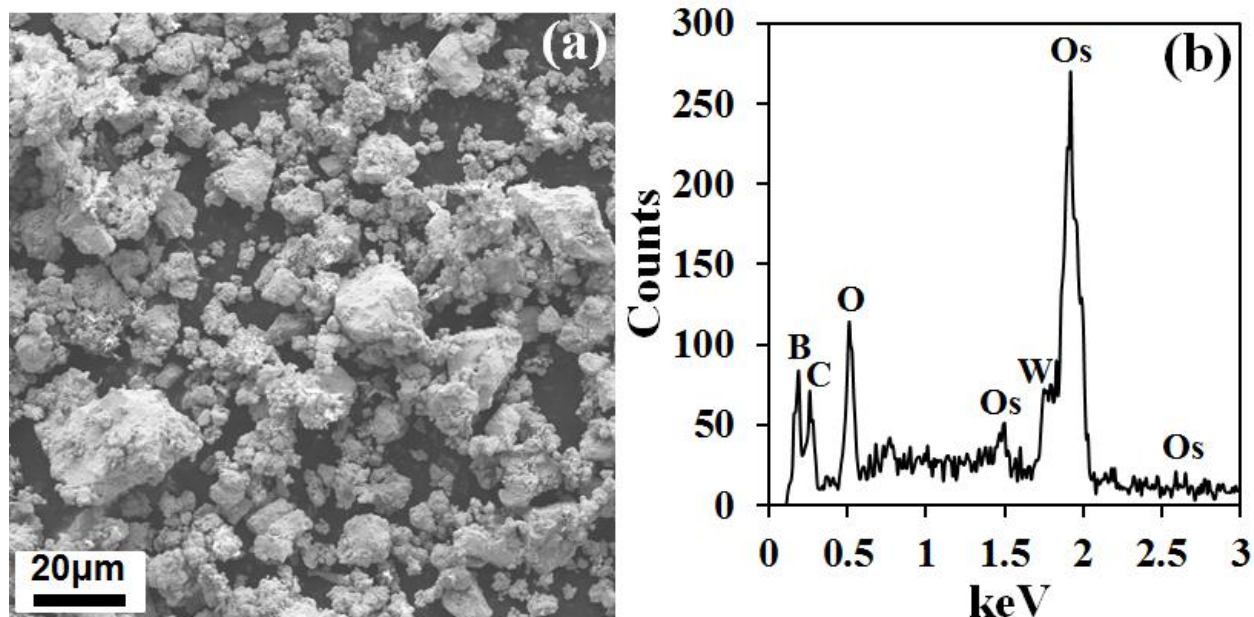


Figure 33: A SEM micrograph (a) and EDS (b) of  $\text{OsB}_2$  powder after 18 hours of milling.

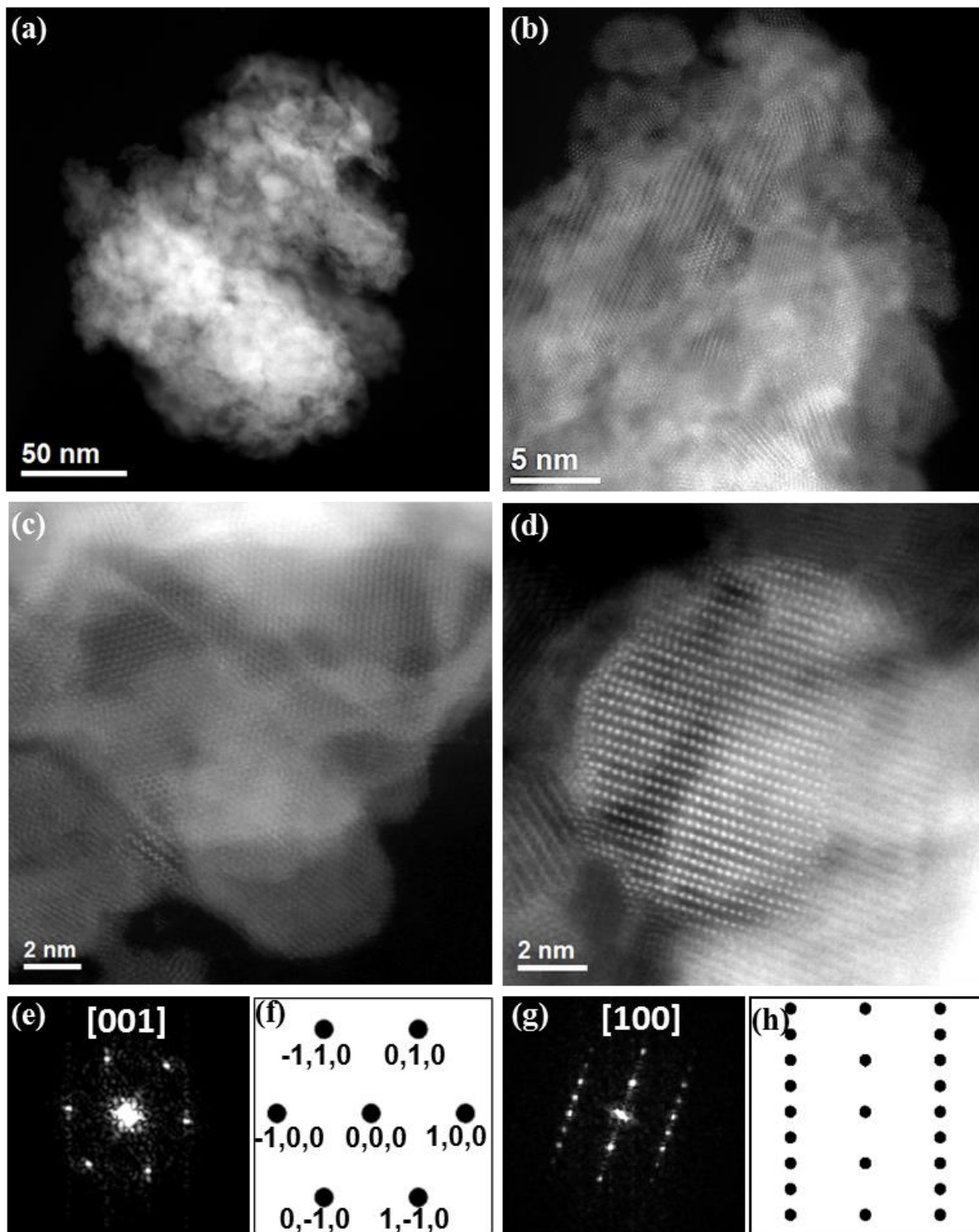


Figure 34: HAADF-STEM images of  $\text{OsB}_2$  powder (a,b), individual  $\text{OsB}_2$  nanocrystallites (c,d) with corresponding fast Fourier transforms (e,g) and simulated diffraction patterns (f,h).

### 3.4 Conclusion

The ReB<sub>2</sub>-type hexagonal OsB<sub>2</sub> structure has been mechanochemically synthesized from elemental B and Os powder with shear stress contributed significantly to the synthesis of the new high-pressure phase. The lattice parameters of the new phase were measured to be  $a=2.916\text{\AA}$  and  $c=7.376\text{\AA}$ . The stability of the new OsB<sub>2</sub> phase was confirmed by high and low temperature XRD where it was found that no phase transformation into orthorhombic OsB<sub>2</sub> phase occurs up to 1050°C, but the negative lattice thermal expansion in  $a$  crystallographic direction was discovered in hexagonal OsB<sub>2</sub> upon heating within 300-500°C temperature range. It was also found that 20wt% of the hexagonal OsB<sub>2</sub> transformed to orthorhombic structure during high-temperature sintering at 1500°C for 5 minutes. The production of hexagonal OsB<sub>2</sub> by mechanochemical means demonstrates the value of alternative synthetic methods for producing new materials.

## CHAPTER 4: THERMAL STABILITY OF HEXAGONAL OsB<sub>2</sub> UNDER ARGON ATMOSPHERE

This work was previously published as “Thermal stability of hexagonal OsB<sub>2</sub>” by Zhilin Xie, Richard G. Blair, Nina Orlovskaya\*, David A. Cullen and E. Andrew Payzant in Journal of Solid State Chemistry, Volume 219, (2014) pp. 210-219 Copyright © 2014 Elsevier Inc. Reprinted with the permission of Elsevier. <http://dx.doi.org/10.1016/j.jssc.2014.07.035>

### 4.1 Introduction

The refractory transition metal boride OsB<sub>2</sub> has received special attention due to its ultra-incompressibility and high stiffness arising from a high degree of B-B and Os-B bond covalency [58]. Although three crystal structures, orthorhombic, hexagonal I ReB<sub>2</sub>-type and hexagonal II AlB<sub>2</sub>-type OsB<sub>2</sub>, have been predicted to exist by local density approximations [120], only the thermodynamically stable oP<sub>6</sub>-type OsB<sub>2</sub> Pmmn orthorhombic structure has been experimentally synthesized [53]. Hexagonal ReB<sub>2</sub>-type OsB<sub>2</sub> was reportedly synthesized 50 years ago [114], however the lattice parameters of the phase correspond to those of OsB<sub>1.1</sub> (JC-PDS 030-0879 reported in 1978 [220]), suggesting that the phase produced was OsB<sub>1.1</sub> and not *h*-OsB<sub>2</sub>. No other reports on the synthesis of hexagonal OsB<sub>2</sub> structure existed until recently [221, 222], but a number of theoretical predictions have shown that o-OsB<sub>2</sub> can be transformed into hexagonal ReB<sub>2</sub>-type or AlB<sub>2</sub>-type OsB<sub>2</sub> structures upon application of pressure [112, 113]. It was calculated that 2.5 to 10.8 GPa was required to induce the orthorhombic to hexagonal ReB<sub>2</sub>-type

OsB<sub>2</sub> phase transformation [112, 113], however these predictions did not specify what type of stress, uniaxial, hydrostatic or shear stress, was used in the calculations. The pressure stability and stress-strain relationship at large structural deformation of orthorhombic OsB<sub>2</sub> has been studied by applying density functional theory [124]. It was shown that the ideal critical stress at which a perfect orthorhombic OsB<sub>2</sub> lattice becomes unstable is equal to 20 GPa in tension but only 9.1 GPa in shear [124], thus indicating that shear stress might play an important role in transforming orthorhombic OsB<sub>2</sub> into hexagonal ReB<sub>2</sub>-type structure. Once formed, hexagonal ReB<sub>2</sub>-type OsB<sub>2</sub> is expected to be a stable phase, as no soft mode at any wave vector of the phonon band structure was found [113]. Experimentally, though, it was shown that orthorhombic OsB<sub>2</sub> exhibits very small volume compressibility with anisotropy present in compressibility of *a* and *c* lattice parameters, when the ceramic was subjected to hydrostatic compression up to 34 GPa [32, 53], no phase change was observed.

Recently, a novel high-pressure hexagonal ReB<sub>2</sub>-type OsB<sub>2</sub> ceramic powder has been successfully synthesized by high-energy mechanochemical synthesis [221, 222]. It is believed that the high shear stress and strain produced during milling played a major role in the formation of the hexagonal structure. In such synthesis, both elastic and plastic shear deformation facilitated the formation of this new phase by the irreversible Os+2B→*h*-OsB<sub>2</sub> solid-state chemical reaction. During high-temperature heating experiments of the *h*-OsB<sub>2</sub> powder in an argon environment, a negative thermal expansion of the hexagonal lattice was observed, where the *a* lattice parameter decreased as temperature increased in 276-426°C temperature range [221]. In addition to the unusual shrinkage, extra diffraction peaks appeared in the high temperature region, which did not belong to the *h*-OsB<sub>2</sub> phase. As a result of such changes, the lattice

parameters of  $h$ -OsB<sub>2</sub> phase changed significantly during heating to 876 °C and cooling back to room temperature. In this work, the thermal stability is studied in greater detail in order to establish the mechanisms driving the lattice contraction and formation of new phases upon heating of hexagonal ReB<sub>2</sub>-type OsB<sub>2</sub> ceramic.

## 4.2 Experimental

Osmium metal and boron powders were used for the mechanochemical synthesis of OsB<sub>2</sub>. Os and B powders with molar ratio of 1:3 were loaded into a tungsten carbide (WC) lined vial (2.25" diameter × 2.5" height) with two 0.5" WC balls. The balls and vial used in the milling were covered with product formed from previous milling syntheses. Information of raw materials and ball milling parameters are shown in Table 6. All loading operations were carried out in an argon-filled glovebox. The vials were sealed with Viton gaskets to reduce oxygen contamination during milling. The milling was performed in a SPEX 8000D mixer mill. Every 30 minutes the milling was interrupted and vials were left for 30 minutes without grinding in order to limit the effects of frictional heating and reduce wear on the mill's motor. After the  $h$ -OsB<sub>2</sub> powder was synthesized, a small quantity was loaded into a fused silica ampule, sealed under vacuum, and annealed up to 6 days at 1050 °C. For the temperature stability experiment, a PANalytical X'Pert Pro MPD system was used to collect X-ray diffraction (XRD) patterns at high temperatures (using an Anton Paar XRK900 reaction chamber) and at low temperatures (using an Oxford PHENiX stage). The OsB<sub>2</sub> sample was protected by flowing pure (99.995%) argon during high temperature (26 °C to 876 °C) XRD experiments and *in vacuo* during low temperature (-225 °C



to 25 °C) XRD experiments. Each scan took about 48 minutes and the scans were collected every 50°C both at high and at low temperature. While there was no direct indication of the presence of oxygen in the high-temperature chamber during the heating experiments, an air leakage was detected during the XRD measurements on the following day. Therefore, the conditions of the heating OsB<sub>2</sub> experiments cannot preclude the availability of an unspecified amount of oxygen in the Anton Paar XRK900 reaction chamber. Refinement of the structure was performed using the HighScore Plus software. The morphology and particle size of the powders were examined in a Zeiss Merlin scanning electron microscope (SEM) equipped with energy dispersive X-ray spectroscopy (EDS) detector. A JEOL JEM2200FS aberration-corrected scanning transmission electron microscope (STEM) was used to obtain images of the nanoparticles in all powders.

Table 6: Reaction information and ball milling parameters.

Product	Boron	Osmium	Milling time	Ball to powder mass ratio	Os to B molar ratio
OsB <sub>2</sub> with ~ 5wt% Os <sub>2</sub> B <sub>3</sub>	99% pure; mixture of amorphous and crystalline; Alfa Aesar	99.95% pure, Heraeus,	20h	2.7	1:3
Os <sub>2</sub> B <sub>3</sub>	98% <sup>11</sup> B enriched; crystalline; Ceradyne	99.95% pure, Heraeus,	54h	2.0	1:3

### 4.3 Results

#### 4.3.1 Phase composition of OsB<sub>2</sub> powder after mechanochemical synthesis at room temperature

Room temperature XRD pattern of *h*-OsB<sub>2</sub> collected before heating experiments are shown in Figure 35A. All peaks found in the diffraction pattern of the powder collected at room temperature before heating were indexed as belonging to hexagonal (*P63/mmc*, 194) OsB<sub>2</sub> with an exception of one low intensity single peak, which was assigned as belonging to the Os<sub>2</sub>B<sub>3</sub> phase. The amount of Os<sub>2</sub>B<sub>3</sub> phase present was calculated by Rietveld refinement to be equal to about 5 wt% after 20 hours of milling and it was considered as an intermediate product of solid state reaction of OsB<sub>2</sub> formation from Os and B raw powders. The presence of Os<sub>2</sub>B<sub>3</sub> compound suggests the following possible route for the synthesis of hexagonal ReB<sub>2</sub>-type OsB<sub>2</sub>. As Os metal possesses a hexagonal *P63/mmc* crystal lattice [223], it is likely that B atoms diffuse into the lattice filling the interstitial sites to first form osmium monoboride, OsB, then OsB<sub>1.1</sub>, followed by Os<sub>2</sub>B<sub>3</sub>, until the hexagonal OsB<sub>2</sub> is finally formed as a major phase. The presence of a small quantity of intermediate Os<sub>2</sub>B<sub>3</sub> phase can possibly be explained by the nature of raw B powder used for mechanochemical synthesis of OsB<sub>2</sub>. The raw B powder contained a mixture of amorphous and crystalline boron. While amorphous boron is more reactive, the crystalline boron contains icosahedral units with strong covalent bonding between boron atoms which are very difficult to break. The breaking of B-B bonds and forming new B-Os bonds was more favorable in the case of the amorphous material as opposed to the crystalline boron. Therefore, while milling, the amorphous boron readily reacts with Os atoms forming the desired *h*-OsB<sub>2</sub> phase, while crystalline boron only forms the Os<sub>2</sub>B<sub>3</sub> phase after 20 hours of milling. As some part of the

boron powder existed as a crystalline phase, the formation of OsB<sub>2</sub> compound was less favored, and a small portion of intermediate Os<sub>2</sub>B<sub>3</sub> phase was detected after 20 hours of milling. The bright-field STEM and SEM micrographs of hexagonal OsB<sub>2</sub> powder after 20 hours of high energy ball milling are shown in Figure 35B and C. The powder consists of small 10-20 nm single crystal nanoparticles (Figure 35B) gathered into larger 2-5 μm agglomerates that can be easily broken apart (Figure 35C).

In order to verify that the hexagonal OsB<sub>2</sub> phase can be formed after high-energy ball milling using only crystalline B as a raw material, crystalline boron powder instead of a mixture of amorphous and crystalline boron was used as a starting material. When crystalline <sup>11</sup>B powder was used as one of the constituents of the mechanochemical synthesis (Figure 36H), the only products (after 54 hours of milling) were a mixture of OsB and Os<sub>2</sub>B<sub>3</sub> phases. The X-ray diffraction pattern of the powder synthesized by mechanochemistry with a mixture of OsB and Os<sub>2</sub>B<sub>3</sub> phases is shown in Figure 35D. After synthesis the powder consisted of 2-5 μm agglomerates composed of small 2-5 nm nanoparticles (Figure 35E and 1F). The lattice parameters and unit cell volume of Os<sub>2</sub>B<sub>3</sub> phase synthesized using crystalline <sup>11</sup>B powder as a raw material are shown in Table 7.

Table 7: Lattice parameters of Os-B compounds.

	Structure	<i>a</i> (Å)	<i>c</i> (Å)	<i>V</i> (Å <sup>3</sup> )	Density (g/cm <sup>3</sup> )	Os-Os distance in <i>a-b</i> plane (Å)	Os-Os distance in <i>c</i> direction (Å)
Os	Hexagonal, <i>P63/mmc</i>	2.734	4.3197	27.96	22.580	2.734	2.675
OsB	Hexagonal, <i>P-6m2</i>	2.876	2.868	20.54	17.102	2.876	2.868
Os <sub>2</sub> B <sub>3</sub>	Hexagonal, <i>P63/mmc</i>	2.908	12.90	94.47	14.501	2.908	2.811 and 3.968
<i>h</i> -OsB <sub>2</sub>	Hexagonal, <i>P63/mmc</i>	2.916	7.376	54.32	12.966	2.916	4.085

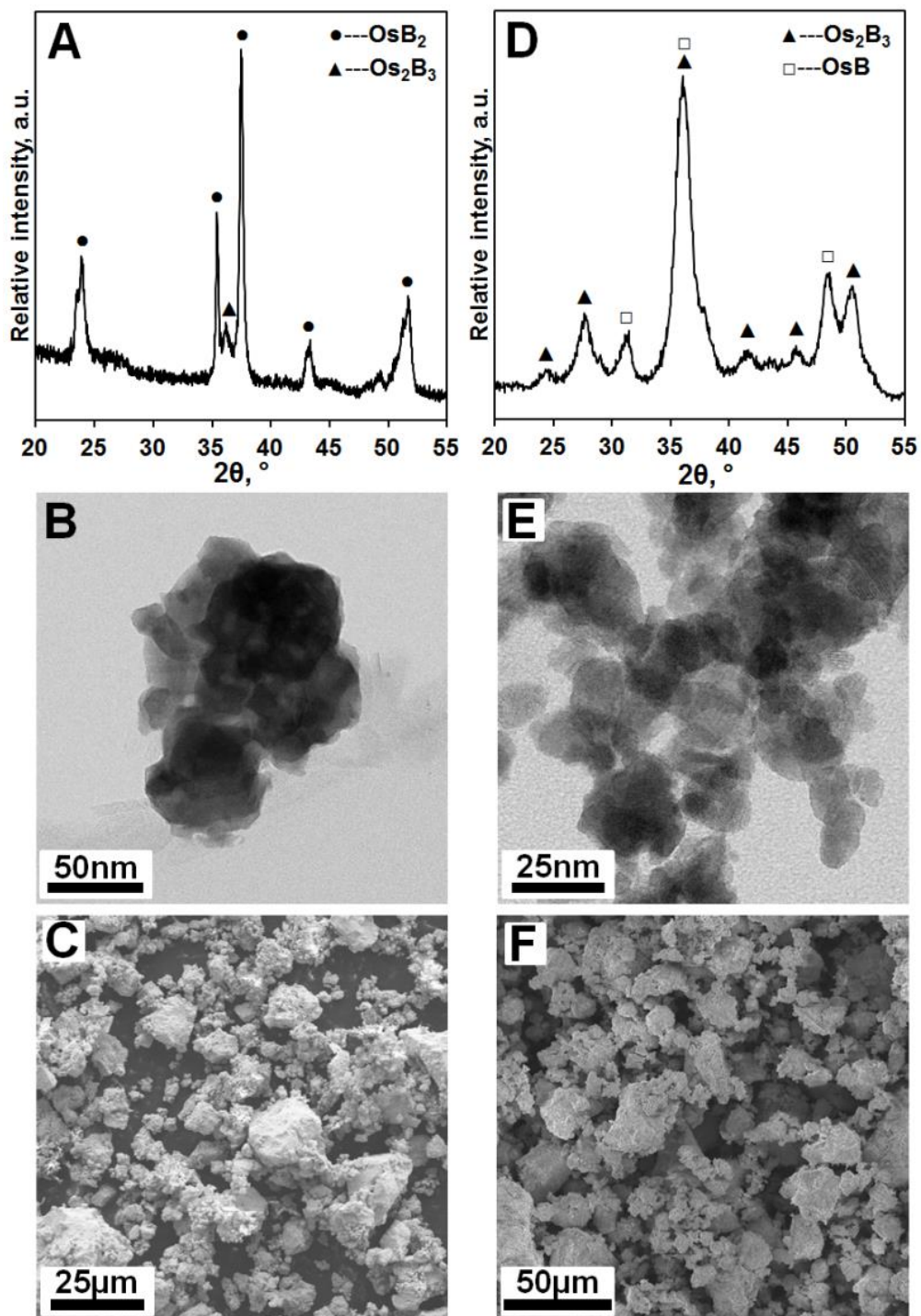


Figure 35: The XRD diffractogram, TEM and SEM images of mechanochemically synthesized  $\text{OsB}_2$  (A, B and C) powder at room temperature before heating experiment and  $\text{Os}_2\text{B}_3$  (D, E and F) produced by ball milling Os and crystalline  $^{11}\text{B}$  mixture for 54h. More TEM images of  $\text{OsB}_2$  and  $\text{Os}_2\text{B}_3$  are shown in Appendix B from Figure 88 to Figure 92.

The difference in the crystal structure of raw boron powders, such as a mixture of amorphous and rhombohedral crystalline phases of B used for synthesis of OsB<sub>2</sub> and purely rhombohedral crystalline <sup>11</sup>B (*R-3m*, No.166) used for synthesis of Os<sub>2</sub>B<sub>3</sub> may be only one factor that affects the product composition. Other factors might contribute to the formation of OsB<sub>2</sub> or Os<sub>2</sub>B<sub>3</sub> reaction products. As in the first case raw boron powder contained a mixture of <sup>10</sup>B and <sup>11</sup>B isotopes, but in the second case enriched <sup>11</sup>B isotope was used as a source, the bond strength between B atoms in the two compounds is different, because of differences in the mass of the <sup>10</sup>B and <sup>11</sup>B isotopes, thus different energy would be required to break B-B bonds to form new compounds during mechanochemistry. In addition, while the same Os powder (Figure 36 A-C) was used for synthesis in both cases, the B powders were not only different isotopes, but also had different particle sizes. While the mixture of amorphous and crystalline B powder consists of relatively small and soft agglomerates with an average particle size of 0.2-1 μm (Figure 36D-F), the <sup>11</sup>B powder consists of large and hard agglomerates with irregular shape, which are difficult to break, with an average particle size of 50-100μm (Figure 36G-I). Therefore, not only the stronger crystalline bonds but also the diffusion pathway for mechanochemical formation of OsB<sub>2</sub> is much longer for <sup>11</sup>B powder, thus preventing the complete reaction from occurring and allowing only the Os<sub>2</sub>B<sub>3</sub> intermediate phase synthesis to complete. It is also important to note that the ratio of the WC balls to the powder under milling was lower in the case where crystalline <sup>11</sup>B was used as a source of B in comparison with the synthesis where a mixture of amorphous and crystalline B was used as a raw material. As the ball weight decreases, it contributes to a decrease in the kinetic impact energy that the balls provided to the powder during milling. All of these differences during the synthesis might be contributing factors to the formation of the

intermediate product with 1:1.5 Os to B stoichiometry instead of formation of the desired hexagonal  $\text{OsB}_2$  in the case when crystalline  $^{11}\text{B}$  isotope powder was used as a raw boron source.

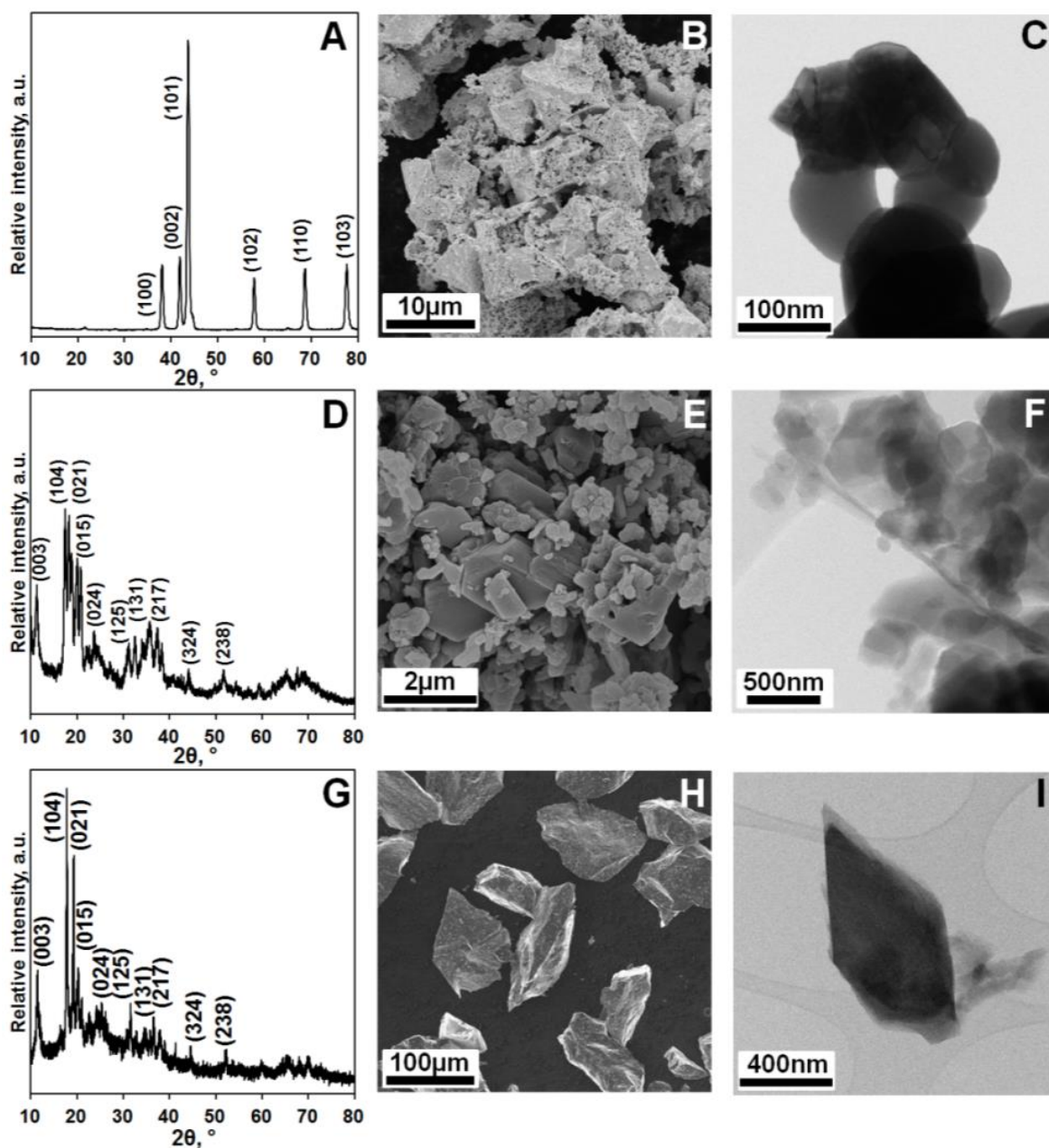


Figure 36: The XRD diffractogram, SEM and bright-field STEM images of osmium metal (A, B and C), amorphous and crystalline boron (D, E and F) and crystalline  $^{11}\text{B}$  (G, H and I). More TEM images of Os, amorphous and crystalline boron, and  $^{11}\text{B}$  are shown in Appendix B from Figure 82 to Figure 87.

#### 4.3.2 High temperature stability and phase composition of hexagonal OsB<sub>2</sub> under Ar

The 2D XRD contour plot along with XRD patterns of *h*-OsB<sub>2</sub> collected at selected temperatures upon heating and cooling under argon are presented in Figure 37. As it was presented in the previous section, the XRD pattern at room temperature contained *h*-OsB<sub>2</sub> and only a small quantity (~5 wt%) of Os<sub>2</sub>B<sub>3</sub> intermediate phase. The powder composition was retained upon heating up to 376°C. However, at 426 °C small quantities of pure metallic Os started to appear (Figure 38). Upon further heating, an increasing amount of Os was detected until 726 °C, where it remained almost constant at 26.6 wt% through heating to 876 °C (Figure 38). While the Os content increased from 2.0 wt% at 426 °C, when it first was detected by XRD, to 26.6 wt% at 876 °C, the OsB<sub>2</sub> content decreased respectively to 68.3 wt% at 876 °C. The Os<sub>2</sub>B<sub>3</sub> phase maintained the same weight percentage (~5 wt%) upon heating and cooling under an argon atmosphere. Once the Os and OsB<sub>2</sub> phases came to some equilibrium at 876 °C, their quantities remained almost constant on cooling with the exception that a small amount of the OsB phase appearing at 826 °C upon cooling (Figure 38). As one can see from the expanded portion of the XRD contour plot (Figure 39A), highlighted by a dash line in Figure 37A, the intensity of the (100) OsB peak can be clearly identified in the XRD pattern (Figure 39B). For comparison, the pattern collected at 876 °C is also provided (Figure 39B) where no traces of (100) OsB peak can be detected, Rietveld refinement indicated a 2.3 wt% of OsB present at 826 °C and, once formed, it remained unchanged on cooling to room temperature.

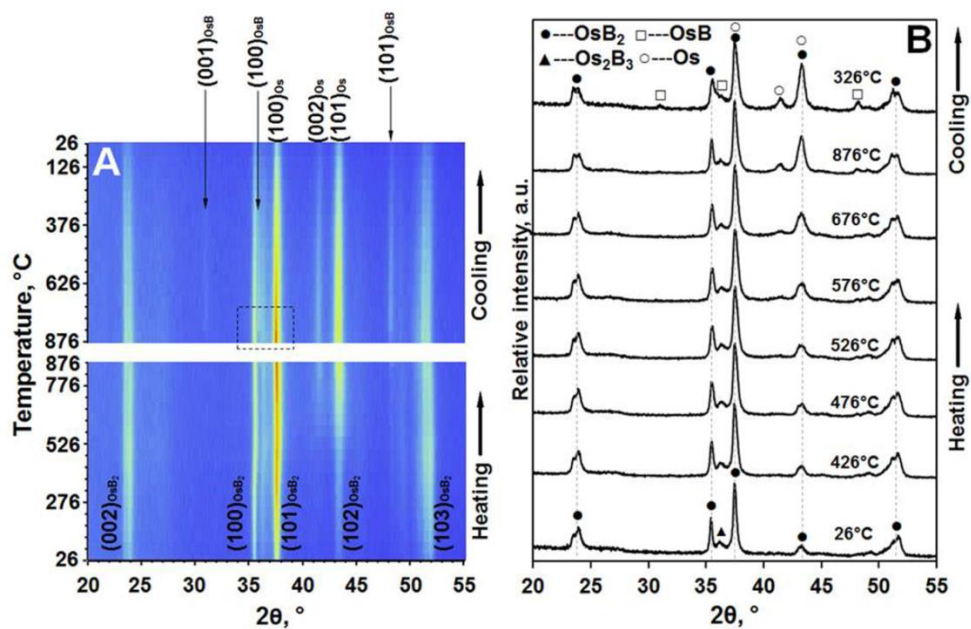


Figure 37: The *in situ* high-temperature XRD contour plot (A) and XRD patterns (B) of *h*-OsB<sub>2</sub> upon heating and cooling under an argon atmosphere.

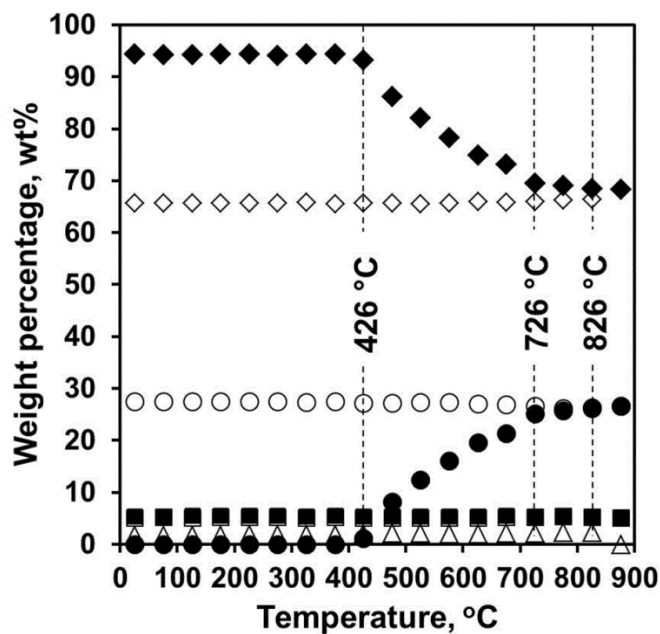


Figure 38: The weight percentage of OsB<sub>2</sub> (◆ or ◇), Os<sub>2</sub>B<sub>3</sub> (■ or □), OsB (Δ) and Os (● or ○) as function of temperature upon heating (filled symbol) and cooling (open symbol) under an argon atmosphere.



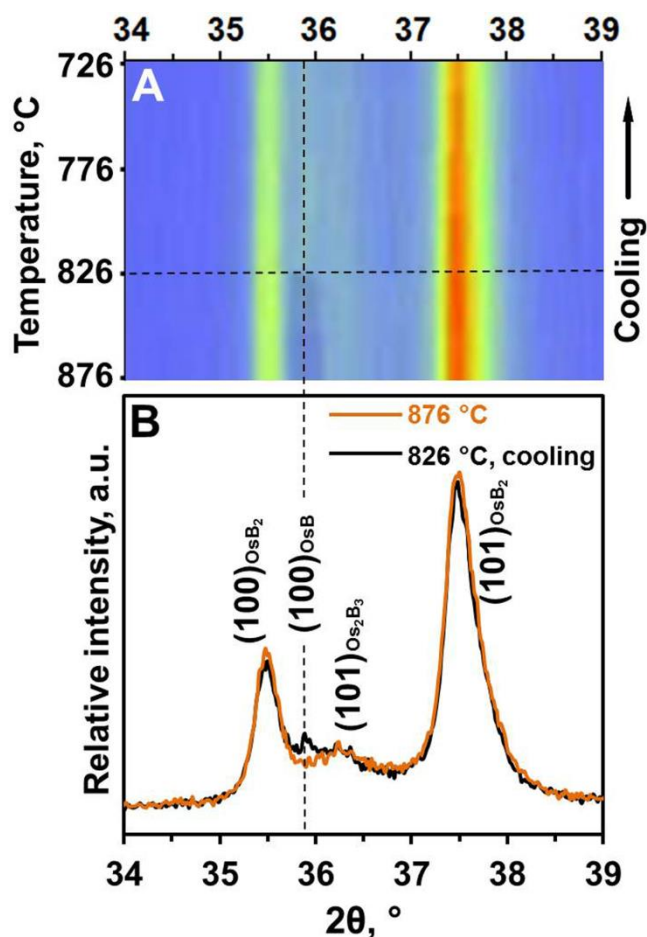


Figure 39: An expanded view (A) of the dash-line box in Figure 37A and the corresponding XRD patterns (B) at 876 °C and 826 °C upon cooling.

#### 4.3.3 Phase composition of OsB<sub>2</sub> powder after mechanochemical synthesis at room temperature

The calculated  $a$  and  $c$  lattice parameters as well as a unit cell volume of  $h$ -OsB<sub>2</sub> upon heating and cooling under Ar is shown in Figure 40. Upon heating, both lattice parameters and unit cell volume of  $h$ -OsB<sub>2</sub> increased, as expected due to thermal expansion, however the expansion of the  $a$  lattice parameter continued only to 276 °C, where a noticeable shrinkage

occurred upon further heating all the way up to 426 °C. While the  $c$  lattice parameter of  $h$ -OsB<sub>2</sub> did not contract in this temperature range, the slope of its expansion became steeper for the  $c$  direction of the lattice starting from 426 °C. The volume of the OsB<sub>2</sub> unit cell decreased in the 326-426 °C temperature range, since the volume is affected by changes both in  $a$  and  $c$  lattice parameters, such that shrinkage of  $a$  lattice parameter contributed to a decrease in the volume of the unit cell. However, above 426 °C both  $a$  and  $c$  lattice parameters along with unit cell volume showed a significant expansion upon further heating. While the slope of expansion of  $a$  lattice parameter was similar in the high temperature 426-876°C range to that at the sub 276°C range, the expansion in  $c$  direction was significantly higher above 376°C in comparison with expansion below 376°C. The increase of the  $a$  lattice parameter as well as the volume of the unit cell of  $h$ -OsB<sub>2</sub> at 426°C coincides with the appearance of pure Os metal detected in the XRD pattern upon heating.

The  $a$  and  $c$  lattice parameters as well as the unit cell volume of the  $h$ -OsB<sub>2</sub> phase decreased upon cooling almost linearly with two different slopes measured both for the  $a$  and  $c$  lattice parameters (Figure 40ABC). It was found that the  $a$  direction of the hexagonal structure shrank faster at higher temperature in comparison with lower temperatures, but the  $c$  direction of the lattice shrank slower at higher temperatures range in comparison with lower temperatures. The unit cell volume decreased linearly upon cooling as shrinkages of both  $a$  and  $c$  lattice parameters contributed uniformly to the volume shrinkage of  $h$ -OsB<sub>2</sub>.

The appearance of detectable quantities of pure Os metal began at 426 °C with an increasing amount detected until 726°C where its quantity remained almost constant at ~ 26.6 wt% up to 876 °C. Above 676°C, the Os content was high enough to refine the lattice parameters

for the Os phase and the  $a$  and  $c$  lattice parameters along with the unit cell volume of newly formed  $h$ -Os metal are shown in Figure 41.

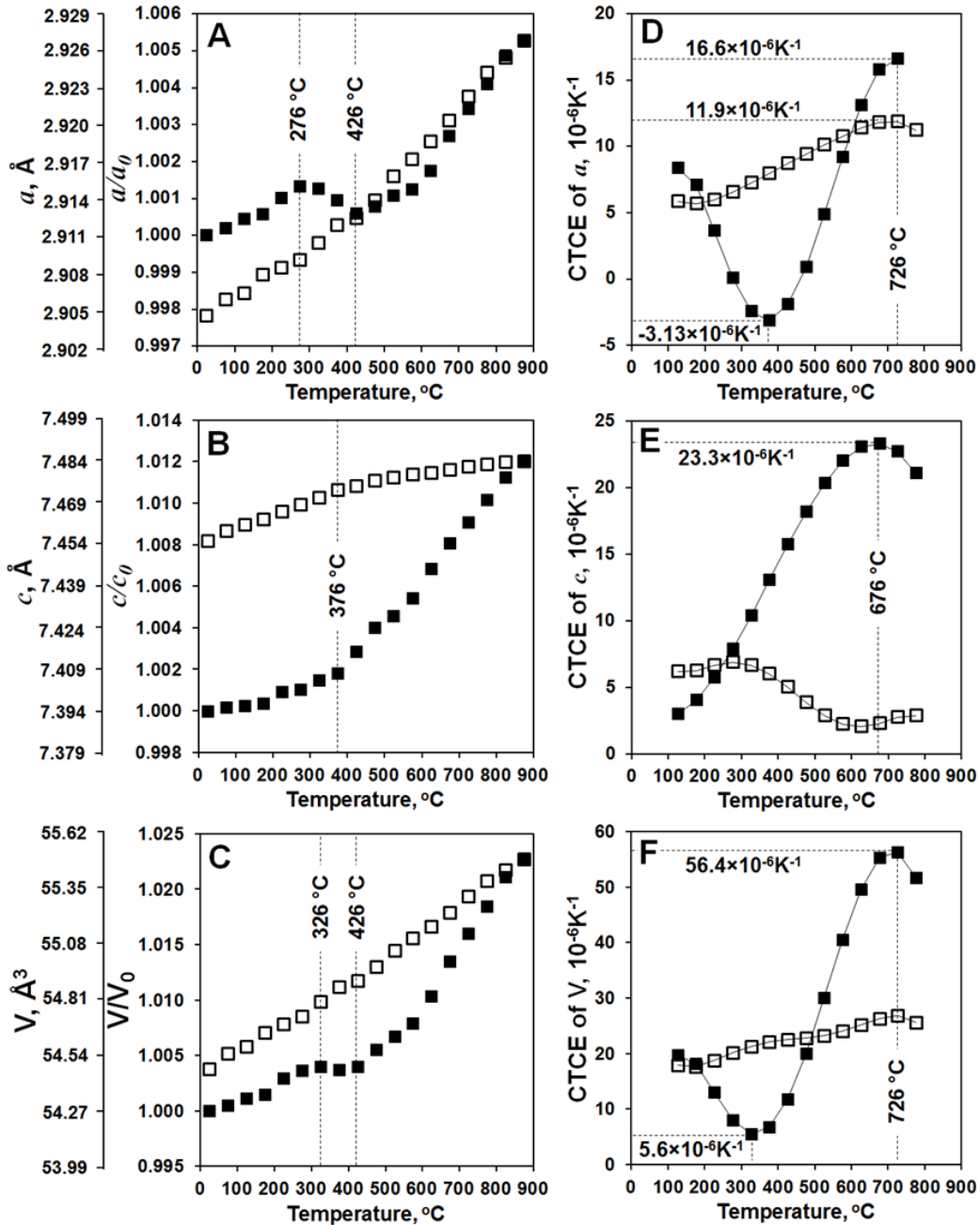


Figure 40: The lattice parameters  $a$  (A),  $c$  (B) and unit cell volume  $V$  (C) of  $OsB_2$  together with CTCE of  $a$  (D),  $c$  (E) and  $V$  (F) as function of temperature upon heating (■) and cooling(□) under an argon atmosphere.

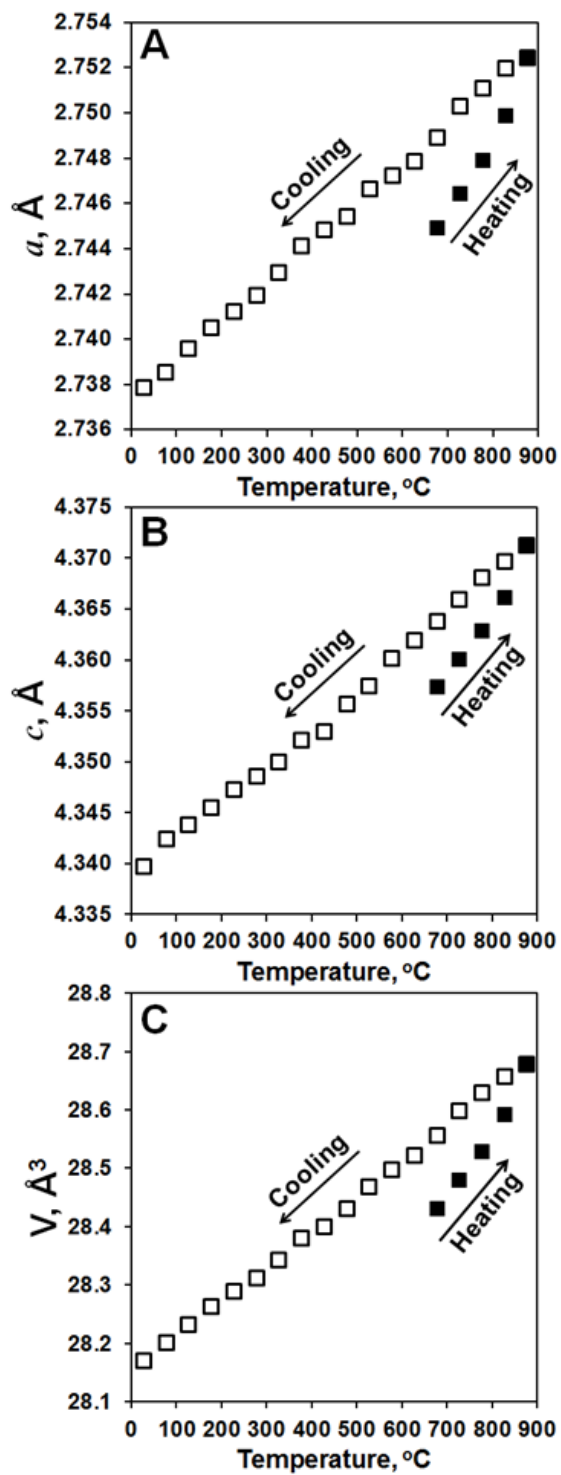


Figure 41: The lattice parameters  $a$  (A),  $c$  (B) and unit cell volume  $V$  (C) of Os as function of temperature upon heating (■) and cooling (□) under an argon atmosphere.

A nearly linear expansion was measured during heating for the  $a$  and  $c$  lattice parameters along with the volume of  $h$ -Os metal, and decreased linearly upon cooling. The difference between coefficients of thermal expansion (CTE) of Os metal upon heating and cooling could possibly be explained by stresses between Os and OsB<sub>2</sub> phases which might appear because of the lattice mismatch between the two phases. The lattice parameters of  $h$ -OsB<sub>2</sub> changed dramatically after the other phases formed upon heating and cooling under Ar. The coefficients of thermal expansion of  $h$ -Os in  $a$ ,  $c$  and  $V$  upon heating and cooling are shown in Table 8. It can be seen in Figure 40A, B and C, while the  $a$  lattice parameter exhibits a thermal shrinkage upon heating, upon cooling it does not exhibit the same behavior, but decreases in an almost linear manner. There is a difference between  $a$  values of  $h$ -OsB<sub>2</sub> for the material before and after heating with  $\Delta a = 6.38 \times 10^{-3}$  Å between the calculations. The  $c$  lattice parameter exhibits even more dramatic changes, and while the  $a$  lattice parameter becomes smaller after heating/cooling, the  $c$  lattice parameter increases by a significant amount. The  $c$  lattice parameter does not show a decrease, as it was observed for the  $a$  lattice parameter values, but there is a change in the slope for the expansion of  $c$  in between 300°C to 400°C temperature range upon heating where at lower temperatures the material expands at a much slower rate in comparison with the expansion above 400°C upon heating. However upon cooling, the thermochemical expansion/shrinkage along  $c$  direction is very different from those observed upon heating. The  $\Delta c$  for the lattice parameter measured before and after heating/cooling experiment was equal to  $6.06 \times 10^{-2}$  Å, which suggests that a significant expansion was observed along the  $c$  direction of  $h$ -OsB<sub>2</sub> when the phase separation and reduction to Os and osmium monoboride (OsB) occurred. As a result of different shrinkage/expansion behavior of the  $a$  and  $c$  lattice parameters, the difference in the

volume of the unit cell of  $h\text{-OsB}_2$  was observed, but the  $\Delta V=0.6145 \text{ \AA}^3$  for the volumes of the material before and after heating was not as large as the difference in the  $c$  lattice parameter. The calculated density of  $h\text{-OsB}_2$  as a function of temperature is shown in Figure 42. Due to negative thermochemical expansion, the density of  $h\text{-OsB}_2$  slightly increased in 300-450°C temperature range, but in general at higher temperatures it decreased from 12.97 g/cm<sup>3</sup> at room temperature before heating to 12.68 g/cm<sup>3</sup> at 876°C. As the lattice parameters of  $h\text{-OsB}_2$  changed after cooling, the room temperature density of  $h\text{-OsB}_2$  was calculated to be 12.92 g/cm<sup>3</sup>.

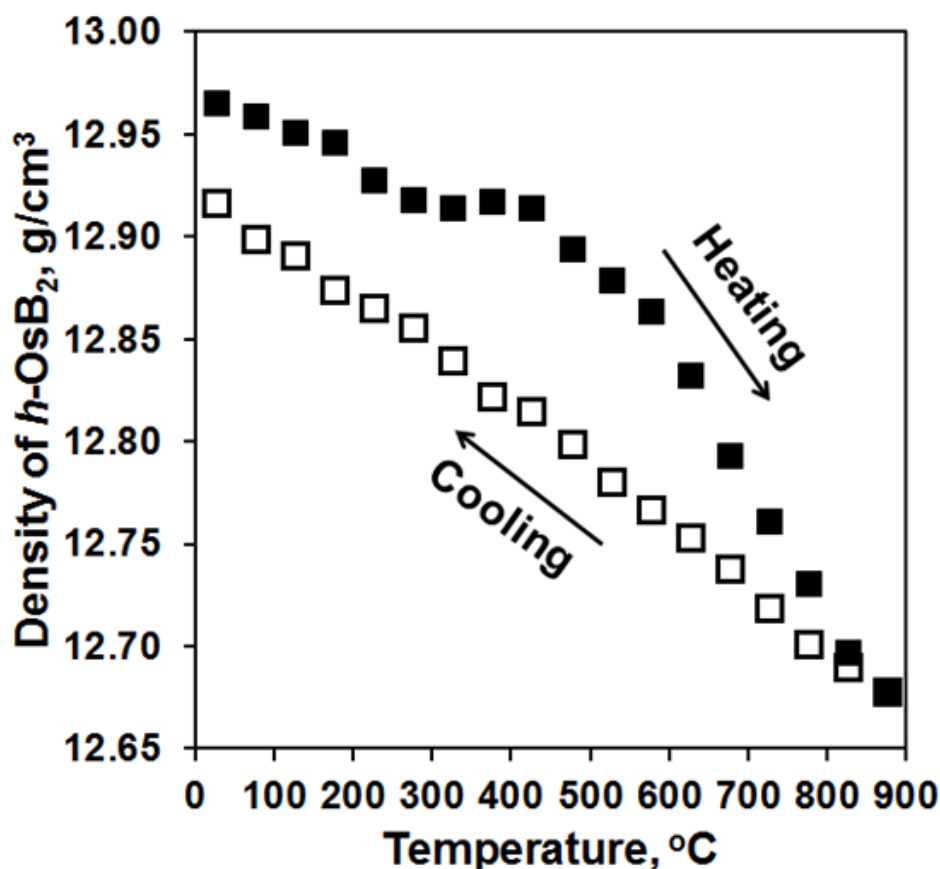


Figure 42: Density of  $h\text{-OsB}_2$  as function of temperature upon heating (■) and cooling (□) under an argon atmosphere.

Figure 40D, E, F shows the calculated coefficient of thermochemical expansion (CTCE) upon heating and cooling of *h*-OsB<sub>2</sub>. Indeed, the negative coefficient of thermochemical expansion is observed along the *a* direction of the lattice upon heating from 276-426 °C. It is also important to note that the thermochemical contraction of the structure along the *c* direction of the lattice was much slower at high temperatures than those observed at lower temperatures upon cooling and that is why the CTCE calculated for thermochemical expansion along the *c* direction is higher at lower (200-300°C) temperatures than those obtained at higher (600-800°C) temperature. The volumetric CTCE did not show negative values, and was rather small in the 276-426°C temperature range with a minimum value of  $5.6 \times 10^{-6}/^{\circ}\text{C}$  at 326°C. While CTCEs of OsB<sub>2</sub> measured along the *a* and *c* crystallographic directions reached 17 and  $23 \times 10^{-6}/^{\circ}\text{C}$  at ~700°C, the volumetric CTCE of the material exhibited much higher values at ~700 °C, with a maximum of  $56 \times 10^{-6}/^{\circ}\text{C}$  at 700°C. Such high volumetric expansion upon heating suggests that the practical usage of OsB<sub>2</sub> at high temperature may be limited, as the material might be sensitive to the tensile thermal residual stresses when in contact with other material and also susceptible to crack growth and spontaneous cracking as it should also be very brittle. Once the stoichiometry of OsB came to the equilibrium upon heating, the CTCEs of the resulting phase exhibited much smaller values both for the *a* and for *c* lattice parameters along with CTCE of the unit cell volume.

Table 8: CTEs of Os metal in *a*, *c* and V upon heating and cooling under an argon atmosphere.

	CTE of <i>a</i> ( $\times 10^{-6}/^{\circ}\text{C}$ )	CTE of <i>c</i> ( $\times 10^{-6}/^{\circ}\text{C}$ )	CTE of V ( $\times 10^{-6}/^{\circ}\text{C}$ )
Heating	13.52	15.69	43.33
Cooling	6.38	8.59	21.59

#### 4.3.4 Low temperature stability of hexagonal OsB<sub>2</sub> *in vacuo*

Although high-temperature experiments under an argon atmosphere showed the formation of new phases, such as *h*-Os and *h*-OsB, the *h*-OsB<sub>2</sub> phase remained stable during cooling to -225°C *in vacuo*. The *a* and *c* lattice parameters along with the unit cell volume of OsB<sub>2</sub> upon cooling are shown in Figure 43. A linear dependence can be seen for all three parameters on cooling. The calculations of coefficients of thermal expansion provided almost identical values for the *a* lattice parameters upon cooling to -225°C and heating back to RT ( $\alpha_{a \text{ cool}}=2.41 \times 10^{-6} \text{ }^\circ\text{C}^{-1}$  and  $\alpha_{a \text{ heat}}=2.22 \times 10^{-6} \text{ }^\circ\text{C}^{-1}$ ), but the values of CTEs along the *c* direction as well as the unit cell volume of hexagonal lattice have small differences for the cooling and heating parts of the experiment. The CTEs calculated from the contraction/expansion of the *c* direction were equal to  $\alpha_{c \text{ cool}}=2.99 \times 10^{-6} \text{ }^\circ\text{C}^{-1}$  and  $\alpha_{c \text{ heat}}=2.86 \times 10^{-6} \text{ }^\circ\text{C}^{-1}$  and CTEs calculated from contraction/expansion of the unit cell volume were equal to  $\alpha_{V \text{ cool}}=7.82 \times 10^{-6} \text{ }^\circ\text{C}^{-1}$  and  $\alpha_{V \text{ heat}}=7.30 \times 10^{-6} \text{ }^\circ\text{C}^{-1}$ . Similar to the calculations performed for the high-temperature experiments, the CTE of the unit cell volume of the *h*-OsB<sub>2</sub> was significantly higher in comparison with each lattice parameter.



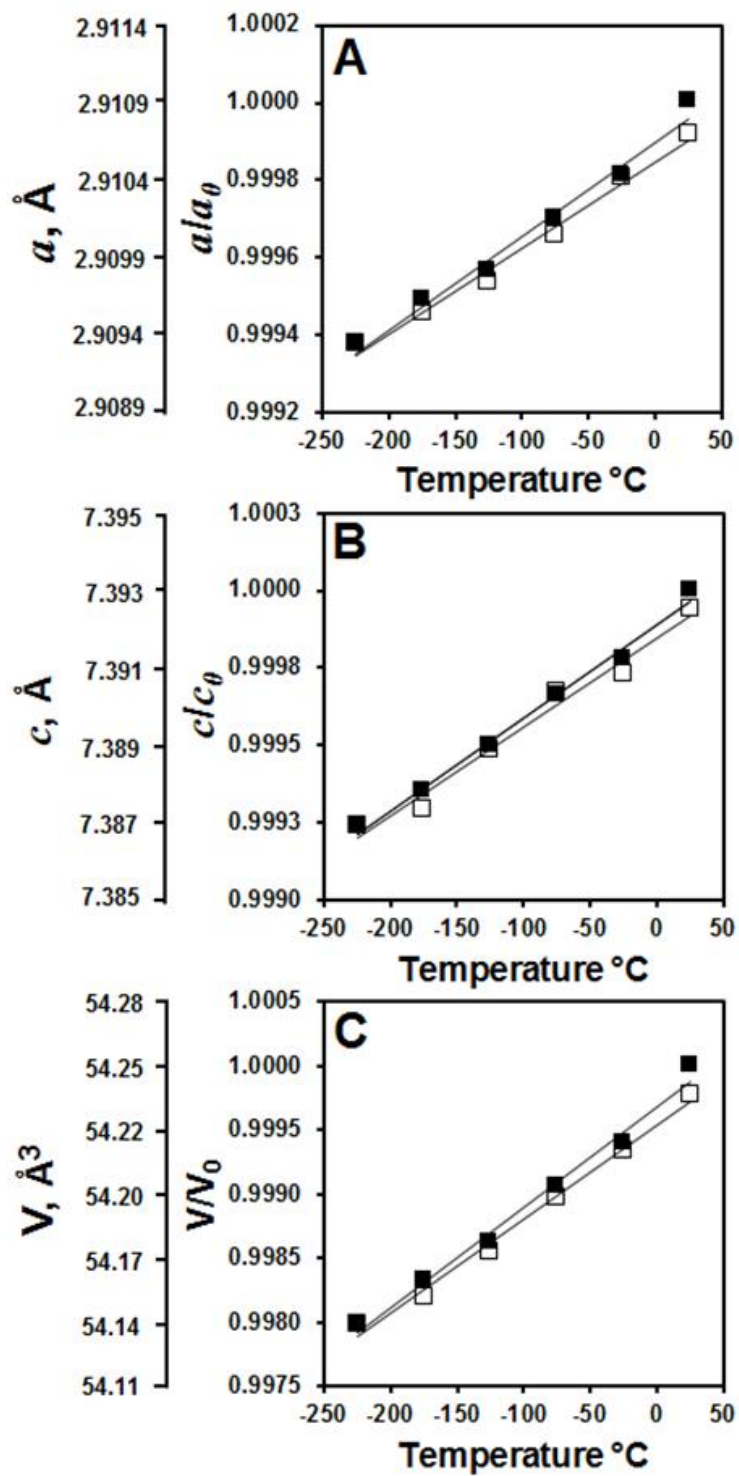
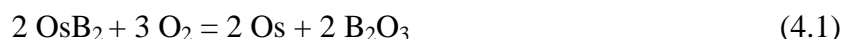


Figure 43: The lattice parameters  $a$  (A),  $c$  (B) and the unit cell volume  $V$  (C) of  $h$ -OsB<sub>2</sub> as function of temperature upon cooling (■) and heating (□) *in vacuo*.

#### 4.4 Discussion

The cooling, to  $-225^{\circ}\text{C}$  *in vacuo*, experiments showed no changes in phase composition or crystal structure of *h*-OsB<sub>2</sub> powder, indicating the stability of the hexagonal ReB<sub>2</sub>-type OsB<sub>2</sub> in the low temperature range. The heating experiments of *h*-OsB<sub>2</sub> under Ar indicated that the phase composition changed during heating as pure metallic Os appeared upon heating and OsB formed upon cooling from high temperature (Figure 38). The appearance of small quantities of pure Os phase upon heating of *h*-OsB<sub>2</sub> can be explained by the presence of small quantities of oxygen in the environment of the heating chamber and the consequent chemical reaction of boron atoms in the *h*-OsB<sub>2</sub> lattice with trace oxygen in the cover gas. The powder produced by ball milling has very high surface area and it is susceptible to oxidation even in the presence of small quantities of oxygen. When a small quantity of O<sub>2</sub> is present, then the following sacrificial reaction can take place where the nanocrystalline and metastable OsB<sub>2</sub> compound is reduced to Os metal and boron oxide, with a possible route for such reduction shown in the Equation 4.1.



A similar sacrificial reaction was used to produce fine Co particles by oxidizing Co<sub>2</sub>B with the formation of Co particles and B<sub>2</sub>O<sub>3</sub> [224].

In the reaction between OsB<sub>2</sub> and O<sub>2</sub>, it is thermodynamically favorable for oxygen to combine with boron, forming B<sub>2</sub>O<sub>3</sub>, which is very difficult to detect as the mass absorption coefficient of B<sub>2</sub>O<sub>3</sub> is 8.26 cm<sup>2</sup>/g and it readily forms an amorphous phase, such that small quantities of B<sub>2</sub>O<sub>3</sub> are not detectable by powder X-ray diffraction. The disproportionate shrinkage of the *a* lattice parameter upon heating can be explained by the formation of boron

oxide in the 276°C - 426°C temperature range by the preferred oxidation of boron atoms in the OsB<sub>2</sub>. When boron atoms are removed from the *h*-OsB<sub>2</sub> lattice to form the B<sub>2</sub>O<sub>3</sub> phase, boron vacancies are left in the *h*-OsB<sub>2</sub> lattice leading to the shrinkage along the *a* direction within the 276°C - 426°C temperature range. The confirmation of decreasing of the *a* lattice parameter in the hexagonal Os-B system as a function of boron stoichiometry is provided in Table 7, where the decrease in the *a* lattice parameter is reported when the stoichiometry change from 1:2 Os to B in OsB<sub>2</sub>, to 1:1.5 Os to B ratio in Os<sub>2</sub>B<sub>3</sub>, to 1:1 Os to B ratio in OsB to 1:0 Os to B ratio in pure Os metal. Therefore, lattice parameters of OsB<sub>2</sub> are affected by both thermal expansion and by chemical expansion by change in the stoichiometry of the compound and formation of boron vacancies under high temperature. The traces of oxygen or water vapor enabling the changes in the stoichiometry of OsB<sub>2</sub> lead to the formation of OsB<sub>2-x</sub> compounds, where if x=0.5 then Os<sub>2</sub>B<sub>3</sub> boride, if x=1.0 then OsB monoboride and if x=2.0 then pure metallic Os phase will form during the sacrificial chemical reaction between OsB<sub>2</sub> ceramic powder and O<sub>2</sub> molecules. Therefore, it is not that *h*-OsB<sub>2</sub> has an inherent negative CTE, but instead exhibits changes in the stoichiometry leading to formation of OsB<sub>2-x</sub> compounds. The *c* lattice parameter does not show such “negative” thermochemical expansion upon heating. The reason for this could be found upon examination of the ReB<sub>2</sub>-type *h*-OsB<sub>2</sub> lattice [221], which has a layered structure with layers packed along *c* direction [221] and, therefore, thermal expansion is much larger along the *c* direction in comparison with the *a* direction. As thermal expansion plays a significant role in increasing the unit cell parameters of *h*-OsB<sub>2</sub> upon heating, the *c* lattice parameter is less affected by removal of B atoms from the lattice in comparison with the much shorter *a* lattice parameter, where the shrinkage of the bond length is visible and the influence of formation of B vacancies

prevails over thermal expansion in a certain temperature range. Upon reaching a critical number of B vacancies due to leaching/removal of B atoms, the hexagonal P63/mmc OsB<sub>2</sub> structure has a significant excess of Os atoms in the lattice which are not bound to B atoms, these Os atoms precipitate out of the *h*-OsB<sub>2</sub> lattice and a pure metallic Os phase is formed, as detected by XRD starting at 426 °C. As *h*-Os metal amount increases from 2.0 wt % at 426°C to 26.6 wt % at 776°C, as the remaining OsB<sub>2</sub> becomes more stoichiometric. Upon further heating from 426°C to 876°C a large expansion of both *a* and *c* lattice parameters was observed. The removal of atoms from *h*-OsB<sub>2</sub> lattice upon heating resulted in very different lattice behavior of the material upon cooling. The shrinkage of the *a* and *c* lattice parameters was observed upon cooling from high temperature to room temperature. The *a* lattice parameter becomes smaller but the *c* lattice parameter of *h*-OsB<sub>2</sub> becomes significantly larger after cooling in comparison to that observed before the heating experiments.

#### 4.5 Conclusion

The phase stability and thermal behavior of novel hexagonal ReB<sub>2</sub>-type OsB<sub>2</sub> powder was studied in the broad temperature range upon heating up to 876 °C under Ar and cooling to -225°C *in vacuo*. It was found that the *h*-OsB<sub>2</sub> was the major phase in the powder after mechanochemical synthesis with a small quantity (~5 wt%) of *h*-Os<sub>2</sub>B<sub>3</sub> also present at room temperature before heating experiments. Os<sub>2</sub>B<sub>3</sub> was identified as an intermediate product of mechanochemical synthesis, where presence of crystalline B in the reagent used for mechanochemical synthesis prevented the formation of pure final product *h*-OsB<sub>2</sub> and small

quantities of  $\text{Os}_2\text{B}_3$  compound formed during milling. The formation of  $\text{Os}_2\text{B}_3$  and  $\text{OsB}$  phases, but not  $h\text{-OsB}_2$ , was confirmed when coarse crystalline  $^{11}\text{B}$  powder was used as a raw B material in high energy ball milling instead of a mixture of amorphous and crystalline B. It was shown that, once synthesized, the  $h\text{-OsB}_2$  phase was stable upon cooling to  $-225^\circ\text{C}$  where no structure changes were observed and linear thermal expansion was measured. However, upon heating, the sacrificial chemical reaction between  $h\text{-OsB}_2$  powder and traces of oxygen and/or water vapor in the heating chamber took place, where B atoms reacted with  $\text{O}_2$  molecules leaving the  $h\text{-OsB}_2$  lattice, forming  $\text{B}_2\text{O}_3$ . This, in turn, led to the formation of boron vacancies in  $\text{OsB}_2$  lattice producing overall B deficiencies and precipitation of a metallic Os phase detectable by X-ray diffraction. Such phase changes lead to the lattice shrinkage and what appeared to be a negative coefficient of thermal expansion of  $h\text{-OsB}_2$  in the  $a$  crystallographic direction. As the changes brought to the shrinkage/expansion of the  $h\text{-OsB}_2$  lattice were caused not only by the change in the temperature, but also by the change in the stoichiometry of the compound, thus we termed it “thermochemical expansion” to emphasize the effects of both temperature and stoichiometry on the phase changes. In addition, the  $\text{OsB}$  phase was detected upon cooling of the powder. The phase changes of  $h\text{-OsB}_2$  were the reason for the appearance of very different room temperature lattice parameters of  $h\text{-OsB}_2$  phase after heating experiments. High values of coefficient of thermochemical expansion of  $h\text{-OsB}_2$ , especially at 700- 800 °C temperature range, might cause stability and reliability problem for practical applications of this novel material recently synthesized by mechanochemistry.

## CHAPTER 5: HEXAGONAL OsB<sub>2</sub> REDUCTION UPON HEATING IN H<sub>2</sub> CONTAINING ENVIRONMENT

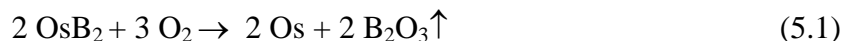
This work was previously published as “Hexagonal OsB<sub>2</sub> reduction upon heating in H<sub>2</sub> containing environment” by Zhilin Xie, Richard Blair, Nina Orlovskaya and E. Andrew Payzant in *Advances in Applied Ceramics*, 2014, Copyright © 2014.

<http://dx.doi.org/10.1179/1743676114Y.0000000212>

### 5.1 Introduction

The synthesis of novel and unreported materials as well as studies of their thermal, physical and chemical properties is of high importance because of the unique properties, which might produce significant improvements in many industrial technologies. [225, 226] Boride ceramics are an important class of the material used in many applications where hardness, high stiffness, oxidation and wear resistance are of utmost importance. Although a wide array of borides has been synthesized [227-229], many compositions are still unknown or poorly investigated and their important properties and behaviors are unknown. There are many metal borides which are synthesized by combining metallic boron with less electronegative metallic or metalloid elements using various techniques such as reduction of metal oxides, electrolysis and direct reaction of the elements. [230-236] Recently significant attention was drawn on the synthesis of ReB<sub>2</sub> and OsB<sub>2</sub> compounds [29, 46, 52, 53, 121, 213, 221], which showed ultra-high stiffness with low lattice compressibility along with remarkable hardness values. While ReB<sub>2</sub> has been reported to exist in a hexagonal (*P63/mmc*, No.194) ReB<sub>2</sub>-type structure, most OsB<sub>2</sub>

syntheses produce an orthorhombic (*Pmmm*, No.59) phase. A theoretically predicted high-pressure hexagonal ReB<sub>2</sub>-type OsB<sub>2</sub> might exhibit even better physical properties in comparison with an orthorhombic OsB<sub>2</sub> phase as it is expected to have a higher packing density of atoms, stronger B-B and stronger B-Os bonds, thus, exhibiting improved properties when compared to orthorhombic OsB<sub>2</sub>. This hexagonal ReB<sub>2</sub>-type OsB<sub>2</sub> ceramic was recently synthesized using high energy mechanochemical synthesis [221, 222], which is a technique well suited to the production of difficult to synthesize metal-boron alloys [237]. The stability of hexagonal OsB<sub>2</sub> was investigated upon heating in Ar containing atmosphere [238]. It was discovered that the hexagonal *hP6* structure of OsB<sub>2</sub> is stable upon heating to 900-1050°C in vacuum or Ar inert atmosphere. However, the presence of small quantities of oxygen led to the occurrence of a sacrificial reaction (Equation 5.1).



This reaction produced changes in the stoichiometry of the parent OsB<sub>2</sub> upon heating. During such a sacrificial reaction, oxygen reacts with OsB<sub>2</sub> and a removal of B atoms from the lattice is realized through the formation of B<sub>2</sub>O<sub>3</sub> followed by the precipitation of pure Os metal. This reaction was observed in the temperature range of 426-726°C. Such changes in phase composition upon heating in an Ar protective atmosphere with traces of oxygen presents resulted in the appearance of negative thermochemical expansion of *a* lattice parameter upon heating as well as significant changes of both *a* and *c* lattice parameters and the unit cell volume after cooling of the material from high-temperature experiments. It was also reported that while it was possible to retain the hexagonal structure upon heating of OsB<sub>2</sub> powder in vacuum, upon sintering of material using spark plasma sintering about 20 wt% of hexagonal structure

transformed into the thermodynamically favored orthorhombic OsB<sub>2</sub> phase. After sintering at 1500°C, 50 MPa for 5 minutes of isothermal dwelling, the spark plasma sintered porous OsB<sub>2</sub> consisted of a mixture of 80 wt% hexagonal and 20 wt% orthorhombic phases. [221] The stability of newly synthesized hexagonal OsB<sub>2</sub> upon heating in a hydrogen containing environment has never been investigated, but is important for understanding of the OsB<sub>2</sub> thermal behavior, which might have significant implications for industrial usage of this material. Here we report our preliminary findings on the stability of ReB<sub>2</sub>-type hexagonal OsB<sub>2</sub> powder upon heating in a 4 vol% H<sub>2</sub>/Ar environment.

## 5.2 Experimental

OsB<sub>2</sub> powder was synthesized using mechanochemical method as described in [221, 238]. After the *h*-OsB<sub>2</sub> powder was synthesized, 3.5 grams of *h*-OsB<sub>2</sub> was loaded into a 6.35mm diameter fused silica ampule in an Ar filled glovebox, sealed under vacuum (~7 Pa), and annealed for 144 hours at 1050 °C. Anton Paar XRK900 reaction chamber was used to heat up OsB<sub>2</sub> powder sample for the high temperature (25°C to 875°C) X-ray diffraction (XRD) experiments. A PANalytical X'Pert Pro MPD system was used to collect XRD patterns at high temperatures. The OsB<sub>2</sub> sample was kept under flowing Ar with 4 vol.-% H<sub>2</sub> reforming gas atmosphere. XRD patterns were collected from 15° to 135° 2θ range with step size of 0.017°. Each scan took about 48 minutes and the scans were collected every 25°C upon heating and cooling. The experiment was stopped at 325°C upon cooling. While there was no indication of presence of oxygen in the high-temperature chamber during the heating experiments, the air



leakage was detected during the following XRD measurements. Small amount of water may also exist due to physisorption and/or chemisorption by the high surface area OsB<sub>2</sub> powder. Therefore, the conditions of the heating OsB<sub>2</sub> experiments cannot preclude the availability of certain unspecified amount of oxygen and water vapor in the Anton Paar XRK900 reaction chamber. After collection of X-ray diffraction patterns, refinement of the structure was performed using the HighScore Plus software.

### 5.3 Results and discussion

The *in situ* XRD results obtained during heating of hexagonal OsB<sub>2</sub> in H<sub>2</sub>/Ar reforming gas are presented in Figure 44. 2D contour plot (Figure 44A) shows the presence of hexagonal ReB<sub>2</sub>-type OsB<sub>2</sub> structure as a major phase at the beginning of heating, where only OsB<sub>2</sub> peaks are present both at room temperature and at all diffraction patterns obtained upon heating up to 400°C. In addition to OsB<sub>2</sub> peaks, one extra peak at  $2\theta=36^\circ$  belonging to Os<sub>2</sub>B<sub>3</sub> structure was also identified (Figure 44B). However, at 450°C, the (002) peak belonging to pure metallic Os appeared and upon further heating the quantity of Os phase increased up to 725°C, where OsB<sub>2</sub> and Os<sub>2</sub>B<sub>3</sub> phases were undetectable and only the Os phase could be detected. Once formed, the metallic Os phase remains stable up to 875°C upon heating and the phase was retained all the way down to the 325°C upon cooling. Therefore, it was found that upon heating of hexagonal OsB<sub>2</sub> ceramic in the reducing environment of H<sub>2</sub>/Ar reforming gas, the complete reduction of OsB<sub>2</sub> to metallic hexagonal Os phase takes place in the 375 - 725°C temperature range.

The results of the quantitative phase analysis of high-temperature XRD data are presented in Figure 45. As one can see from Figure 45, only hexagonal  $\text{OsB}_2$  and a small quantity of  $\sim 5$  wt% of  $\text{Os}_2\text{B}_3$  phases were present in the 25-350 °C temperature range. Above 350 °C, the quantities of boron rich  $\text{OsB}_2$  and  $\text{Os}_2\text{B}_3$  phases began decreasing, while the quantity of the Os phase, which peaks first appeared at 450°C, continuously grew. The  $\text{Os}_2\text{B}_3$  phase completely disappeared at 575°C while no quantities of hexagonal  $\text{OsB}_2$  phases could be detected above 725°C. Once heated above 725 °C, only the Os phase was retained even upon cooling.

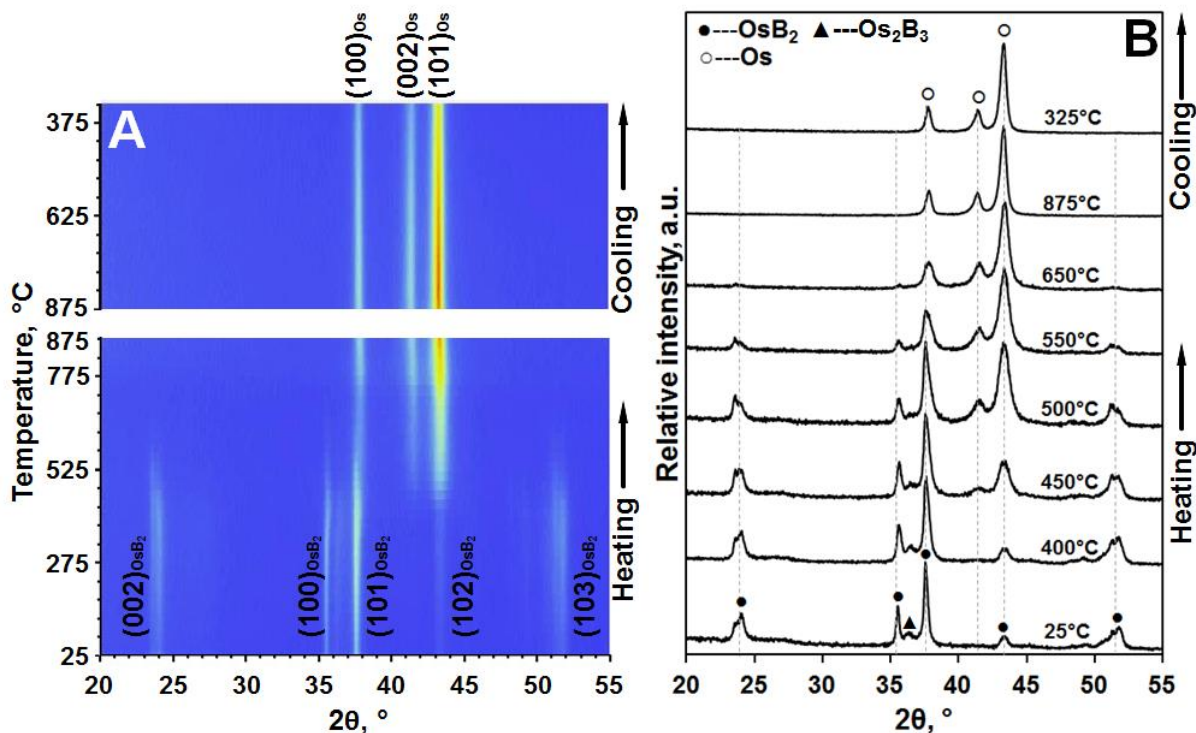


Figure 44: *In situ* high-temperature XRD contour plot (A) and XRD patterns (B) of  $h\text{-OsB}_2$  upon heating and cooling under 4 vol%  $\text{H}_2/\text{Ar}$  reforming gas atmosphere.

The  $a$  and  $c$  lattice parameters along with the unit cell volume of hexagonal  $\text{OsB}_2$  phase as a function of temperature upon heating in 4vol.-%  $\text{H}_2/\text{Ar}$  reforming gas are shown in Figure

46. Similarly to the results upon heating of OsB<sub>2</sub> in Ar with traces of oxygen [221], the lattice expansion both in *a* and *c* direction along with volumetric expansion occurred upon heating from room temperature to about 300°C, however, upon reaching 325°C, the shrinkage of *a* lattice parameter began with a significant decrease from 325°C, where *a* was equal to 2.915Å, to 425°C, where *a* became equal to 2.912Å. Then, upon further temperature increase from 425°C the *a* lattice parameter of OsB<sub>2</sub> started increasing again until 625°C where the OsB<sub>2</sub> phase could still be identified by XRD. Such shrinkage of the *a* lattice parameter was responsible for the negative coefficient of thermochemical expansion (CTCE) in the 300 - 425°C temperature range (Figure 46D and F). The smallest value of the CTCE measured at 375°C was equal to  $-7.0 \times 10^{-6}$ /K in *a* crystallographic direction of the lattice as shown in Figure 46D. The *c* lattice parameter does not decrease upon heating, however, as one can see from Figure 46B, it expands much faster at higher temperatures (400 - 675°C) in comparison with its expansion in RT- 300°C temperature range. The lowest value of CTCE in *c* crystallographic direction was equal to  $3.9 \times 10^{-6}$ /K at 225°C, while the largest was equal to  $25.0 \times 10^{-6}$ /K at 525°C (Figure 46E). The volume of the unit cell of OsB<sub>2</sub> decreases in 325 - 400°C temperature range, but the shrinkage is not such significant as in *a* direction of the lattice, therefore the coefficient of thermochemical expansion does not reach such high negative values as the shrinkage in *a* direction brings (Figure 46F). Yet, the changes in the volume of hexagonal OsB<sub>2</sub> upon heating in H<sub>2</sub>/Ar are the most dramatic as coefficient of thermochemical expansion varies from  $-1.8 \times 10^{-6}$ /K at 325°C to  $43.5 \times 10^{-6}$ /K at 550°C. Such difference in CTCE of OsB<sub>2</sub> at different temperatures would be a significant problem for practical applications of the material, unless the effect will find an advantageous use.

The calculated lattice parameters along with the unit cell volume of newly formed hexagonal Os metallic phase are shown in Figure 47. No dramatic changes of lattice parameters, such as in hexagonal OsB<sub>2</sub>, can be detected upon Os heating in H<sub>2</sub>/Ar reforming gas and almost linear thermal expansion is observed during both heating and cooling of the phase. The calculated CTEs of Os metal are presented in Table 9.

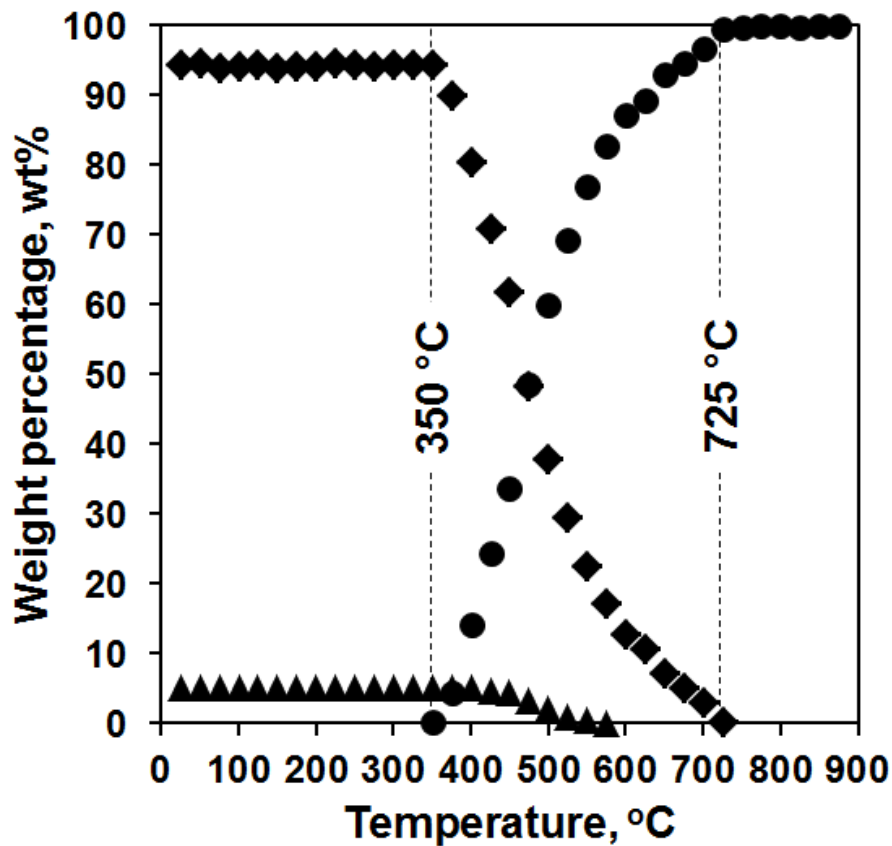


Figure 45: Weight percentage of OsB<sub>2</sub> (♦), Os<sub>2</sub>B<sub>3</sub> (▲) and Os (●) as function of temperature upon heating under 4 vol% H<sub>2</sub>/Ar reforming gas atmosphere.

Table 9: CTEs of Os metal in *a*, *c* and *V* upon heating and cooling under 4 vol% H<sub>2</sub>/Ar reforming gas atmosphere.

	CTE of <i>a</i> (×10 <sup>-6</sup> /°C)	CTE of <i>c</i> (×10 <sup>-6</sup> /°C)	CTE of <i>V</i> (×10 <sup>-6</sup> /°C)
Heating	9.781	14.262	34.221
Cooling	5.795	8.694	20.546

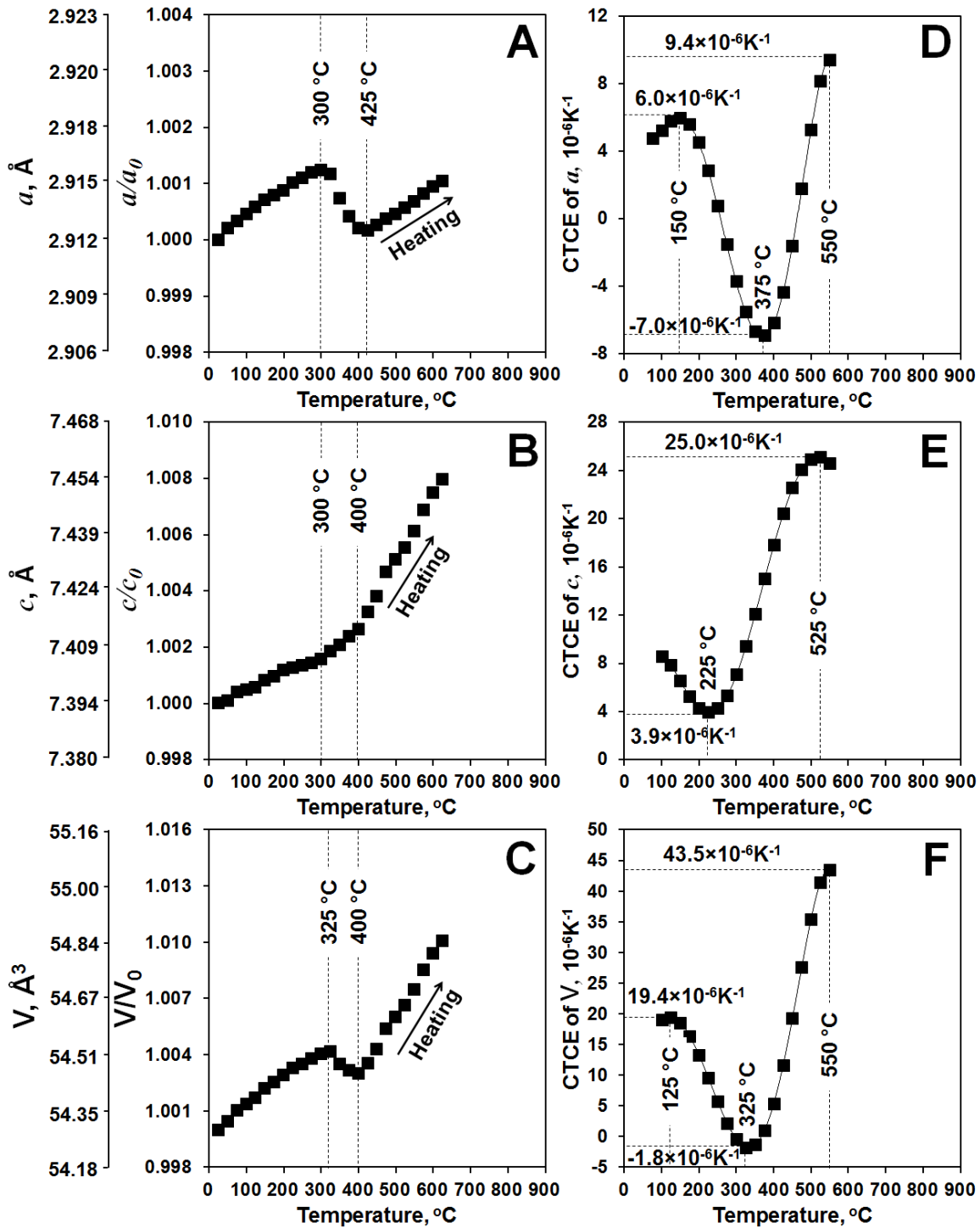


Figure 46: Lattice parameter  $a$  (A),  $c$  (B) and unit cell volume  $V$  (C) of  $\text{OsB}_2$  together with CTCEs of  $a$  (D),  $c$  (E) and  $V$  (F) as function of temperature upon heating under 4 vol%  $\text{H}_2/\text{Ar}$  reforming gas atmosphere.

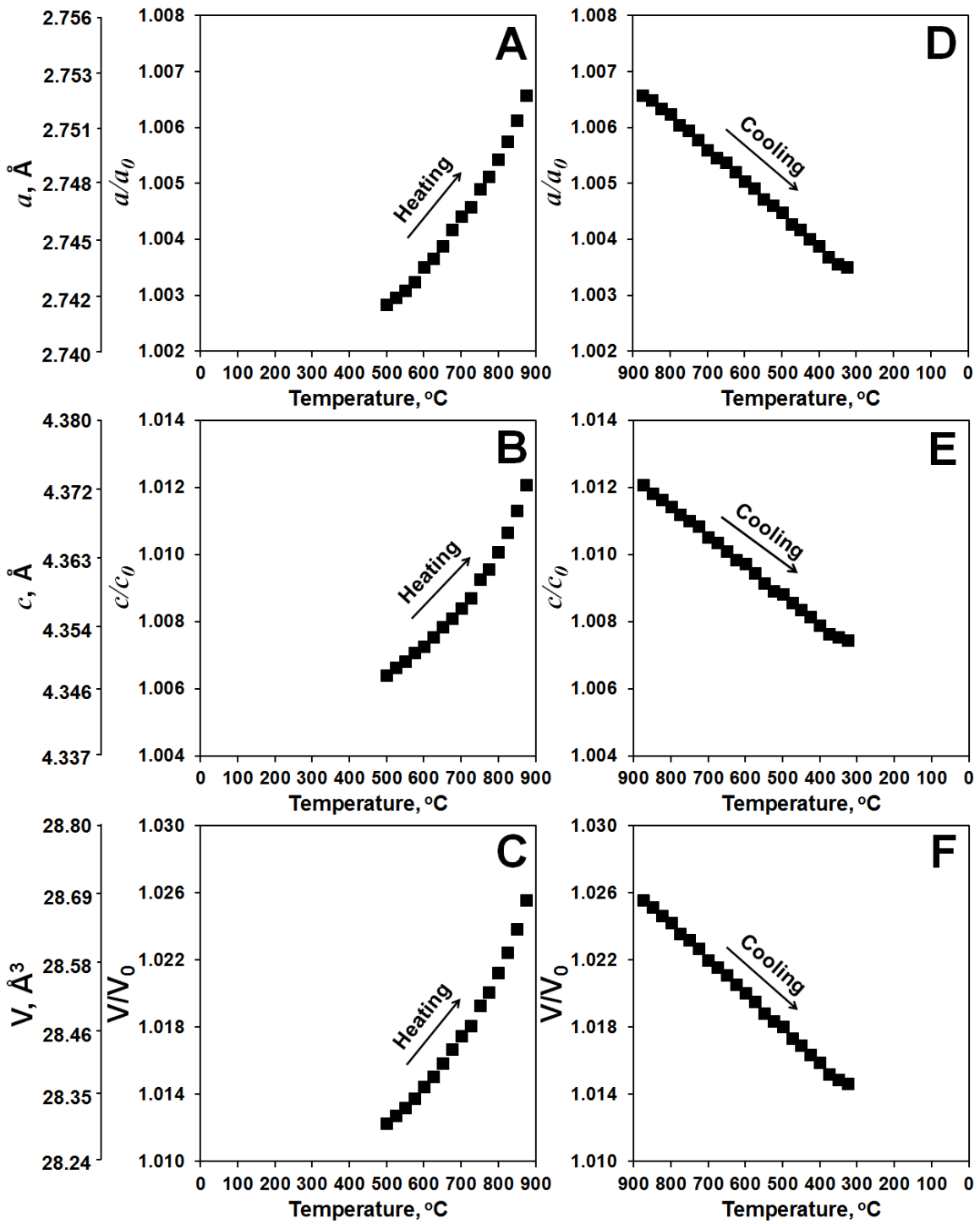


Figure 47: Lattice parameter  $a$ ,  $c$  and unit cell volume  $V$  of Os as function of temperature upon heating (A, B, C) and cooling (D, E, F) under 4 vol%  $H_2/Ar$  reforming gas atmosphere.

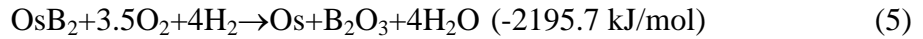
Because of the possibility of leakage into the high-temperature stage during the heating experiments under H<sub>2</sub>/Ar reforming gas there is a possibility of O<sub>2</sub> molecules from air to enter the chamber, the exact reason for such complete reduction of OsB<sub>2</sub> to metallic Os is unknown. However, if O<sub>2</sub> molecules are present, then, similar to [238], the disappearance of OsB<sub>2</sub> with its complete reduction to metallic Os could be explained by oxygen presence, where the sacrificial reaction (1) can take place leading to complete disappearance of OsB<sub>2</sub> and appearance of Os and B<sub>2</sub>O<sub>3</sub> as reaction products. While Os metal was detected and become the only phase detected upon heating of OsB<sub>2</sub> under reforming gas, no traces of B<sub>2</sub>O<sub>3</sub> phase were detected by XRD. B<sub>2</sub>O<sub>3</sub> is very difficult to detect by X-ray because it could also exist in the amorphous state after melting and it also evaporates out of the hot zone. The appearance of the O<sub>2</sub> leak during the experiment would explain the phase changes and appearance of negative thermochemical expansion of *a* lattice parameter of OsB<sub>2</sub>. The enthalpy of formation and redox potential considerations support formation of Os by interaction of OsB<sub>2</sub> with presence of O<sub>2</sub> in H<sub>2</sub>/Ar reforming gas. While the oxygen can easily react with available hydrogen molecules, the enthalpy of formation for gaseous water is -241.8 kJ/mol [239], which is much less than that of B<sub>2</sub>O<sub>3</sub> (-1273.5 kJ/mol) [239] and also less than that for osmium (IV) oxide (-337.2 kJ/mol) [239]. The enthalpy considerations support the fact that boron would get oxidized first before hydrogen and osmium reactions with oxygen forming a liquid with a melting point of 450 °C and evaporation temperature of 1860 °C, thus making reaction (3) entropically favored as well. Os would be oxidized to OsO<sub>4</sub> with enough oxygen molecules present but B<sub>2</sub>O<sub>3</sub> must be formed first since its formation is enthalpically favored. In a hydrogen environment the reduction of OsO<sub>4</sub> by hydrogen (Equation 5.2) is favored by -630 kJ/mol.



Therefore, one can write the sacrificial reaction of OsB<sub>2</sub> with H<sub>2</sub> in O<sub>2</sub> presence as consisting of two reaction steps (Equations 5.3 and 5.4). [112]



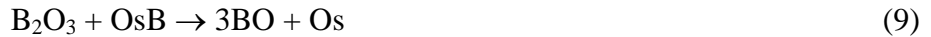
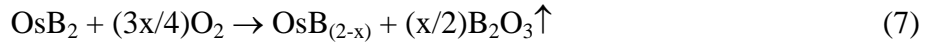
The overall sacrificial reaction is presented in Equation 5.5.



If boron monoxide (BO) is formed instead to B<sub>2</sub>O<sub>3</sub>, the reaction is less favored (Equation 5.6).



The schematic of the steps of OsB<sub>2</sub> reduction are presented in Figure 48. Previous work has suggested that BO is a transient species responsible for the oxygen etching of boron and is formed from B<sub>2</sub>O<sub>3</sub>. [231, 241] Similarly metal diborides such as OsB<sub>2</sub> could be oxidatively etched by the formation and partial sublimation of B<sub>2</sub>O<sub>3</sub> (Equations 5.7-5.10).





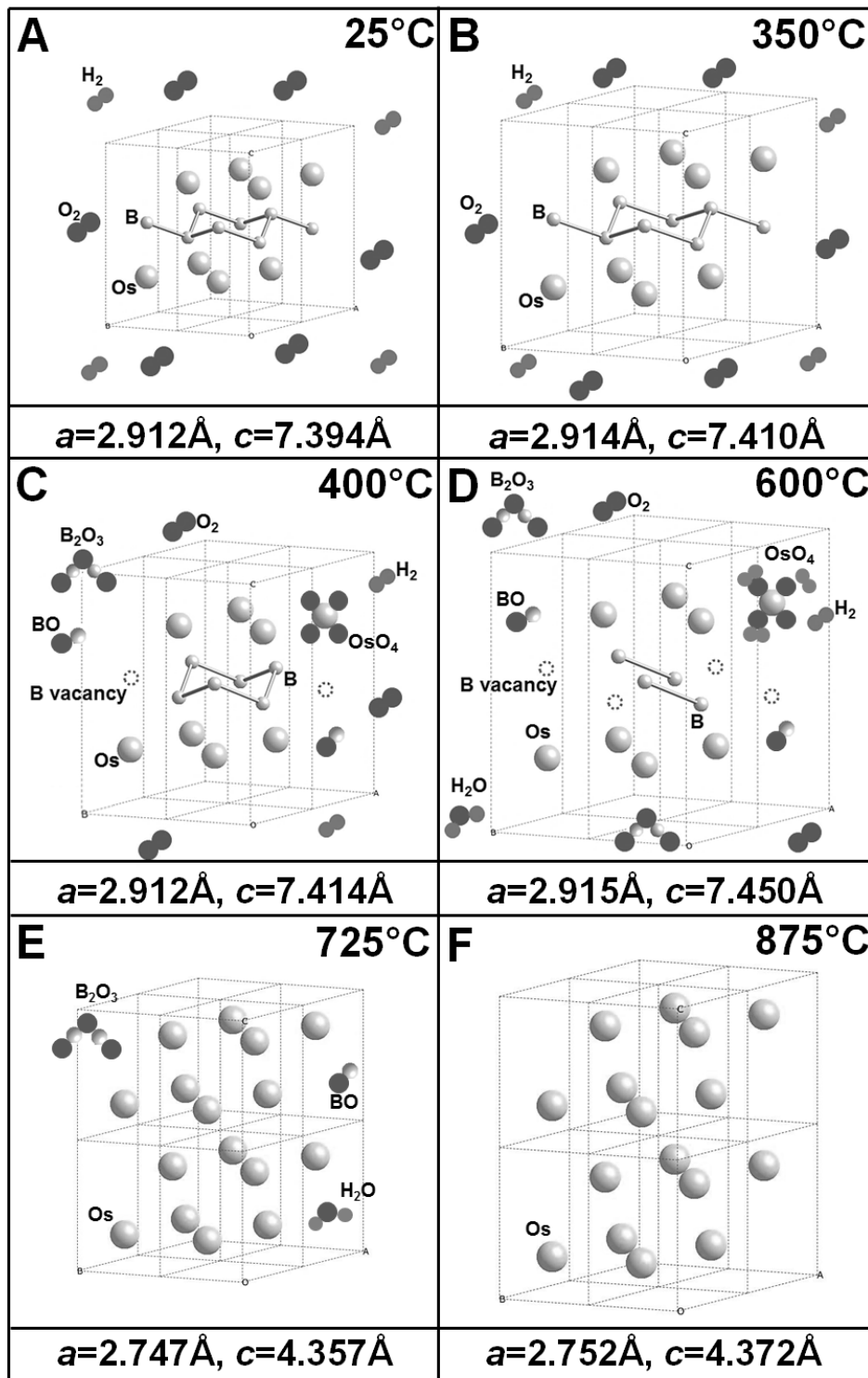


Figure 48: The schematic of the steps of OsB<sub>2</sub> reduction to metallic Os upon heating in H<sub>2</sub> and O<sub>2</sub> containing environment.

Previous studies have shown that the valence state of Os in OsB<sub>2</sub> compound [242] is 0 while the boron atoms are both oxidized and reduced from elemental boron to become half B<sup>3+</sup> and half B<sup>3-</sup> for unit cell neutrality. The existence of zero valent osmium in *h*-OsB<sub>2</sub> is possible because of the layered nature of the crystal structure of OsB<sub>2</sub> where layers of Os atoms not carrying charges are sandwiched between sheets of B layers which are charged positively and negatively in both sides of Os sheets. If one would remove, by etching or other means, the layers of Os atoms from the lattice, it would be possible to obtain 2D B sheets. With such arrangements of the distribution of charges in OsB<sub>2</sub>, the reaction  $2\text{OsB}_2 + 3\text{O}_2 \rightarrow 2\text{Os} + 2\text{B}_2\text{O}_3$  requires six oxygen atoms to be reduced (12e<sup>-</sup>) and 2 B (3-) atoms to get oxidized to B (3+) state (12e<sup>-</sup>).

#### 5.4 Conclusions

The thermal stability of novel hexagonal ReB<sub>2</sub>-type OsB<sub>2</sub> phase upon heating in 4 vol.-% H<sub>2</sub>/Ar reforming gas was investigated. It was found the OsB<sub>2</sub> was very easily and totally reduced to the pure Os metallic phase in the 375-725°C temperature range, where the first peaks of metallic Os were detected at 450°C and the *h*-OsB<sub>2</sub> phase completely disappeared upon heating above 725°C. Although significant negative coefficient of thermochemical expansion of OsB<sub>2</sub> phase was observed, it can be explained by presence of oxygen in the thermal chamber.

## CHAPTER 6: THERMAL ANALYSIS OF HEXAGONAL OsB<sub>2</sub>

### 6.1 Introduction

Boron rich solids play an important role in many industrial applications. Many of them have superior mechanical properties [243, 244], high wear resistance [245, 246], high catalytic activity [247], and excellent electron emission properties (LaB<sub>6</sub>) [248, 249], while some of the borides are rather stable in oxygen containing environment at room temperature (B<sub>4</sub>C, TiB<sub>2</sub>, etc) [243, 244, 250] or even at high temperatures [226, 228, 232, 233, 235], however for many borides the presence of oxygen molecules possess a significant treat because they are prone to the oxidation and form very easily volatile B<sub>2</sub>O<sub>3</sub> and BO compounds that significantly decrease their useful applications. Recently a number of publications appeared on synthesis and properties of ReB<sub>2</sub> and OsB<sub>2</sub> compounds, which were reported to have remarkable mechanical properties, such as hardness and stiffness, but the stability of the compounds upon the contact with oxygen molecules was very questionable. It was reported that interaction of ReB<sub>2</sub> with water moisture present in air at the room temperature led to formation of the perrhenic acid with a complete degradation of properties of the material [213]. The minor presence of oxygen molecules upon heating of hexagonal OsB<sub>2</sub> nanopowder induced an interaction of O<sub>2</sub> with boron atoms in OsB<sub>2</sub> lattice resulting in the formation of boron vacancies, negative thermochemical expansion, formation of boron oxides, and even precipitation of metallic Os [251]. A schematic of O<sub>2</sub> interactions with OsB<sub>2</sub> lattice upon heating in Ar where a minor presence of oxygen was detected

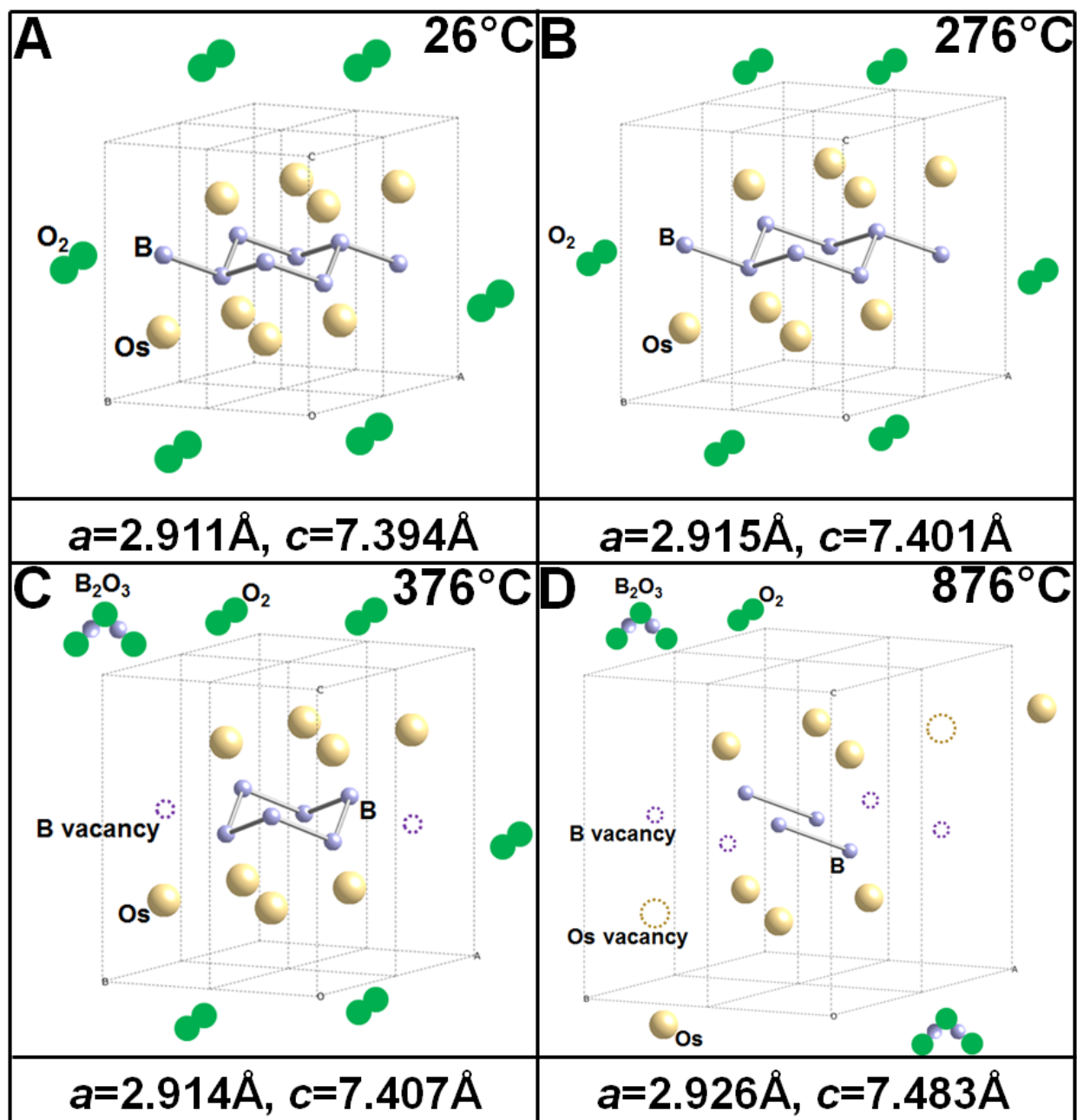


Figure 49: A schematic of O<sub>2</sub> interactions with OsB<sub>2</sub> lattice at different temperature upon heating in Ar where a minor presence of oxygen.

is shown in Figure 49. Even when the presence of strongly reducing H<sub>2</sub> containing environment was used upon heating, the traces of oxygen helped facilitating the complete reduction of OsB<sub>2</sub>

to metallic Os [252], thus rising many questions about usefulness of the compound when O<sub>2</sub> molecules are present even in non-significant quantities. Yet, while certain progress are achieved in understanding of thermal stability of hexagonal OsB<sub>2</sub> phase upon heating when O<sub>2</sub> molecules were present, still many questions remained opened, such as what would be the stability of OsB<sub>2</sub> in the low oxygen partial pressure environment, such as high vacuum microscope column or if there is any specific O<sub>2</sub>-OsB<sub>2</sub> surface interactions upon heating. This paper will present our results of studying the thermal behavior of hexagonal OsB<sub>2</sub> nanopowder upon heating as studied by thermogravimetry (TG), coupled with mass spectroscopy (MS), differential scanning calorimetry (DSC), and high temperature transmission electron microscopy (TEM), while the characterization of the nanopowder was also performed by secondary ion mass spectroscopy (SIMS) to identify the impurity present in the nanopowder before heating.

## 6.2 Experimental

The hexagonal OsB<sub>2</sub> powder was synthesized with mechanochemical method as described in section 3.2 and 4.2. After synthesis, the powder was annealed at 1050°C for 144 hours *in vacuo*. Adept 1010 Dynamic SIMS System (Physical Electronics USA) has been used to collect mass spectra for the samples. Cs primary beam of 3kV and 25nA or 50nA was rastered over area 1000×1000µm. Both negative and positive secondary ions were collected. An auxiliary e-gun was used for charge neutralization. A thermogravimetric (TG, TA Instruments) - mass spectrometer (MS, ThermoStar) system was used to measure the weight changes of the sample upon heating up to 1000°C and also to monitor the off-gas composition while heating. A

differential scanning calorimetry (DSC, TA Instruments) was also used to study the thermal stability of hexagonal OsB<sub>2</sub> with 2 heating runs up to 500 °C and 1 cooling run to room temperature. Both TG and DSC were performed with a helium flow. A JEOL JEM2200FS aberration-corrected scanning transmission electron microscope (STEM) was used to obtain images of the nanoparticles while the powder was under heating in the column.

### 6.3 Results and Discussion

The hexagonal OsB<sub>2</sub> nanopowder was synthesized using mechanochemistry. [221, 251] To remove the strain introduced during high energy ball milling the powder was annealed at 1050°C for 144 hours *in vacuo*. After annealing, it consisted mostly of hexagonal OsB<sub>2</sub> phase (95 wt%), but small quantities of Os<sub>2</sub>B<sub>3</sub> phase (5 wt%) has also been detected by XRD. A number of impurities, such as Li, Mg, Al, Si, K, Cr, Fe, Co, Ce positive ions as well as F, Cl, O and H negative ions have been identified by SIMS as present in hexagonal OsB<sub>2</sub> powder after synthesis and annealing (Figure 50). Co may be from the milling vial and milling media, in which the Co is used as binder. Other metal impurities may be from the raw Os metal powder, which was used for the synthesis. The existence of O and H suggested that the powder was partially oxidized and absorbed moisture.

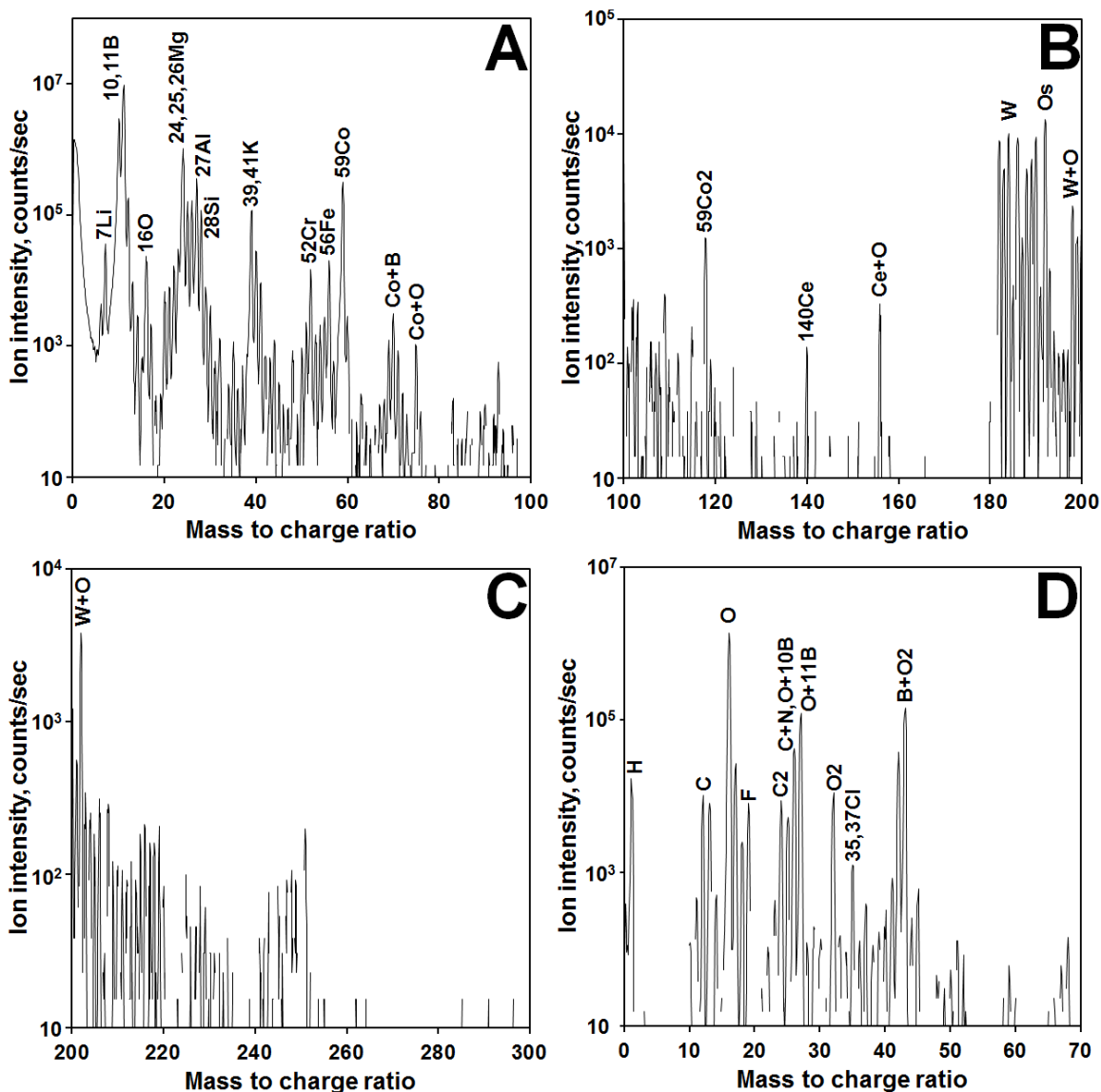


Figure 50: Positive secondary ion mass spectroscopy (A, B and C) and negative secondary ion mass spectroscopy (D).

Upon heating of OsB<sub>2</sub> powder in flowing the gas the weight changes were recorded by TG and the off-gasses are analyzed by the attached mass spectrometer (Figure 51A and B). A significant decrease in the weight of the powder was observed at the beginning of the heating up to 255°C, where the weight continued to stay more or less stable until the increase of the weight of the powder initiated at the 378 °C. The weight increase continued up to 1000 °C where it

facilitated even further, as one can see in the change of the slope of weight–temperature plot. The analysis of off-gas by the mass spectrometer indeed revealed a presence of both oxygen molecules and atoms, along with water vapors, as well as  $N_2$ ,  $CO_2$  gases, indicative the presence of air gas during the annealing in flowing He (Figure 51B). To detect possible chemical reactions or phase transitions which might occur upon heating of hexagonal  $OsB_2$  nanoparticles, the DSC scanning of  $OsB_2$  powder was also performed. Two endothermic peaks appeared at low temperatures upon heating of the powder. The onset of the first peak occurred at  $100\text{ }^\circ\text{C}$  due to boiling of water absorbed on the surface of nanopowder. The second smaller peak was associated with a decomposition of boric acid ( $H_3BO_3$ ), which occurred at  $145.8\text{ }^\circ\text{C}$ . What is interesting that after first heating till  $500\text{ }^\circ\text{C}$ , no peaks were detected to occur both upon cooling of the hexagonal  $OsB_2$  powder and upon heating of the powder till  $500\text{ }^\circ\text{C}$  for a second time. Thus, one can conclude that the weight loss at the beginning of heating was associated with the desorption, decomposition and removal of the  $H_2O$  and  $H_3BO_3$  from the surface, which the weight gain upon further heating was initiated by the surface oxidation of  $OsB_2$  nanopowder as oxygen species were present in the environment when TG experiment was running.



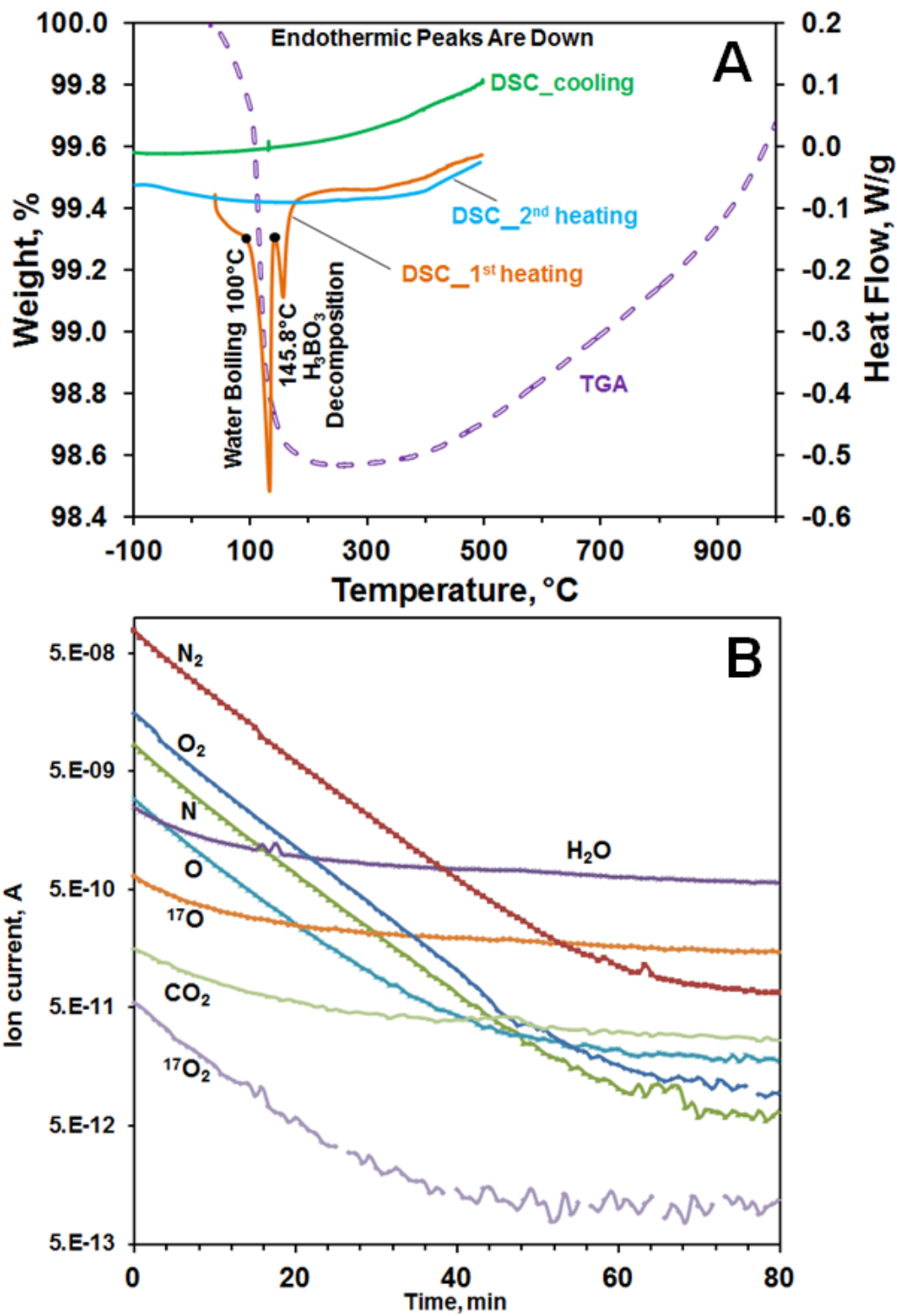


Figure 51: The thermogravimetric analysis and differential scanning calorimetry (A) and the mass spectra of off-gas (B).

The *in situ* high temperature TEM has recorded the changes for a few hexagonal OsB<sub>2</sub> crystallites versus temperature upon heating. As shown in Figure 52, the distances between lattice fringes increase with temperature increased. It can be clearly seen from Figure 53 that the distances between lattice fringes increased slowly before 300 °C, but the slope changed significantly after the temperature is higher than 300 °C. At the maximum measured temperature, 900°C, the distance of lattice fringe has changed to 0.417 nm from 0.396 nm at room temperature. The increase of the distances between lattice fringes is due to the thermal expansion of the hexagonal OsB<sub>2</sub> lattice. Here the powder did not show negative thermochemical expansion as observed in [221, 251] is because the high vacuum in the TEM column eliminated the possibility of oxidation of the hexagonal OsB<sub>2</sub>. Thus the negative thermochemical expansion does not exist. From Figure 52, the crystallite sizes have also been measured and presented statistically in Figure 53. The changes on the left side of images in Figure 52 have shown that the crystallite size increases and the crystallite number decreases with temperature increases. From the crystallite sizes versus temperature curve (Figure 53), the obvious slope change started from 700 °C, where crystallite size increased tremendously. At the maximum measured temperature, the average crystallite area has changed to ~68 nm<sup>2</sup> from ~5 nm<sup>2</sup> at room temperature. The changes in other particles are also shown from to Figure 54 to Figure 55.

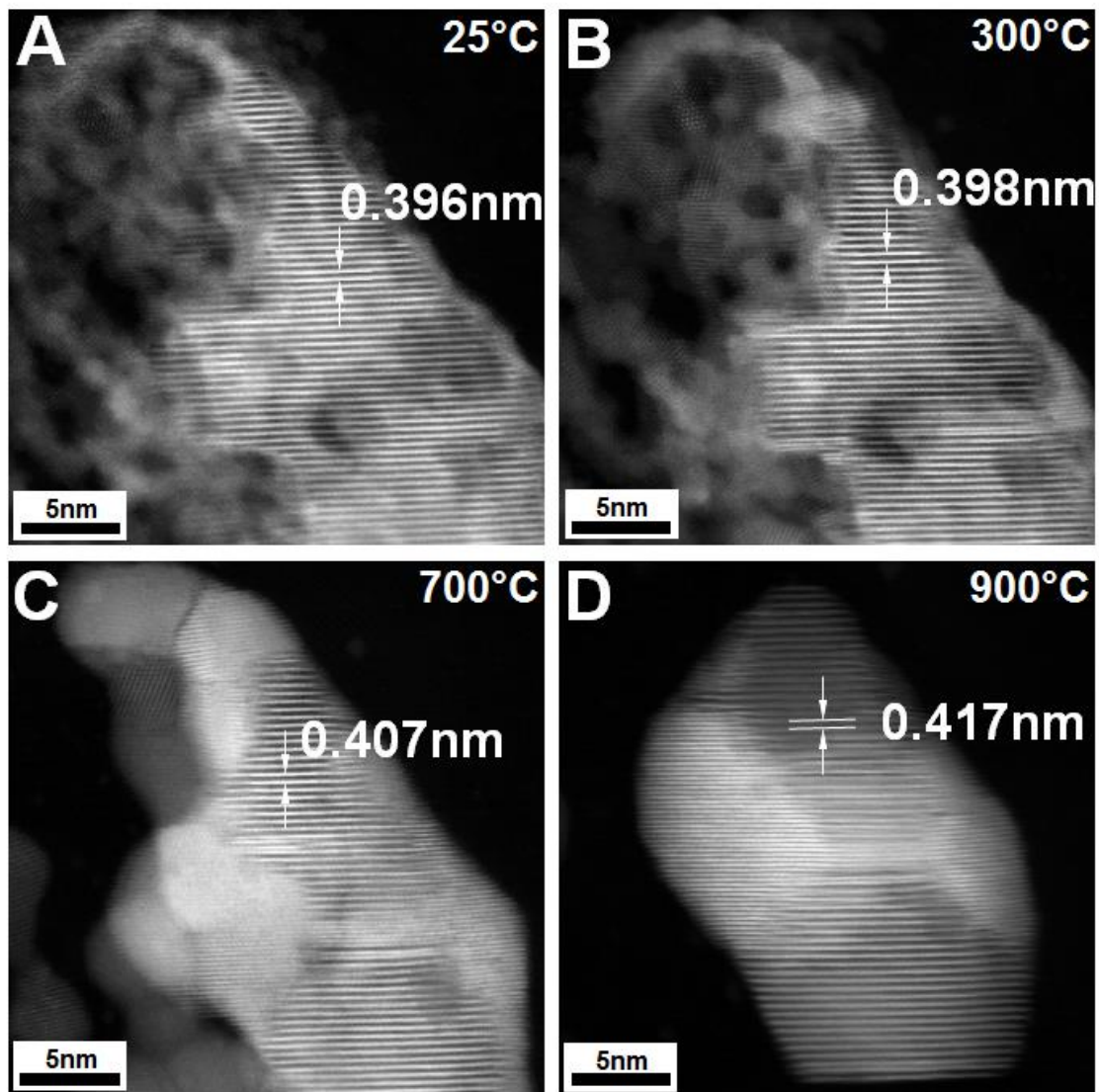


Figure 52: *In situ* high temperature TEM micrographs of hexagonal  $\text{OsB}_2$  at 25°C (A), 300°C (B), 700°C (C) and 900°C (D).

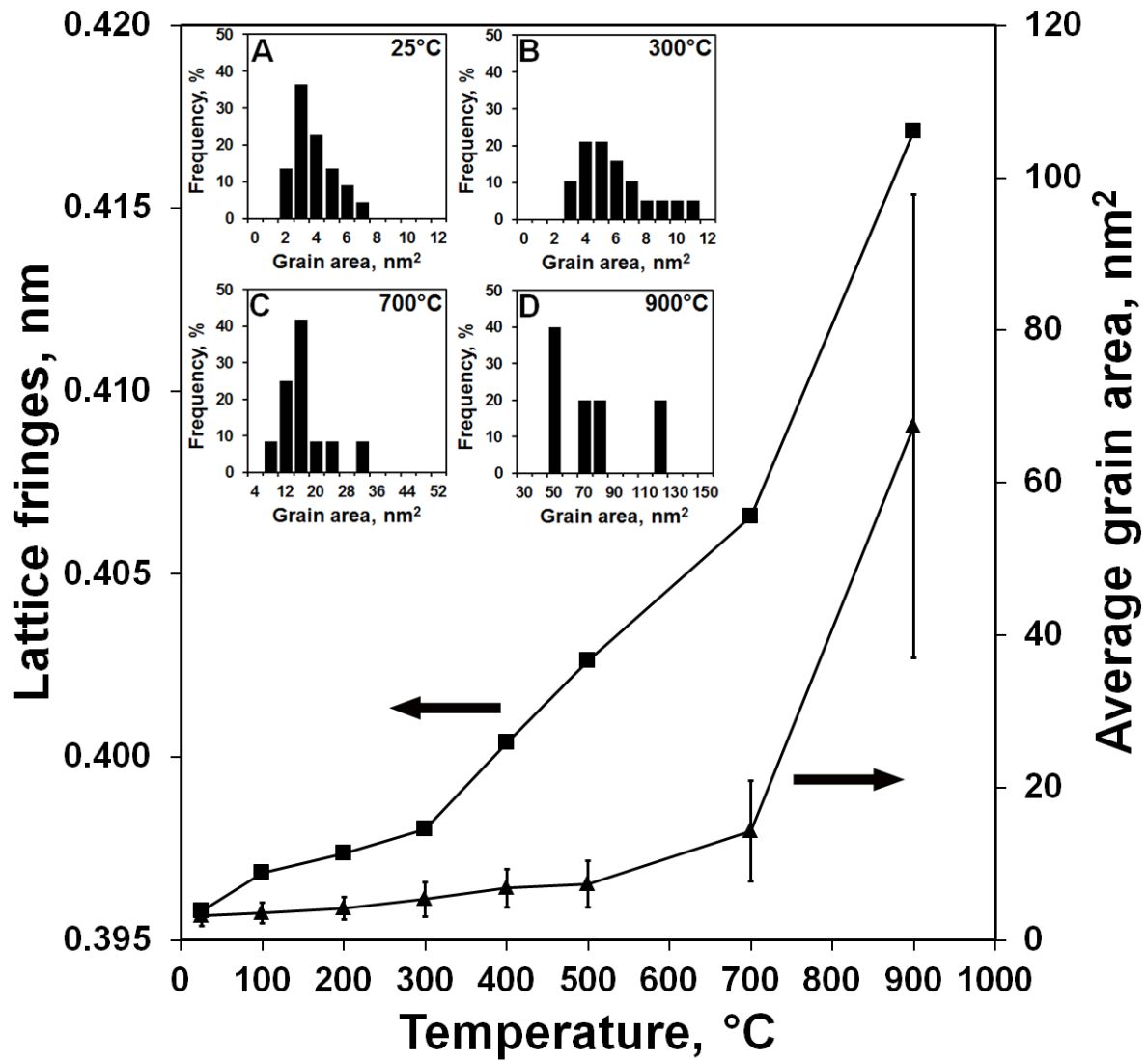


Figure 53: Lattice fringes and average grain area as function of temperature and grain area distribution of OsB<sub>2</sub> at 25°C (A), 300 °C (B) 700°C (C) and 900 °C (D).

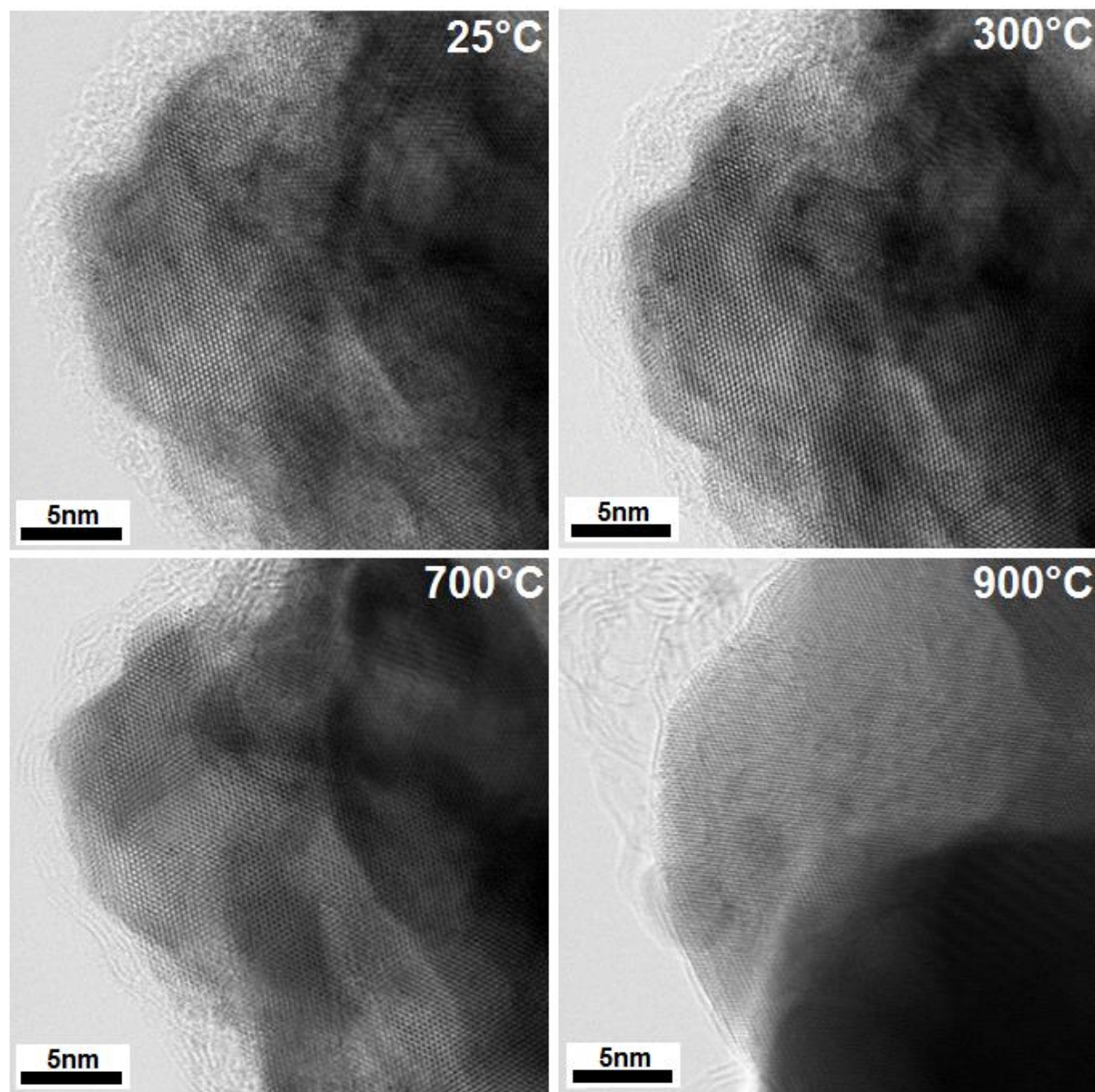


Figure 54: *In situ* high temperature TEM micrographs of hexagonal  $\text{OsB}_2$  at 25°C (A), 300°C (B), 700°C (C) and 900°C (D).



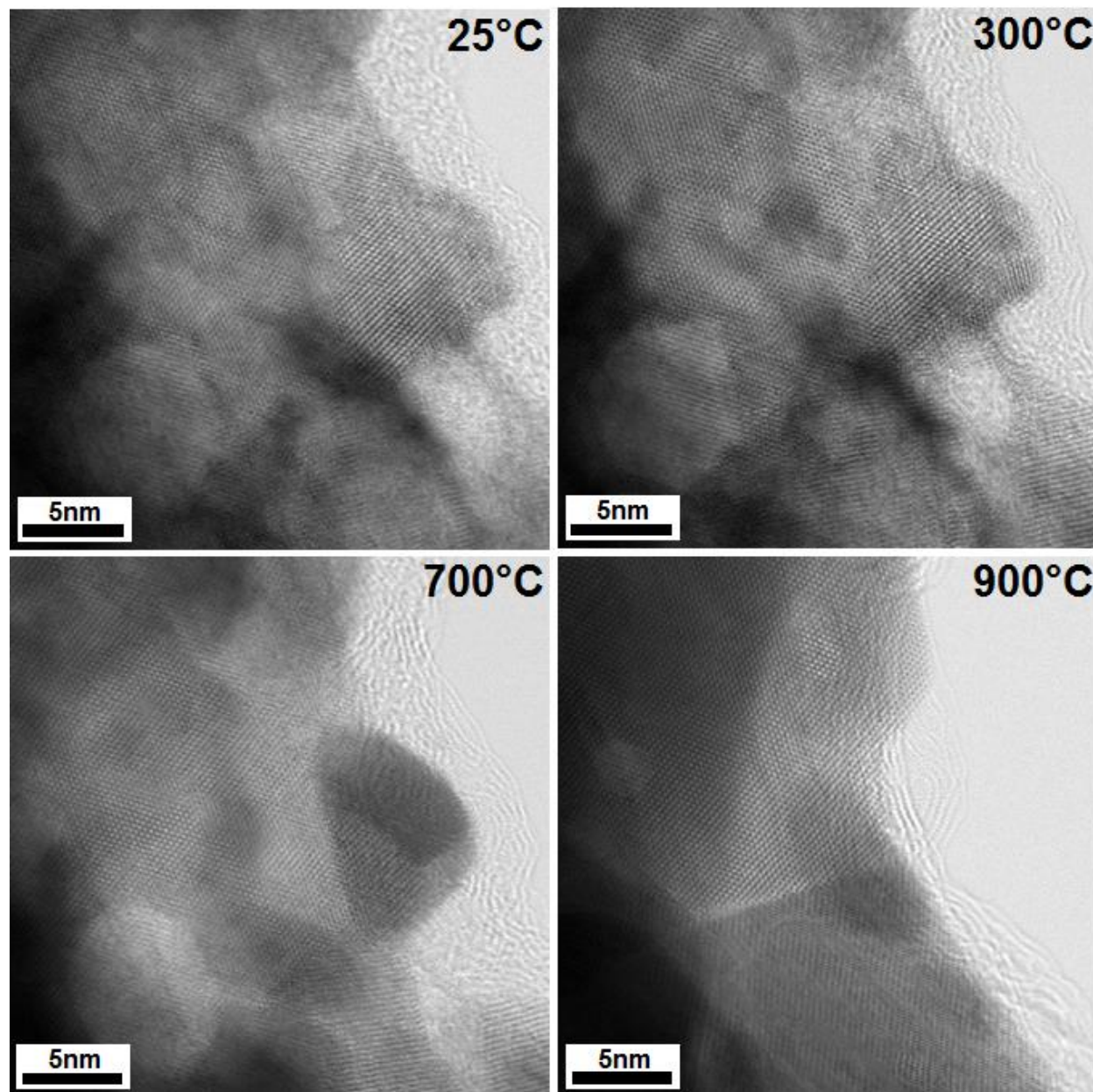


Figure 55: *In situ* high temperature TEM micrographs of hexagonal OsB<sub>2</sub> at 25°C (A), 300°C (B), 700°C (C) and 900°C (D). More *in situ* high temperature TEM micrographs are shown in Appendix B from Figure 93 to Figure 97.

## 6.4 Conclusions

The purity of synthesized hexagonal OsB<sub>2</sub> was studied with secondary ion mass spectroscopy. Metal impurities such as Li, Mg, Al, Si, K, Cr, Fe, Co and Ce, as well as non-metal impurities such as F, Cl, O and H were observed. The presence of O and H suggested that the powder was partially oxidized and absorbed moisture. This is consistent with the appearance of the 2 peaks in first heating cycle of the DSC curve, due to the evaporation of water and decomposition of boric acid. The weight loss part in the TG curve is due to evaporation of water, and the weight gain part is due to the oxidation of the powder. The sintering process of the hexagonal OsB<sub>2</sub> particles has also been studied by *in situ* high temperature TEM. The thermal expansion of hexagonal OsB<sub>2</sub> was reflected in the expansion of the lattice fringes.

## CHAPTER 7: HEXAGONAL OsB<sub>2</sub>: SINTERING, MICROSTRUCTURE AND MECHANICAL PROPERTIES

### 7.1 Introduction

Modern materials science and engineering places a significant emphasis on the rational design and processing of new materials possessing superior mechanical and functional properties, and novel hard materials are one of the focal points of this development [4-9, 146]. The synthesis and discovery of novel metastable ceramic compounds are of the major importance both from a fundamental science point of view and for the advances in industrial applications. Borides are an important class of the ceramic materials exhibiting many unique properties [29, 52, 53, 244, 253] and, therefore, much research has been performed to design and develop new boride compositions by different routes [29, 45, 53, 57, 71-73, 144]. Recently, the mechanochemical synthesis of hexagonal ReB<sub>2</sub>-type OsB<sub>2</sub> ceramics has been reported [221, 222]. The synthesis was done utilizing high energy ball milling of elemental Os and B powder by WC balls, where the presence of severe shear stress facilitated the solid state formation of previously unknown metastable hexagonal *P63/mmc* phase of OsB<sub>2</sub> during mechanochemical synthesis. The obtained hexagonal OsB<sub>2</sub> powder with  $a=2.916\text{\AA}$  and  $c=7.376\text{\AA}$  lattice parameters was studied for high-temperature stability in different environments and it was concluded that its structure was stable upon heating at 1050°C for a significant period of time *in vacuo*. It was reported that the crystallite size of hexagonal OsB<sub>2</sub> increased from 5.1 nm to 19.8



nm after annealing at 1050°C for 6 days in *vacuo* as measured by FWHM of (101) peak from X-ray diffraction pattern [221], and the crystalline grain size increased from 4.8 nm at RT to 8.2 nm at 900°C after heating the powder in a TEM microscope column for about 1 hour. [254] It was also possible to retain the ReB<sub>2</sub>-type hexagonal structure after densification of OsB<sub>2</sub> powder using spark plasma sintering. The SPS was performed at 1500°C for 5 minutes, where a porous bulk OsB<sub>2</sub> ceramic was produced containing a mixture of ~80wt% hexagonal OsB<sub>2</sub> (*h*-OsB<sub>2</sub>) and ~20wt% orthorhombic OsB<sub>2</sub> (*o*-OsB<sub>2</sub>) phases. [221]

The mechanical behavior of orthorhombic OsB<sub>2</sub> was studied to some extent in the past. [29, 32, 53, 94, 114, 115, 121, 124, 126] In one of the first publications, the remarkably high resistance to bond shrinkage in orthorhombic OsB<sub>2</sub> at applied compressive stresses was reported [53]. The bulk modulus of orthorhombic OsB<sub>2</sub> measured using high-pressure X-ray diffraction was calculated to be in the range of 365-395 GPa depending on fitting parameters. It was also shown that *b*-direction of the lattice is most compressible, while the *c*-direction is the least compressible in *o*-OsB<sub>2</sub>. It was noticed that compressibility along *c*-axis (001) was even less than the analogous linear compressibility of diamond. Furthermore, it was suggested that *o*-OsB<sub>2</sub> has hardness higher than that of sapphire, as it was possible to scratch sapphire windows with the *o*-OsB<sub>2</sub> powder [53]. The hardness of (001) plane of *o*-OsB<sub>2</sub>, produced by arc-melting, was reported to be equal to 36 GPa in the 0.6-0.8N loading range and it decreased to 30 GPa when the load increased to 1N [121]. In another paper, Vickers hardness of *o*-OsB<sub>2</sub> was also reported to be about 37 GPa with the applied load at 0.245N [29], but decreased to less than 20 GPa when applied load increased to 2N. The anisotropy in hardness value was also reported with an average hardness along <001> crystallographic direction measured to be equal to 12.5 GPa and along

$\langle 100 \rangle$  direction measured to be equal to 23.2 GPa at 1.96N maximum applied load. Such anisotropy in hardness was explained by highly covalent bonding with a very short bond length of 1.80 Å in the  $\langle 100 \rangle$  direction and, in contrast, the absence of meaningful B-B bonds in  $\langle 001 \rangle$  direction with the closest B-B distance equal to 4.10 Å. In the same paper the average nanoindentation hardness using Berkovich indenter was reported to be equal to  $21.6 \pm 3.0$  GPa at the maximum load of 490mN. The Young's modulus of *o*-OsB<sub>2</sub> was measured to be  $410 \pm 35$  GPa by nanoindentation [29]. The ideal shear strength of OsB<sub>2</sub> was estimated in [124] and it was reported to be rather low (9.1 GPa), which means that *o*-OsB<sub>2</sub> might not be suitable for the practical applications where shear stress plays a significant role. In addition to the experimental work on measuring of hardness and Young's modulus, a few papers have been published on the mechanical properties of *o*-OsB<sub>2</sub> estimated by first-principles calculations [58, 94, 112, 123, 126, 131] The hardness along the *c* axis was reported to be estimated as 45.5 GPa, along the *a* axis was reported as 25.6 GPa, and along the *b* axis was equal to 37 GPa for *o*-OsB<sub>2</sub> [94]. The model used in [94] was based on the bond strengths of the nearest neighboring atoms and on the projections of the direction of these bonds into the plane of indentation. The highest value of hardness along the *c*-axis was explained by high concentration of B-B bonds, which form hexagonal B rings perpendicular to the *c* axis with the large electron densities in short and highly directional strong B-B bonds. Such availability of B-B bonds results in the highest value of hardness along the *c*-axis in *o*-OsB<sub>2</sub> [94]. It was shown that transversely oriented bonds are the key factor determining hardness and it was also shown that no clear relationship exists between hardness and bulk modulus of a material. The estimated hardness of *o*-OsB<sub>2</sub> equal to 27.9 GPa was reported in [126]. In the same paper the calculations of Young's, shear and bulk moduli

were reported along with hardness. For the calculations, the experimentally determined structural data were used as input parameters in the model [114, 115]. One of the structures reported in [114] was wrongfully identified as *h*-OsB<sub>2</sub>, while most likely the phase under investigation was OsB<sub>1.1</sub>; that is why no report on experimentally produced ReB<sub>2</sub>-type OsB<sub>2</sub> material can be found. Thus, mechanical properties of *o*-OsB<sub>2</sub> have been reported in a number of publications [29, 32, 53, 94, 121, 126, 255], however the mechanical behavior of the newly synthesized *h*-OsB<sub>2</sub> phase is unknown. It is fair to expect that the mechanical properties, namely H and E, could be higher for *h*-OsB<sub>2</sub> than those of *o*-OsB<sub>2</sub> structure, as the density of hexagonal OsB<sub>2</sub> is higher, the unit cell is smaller, and, therefore, the bonds are stronger in this ceramic compound, thus giving advantage in improvement of mechanical properties of hexagonal over orthorhombic OsB<sub>2</sub> phase. In this paper we report the details of the processing of bulk OsB<sub>2</sub>, its microstructure and some of its mechanical properties, namely hardness, Young's modulus and indentation stress – indentation strain deformation behavior as measured by nanoindentation.

## 7.2 Experimental

Osmium metal powder (99.95% pure, Heraeus, South Africa) and boron powder (99% pure, -325 mesh, a mixture of amorphous and crystalline phases, Alfa Aesar) were used for the mechanochemical synthesis of OsB<sub>2</sub>. Enough Os and B powders (molar ratio 1:3) were loaded into a WC vial with two 12.7mm WC balls to produce a ball to powder weight ratio of 2.7:1. The balls and vial used in the milling were covered with OsB<sub>2</sub> product formed from previous milling syntheses. All loading operations were carried out in an argon-filled glovebox. The vials were

sealed with Viton gaskets to reduce oxygen contamination during milling. The milling was performed in a SPEX 8000D mixer mill for a total of 20 hours. Every 30 minutes the milling was interrupted and vials were left for 30 minutes without grinding in order to decrease the vials' temperature and reduce wear on the mill's motor. The synthesized OsB<sub>2</sub> powder was sintered using fast current assisted technique (SPS25–10, Thermal Technologies, CA). The sintering of the powder packed in the graphite die was performed at 1500°C, 50MPa for 5 minutes with the heating and loading rates of 47°C/min and 10MPa/min, respectively. A PANalytical X'Pert Pro MPD system was used to collect XRD pattern of the bulk OsB<sub>2</sub> sample after SPS. The polished sample surface was examined in a Zeiss Merlin scanning electron microscope (SEM) equipped with energy dispersive X-ray spectroscopy (EDS) detector. Electron backscatter diffraction (EBSD) analysis was performed in a JEOL JSM 6500F equipped with an EDAX EBSD system. The specimens were prepared for EBSD by mounting in epoxy and mechanically polishing the surface, with a final polish using colloidal silica. Electron transparent cross sections were prepared for transmission electron microscopy (TEM) analysis by focused ion beam (FIB) milling. An image was taken during the FIB milling, as shown in Figure 56. Additional thinning was performed using a Fishione Nanomill. Electron diffraction patterns were acquired in an FEI Tecnai operated at 200kV and bright-field scanning transmission electron microscopy (STEM) images were recorded in a JEOL 2200FS. Nanoindentation tests were performed using Hysitron nanoindenter equipped by a conical indenter with a tip radius of 0.222µm at École Polytechnique Fédérale de Lausanne (EPFL), Switzerland. Micrographs of the impressions were taken with SEM.

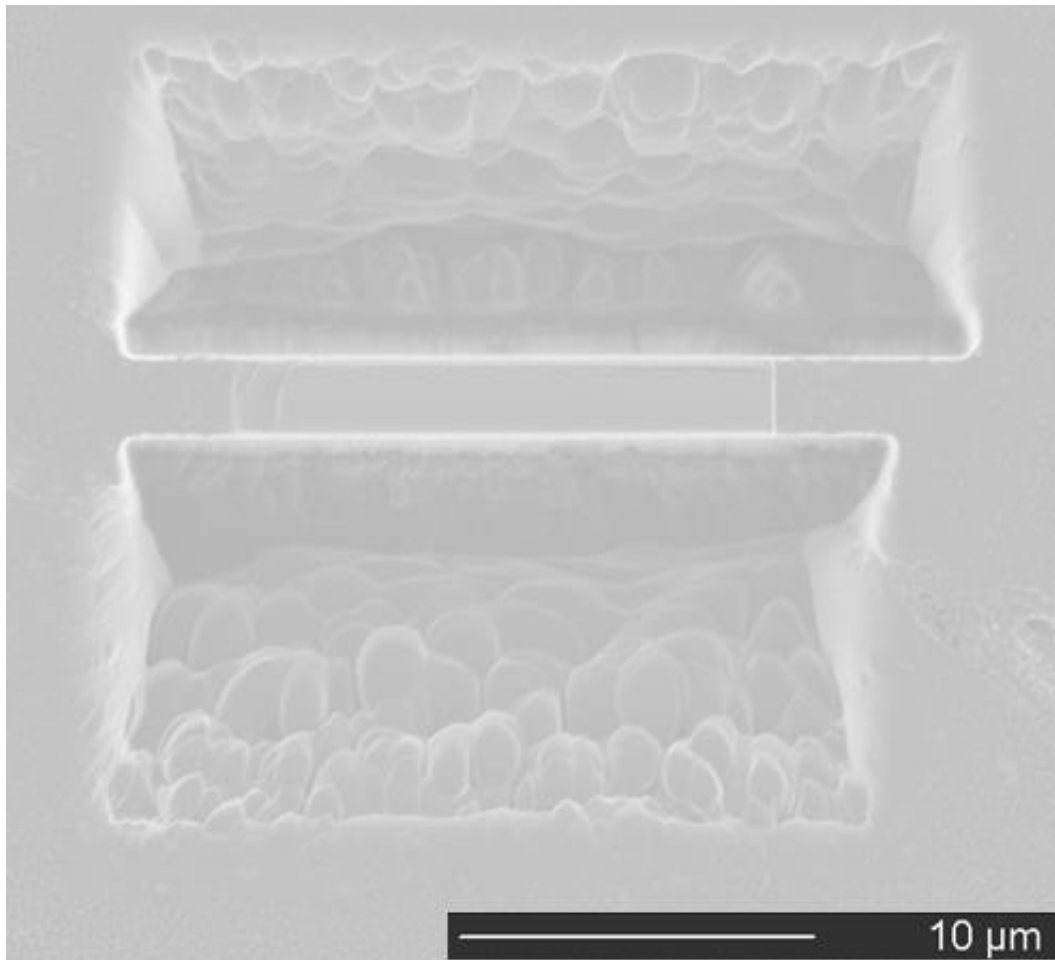


Figure 56: An image of the sintered OsB<sub>2</sub> sample during FIB milling (TEM sample preparation).

### 7.3 Results and discussion

#### 7.3.1 SPS of OsB<sub>2</sub>

The temperature and pressure applied during SPS of hexagonal OsB<sub>2</sub> powder along with the powder shrinkage measured during sintering are presented in Figure 57. As one can see from Figure 57 at the beginning of the heating, the small expansion of the material was observed, which is explained by the thermal expansion of the lattice as temperature rises. The temperature

was not high enough at the beginning of heating to initiate diffusion and start the densification of the powder, therefore it is not expected that a sintering process accompanied by shrinkage would occur at such low temperatures upon heating. Only expansion of the sample due to thermal expansion of the material's lattice can be detected upon heating from room temperature to around 685°C before the pressure was applied. Upon further increase of the temperature from 685°C to 1000°C the sintering process slowly started as a small shrinkage of the material can be seen in this temperature range. At 1000°C the pressure was applied, reaching 50MPa maximum pressure at 1220°C resulting in a significant densification of the whole powder (Figure 57). Upon further temperature increase, a small shrinkage was observed in 1425-1500°C temperature range and then slow densification continued upon isothermal dwell at 1500°C for 5 minutes. While a certain non-significant amount of shrinkage occurred during the isothermal dwell, the process did not come to the finish and therefore the material did not become fully dense. After 5 minutes dwell time, the cooling of material was initiated and, as the temperature started decreasing, the further shrinkage of the bulk sample occurred mainly because of the shrinkage of the lattice upon temperature decrease. Thus, as a result of incomplete densification of *h*-OsB<sub>2</sub>, a rather porous bulk material was produced. The OsB<sub>2</sub> pellet after spark plasma sintering is shown in Figure 58. The X-ray analysis of the bulk OsB<sub>2</sub> revealed that while before sintering only *h*-OsB<sub>2</sub> with small (5 wt%) amount of Os<sub>2</sub>B<sub>3</sub> was present, after sintering no Os<sub>2</sub>B<sub>3</sub> phase was identified in the material. However, a part of the hexagonal OsB<sub>2</sub> lattice transformed into orthorhombic structure (Figure 59). The bulk material after sintering consisted of 80 wt% of hexagonal (*P63/mmc*) OsB<sub>2</sub> and 20 wt% of orthorhombic (*Pmmm*) OsB<sub>2</sub> phase, as identified by Rietveld refinement of XRD pattern, and no any other phase was found as all peaks were assigned to *h*-OsB<sub>2</sub> or *o*-OsB<sub>2</sub>

structures. The similar phase composition of the spark plasma sintered OsB<sub>2</sub> was identified by electron backscatter diffraction (EBSD), where 77.3 wt% of the grains were identified as belonging to the hexagonal OsB<sub>2</sub> structure and the rest 22.7 wt% were identified as an orthorhombic OsB<sub>2</sub> (Figure 59). Some areas presented as a black phase on EBSD map might belong to the rhombohedral B (*r*-B), however, the possible *r*-B regions did not generate enough signal to be positively indexed as elemental B. Thus, the locations are identified as either pores or *r*-B in the EBSD phase map. The EBSD map showing grains misorientation after sintering is presented in Figure 59. The measured density of the sintered material was equal to 9.46 g/cm<sup>3</sup>, thus the simple calculations revealed that material contained 26.9% of porosity. In the density calculations the 12.97 g/cm<sup>3</sup> theoretical density of *h*-OsB<sub>2</sub> [221] and 12.83 g/cm<sup>3</sup> theoretical density of *o*-OsB<sub>2</sub> [115] were used.

### 7.3.2 Microstructure of sintered OsB<sub>2</sub>

The optical micrograph of a polished surface of OsB<sub>2</sub> ceramic after SPS is shown in Figure 60A. As one can see from Figure 60A, the OsB<sub>2</sub> sample has macroscopically very inhomogeneous regions after sintering where areas with high level of porosity are adjacent to the areas with lower porosity. The more dense regions, with an average size of 105 μm are typically surrounded by large pores and other highly defective areas. The STEM micrograph of OsB<sub>2</sub> after FIB followed by ion milling is shown in Figure 60B, where porous regions along with ceramic grains can be seen. The SEM images of the polished surface were taken both with secondary (Figure 60C) and backscattered (Figure 60D) electron detectors showing some non-homogeneous distribution of elements as well as presence of the porosity. The different contrast

between grains in Figure 60D taken by the back-scattered electron detector could be explained both by difference in the content of elements and also difference in crystallographic orientation of the grain. Both the TEM (Figure 60B) and EBSD (Figure 60B) along with SEM (Figure 60C and D) images were used to calculate an average grain size of OsB<sub>2</sub> after sintering. The obtained results with a distribution of grain sizes are presented in Figure 61, where the average grain size of OsB<sub>2</sub> was calculated to be equal to 0.56 μm. The TEM micrographs with corresponding electron diffractions as well as images of lattice fringes of typical hexagonal and orthorhombic OsB<sub>2</sub> grains are shown in Figure 62. Both hexagonal and orthorhombic grains have rather sharp and well defined facets, clear grain boundaries. Electron diffraction shows that the grain presented in Figure 62A has a hexagonal structure and is oriented along [110] direction as shown in Figure 62B, and the grain presented in Figure 62D has an orthorhombic structure with orientation of along [100] direction as presented in Figure 62E. The corresponding lattice fringes of the two grains are presented in Figure 62C and F along with FFT patterns of the corresponding structures. As one can see in Figure 62A, the hexagonal grain exhibits the presence of well-defined linear defects, which could be either dislocations or even tiny micro-cracks present along the length of the grain. One of the possible reasons that such defects exist inside grains of OsB<sub>2</sub> is the damage by focused ion beam during sample's preparation for TEM study, but regardless of the reason, the presence of such defects is indication of the brittle nature of OsB<sub>2</sub> since such defects might easily facilitate the brittle failure of the grain and be responsible for high overall brittleness of the OsB<sub>2</sub>.



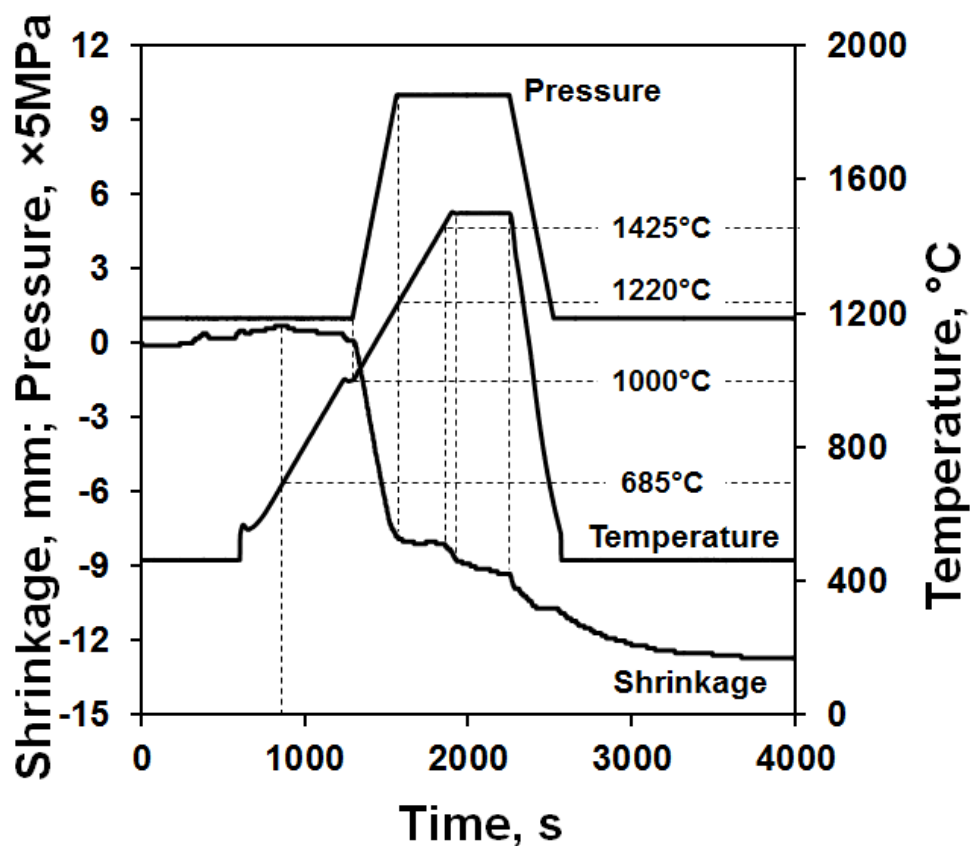


Figure 57: A sintering regime used for densification of hexagonal  $\text{OsB}_2$  powder. Both temperature, pressure, and shrinkage data were collected during spark plasma sintering as a function of time.



Figure 58: The  $\text{OsB}_2$  sample after spark plasma sintering (left), and a US quarter coin (right) for comparison of the sizes.

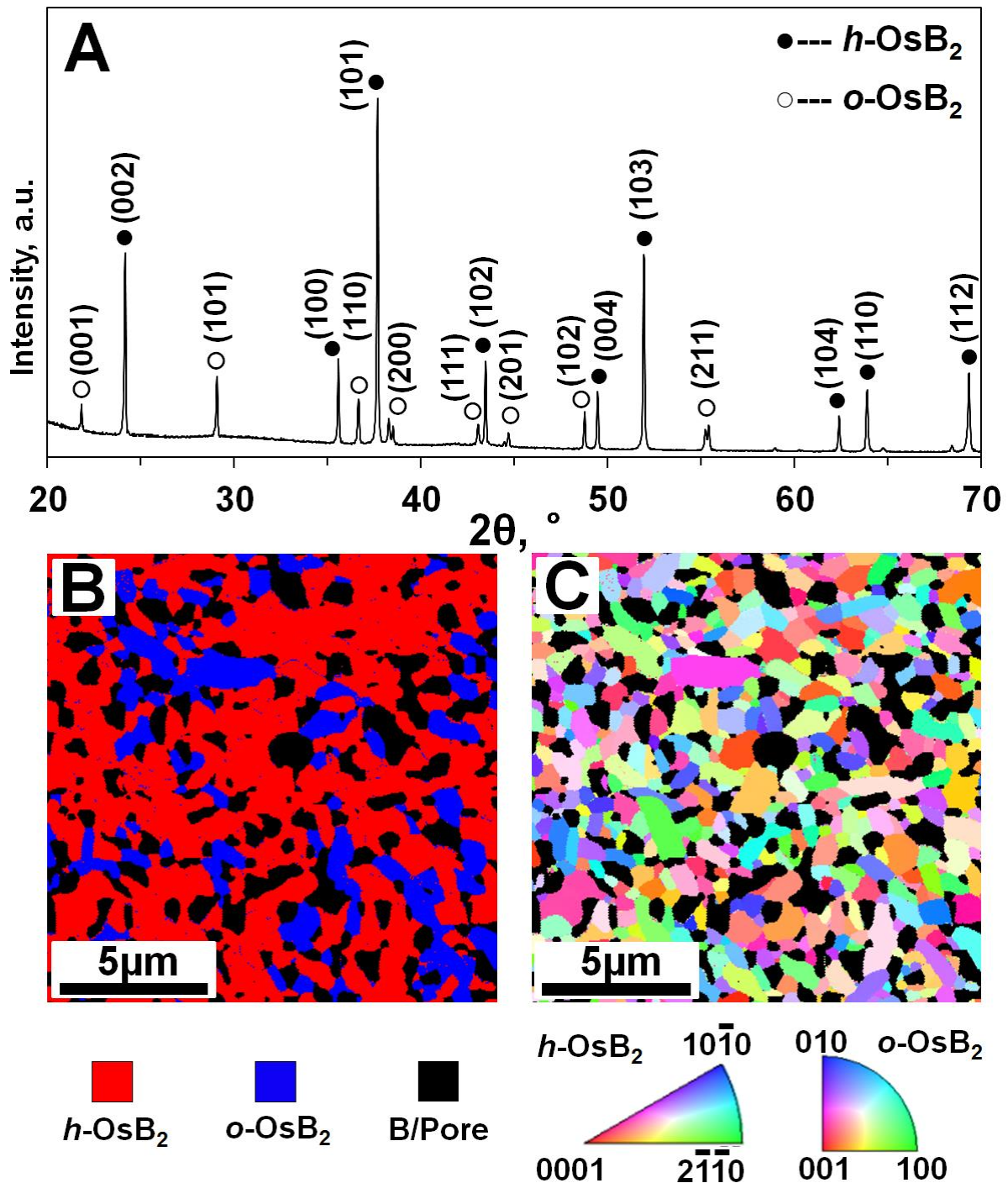


Figure 59: X-ray diffraction pattern of sintered OsB<sub>2</sub> ceramics (A), along with a phase composition map (B) and corresponding EBSD map (C) where the phase content (A and B) as well as crystallographic orientation of each individual OsB<sub>2</sub> grain could be identified (C).

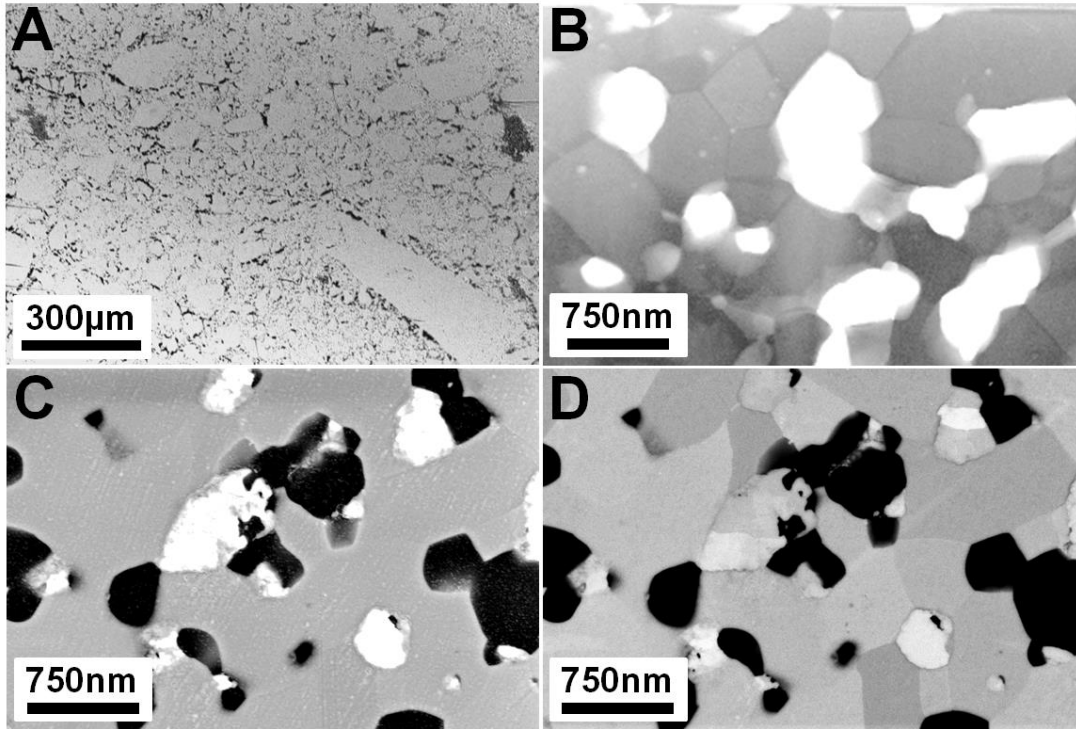


Figure 60: Microstructure of  $\text{OsB}_2$  after SPS (A). The optical micrograph shows a nonhomogeneous densification. (B) TEM micrograph of  $\text{OsB}_2$  where the grains are clearly visible but also quite a high numbers of pores are also present. (C) SEM micrograph of  $\text{OsB}_2$  polished surface taken using InLens detector and (D) the SEM micrograph of the same  $\text{OsB}_2$  surface as in (C) but produced using backscattered ESB detector.

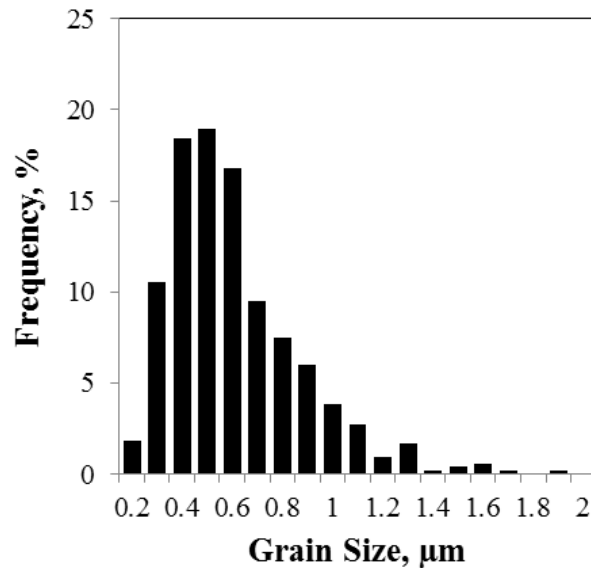


Figure 61: Grain size distribution of  $\text{OsB}_2$  ceramics after SPS calculated from the results presented in Figure 59C, Figure 60B and D. The average grain size is equal to  $0.56\mu\text{m}$  thus the produced  $\text{OsB}_2$  is a submicron ceramics.

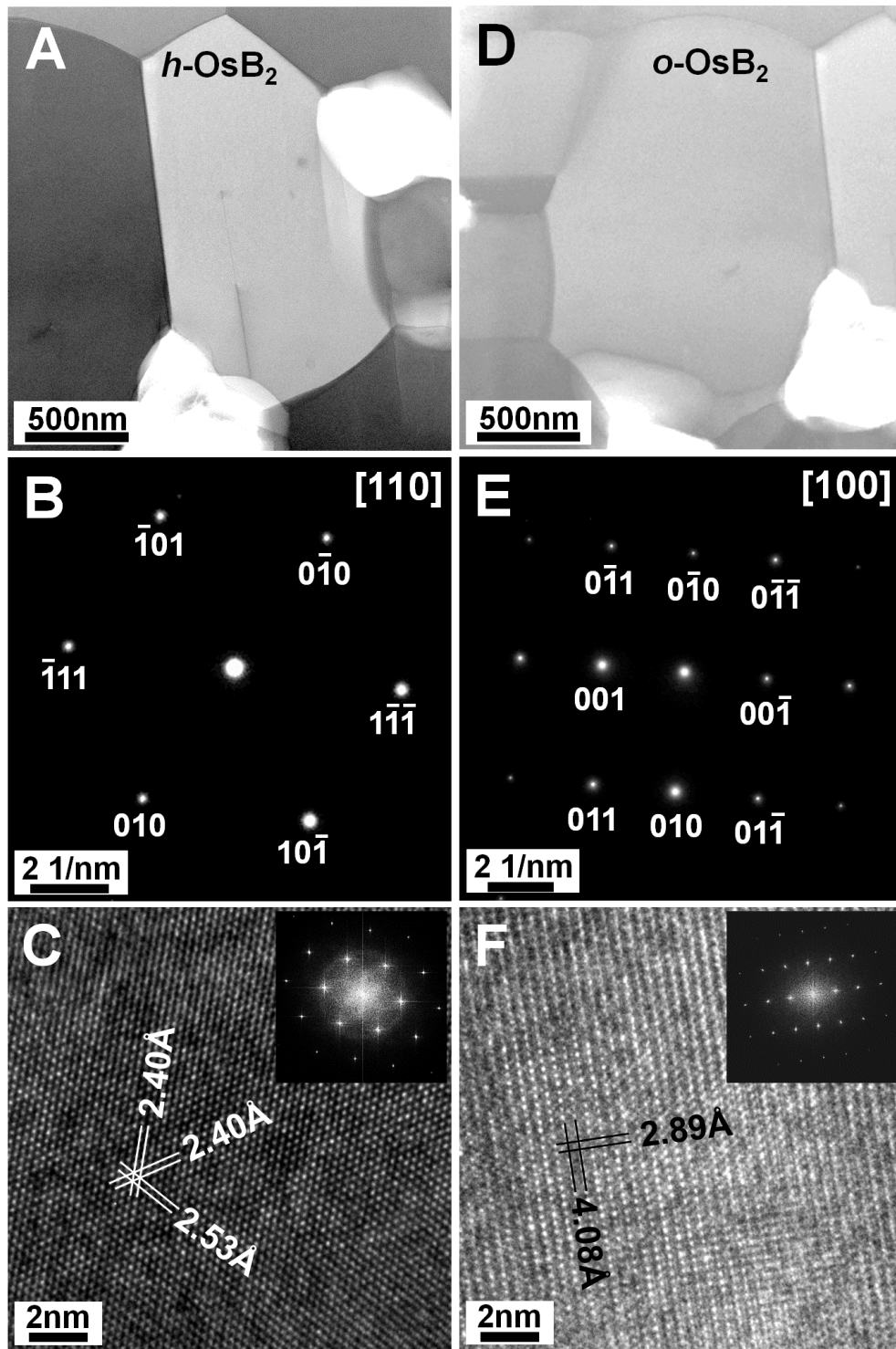


Figure 62: TEM micrographs of hexagonal (A) and orthorhombic (D) OsB<sub>2</sub> grains with the corresponding electron diffraction patterns (B and E, respectively), along with their high resolution images and the corresponding FFT patterns (C and F).

The distribution of elements in the OsB<sub>2</sub> ceramics after sintering was studied by EDS. Figure 63 shows the overlapping EDS spectra collected from the area 1 (within a pore) and 2 (at the surface of material surrounding a pore) where it is shown that the high B concentration within the pore with some amount of O and no Os present in area 1, while the Os and some quantity of B along with O and W peaks can be detected from area 2 of the polished surface. Thus, it was detected that certain B and O rich phase(s) exist inside pores. The Os, B and O maps of OsB<sub>2</sub> ceramic were also created and they are shown in Figure 64. The maps show that the separation of Os and B was observed in OsB<sub>2</sub> ceramics, as it was found that the high concentration of B has always been detected in the grains where Os was deficient (Figure 64 a, b and c), similar to the results presented in Figure 63. The boron concentration within the identified locations was much higher in comparison with the rest of the area mapped by EDS. Some oxygen was also detected within pores (Figure 64d), but locations did not overlap regularly with Os or B signals.

TEM of the phases located within pores of sintered OsB<sub>2</sub> was performed (Figure 65), and suggested the presence of two types of phases. One phase (Figure 65A) was identified as rhombohedral elemental B, as shown in the corresponding electron diffraction (Figure 65B). The presence of small grains (Figure 65D) with an average grain size of 188nm in another examined pore (Figure 65C) was also discovered, which based on EDS analysis, was assigned to the B<sub>2</sub>O<sub>3</sub> phase. As the quantity of both *r*-B and B<sub>2</sub>O<sub>3</sub> was not sufficient to be detected by X-ray analysis, XRD pattern did not show their presence, as only *h*- and *o*-OsB<sub>2</sub> phases were detected (Figure 59A).

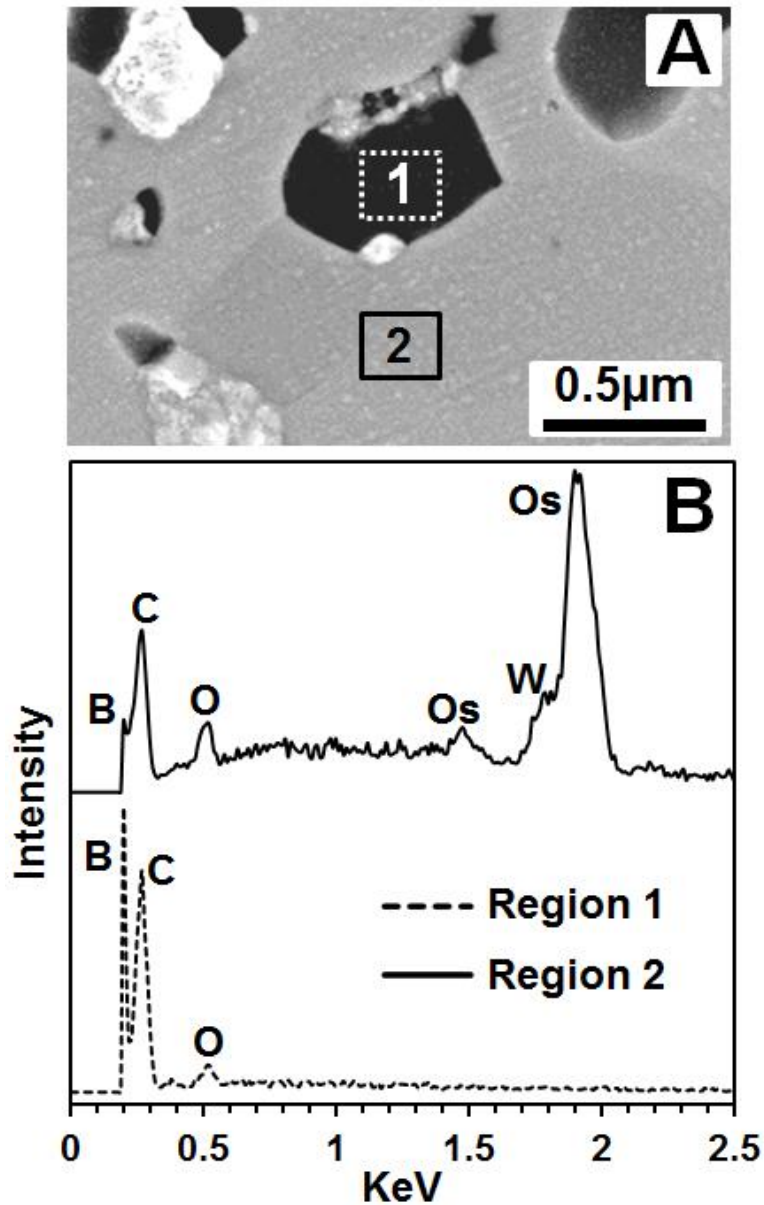


Figure 63: SEM micrograph of the polished  $\text{OsB}_2$  ceramics with corresponding EDS spectra collected at two different areas on the surface. The area 1 highlighted within dark field (a pore), enriched in B while no Os can be detected, while the area 2 highlighted at the surface of  $\text{OsB}_2$  ceramics surrounding the pore is enriched in Os.



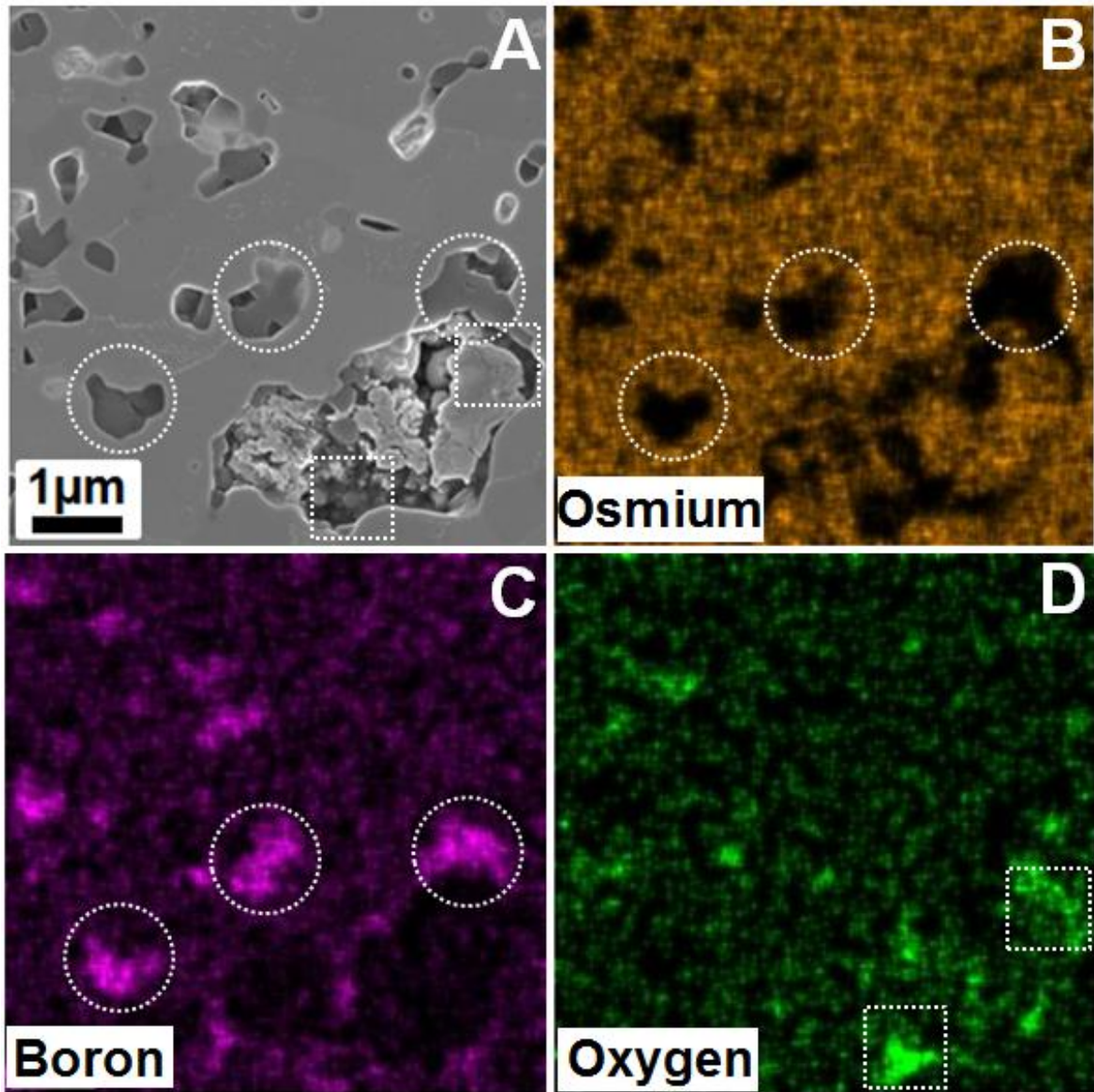


Figure 64: SEM micrograph of the polished surface of OsB<sub>2</sub> ceramics after sintering with corresponding distribution of Os (B), B (C), and O (D) elements collected as EDS maps.

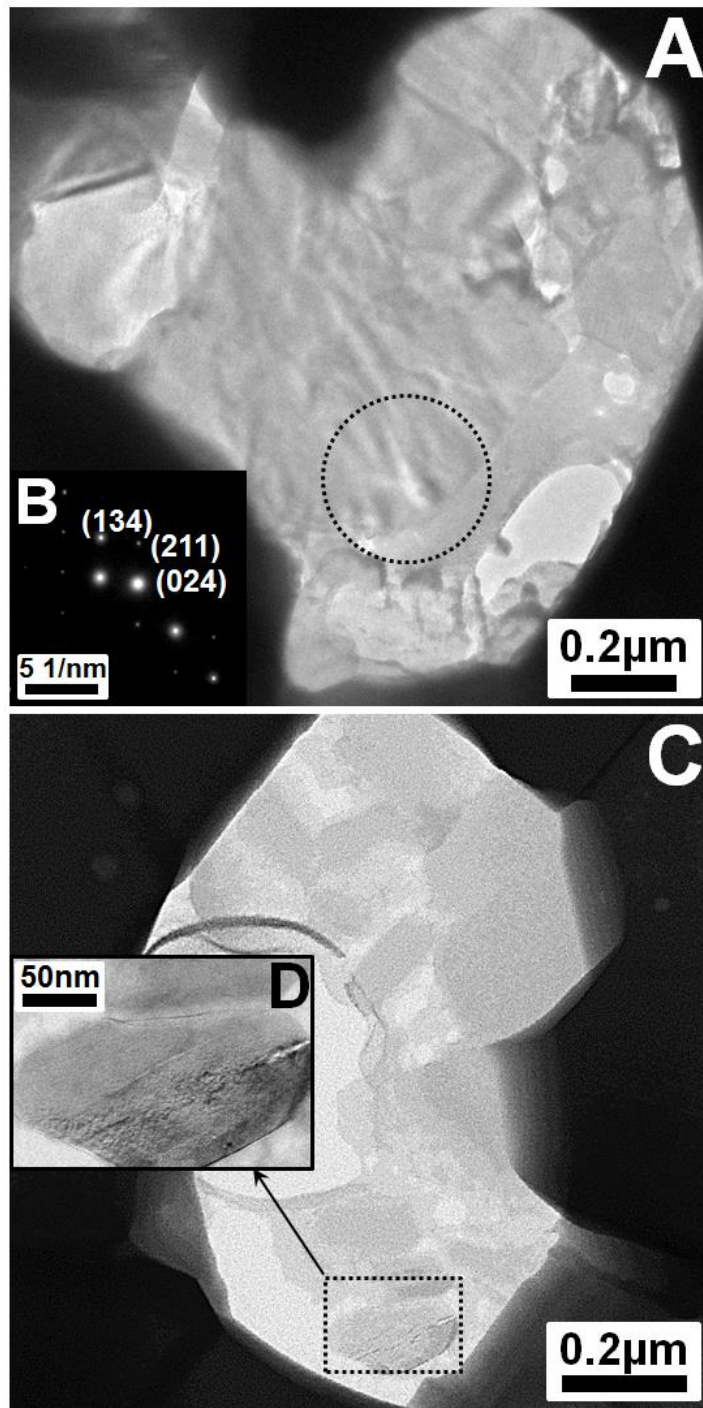


Figure 65: TEM image of the material present within a pore in OsB<sub>2</sub> sample after sintering (A); the corresponding electron diffraction pattern of the area highlighted with a dashed circle (B); TEM micrograph of the material located in a different pore (C); along with higher resolution image of the selected location with a pore highlighted with a dashed rectangle (D).



### 7.3.3 Mechanical behavior of OsB<sub>2</sub>

(1) Calculation of hardness, Young's modulus, indentation stress – indentation strain deformation behavior, elasticity and ductility indices

The nanoindentation load-displacement plots obtained by using both spherical and Berkovich sharp indenters were used for the calculation of both hardness and Young's modulus of OsB<sub>2</sub> and for conversion of load-displacement into indentation stress – indentation strain plots. The Oliver and Pharr method [125] was used for the extraction of hardness and Young's modulus values, where  $E_r$  is a so called reduced modulus of the indenter and the specimen system is expressed as

$$\frac{1}{E_r} = \frac{1-\nu_s^2}{E_s} + \frac{1-\nu_i^2}{E_i} \quad (6.1)$$

for the case if the indenter is assumed to behave as an elastic solid and  $\nu$  is the Poisson's ratio,  $E$  is the Young's modulus, and the subscripts  $s$  and  $i$  refer to the specimen and the indenter, respectively. From the unloading part of the load-displacement curve the effective  $E_r$  can be estimated as

$$E_r = \frac{\sqrt{\pi}}{2} \frac{S}{\sqrt{A}} \quad (6.2)$$

where  $S$  is taken as the slope of the unloading curve at the beginning of unloading and  $A$  is the projected contact area.  $A$  is determined from a nanoindenter area function  $A(h_c)$ , where  $h_c$  is the distance from the contour of contact to the maximum penetration depth. The following expression was proposed for the computation of  $h_c$  [125]

$$h_c = h - \frac{3P}{4S} \quad (6.3)$$

where  $h$  and  $P$  are the displacement and the load from measured nanoindentation diagram. It was determined that the area function  $A(h_c)$  was presented by the following equations

$$A(h_c) = -3.14h_c^2 + 1397h_c \text{ [nm}^2\text{]} \quad (6.4)$$

for spherical diamond nanoindenter used in the present studies. The hardness of the material was determined using the following standard equation:

$$H = \frac{P}{A} \quad (6.5)$$

where  $P$  is the maximum load of nanoindentation,  $A$  can be found using Eq. (4) or from SEM image of corresponding impression. From the contact area  $A$  the radius of contact for certain  $h$  and  $P$  can be calculated as

$$a = \sqrt{\frac{A}{\pi}} \quad (6.6).$$

Once the radius is calculated, then the following equations were used for conversion of load-displacement into indentation stress-indentation strain plots [256]

$$\sigma_{ind} = \frac{P}{\pi a^2} \quad (6.7)$$

and

$$\varepsilon_{ind} = \frac{4h}{3\pi a} \quad (6.8).$$

By converting load-displacement data into indentation stress-indentation strain plots the elastic part

$$\sigma_{ind} = E_r \varepsilon_{ind} \quad (6.9)$$

of the loading segment of nanoindentation diagram can be revealed as well as a yield point, where the deviation from the linear behavior and the onset of plastic deformation can be visualized.

The material can be also characterized by elasticity and ductility indices. The elasticity index is defined as

$$I_E = H / E_r , \quad (6.10),$$

where  $H$  is the hardness and  $E^*$  is the reduced modulus [257-259]. The elasticity index of the most brittle ceramics ranges from 0.3 to 0.05 and of ductile metals from 0.005 to 0.001 [257, 258]. The indentation ductility index was defined as follows [257]:

$$D = \frac{U_r}{U_t} = \frac{h_r}{h_{\max}} , \quad (6.11)$$

where  $U_r$  is the consumed energy for creating the residual impression,  $U_t$  is the total work at maximum load,  $h_r$  is the residual depth of indentation,  $h_{\max}$  is the maximum depth of indentation at maximum load. The ductility index must be 1 for a purely plastic (purely ductile) body without elastic recovery during unloading and 0 for a purely elastic body exhibiting a complete unloading recovery in an elastic manner. With the increase in the elasticity index, the ductility index decreases from 1 to 0. [257]

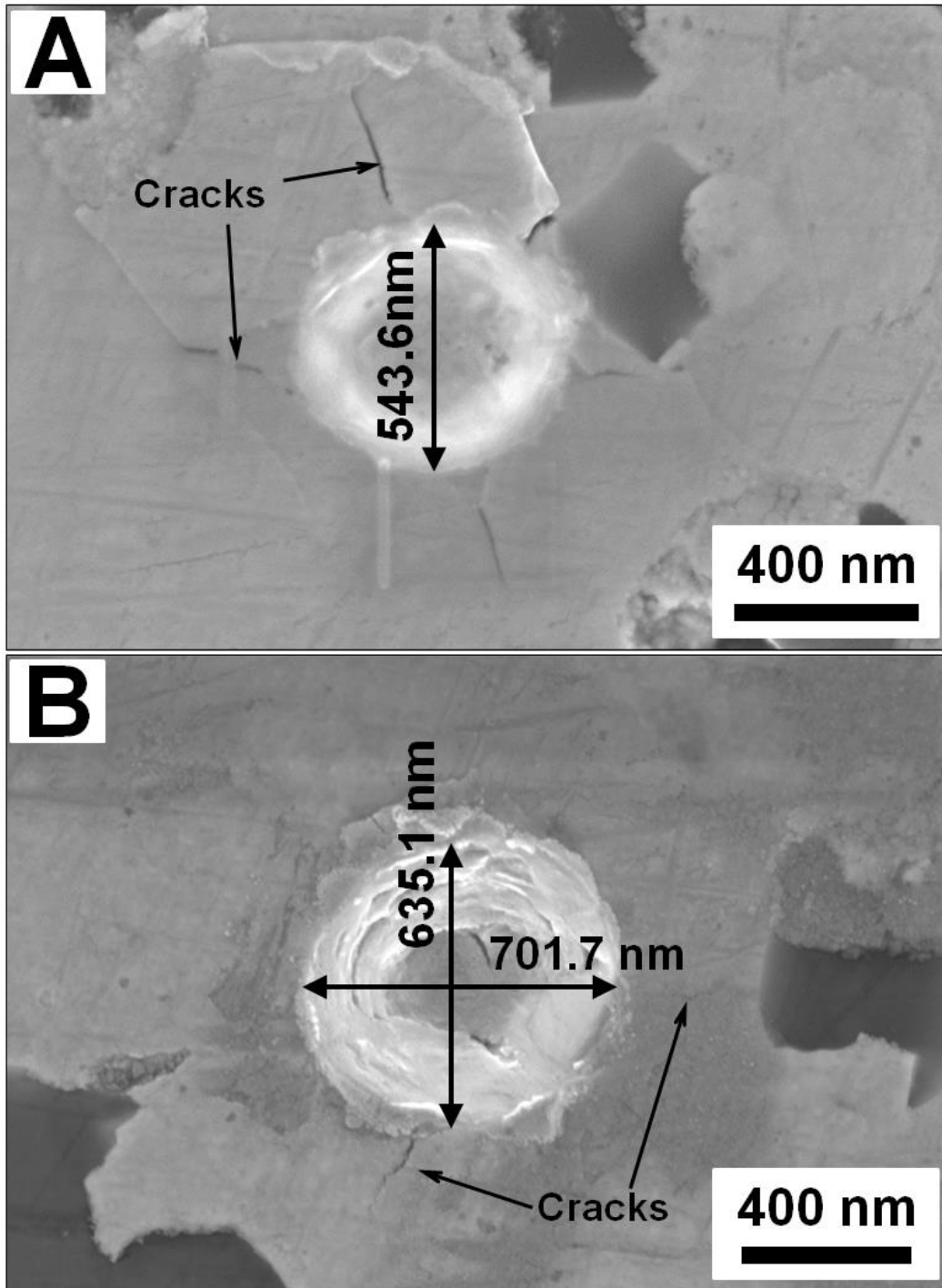


Figure 66: SEM micrograph of the two impressions produced by nanoindentation of polished OsB<sub>2</sub> surface with a spherical indenter with a load of 8 mN.

(2) Hardness, Young's modulus, indentation stress – indentation strain behavior, elasticity and ductility indices of OsB<sub>2</sub>

The direct measurements of the OsB<sub>2</sub> hardness after SPS were performed using equation (5). The nanoindentation was performed with a spherical diamond indenter to the maximum load of 8mN and the area of the residual impressions was estimated from the SEM micrographs. The average hardness value obtained by direct measurements of the projected area of the impressions was equal to 34.24±3 GPa. The typical impression is shown in Figure 66A. It is visible from the image that, while the hardness of the material is rather high in this location, the radial cracks have been formed even at such low maximum load as 8mN. The formation and propagation of the radial cracks during the indentation is an indication of the brittleness of the OsB<sub>2</sub> ceramics. While most of the impressions produced during the indentation using conical indenter at 8mN maximum load looked like the one presented in Figure 66A, one of the 25 impressions had a very different pattern with a number of layers squeezed out of the material during indentation (Figure 66B). The diameter of the impression was much bigger in comparison to the average value of other impressions, providing the hardness values of only 22.8 GPa. It is possible that, since material is not homogenous and some phases do not belong to OsB<sub>2</sub> and are non-detectable by XRD, the indentation was made into B grain presents or even in B<sub>2</sub>O<sub>3</sub> phases, thus showing lower value of hardness.

To estimate hardness and Young's modulus of OsB<sub>2</sub> [125], the nanoindentation was performed in the displacement control mode with the maximum depth of penetration not to exceeding 70nm. The total of 50 impressions has been made and 50 load-displacement diagrams have been collected, which were used for the calculation of hardness and Young's modulus from

the beginning portion of the unloading curve, as well as for the conversion of load - displacement into indentation stress - indentation strain plots. For the calculation of Young's modulus by Oliver and Pharr's technique, the value of Poisson's ratio of material is required. However, as no measured values of Poisson's ratio were found in the literature for hexagonal OsB<sub>2</sub>, the 0.18 value were taken for the calculations, as the compound is very stiff and rather hard. In one of the publications [126], 0.27 was provided as a calculated Poisson's ratio for the orthorhombic OsB<sub>2</sub> phase, however, such relatively high values are more characteristic for more soft ceramics, while stiff ceramics, such as B<sub>4</sub>C, TiB<sub>2</sub> and ZrB<sub>2</sub> are all reported as having 0.14-0.18 values of Poisson's ratio. Thus, for the estimation of Young's modulus of OsB<sub>2</sub> using nanoindentation load-displacement diagrams, the arbitrary 0.18 value for Poisson's ratio was used. The difference in estimated Young's modulus values is not significant, as when Poisson's ratio is  $0.18 \pm 0.018$ , relative error for Young modulus is only 0.7%. By analyzing the available load-displacement plots, it was found that the majority of the diagrams (36 out of 50) contained the so called "pop-in" events at the loading portion of the plots. The example of such diagram and its conversion to the indentation stress – indentation strain plot is shown in Figure 67. The hardness calculated from such diagrams was equal to  $31 \pm 9$  GPa and Young's modulus was calculated to be equal to  $574 \pm 112$  GPa. Upon conversion of the load – displacement diagram (Figure 67A) into indentation stress – strain diagram (Figure 67B), one can see that a very high stress level exists below the spherical diamond indenter during indentation. In addition to the possibility of estimation of level of stress and strain during nanoindentation, another advantage of the conversion of load – displacement into stress – strain data is a possibility to estimate a "yield" stress of the material, as it is typical that at the beginning of loading the indentation stress is

directly proportional to the indentation strain and it is only after achieving certain “yield” stress that the deviation from the linear deformation starts taking place. An example of the “yield” stress  $\sigma_y$  estimation is presented in Figure 67B. The  $\sigma_y$  calculated using all 36 indentation plots provided the  $23 \pm 7$  GPa average value. Thus, the nanoindentation experiments indicated that both hexagonal and orthorhombic OsB<sub>2</sub> phases are relatively hard and rather stiff with a high yield stress values, as determined by hardness, Young’s modulus, “yield” stress and indentation stress – indentation strain deformation behavior. As it was measured the average grain size of OsB<sub>2</sub> ceramics after SPS was equal to 0.56 $\mu$ m, most likely that the measured values of hardness and Young’s modulus have been obtained from indentations in single grains with their unique crystallographic orientations. However, since as many as 36 grains were indented, the average values of E and H can provide the reliable data on the properties of OsB<sub>2</sub> ceramics. While the measured E and H values could be obtained from grains belonging both to hexagonal and to orthorhombic OsB<sub>2</sub> phases, as it was not possible to discriminate the phases in the measurements, however the objective lenses of the microscope allowed avoiding of performing nanoindentation in the pores and other defective areas visible optically.

In addition to the 36 load – displacement diagrams, where pop-in events were present, different type of indentation behavior was found, where no pop-in events were found upon loading or low mechanical properties were obtained. An example of such diagram is shown in Figure 68. The hardness and Young’s modulus calculated from these 14 load – displacement diagrams were significantly lower in comparison with 36 diagrams where pop-in events were present. The reported average hardness and Young’s modulus values were equal to  $16 \pm 3$  GPa and  $368 \pm 91$  GPa, respectively. The estimated average “yield” stress of such indents was equal

to  $17 \pm 7$  GPa and the maximum indentation stress was calculated to be equal to  $\sim 30$  GPa, while the indentation stress could easily reach up to 50 GPa at the maximum load when indenting more hard OsB<sub>2</sub> phases present in the material. The scanning probe micrograph (SPM) images of the OsB<sub>2</sub> surfaces before and after indentation where the spherical impression was visible are presented in Figure 69. Thus, it is possible to estimate that a mixture of hard and relatively soft phases exist in the OsB<sub>2</sub> sample indicating an inhomogeneous nature of the material after densification by SPS.

In addition to the hardness, Young's modulus, indentation yield stress as well as stress-strain deformation behavior, the elasticity and ductility indices of OsB<sub>2</sub> ceramics have also been calculated using nanoindentation results. It was calculated that according to the Equations (10) and (11), the elasticity index was equal to 0.07 and the ductility index was equal to 0.44. For comparison, the elasticity and ductility indices of copper (Cu) are equal to 0.02 and 0.95, respectively [257], while the elasticity indices of Al<sub>2</sub>O<sub>3</sub>, SiC and Si<sub>3</sub>N<sub>4</sub> ceramics are equal to 0.08, 0.13 and 0.175, respectively and their ductility indices are equal to 0.68, 0.57 and 0.59, respectively [257]. The elasticity and ductility indices of glass are equal to 0.19 and 0.54, respectively [257]. Thus, the elasticity index of OsB<sub>2</sub> ceramics is in the lower range of traditional Al<sub>2</sub>O<sub>3</sub>, SiC, Si<sub>3</sub>N<sub>4</sub>, and glass materials, while the ductility index is much lower in comparison even with a glass, such low values of both indices give an indication of the highly brittle nature of OsB<sub>2</sub> ceramics.



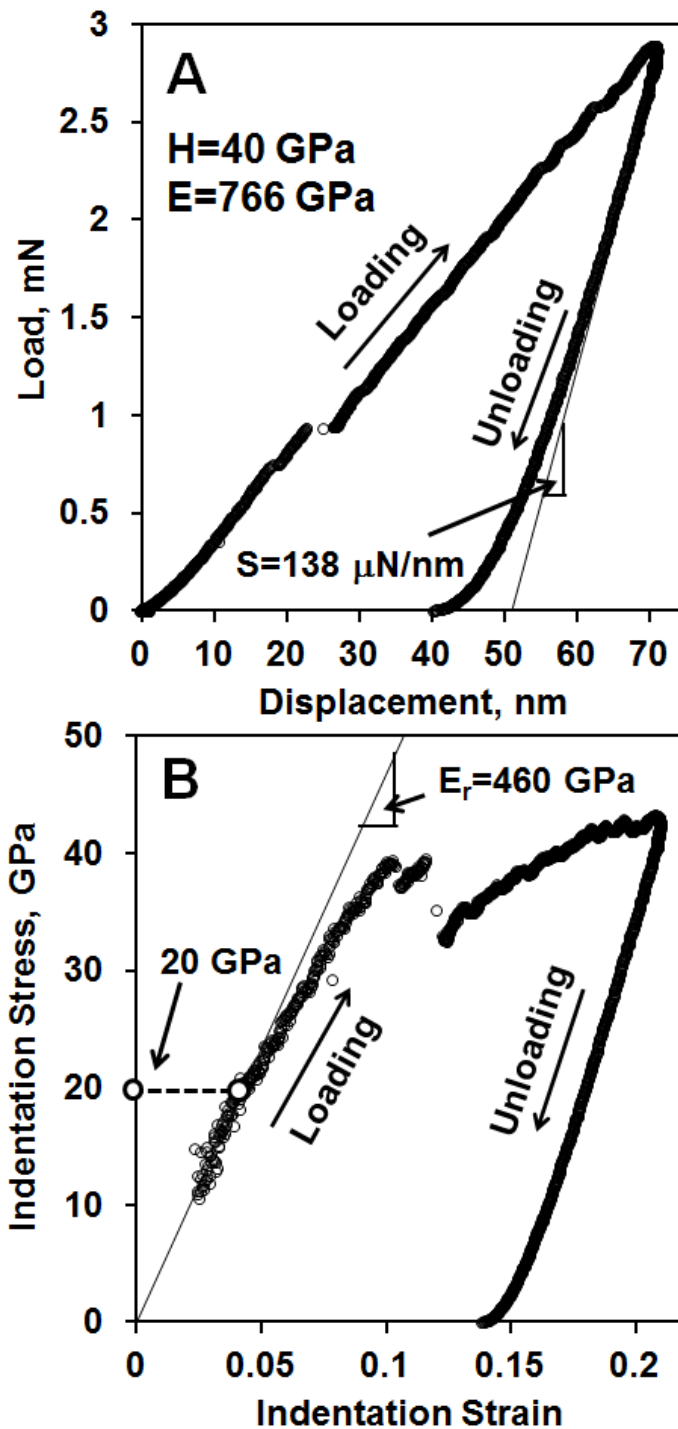


Figure 67: Load–displacement (A) and recalculated indentation stress – indentation strain (B) diagrams produced by nanoindentation of polished OsB<sub>2</sub> surface where “pop-in” events were present during the loading portion of the load-displacement curve.

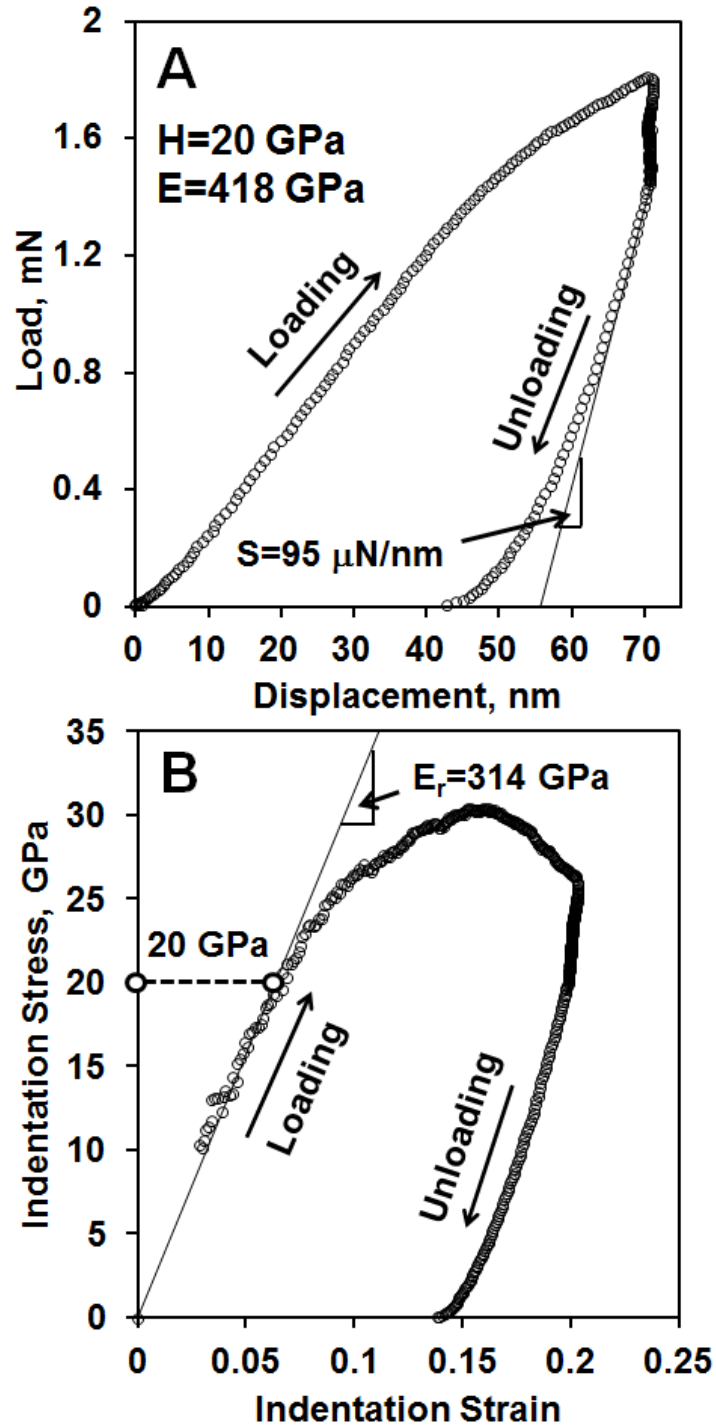


Figure 68: Load – displacement (A) and recalculated indentation stress – indentation strain (B) diagrams produced by nanoindentation of polished  $\text{OsB}_2$  surface where no pop-in event was present during loading or unloading portions of the load-displacement curve.

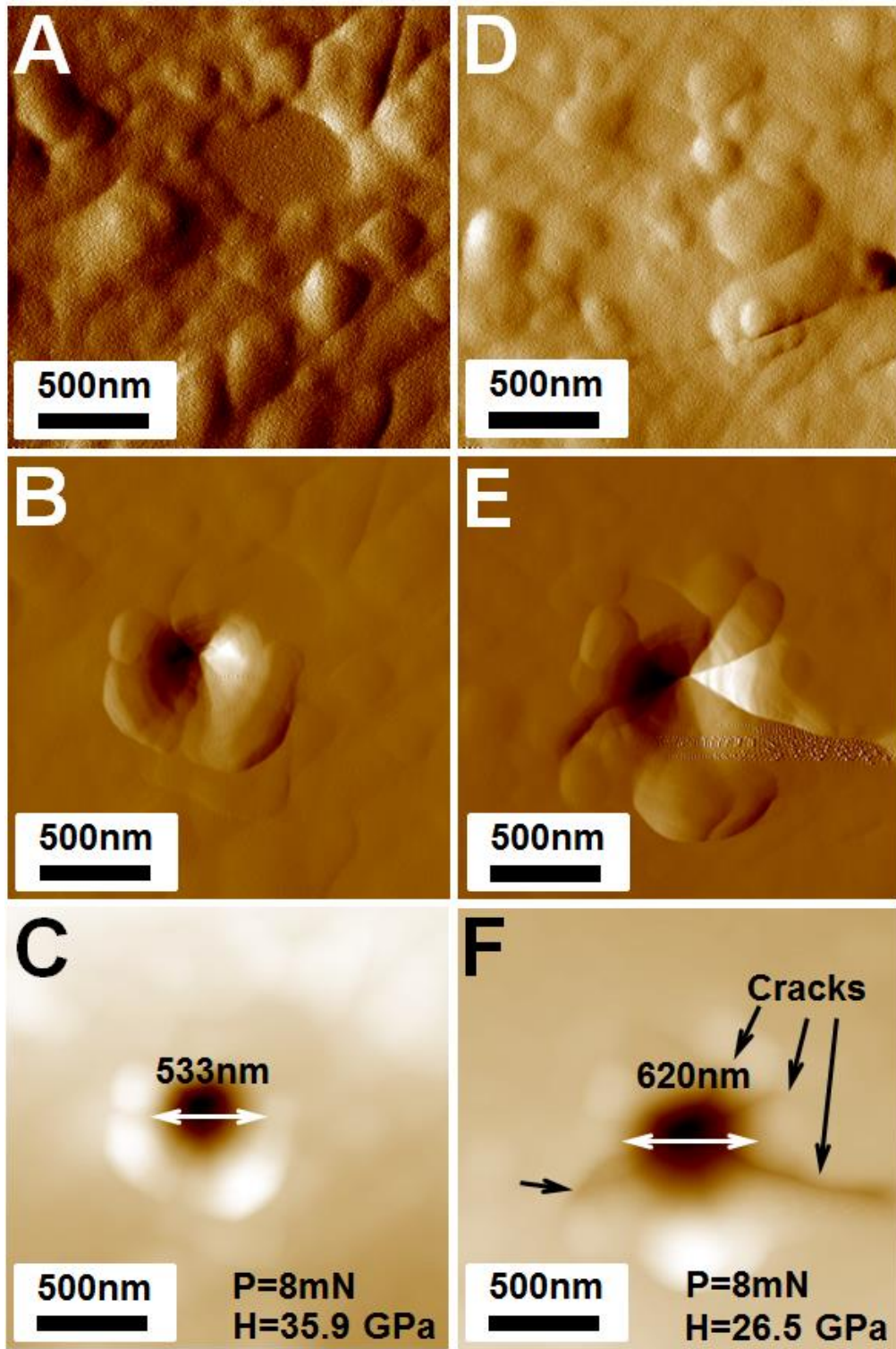


Figure 69: The scanning probe micrographs of the OsB<sub>2</sub> surfaces before (A, D) and after (B, C, E and F) indentation.

## 7.4 Conclusions

The ReB<sub>2</sub>-type OsB<sub>2</sub> powder synthesized by mechanochemistry was densified by spark plasma sintering for the first time. The obtained bulk material contained a significant amount of porosity and, also, it was discovered that during the direct current sintering the transformation from hexagonal (*P63/mmc*) to orthorhombic (*Pmmn*) structure has occurred. Thus, the ceramics after sintering contained 26.9% of porosity and a mixture of ~80 wt% hexagonal and ~20 wt% of orthorhombic phases as it was detected both by X-ray and EBSD analysis.

The average grain size of the OsB<sub>2</sub> ceramics after sintering was equal to 0.56 μm and the TEM analysis allowed to identify the hexagonal and orthorhombic grains. It was discovered that much higher concentration of B was observed within separate locations. The EDS maps showed that the concentrations of Os and B do not coincide, and there were separate areas found on the maps that were enriched in B content, while Os were practically absent in those locations. At the same time, there were other areas which showed Os deficiency, but they were enriched in oxygen. It was suggested that such boron enriched area might contain rhombohedral B, while those areas enriched in O might be the residues of B<sub>2</sub>O<sub>3</sub> or BO phase.

An attempt was made to probe the mechanical behavior of the SPSed OsB<sub>2</sub> ceramics using nanoindentation. It was calculated that the average hardness and Young's modulus of the indented material was equal to 31±9 GPa and 574±112 GPa, respectively, while the highest value of hardness and Young's modulus measured reached 45 GPa and 773 GPa, respectively. Such differences could be explained that the indentations have mostly been made in separate grains thus each individual grain's crystallographic orientation affected the measured values.

However, because of a significant number of the indentations have been made in different grains, the average values might lie rather close to the true values of hardness and Young's modulus of the ceramic. It was also measured that certain area of the material exhibited lower values of hardness and Young's modulus.

The produced bulk  $\text{OsB}_2$  ceramics was not dense and homogeneous and its mechanical properties varied significantly depending on the location of indentation. Therefore, the conclusion is that it is possible to retain metastable high-pressure  $\text{ReB}_2$ -type hexagonal  $\text{OsB}_2$  during sintering and the potential for the structure to exhibit superior hardness and stiffness is rather high. More studies are needed to find and optimize the sintering regime to produce dense and homogeneous hexagonal  $\text{OsB}_2$ , which would exhibit superior hardness and stiffness.

## CHAPTER 8: SYNTHESIS OF NEW IrB<sub>2</sub> PHASES AND Ir SEGREGATION AT HIGH TEMPERATURE

### 8.1 Introduction

Borides are utilized in a range of industrial applications due to their unique electrical, thermal, mechanical and catalytic properties. In particular, transition metal diborides are of special interest. Titanium diboride (TiB<sub>2</sub>) ceramics have a very high Young's modulus of 565 GPa [243], zirconium and hafnium diboride (ZrB<sub>2</sub> and HfB<sub>2</sub>, respectively) composites exhibit high oxidation resistance [232, 260], magnesium diboride (MgB<sub>2</sub>) is a superconducting phase with a  $T_c$  among the highest of the conventional superconductors [261] and niobium diboride (NbB<sub>2</sub>) nanoparticles have applications in catalysis as well as reversible hydrogen storage [247]. While many of the diborides find practical uses as abrasion and oxidation resistant coatings, there is an ongoing search for new phases and compositions that might possess interesting and useful properties. In the recent years, Re, Os, Rh, Cr, and W borides have been studied as for their ultra-hardness and superior stiffness [29, 52-54, 57, 262]. Interestingly, no experimental evidence exists for IrB<sub>2</sub> even though the other elements in the group readily form diborides. Although, first principles calculations have predicted that IrB<sub>2</sub>, which is expected to adopt an orthorhombic OsB<sub>2</sub>-type structure, would be a thermodynamically stable form, no IrB<sub>2</sub> phases have been synthesized experimentally [263], however, a number of compounds have been prepared in the Ir-B system with lower than a 1:2 metal: boron stoichiometry. Phases such as IrB<sub>1.35</sub> and IrB<sub>1.1</sub> as well as the metal-rich phases IrB<sub>0.9</sub> and IrB<sub>0.7</sub> have been reported in a number

of publications [77, 116, 135, 136, 264] and some of their properties were investigated [43, 57, 141, 144]. Very high Vickers hardness of 49.8 GPa at 0.49N load was reported for IrB<sub>1.35</sub> [57]. It has been predicted [123, 265] that the mechanical properties of borides could be improved by increasing the concentration of boron atoms in the sublattice of the transition metals, as increase in boron atom concentration in a boride's unit cell would increase the amount of the covalent bonding in the lattice, which would improve the strength, hardness and stiffness of the ceramics. Therefore, increasing the boron content in the iridium sublattice should produce a material with superior mechanical properties coupled with the chemical stability of iridium.

Recently mechanochemical syntheses have been successfully employed in the preparation of such difficult to process boron rich solids as ReB<sub>2</sub> and OsB<sub>2</sub> ceramics. [213, 221] High energy ball milling of rhenium and osmium metal powders with an elemental boron powders for an extended periods of time using WC media and balls allowed production of hexagonal ReB<sub>2</sub> and OsB<sub>2</sub> phases. In fact, this approach is the only currently known route to hexagonal OsB<sub>2</sub> – a metastable high-pressure phase that had never been experimentally reported before. [221] The strain driven solid state chemical reactions were driven by high impacts produced by the grinding media during milling [162, 178, 194, 266]. Both axial and shear stresses contribute to the fracture of particles followed by solid state diffusion reactions leading to the formation of new compounds (Figure 70A). Shear stress and strain play a major role in the mechanochemical synthesis as shear strength of many compounds is much lower in comparison with compressive strength, thus if shear deformations are present, the solid state synthesis could be favored over approaches where only axial or hydrostatic pressure is acting alone. The estimated maximum macroscopic axial and shear stresses present during mechanochemical

synthesis of Os-B compound as a function of contact area are shown in Figure 70B. Macroscopic axial stresses will result in atomic level shear stress through plastic deformation. The yield strength of iridium is approximately 100 MPa. A majority of the impacts generated in the mill are above this value. A movie illustrating the ball movement and shear stresses during high energy ball milling can be found in the online supporting information. Mechanochemical approaches to synthesis represent a very promising route to production of difficult to synthesize ceramics. Additionally, this method has the capability of producing metastable compounds that cannot be such easily processed by other available means. Thus, it is very appealing to utilize the high energy ball milling technique to produce high borides in Ir-B system, such as IrB<sub>2</sub> phases.

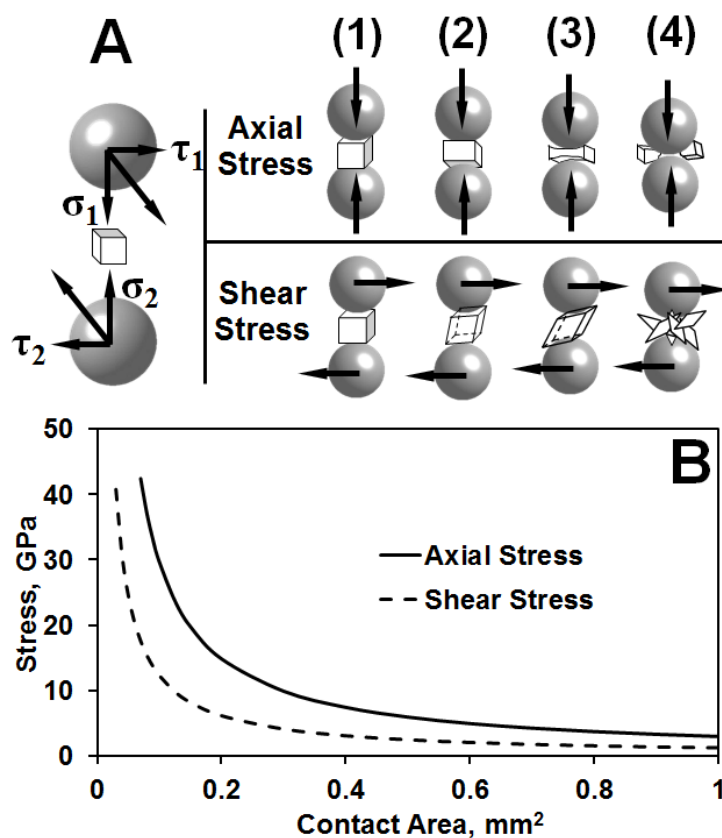


Figure 70: Mechanism of high energy ball milling (A) and maximum axial and shear stresses present during mechanochemical synthesis of Os-B compound as a function of contact area (B).



While  $\text{ReB}_2$ ,  $\text{OsB}_2$ , and  $\text{IrB}_{1.1}$  and  $\text{IrB}_{1.35}$  have been reported as ceramics with high mechanical properties, the stability issues of these materials was immediately of a concern. Thus, for example, the results on hardness of hexagonal  $\text{ReB}_2$  [52] were questioned in [66], where the statement on low hardness of  $\text{ReB}_2$  was expressed. However in both publications, the time dependent exposure of  $\text{ReB}_2$  ceramics to oxygen/water vapor containing species was not addressed at all. However such exposure has a detrimental effect on properties and might explain the discrepancies in the reported results, as it is well known that when  $\text{ReB}_2$  or  $\text{OsB}_2/\text{Ir-B}$  compounds are not properly stored in the protective environment and exposed to oxygen containing species even at ambient, they react with oxygen or water molecules present in the atmosphere. The products of such reactions could be perhenic acid, which formed after one year storage of  $\text{ReB}_2$  powder inside the plastic bag without protective atmosphere of glovebox at ambient conditions [213], or when the total reductions of  $\text{OsB}_2$  nanopowder to metallic Os upon heating in the  $\text{H}_2$  containing reducing atmosphere where  $\text{O}_2$  molecules present [251, 252]. Thus, if the indentations and measurements of hardness and Young's modulus of the  $\text{ReB}_2$  or  $\text{OsB}_2$  ceramics were made immediately after processing then the reported high values might well correspond to the intrinsic  $\text{ReB}_2$  or  $\text{OsB}_2$  behavior.

In case where samples were allowed to dwell at ambient without proper storage procedure in Ar or  $\text{N}_2$  protective atmosphere with low oxygen partial pressure concentrations, then the surface properties of the compound would degrade, because of the formation of the products of the absorption or/and chemical reactions between a boride and oxygen containing species in the atmosphere, leading to a significant degradation in measured values of hardness and Young's modulus simply because the measured values represent the behavior of degraded

surface layer species and not pure  $\text{ReB}_2$  or  $\text{OsB}_2$  compounds. Thus it was established that the oxygen containing species available in the environment even at ambient affect not only the chemical and phase compositions of the borides, but also their properties. One of the conclusions of the work on thermal stability issues of  $\text{OsB}_2$  was that oxygen react with boron atoms in the lattice of the compound thus creating boron vacancies and bringing changes to the stoichiometry of  $\text{OsB}_2$  to the extent that Os atoms are induced to segregate out of lattice forming Os metal precipitates in a significant quantities detectable by X-ray analysis.

The previous work on stability of  $\text{ReB}_2$  and  $\text{OsB}_2$  ceramics and their interactions with oxygen containing species in the surrounding atmosphere brought a guest on possibility of synthesis of  $\text{IrB}_2$  compounds as well as other possible phases in Ir-B system. Of course, once formed for example by mechanochemistry, the stability of the Ir-B phases would be of high interest, as their interaction with oxygen might be one of the reasons as to why lower content borides, such as  $\text{IrB}_{1.1}$  and  $\text{IrB}_{1.35}$  have always been reported in the past, and no  $\text{IrB}_2$  compounds synthesized. Here we report by our attempt to produce Ir-B compounds by mechanochemistry as well as study the effect of high temperature annealing on phase composition and microstructure of Ir-B after mechanochemical synthesis.

## 8.2 Experimental

Iridium metal powder (Precious Metal Purchase, 99.9% pure) and boron powder (Alfa Aesar, 99% pure, -325 mesh, amorphous and crystalline) were used as received. A total of 11.7 grams of iridium and boron powders (molar ratio Ir:B=1:3) were loaded into a Spex tungsten

carbide vial with two 12.7mm diameter tungsten carbide balls as milling media, which produced a ball to powder weight ratio about 2.74. All loading operations were carried out in an argon-filled glovebox. The milling vial and media were coated with Iridium boron (boride) powders from the previous milling. The grinding was done by a Spex 8000 Mixer/Mill for a total of 90 hours. Every 30 minutes the milling was interrupted and vials were left for 30 minutes without grinding in order to decrease the vials' temperature and reduce wear on the mill's motor. Every 5, 10 or 20 hours, a small amount of sample was removed for phase analysis by X-ray diffraction (XRD) method. After 30 hours of milling, 1 gram of powder was annealed *in vacuo* at 1050°C for 48 hours. After 90 hours of milling, another 1 gram of powder was annealed under the same condition but for 72 hours. All the collections of ground powder were done in the argon filled glovebox. A PANalytical X'Pert Pro MPD system with a copper source (Cu K $\alpha$ l = 1.5418Å) was used to record X-ray diffraction patterns of the powder. Refinement of the structure was performed using the HighScore Plus software. The morphology and particle size of the powders were examined in a Zeiss Merlin scanning electron microscope (SEM) equipped with a silicon drift energy dispersive X-ray spectroscopy (EDS) detector capable of detecting low Z elements such as B. A JEOL JEM2200FS aberration-corrected scanning transmission electron microscope (STEM) was used to obtain high-resolution images of the iridium boride nanoparticles.

### 8.3 Results and Discussion

The X-ray diffraction patterns of Ir and B powders used for mechanochemical synthesis of Ir-B compounds are shown in Figure 71A and Figure 72A, respectively. The Ir metal used as a

reactant for the synthesis was crystallized in cubic symmetry ( $Fm-3m$ , #225,  $a=3.8394$ ) and a boron source used in the synthesis was a mixture of amorphous and crystalline rhombohedral  $R-3m$  structure (#166,  $a=10.925$  and  $c=23.814$ ) phases. The representative scanning electron micrographs of the Ir and B powders are shown in Figure 71B and Figure 72B, respectively. The average particle size of Ir powder was measured to be 21  $\mu\text{m}$ , and the average particle size of B powder was 44  $\mu\text{m}$  where a bimodal distribution of grain sizes was present. High resolution high-angle annular dark-field (HAADF) STEM images with atomic resolution of B lattice fringes are shown in Figure 72C. The lamella type features appear as light stripes (Figure 72C) separated between each other with a less dense packing of B atoms in direction. The different ordering of the stripes in the nearby from each location can often be observed too (Figure 72C).

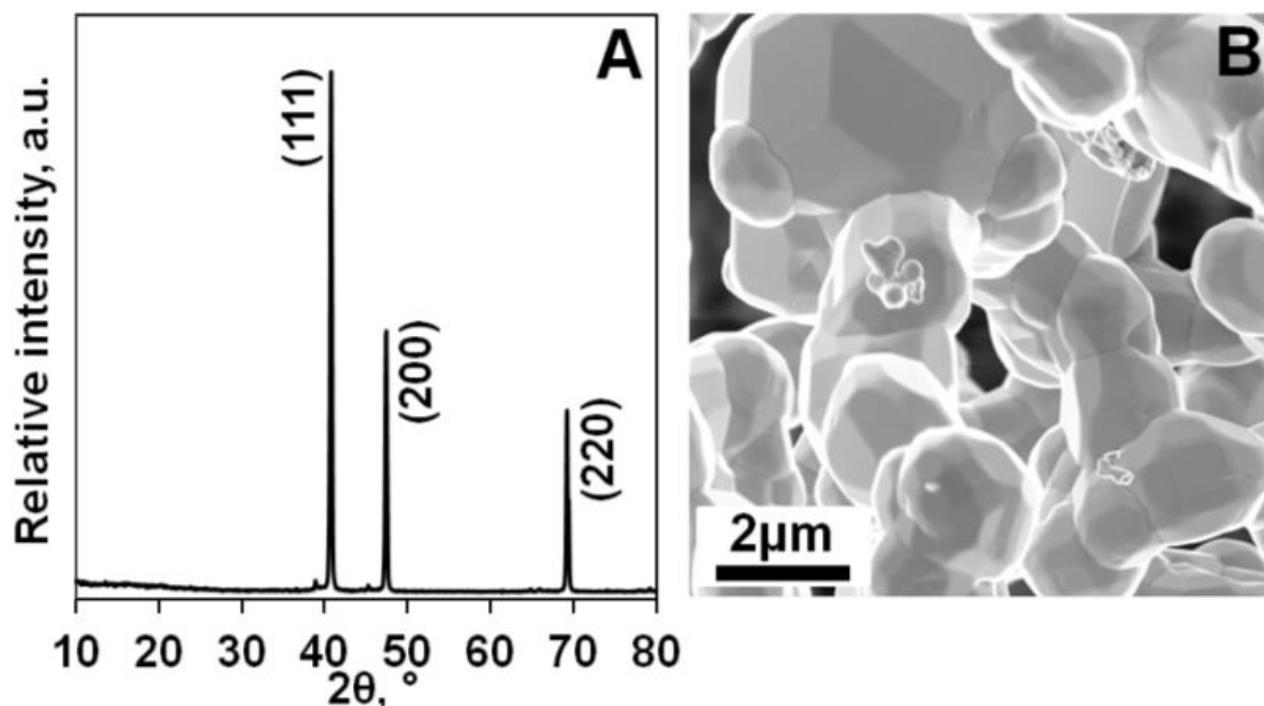


Figure 71: XRD pattern (A), SEM (B) micrographs of raw iridium powder.

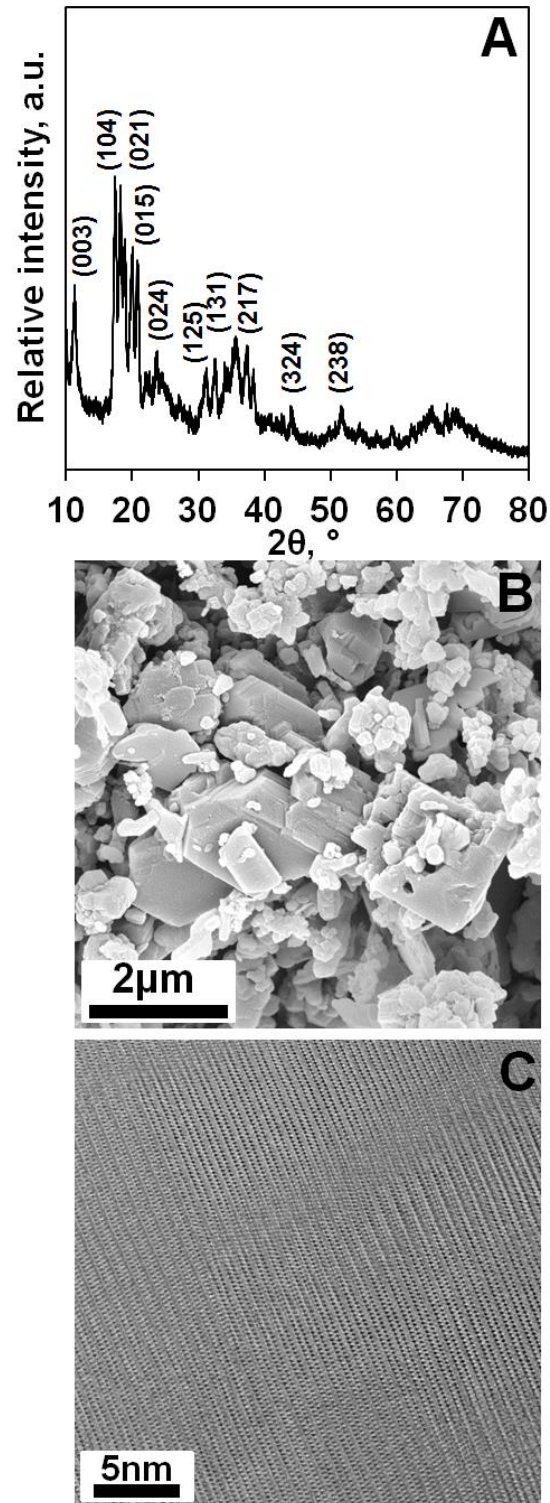


Figure 72: XRD pattern (A), SEM (B) and TEM (C) micrographs of raw boron powder.

The product of Ir and B powder mixture milling was analyzed by X-ray diffraction after high energy grinding of the defined periods of time (Figure 73). After the first 5 hours of grinding the XRD pattern of the Ir and B batch still showed the presence of significant amount of Ir metal (85.5 wt.%) but also small peaks associated with IrB<sub>1.1</sub> phase appeared. The estimated content of IrB<sub>1.1</sub> phase was equal to 14.5 wt.% as calculated by Rietveld refinement (Figure 73). After 10 hours of grinding the amount of IrB<sub>1.1</sub> phase increased significantly to 48 wt.%, while the amount of Ir phase decreased, but also the peaks associated with IrB<sub>1.35</sub> phase appeared. After 15 and 20 hours of milling the amount of Ir metal phase decreased dramatically, while the amount of IrB<sub>1.1</sub> and IrB<sub>1.35</sub> phases increased. After 30 hours of grinding the Ir peaks were completely absent and only Ir-B phases were present in the batch. As during the milling the severe plastic deformation become stored in the powder, a significant broadening of the peaks occurred leading to the peaks' overlapping and thus difficulties in the phase refinement. A significant broadening of the peaks prevented the authors from quantitative identification of the phases present by Rietveld refinement of the XRD patterns after 15 hours of milling as well as for a longer milling time, and therefore no definite presence of IrB<sub>2</sub> or other non-reported structures could be confirmed by XRD in the Ir-B system after mechanochemical synthesis.

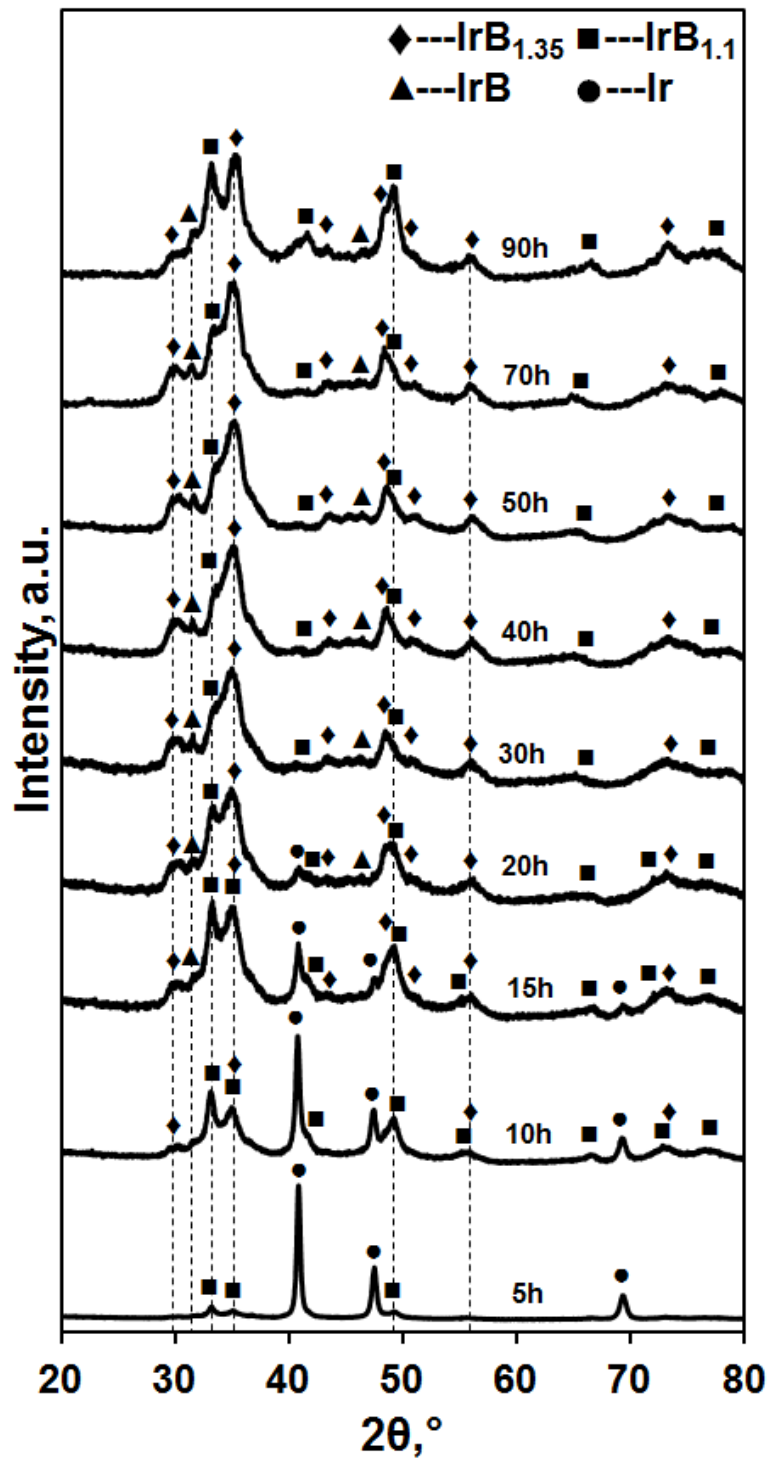


Figure 73: XRD patterns of Ir and B powder mixture at different milling time.

While it was difficult to identify the presence of hexagonal  $\text{IrB}_2$  structure after 90 hours of milling by XRD, however, the high resolution TEM analysis has definitely identified the formation of  $\text{IrB}_2$  nanoparticles that crystallized in the hexagonal structure. The micrograph of the typical aggregate of Ir-B powder after 90 hours of ball milling is shown in Figure 74A. It consists of the tiny crystallites and each of them being a single crystalline phase (Figure 74B and C). Some of the particles present in the Ir-B batch after 90 hours of ball milling resemble the structure of pure boron particles used as raw material for the milling. The micrograph with one of such particles is presented in Figure 74D. The particle in Figure 74D image most likely represents the small quantity of the non-reacted B. There were a number of tiny  $\sim 2\text{nm}$  particles found by TEM analysis that show a hexagonal symmetry (Figure 74E.). Such hexagonal shaped crystallites belong to  $\text{IrB}_2$  phase which is predicted to crystalize in hexagonal  $\text{ReB}_2$ - or  $\text{AlB}_2$ -type structures [43, 263]. The FFT pattern of the particle presented in Figure 74E show the correspondence to  $\text{AlB}_2$ -type  $\text{IrB}_2$  lattice oriented in  $[011]$  zone axis. At the same time, another Ir-B phase is also present in the batch in a significant quantity where FFT simulation revealed an existence of a tetragonal symmetry and it has been confirmed that the particle is  $\text{IrB}_{1.1}$  phase.



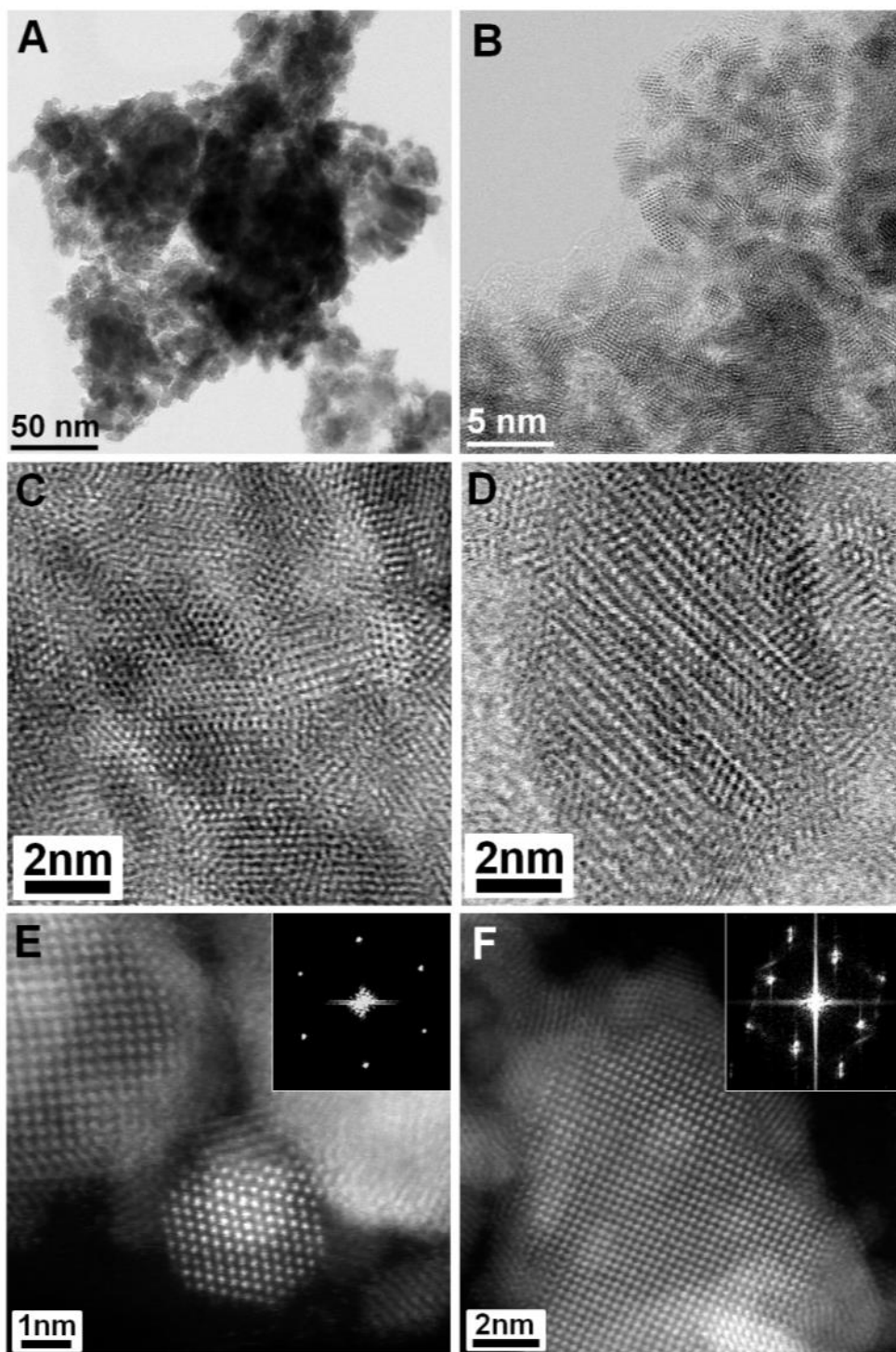


Figure 74: TEM of the Ir and B mixture after 90 hours of ball milling.

The SEM image of the Ir-B powder after 90 hours of high energy ball milling along with corresponding EDS pattern is shown in Figure 75. As one can see from Figure 75A the powder is agglomerated in the small almost spherical particles with sizes of agglomerates range in between 0.1 to 1.2  $\mu\text{m}$ . These agglomerates consist of the number of small aggregate and crystallites. While both Ir and B existence was confirmed by EDS analysis, a presence of rather significant quantities of oxygen was also detected (Figure 75B). Such presence of oxygen can play a detrimental role on the stability of Ir-B ceramics. It was hypothesized that by reacting with B atoms in the Ir-B lattice the oxygen can eventually alter the stoichiometry of Ir-B phase by forming boron monoxide (BO) and boron oxide ( $\text{B}_2\text{O}_3$ ) phases, with a corresponding decrease of the number of boron atoms retained in Ir-B structure. Similar stability issues in the presence of oxygen molecules were reported in another hard to synthesize metastable  $\text{OsB}_2$  ceramics also produced by mechanochemistry [221, 251]. In [251], it was found that oxygen molecules attack boron atoms in the  $\text{OsB}_2$  crystal forming highly volatile BO and  $\text{B}_2\text{O}_3$  oxides and, simultaneously, leaving boron vacancies in the  $\text{OsB}_2$  lattice upon B atoms departure. This formation of boron vacancies led to the stability problems with an excess of Os atoms in  $\text{OsB}_2$  lattice followed by segregation (precipitation) of metallic Os from the lattice. Similar reactions between oxygen and boron atoms in  $\text{IrB}_2$  lattice upon exposure of iridium diboride to  $\text{O}_2$  molecules might be one of the reasons why  $\text{IrB}_2$  structures have not been experimentally reported up to date and only  $\text{IrB}_{1.1}$  and  $\text{IrB}_{1.35}$  phases are known to exist, as both chemical and phase compositions of  $\text{IrB}_2$  phases are changed when boron atoms are removed from  $\text{IrB}_2$  lattice. A schematic of a possible removal process of B atoms from  $\text{ReB}_2$ -type or  $\text{AlB}_2$ -type  $\text{IrB}_2$  ceramics

is shown in Figure 76, which leads to the formation of thermodynamically stable IrB<sub>1.1</sub> and IrB<sub>1.35</sub> phases.

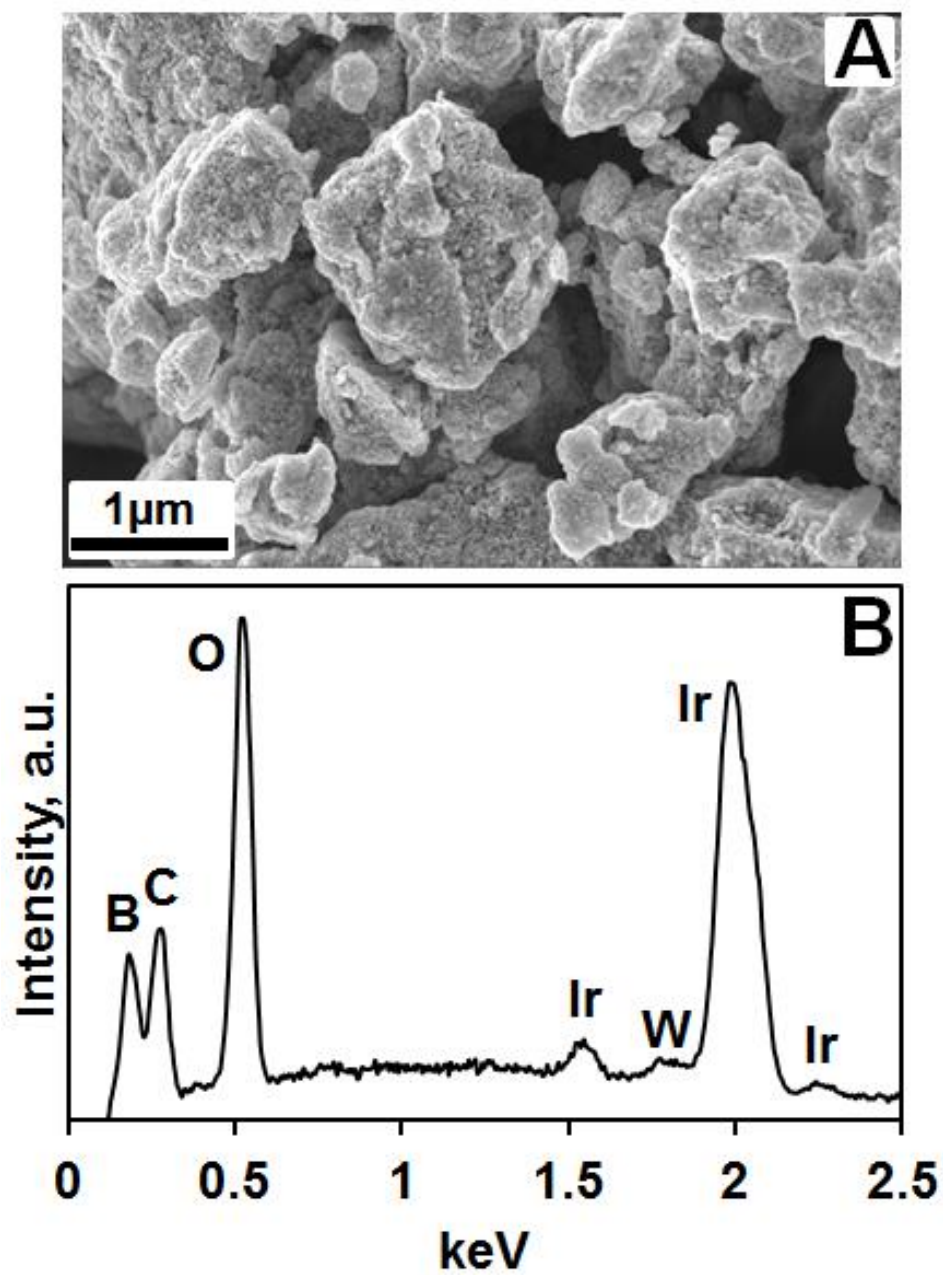


Figure 75: SEM (A) and EDS (B) of Ir and B powder mixture after 90 hours of ball milling.

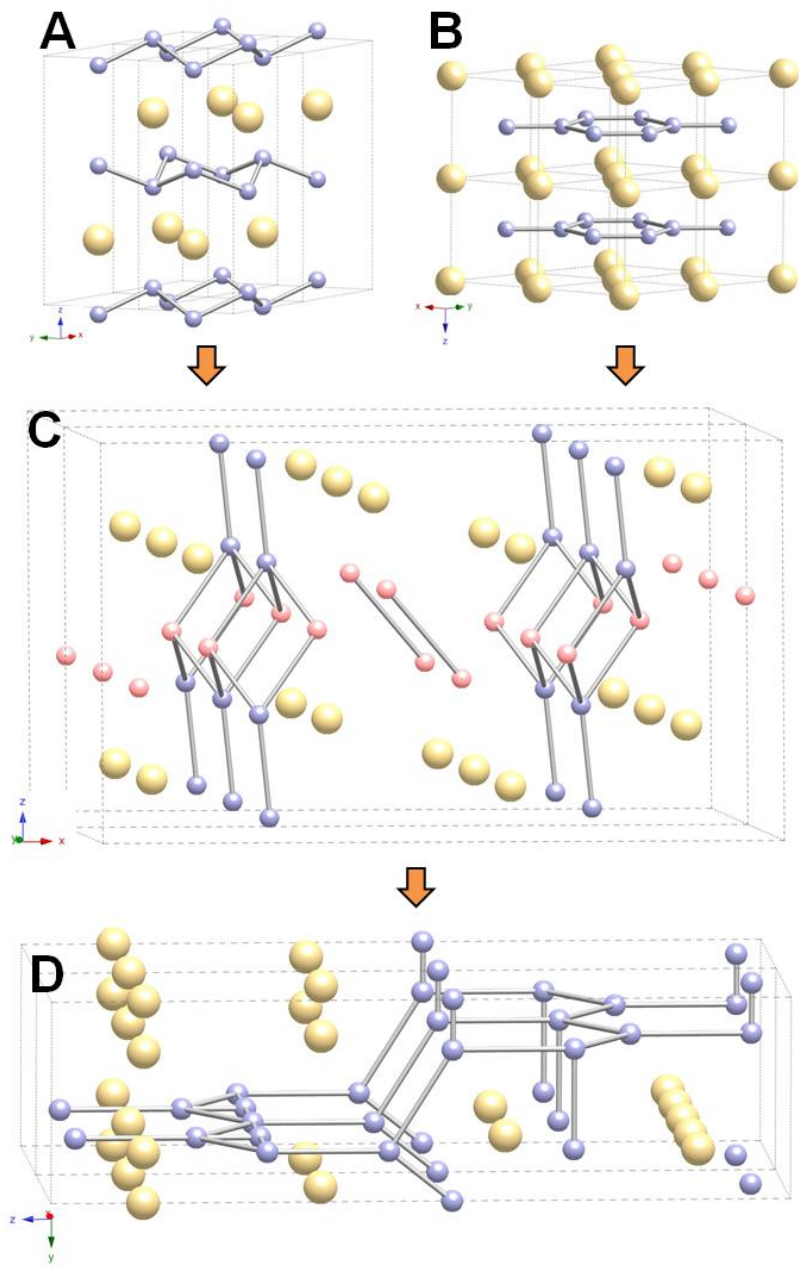


Figure 76: Schematic of oxidation of higher iridium borides to lower borides:  $\text{ReB}_2$ -type  $\text{IrB}_2$  (A),  $\text{AlB}_2$ -type  $\text{IrB}_2$  (B),  $\text{IrB}_{1.35}$  (C) and  $\text{IrB}_{1.1}$  (D). The larger yellow spheres are iridium atoms, and the smaller blue or pink spheres are boron atoms. The boron vacancies can only exist at the blue sphere sites.

After the Ir-B powder was ball-milled for 30 hours, the annealing of the powder was performed at  $1050\text{ }^\circ\text{C}$  *in vacuo* in a sealed quartz tube for 48 hours. After annealing, the phase

compositions of the powders were analyzed by X-ray diffraction with diffraction patterns of the products presented in Figure 77A. As one can see from Figure 77A, a mixture of four Ir-B phases is present in the batch after 30 hours of milling and 48 hours of annealing. Along with IrB<sub>1.35</sub> structure two previously non-reported ReB<sub>2</sub>-type and AlB<sub>2</sub>-type structures as well as a new orthorhombic iridium monoboride (IrB) structure have been identified. Rietveld refinement of the XRD pattern showed that the Ir-B batch after 30 hours of milling and 48 hours of annealing consisted of 73.1 wt% of IrB<sub>1.35</sub> phase, 7.2 wt% of ReB<sub>2</sub>-type and 4.6 wt% of AlB<sub>2</sub>-type IrB<sub>2</sub> phases, and 15.1 wt% of a new IrB phase. The lattice parameters of all four phases are presented in Table 10 along with the lattice parameters of the phases predicted in the literature. While IrB<sub>1.35</sub> and the two IrB<sub>2</sub> structures show a good correspondence between measured predicted lattice parameters, the IrB phase, while possess the structure predicted in [263], possesses lattice parameters significantly different from the ones predicted.

Table 10: Crystal structures and lattice parameters of iridium borides.

Compound	Structure	<i>a</i> (Å)	<i>b</i> (Å)	<i>c</i> (Å <sup>3</sup> )
IrB <sub>1.1</sub>	Tetragonal, I41/amd	2.807	2.807	10.245
IrB <sub>1.35</sub>	Monoclinic, C12/m1	10.524	2.897	6.085
IrB	Orthorhombic, Pnma	5.540	3.238	6.239
<i>P</i> <sub>1</sub> -IrB [263]	Orthorhombic, Pnma	4.428	2.870	7.021

After the Ir-B powder was ball milled for 90 hours, the annealing of the Ir-B powder was performed at 1050 °C *in vacuo* in a sealed quartz tube for 72 hours. After annealing, the phase compositions of the powders were analyzed by regular laboratory X-ray diffraction with diffraction patterns of the products presented in Figure 77B. As one can see from Figure 77B, a mixture of three Ir-B phases is present in the powder after 90 hours of milling and 72 hours of annealing. Along with IrB<sub>1.35</sub> and IrB<sub>1.1</sub> structure, the orthorhombic iridium monoboride (IrB) structure has also been identified. Rietveld refinement of the XRD pattern showed that the Ir-B

batch after 90 hours of milling and 72 hours of annealing consisted of 51.9 wt% of IrB<sub>1.35</sub> phase, 34.0 wt% of IrB<sub>1.1</sub> and 14.1 wt% of the new IrB phase.

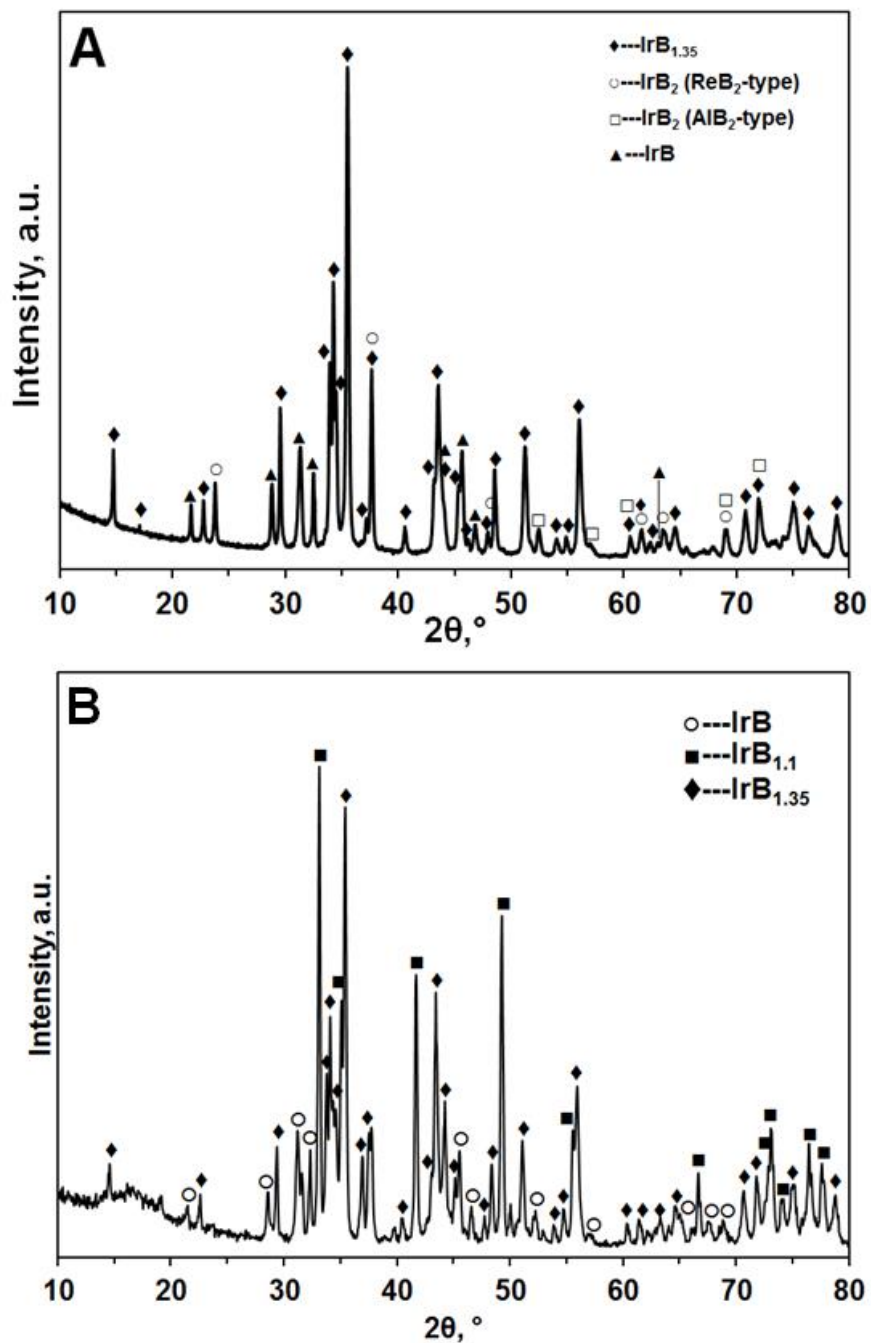


Figure 77: XRD patterns of Ir and B powder mixture after 30 hours of ball milling and 48 hours of annealing (A), and 90 hours of ball milling and 72 hours of annealing (B).

The TEM analysis was also performed on the Ir-B powder after 90 hours of ball milling and 72 hours of annealing at 1050°C *in vacuo*. After the annealing, the size of the crystallites grown significantly in comparison with the size of the powder after 90 hours of milling without annealing. The average crystallite size of the powder after annealing was  $60.7 \pm 18.2$  nm as measured from TEM Figure 78A. Not a single hexagonal shaped particle was observed in this batch, but what was found, that after annealing the segregation of Ir atoms either along the domain boundaries of the particles or in separate rounded clusters were observed (Figure 79). The segregation of individual Ir atoms along disordered highly defective stripes was revealed by high resolution TEM (Figure 79 A-D). While the bright field images of the areas of interest showed the appearance of such disordered thin and long areas inside the grains (Figure 79A and C), the use of Z contrast allowed to confirm the segregation of Ir individual atoms inside of these disordered long stripes (Figure 79 B and D) and determine the precise/exact location of each individual atom (Figure 80). Another example of the segregation of the triplets' Ir atoms along the defect is shown in Figure 81. In addition to such "line" segregation of Ir atoms, the metal clustering occurred (Figure 79 E and F). During the annealing the segregation of Ir into high concentration areas of individual atoms might create an opportunities for designing of excellent catalysts as such less than 2 nm nanoclusters might exhibit superior catalytic properties, as it is known that Ir metal is a very good catalyst for many chemical and electrochemical reactions.

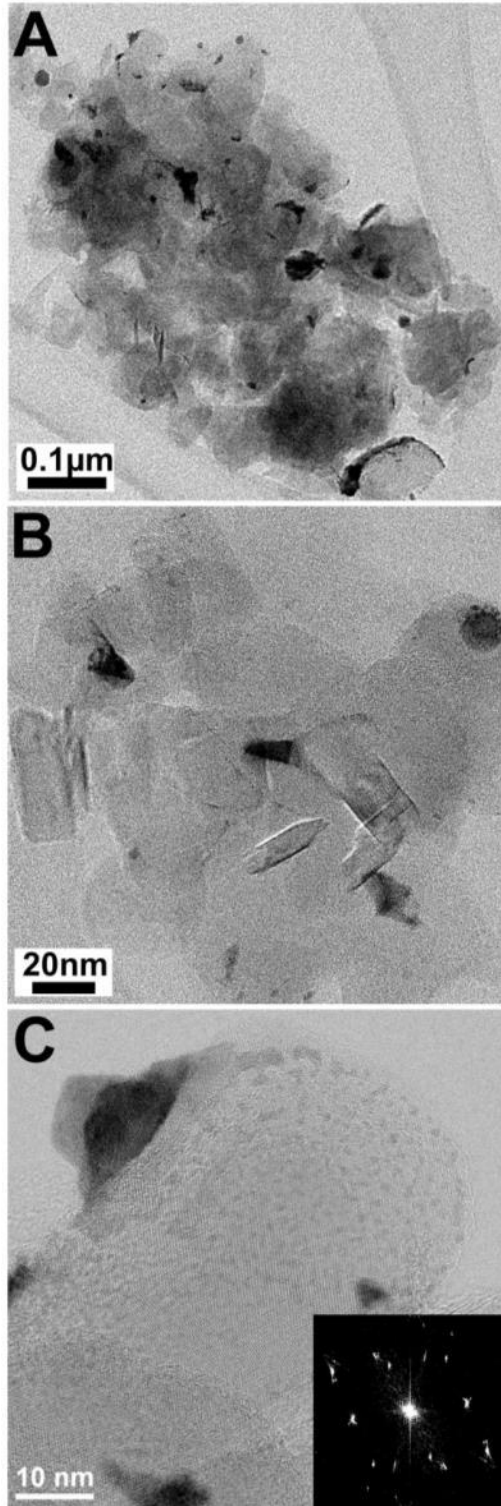


Figure 78: TEM of the Ir and B mixture after 90 hours of ball milling and 72 hours of annealing.



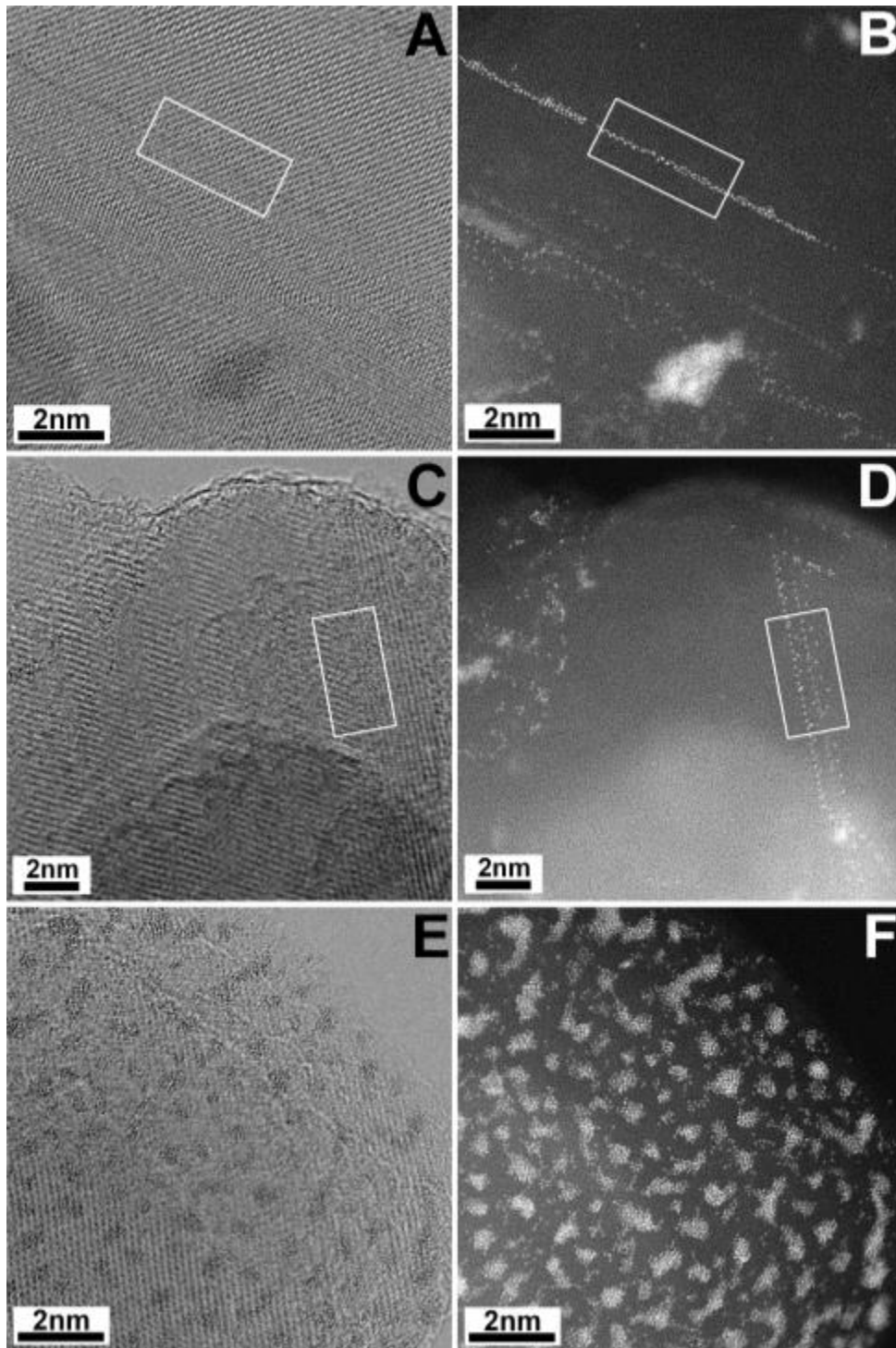


Figure 79: STEM images of the Ir and B mixture after 90 hours of ball milling and 72 hours of annealing. (A), (C) and (E) are bright field micrographs; (B), (D) and (F) are high angle annular dark field micrograph.

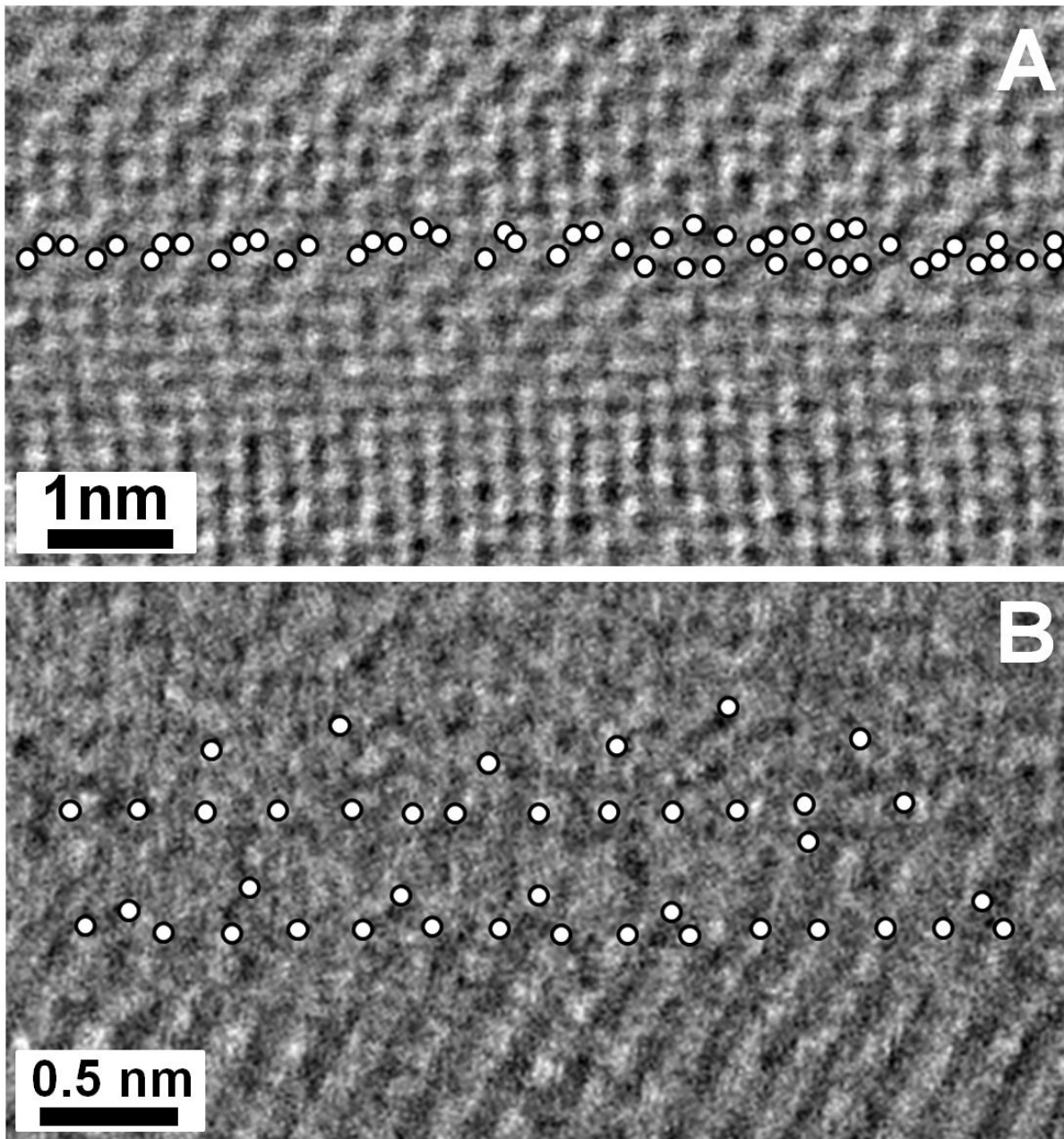


Figure 80: High resolution STEM bright field micrographs showing the identified locations of individual Ir atoms. (A) is an expanded view of the area highlighted with a box in Fig 9 (A); (B) is an expanded view of the area highlighted with a box in Fig 9 (C).

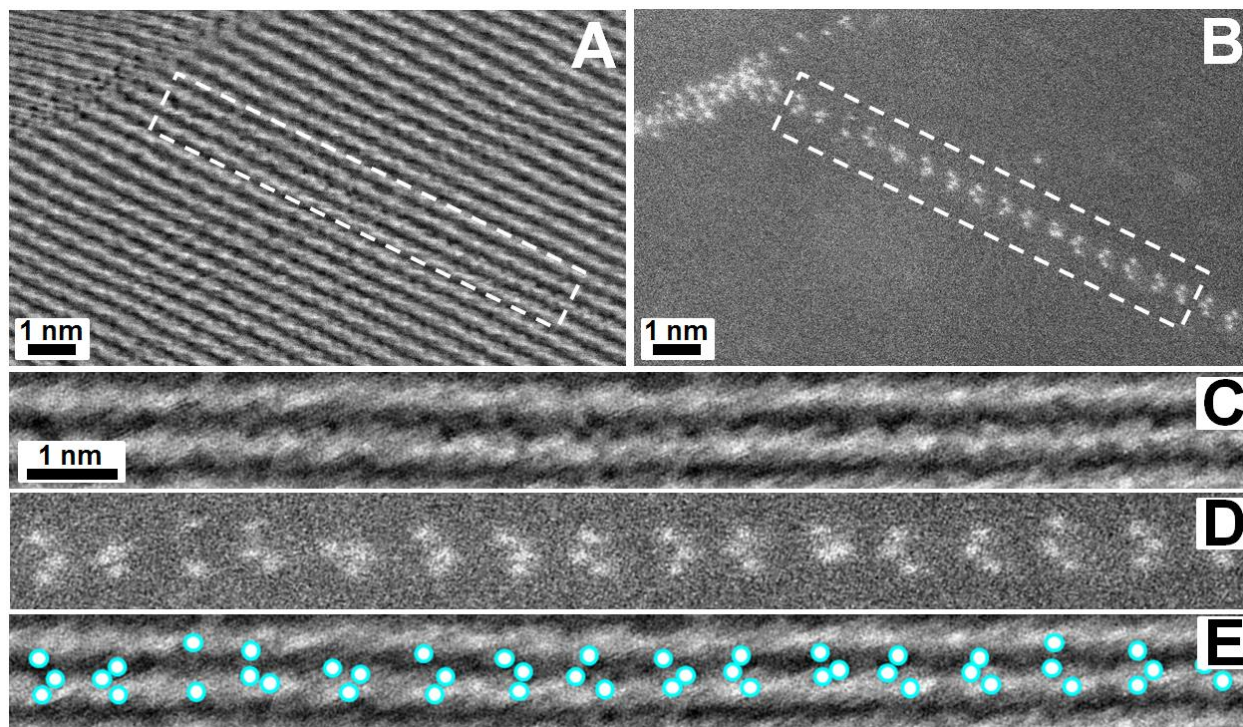


Figure 81: Ir atoms segregation along the disordered defective domain out of IrB<sub>2</sub> lattice after annealing at 1050 °C for 72 hours. Bright field high resolution STEM micrograph (A); high angle annular dark field STEM micrograph (B); magnified image of lattice fringes (C) of the area selected in (A); magnified image of triplets of Ir atoms (D) of the area selected in (B); the marked locations of Ir atoms where the central atom of the each triplet located inside of the lattice fringe (E). The magnification is identical for (C), (D) and (E) images

There is a high likelihood that such segregation of Ir into a separate lines or clusters' areas caused by the reaction of Ir-B phases with the oxygen present in atmosphere during annealing in small quantities. As it was established in a previous study of thermal stability of hexagonal OsB<sub>2</sub> [251], that oxygen molecules react with boron residing in OsB<sub>2</sub> lattice forming boron oxides, which lead to occurrence of sacrificial reactions between OsB<sub>2</sub> and O<sub>2</sub> leading to the reduction of OsB<sub>2</sub> to metallic Os and formation of B<sub>2</sub>O<sub>3</sub>. As both hexagonal OsB<sub>2</sub> and a mixture of Ir-B phases were produced by high energy ball milling, both of these powders have very high surface areas and they both should be highly susceptible to oxidation when in the presence of small quantities of oxygen. As in the sacrificial reaction between OsB<sub>2</sub> and O<sub>2</sub>, it is

thermodynamically favorable for oxygen to react with boron forming boron oxides, creating boron vacancies in  $\text{OsB}_2$  hexagonal lattice and eventually pushing Os atoms out of the structure. The similar effect of oxygen can exist in case when  $\text{IrB}_2$  hexagonal lattices are formed by mechanochemistry. The small quantities of oxygen present in the atmosphere during high temperature annealing cause chemical reactions with boron atoms residing in the  $\text{IrB}_2$  lattice, which lead to formation of boron oxides and at the same time cause a segregation of Ir in the highly defective and disordered lattice spaces. The differences in sacrificial reactions between hexagonal  $\text{OsB}_2$  and  $\text{IrB}_2$  might lie in the fact that  $\text{OsB}_2$  react with  $\text{O}_2$  more easily in comparison with  $\text{IrB}_2$  and, in addition,  $\text{OsB}_2$  does not have thermodynamically stable  $\text{OsB}_x$  (where  $1 < x < 2$ ) phases. Therefore the sacrificial reactions between  $\text{OsB}_2$  and  $\text{O}_2$  leads to the formation of Os metal in quantities detectable by X-ray analysis, while in the case of  $\text{IrB}_2$  the sacrificial reaction leads to 1) a formation of thermodynamically stable  $\text{IrB}_{1.1}$  and  $\text{IrB}_{1.35}$  phases and 2) a segregation of Ir atoms in a separate areas/clusters thus leaving behind the area with the lattice of pure boron. After such separation of Ir atoms in line defects in Ir-B phases, the large areas of the particles left without Ir metal atoms in the lattice, thus forming enriched boron or pure boron atoms domains, the microstructure of which closely resemble the microstructure of pure B powder (Figure 72C).

#### 8.4 Conclusions

The Ir-B ceramic nanopowder was synthesized by mechanochemical synthesis. Ir and B elemental powder were milled in a high energy ball milling for 90 hours using WC grinding media. After 30 hours of milling, 1 gram of powder was annealed at  $1050\text{ }^\circ\text{C}$  for 48 hours, and

another 1 gram of powder were annealed at 1050 °C for 72 hours to remove the strain induced by grinding and also to improve the crystallinity of the powder. The products of solid state reactions between Ir metal and B powders before and after annealing were analyzed by X-ray diffraction and TEM.

The formation of new orthorhombic IrB, AlB<sub>2</sub>-type and ReB<sub>2</sub>-type of IrB<sub>2</sub> after 30 hours of ball milling and 48 hours of annealing were identified by XRD. While only IrB<sub>1.35</sub>, IrB<sub>1.1</sub> and IrB phases were identified by XRD after 90 hours of grinding, however, the presence of AlB<sub>2</sub>-type IrB<sub>2</sub> particles was confirmed by high resolution TEM. The presence of O impurities was confirmed by EDS analysis in the powder after 90 hours of milling and such oxygen impurities were identified as responsible for leaching of B atoms from the IrB<sub>2</sub> lattice and formation of Ir-B phases with lower than 2 content of boron. The more thermodynamically stable phases, where oxygen is present, are IrB<sub>1.35</sub>, IrB<sub>1.1</sub> and IrB. After annealing of the synthesized powder the IrB<sub>1.35</sub>, IrB<sub>1.1</sub> and IrB phases were identified as present in the batch. The significant increase of the particle size of the powder was detected that the average particle size before annealing was equal to  $9.0 \pm 2.2$  nm, but after annealing for 72 hours it increased to  $60.7 \pm 18.2$  nm. The Ir segregation along the disordered domains was observed forming the rows of Ir single atoms in between boron lattice, Ir segregation in separate clusters was also confirmed. It is expected that such Ir segregated out of boron lattice Ir-B nanopowders could be a very active catalyst material that can be utilized in many chemical and electrochemical reactions used for example in combustion and fuel cells to promote oxygen reduction reactions or fuel oxidation process.

## CHAPTER 9: CONCLUSIONS AND FUTURE WORK

Great success has been achieved in the synthesis of Re, Os and Ir diborides with mechanochemical approach, i.e., high energy ball milling. It has shown that  $\text{ReB}_2$  powders can be synthesized mechanochemically from elemental crystalline Re and amorphous B powders in the stoichiometric 1:2 ratio. A complete reaction was realized after 70-80 hours of milling in a SPEX-8000 high energy ball mill. By using this approach we have eliminated the need for excess boron reported by others. The synthesized powders were agglomerates of small crystallites as evidenced by SEM. High resolution TEM showed that the material had a clear crystalline structure. It is our expectation that powders free of excess of boron will facilitate a thorough understanding of the role composition on the hardness and elastic moduli of  $\text{ReB}_2$  ceramics. This is also a scalable solution that will ultimately allow larger quantities of this material to be prepared.

The  $\text{ReB}_2$ -type hexagonal  $\text{OsB}_2$  structure also has been mechanochemically synthesized from elemental B and Os powder with shear stress contributed significantly to the synthesis of the new high-pressure phase. The lattice parameters of the new phase were measured to be  $a=2.916\text{\AA}$  and  $c=7.376\text{\AA}$ . The production of hexagonal  $\text{OsB}_2$  by mechanochemical means demonstrates the value of alternative synthetic methods for producing new materials. The phase stability and thermal behavior of novel hexagonal  $\text{ReB}_2$ -type  $\text{OsB}_2$  powder was studied in the broad temperature range upon heating up to  $876\text{ }^\circ\text{C}$  under Ar and cooling to  $-225\text{ }^\circ\text{C}$  *in vacuo*. It was found that the *h*- $\text{OsB}_2$  was the major phase in the powder after mechanochemical synthesis with a small quantity ( $\sim 5\text{ wt}\%$ ) of *h*- $\text{Os}_2\text{B}_3$  also present at room temperature before heating

experiments.  $\text{Os}_2\text{B}_3$  was identified as an intermediate product of mechanochemical synthesis, where presence of crystalline B in the reagent used for mechanochemical synthesis prevented the formation of pure final product  $h\text{-OsB}_2$  and small quantities of  $\text{Os}_2\text{B}_3$  compound formed during milling. The formation of  $\text{Os}_2\text{B}_3$  and OsB phases, but not  $h\text{-OsB}_2$ , was confirmed when coarse crystalline  $^{11}\text{B}$  powder was used as a raw B material in high energy ball milling instead of a mixture of amorphous and crystalline B. It was shown that, once synthesized, the  $h\text{-OsB}_2$  phase was stable upon cooling to  $-225^\circ\text{C}$  where no structure changes were observed and linear thermal expansion was measured. However, upon heating, the sacrificial chemical reaction between  $h\text{-OsB}_2$  powder and traces of oxygen and/or water vapor in the heating chamber took place, where B atoms reacted with  $\text{O}_2$  molecules leaving the  $h\text{-OsB}_2$  lattice, forming  $\text{B}_2\text{O}_3$ . This, in turn, led to the formation of boron vacancies in  $\text{OsB}_2$  lattice producing overall B deficiencies and precipitation of a metallic Os phase detectable by X-ray diffraction. Such phase changes lead to the lattice shrinkage and what appeared to be a negative coefficient of thermal expansion of  $h\text{-OsB}_2$  in the  $a$  crystallographic direction. As the changes brought to the shrinkage/expansion of the  $h\text{-OsB}_2$  lattice were caused not only by the change in the temperature, but also by the change in the stoichiometry of the compound, thus we termed it “thermochemical expansion” to emphasize the effects of both temperature and stoichiometry on the phase changes. In addition, the OsB phase was detected upon cooling of the powder. The phase changes of  $h\text{-OsB}_2$  were the reason for the appearance of very different room temperature lattice parameters of  $h\text{-OsB}_2$  phase after heating experiments. High values of coefficient of thermochemical expansion of  $h\text{-OsB}_2$ , especially at 700- 800 °C temperature range, might cause stability and reliability problem for practical applications of this novel material recently synthesized by mechanochemistry.



The thermal stability of novel hexagonal  $\text{ReB}_2$ -type  $\text{OsB}_2$  phase upon heating in 4 vol. %  $\text{H}_2/\text{Ar}$  reforming gas was investigated. It was found that the  $\text{OsB}_2$  was very easily and totally reduced to the pure Os metallic phase in the 375-725°C temperature range, where the first peaks of metallic Os were detected at 450°C and the  $h$ - $\text{OsB}_2$  phase completely disappeared upon heating above 725°C. Although significant negative coefficient of thermochemical expansion of  $\text{OsB}_2$  phase was observed, it can be explained by presence of oxygen in the thermal chamber. The purity of synthesized hexagonal  $\text{OsB}_2$  was studied with secondary ion mass spectroscopy. Metal impurities such as Li, Mg, Al, Si, K, Cr, Fe, Co and Ce, as well as non-metal impurities such as F, Cl, O and H were observed. The presence of O and H suggested that the powder was partially oxidized and absorbed moisture. This is consistent with the appearance of the 2 peaks in first heating cycle of the DSC curve, due to the evaporation of water and decomposition of boric acid. The weight loss part in the TG curve is due to evaporation of water, and the weight gain part is due to the oxidation of the powder. The sintering process of the hexagonal  $\text{OsB}_2$  particles has also been studied by *in situ* high temperature TEM. The thermal expansion of hexagonal  $\text{OsB}_2$  was reflected in the expansion of the lattice fringes.

The  $\text{ReB}_2$ -type  $\text{OsB}_2$  powder synthesized by mechanochemistry was densified by spark plasma sintering for the first time. The obtained bulk material contained a significant amount of porosity and, also, it was discovered that during the direct current sintering the transformation from hexagonal ( $P63/mmc$ ) to orthorhombic ( $Pmnm$ ) structure has occurred. Thus, the ceramics after sintering contained 26.9% of porosity and a mixture of ~80 wt% hexagonal and ~20 wt% of orthorhombic phases as it was detected both by X-ray and EBSD analysis.



The average grain size of the OsB<sub>2</sub> ceramics after sintering was equal to 0.56 μm and the TEM analysis allowed to identify the hexagonal and orthorhombic grains. It was discovered that much higher concentration of B was observed within separate locations. The EDS maps showed that the concentrations of Os and B do not coincide, and there were separate areas found on the maps that were enriched in B content, while Os were practically absent in those locations. At the same time, there were other areas which showed Os deficiency, but they were enriched in oxygen. It was suggested that such boron enriched area might contain rhombohedral B, while those areas enriched in O might be the residues of B<sub>2</sub>O<sub>3</sub> or BO phase.

An attempt was made to probe the mechanical behavior of the SPSed OsB<sub>2</sub> ceramics using nanoindentation. It was calculated that the average hardness and Young's modulus of the indented material was equal to 31±9 GPa and 574±112 GPa, respectively, while the highest value of hardness and Young's modulus measured reached 45 GPa and 773 GPa, respectively. Such differences could be explained that the indentations have mostly been made in separate grains thus each individual grain's crystallographic orientation affected the measured values. However, because of a significant number of the indentations have been made in different grains, the average values might lie rather close to the true values of hardness and Young's modulus of the ceramic. It was also measured that certain area of the material exhibited lower values of hardness and Young's modulus.

The produced bulk OsB<sub>2</sub> ceramics was not dense and homogeneous and its mechanical properties varied significantly depending on the location of indentation. Therefore, the conclusion is that it is possible to retain metastable high-pressure ReB<sub>2</sub>-type hexagonal OsB<sub>2</sub> during sintering and the potential for the structure to exhibit superior hardness and stiffness is

rather high. More studies are needed to find and optimize the sintering regime to produce dense and homogeneous hexagonal  $\text{OsB}_2$ , which would exhibit superior hardness and stiffness.

The Ir-B ceramic nanopowder was synthesized by mechanochemical synthesis as well. Ir and B elemental powder were milled in a high energy ball milling for 90 hours using WC grinding media. The formation of new orthorhombic IrB,  $\text{AlB}_2$ -type and  $\text{ReB}_2$ -type of  $\text{IrB}_2$  after 30 hours of ball milling and 48 hours of annealing were identified by XRD. While only  $\text{IrB}_{1.35}$ ,  $\text{IrB}_{1.1}$  and IrB phases were identified by XRD after 90 hours of grinding, however, the presence of  $\text{AlB}_2$ -type  $\text{IrB}_2$  particles was confirmed by high resolution TEM. The presence of O impurities was observed by EDS analysis in the powder after 90 hours of milling and such oxygen impurities were identified as responsible for leaching of B atoms from the  $\text{IrB}_2$  lattice and formation of Ir-B phases with lower than 2 content of boron. The more thermodynamically stable phases, where oxygen is present, are  $\text{IrB}_{1.35}$ ,  $\text{IrB}_{1.1}$  and IrB. After annealing of the synthesized powder the  $\text{IrB}_{1.35}$ ,  $\text{IrB}_{1.1}$  and IrB phases were identified as present in the batch. The significant increase of the particle size of the powder was detected that the average particle size before annealing was equal to  $9.0 \pm 2.2$  nm, but after annealing for 72 hours it increased to  $60.7 \pm 18.2$  nm. The Ir segregation along the disordered domains was observed forming the rows of Ir single atoms in between boron lattice, Ir segregation in separate clusters was also confirmed. It is expected that such Ir segregated out of boron lattice Ir-B nanopowders could be a very active catalyst material that can be utilized in many chemical and electrochemical reactions used for example in combustion and fuel cells to promote oxygen reduction reactions or fuel oxidation process.

The production of new hexagonal  $\text{OsB}_2$ ,  $\text{IrB}_2$  and the orthorhombic  $\text{IrB}$  by mechanochemical means demonstrated the value of alternative synthetic methods for producing new materials. It is believed that other transition metal boride may be synthesized with this method. Thus, it is very worthwhile to try this method in the synthesis of other predicted materials in the future. One of the biggest disadvantages of the high energy ball milling method is that it introduces contamination from milling vial or milling media. Besides, it consumes a lot of time and raw materials by trial and error to find out the appropriate milling parameters, such as milling time, ball to powder ratio, number of balls, etc. Thus, these problems are to be solved in the future. Since the new hexagonal  $\text{OsB}_2$  has been produced, which has the same crystal structure as  $\text{ReB}_2$  but only slightly different lattice parameters, it is possible to make hexagonal Re-Os diboride solid solution. The mechanical properties of the solid solution may be more superior to any of the osmium or rhenium diborides. While the segregation of the Ir atoms in the iridium borides was observed, the catalytic behavior of the materials may be very interesting because the individually scattered iridium atoms should have very high catalytic activity.

## APPENDIX A: COPYRIGHT PERMISSION LETTERS

---

### CAMBRIDGE UNIVERSITY PRESS LICENSE TERMS AND CONDITIONS

Oct 18, 2014

---

---

This is a License Agreement between Zhilin Xie ("You") and Cambridge University Press ("Cambridge University Press") provided by Copyright Clearance Center ("CCC"). The license consists of your order details, the terms and conditions provided by Cambridge University Press, and the payment terms and conditions.

**All payments must be made in full to CCC. For payment instructions, please see information listed at the bottom of this form.**

License Number	3492280694875
License date	Oct 18, 2014
Licensed content publisher	Cambridge University Press
Licensed content publication	Journal of Materials Research
Licensed content title	Mechanochemical synthesis of ReB <sub>2</sub> powder
Licensed content author	Nina Orlovskaya, Zhilin Xie, Mikhail Klimov, Helge Heinrich, David Restrepo, Richard Blair and Challapalli Suryanarayana
Licensed content date	Aug 26, 2011
Volume number	26
Issue number	21
Start page	2772
End page	2779
Type of Use	Dissertation/Thesis
Requestor type	Author
Portion	Full article
Author of this Cambridge University Press article	Yes
Author / editor of the new work	Yes
Order reference number	None
Territory for reuse	World
Title of your thesis / dissertation	Rhenium, Osmium and Iridium Diborides by Mechanochemistry: Synthesis, Structure, Thermal Stability and Mechanical Properties
Expected completion date	Dec 2014
Estimated size(pages)	300
Billing Type	Invoice
Billing address	1713 Tealbriar Ave. OVIEDO, FL 32765 United States
TAX (0.00%)	0.00 USD
Total	0.00 USD
Terms and Conditions	

**ELSEVIER LICENSE  
TERMS AND CONDITIONS**

Oct 18, 2014

---

This is a License Agreement between Zhilin Xie ("You") and Elsevier ("Elsevier") provided by Copyright Clearance Center ("CCC"). The license consists of your order details, the terms and conditions provided by Elsevier, and the payment terms and conditions.

**All payments must be made in full to CCC. For payment instructions, please see information listed at the bottom of this form.**

Supplier	Elsevier Limited The Boulevard, Langford Lane Kidlington, Oxford, OX5 1GB, UK
Registered Company Number	1982084
Customer name	Zhilin Xie
Customer address	1713 Tealbriar Ave. OVIEDO, FL 32765
License number	3492231081341
License date	Oct 18, 2014
Licensed content publisher	Elsevier
Licensed content publication	Journal of Solid State Chemistry
Licensed content title	Novel high pressure hexagonal OsB <sub>2</sub> by mechanochemistry
Licensed content author	Zhilin Xie, Moritz Graule, Nina Orlovskaya, E. Andrew Payzant, David A. Cullen, Richard G. Blair
Licensed content date	July 2014
Licensed content volume number	215
Licensed content issue number	n/a
Number of pages	6
Start Page	16
End Page	21
Type of Use	reuse in a thesis/dissertation
Portion	full article
Format	both print and electronic
Are you the author of this Elsevier article?	Yes
Will you be translating?	No
Title of your thesis/dissertation	Rhenium, Osmium and Iridium Diborides by Mechanochemistry: Synthesis, Structure, Thermal Stability and Mechanical Properties
Expected completion date	Dec 2014
Estimated size (number of pages)	300
Elsevier VAT number	GB 494 6272 12
Permissions price	0.00 USD

**ELSEVIER LICENSE  
TERMS AND CONDITIONS**

Oct 18, 2014

---


This is a License Agreement between Zhilin Xie ("You") and Elsevier ("Elsevier") provided by Copyright Clearance Center ("CCC"). The license consists of your order details, the terms and conditions provided by Elsevier, and the payment terms and conditions.

**All payments must be made in full to CCC. For payment instructions, please see information listed at the bottom of this form.**

Supplier	Elsevier Limited The Boulevard, Langford Lane Kidlington, Oxford, OX5 1GB, UK
Registered Company Number	1982084
Customer name	Zhilin Xie
Customer address	1713 Tealbriar Ave. OVIEDO, FL 32765
License number	3492280856298
License date	Oct 18, 2014
Licensed content publisher	Elsevier
Licensed content publication	Journal of Solid State Chemistry
Licensed content title	Thermal stability of hexagonal OsB <sub>2</sub>
Licensed content author	Zhilin Xie, Richard G. Blair, Nina Orlovskaya, David A. Cullen, E. Andrew Payzant
Licensed content date	November 2014
Licensed content volume number	219
Licensed content issue number	n/a
Number of pages	10
Start Page	210
End Page	219
Type of Use	reuse in a thesis/dissertation
Intended publisher of new work	other
Portion	full article
Format	both print and electronic
Are you the author of this Elsevier article?	Yes
Will you be translating?	No
Title of your thesis/dissertation	Rhenium, Osmium and Iridium Diborides by Mechanochemistry: Synthesis, Structure, Thermal Stability and Mechanical Properties
Expected completion date	Dec 2014
Estimated size (number of pages)	300
Elsevier VAT number	GB 494 6272 12
Permissions price	0.00 USD
VAT/Local Sales Tax	0.00 USD / 0.00 GBP

## Advances in applied ceramics : structural, functional and bioceramics

**Order detail ID:** 65925800  
**Order License Id:** 3503200522913  
**ISSN:** 1743-6753  
**Publication Type:** Journal  
**Volume:**  
**Issue:**  
**Start page:**  
**Publisher:** Maney Publishing  
**Author/Editor:** Institute of Materials, Minerals, and Mining

**Permission Status:**  **Granted**

**Permission type:** Republish or display content  
**Type of use:** Thesis/Dissertation

[Hide details](#)

<b>Requestor type</b>	Author of requested content
<b>Format</b>	Print, Electronic
<b>Portion</b>	chapter/article
<b>Title or numeric reference of the portion(s)</b>	Hexagonal OsB2 reduction upon heating in H2 containing environment
<b>Title of the article or chapter the portion is from</b>	Hexagonal OsB2 reduction upon heating in H2 containing environment
<b>Editor of portion(s)</b>	N/A
<b>Author of portion(s)</b>	Z. L. Xie; R. G. Blair; N. Orlovskaya; E. A. Payzant
<b>Volume of serial or monograph</b>	N/A
<b>Issue, if republishing an article from a serial</b>	N/A
<b>Page range of portion</b>	
<b>Publication date of portion</b>	2014
<b>Rights for</b>	Main product
<b>Duration of use</b>	Life of current edition
<b>Creation of copies for the disabled</b>	no
<b>With minor editing privileges</b>	no
<b>For distribution to</b>	Worldwide
<b>In the following language(s)</b>	Original language of publication
<b>With incidental promotional use</b>	no
<b>Lifetime unit quantity of new product</b>	Up to 499
<b>Made available in the following markets</b>	Education
<b>The requesting person/organization</b>	Zhilin Xie
<b>Order reference number</b>	
<b>Author/Editor</b>	Zhilin Xie
<b>The standard identifier</b>	N/A
<b>The proposed price</b>	N/A
<b>Title</b>	Rhenium, Osmium and Iridium Diborides by Mechanochemistry: Synthesis, Structure, Thermal Stability and Mechanical Properties

---

**ELSEVIER LICENSE  
TERMS AND CONDITIONS**

Nov 05, 2014

---

This is a License Agreement between Zhilin Xie ("You") and Elsevier ("Elsevier") provided by Copyright Clearance Center ("CCC"). The license consists of your order details, the terms and conditions provided by Elsevier, and the payment terms and conditions.

**All payments must be made in full to CCC. For payment instructions, please see information listed at the bottom of this form.**

Supplier	Elsevier Limited The Boulevard, Langford Lane Kidlington, Oxford, OX5 1GB, UK
Registered Company Number	1982084
Customer name	Zhilin Xie
Customer address	1713 Tealbriar Ave. OVIEDO, FL 32765
License number	3502640105017
License date	Nov 05, 2014
Licensed content publisher	Elsevier
Licensed content publication	International Journal of Refractory Metals and Hard Materials
Licensed content title	Design of hard crystals
Licensed content author	J.J. Gilman, R.W. Cumberland, R.B. Kaner
Licensed content date	January–March 2006
Licensed content volume number	24
Licensed content issue number	1-2
Number of pages	5
Start Page	1
End Page	5
Type of Use	reuse in a thesis/dissertation
Intended publisher of new work	other
Portion	figures/tables/illustrations
Number of figures/tables/illustrations	1
Format	both print and electronic
Are you the author of this Elsevier article?	No
Will you be translating?	No
Title of your thesis/dissertation	Rhenium, Osmium and Iridium Diborides by Mechanochemistry: Synthesis, Structure, Thermal Stability and Mechanical Properties
Expected completion date	Dec 2014
Estimated size (number of pages)	300
Elsevier VAT number	GB 494 6272 12



**ELSEVIER LICENSE  
TERMS AND CONDITIONS**

Nov 05, 2014

---

This is a License Agreement between Zhilin Xie ("You") and Elsevier ("Elsevier") provided by Copyright Clearance Center ("CCC"). The license consists of your order details, the terms and conditions provided by Elsevier, and the payment terms and conditions.

**All payments must be made in full to CCC. For payment instructions, please see information listed at the bottom of this form.**

Supplier	Elsevier Limited The Boulevard, Langford Lane Kidlington, Oxford, OX5 1GB, UK
Registered Company Number	1982084
Customer name	Zhilin Xie
Customer address	1713 Tealbriar Ave. OVIEDO, FL 32765
License number	3502631257315
License date	Nov 05, 2014
Licensed content publisher	Elsevier
Licensed content publication	Journal of Alloys and Compounds
Licensed content title	Preparation of ReB <sub>2</sub> single crystals by the floating zone method
Licensed content author	Shigeki Otani, Takashi Aizawa, Yoshio Ishizawa
Licensed content date	5 May 1997
Licensed content volume number	252
Licensed content issue number	1-2
Number of pages	3
Start Page	L19
End Page	L21
Type of Use	reuse in a thesis/dissertation
Intended publisher of new work	other
Portion	figures/tables/illustrations
Number of figures/tables/illustrations	1
Format	both print and electronic
Are you the author of this Elsevier article?	No
Will you be translating?	No
Title of your thesis/dissertation	Rhenium, Osmium and Iridium Diborides by Mechanochemistry: Synthesis, Structure, Thermal Stability and Mechanical Properties
Expected completion date	Dec 2014
Estimated size (number of pages)	300
Elsevier VAT number	GB 494 6272 12

---

**THE AMERICAN ASSOCIATION FOR THE ADVANCEMENT OF SCIENCE LICENSE  
TERMS AND CONDITIONS**

Nov 06, 2014

---

This is a License Agreement between Zhilin Xie ("You") and The American Association for the Advancement of Science ("The American Association for the Advancement of Science") provided by Copyright Clearance Center ("CCC"). The license consists of your order details, the terms and conditions provided by The American Association for the Advancement of Science, and the payment terms and conditions.

**All payments must be made in full to CCC. For payment instructions, please see information listed at the bottom of this form.**

License Number	3503101475300
License date	Nov 06, 2014
Licensed content publisher	The American Association for the Advancement of Science
Licensed content publication	Science
Licensed content title	Synthesis of Ultra-Incompressible Superhard Rhenium Diboride at Ambient Pressure
Licensed content author	Hsiu-Ying Chung, Michelle B. Weinberger, Jonathan B. Levine, Abby Kavner, Jenn-Ming Yang, Sarah H. Tolbert, Richard B. Kaner
Licensed content date	Apr 20, 2007
Volume number	316
Issue number	5823
Type of Use	Thesis / Dissertation
Requestor type	Scientist/individual at a research institution
Format	Print and electronic
Portion	Figure
Number of figures/tables	1
Order reference number	None
Title of your thesis / dissertation	Rhenium, Osmium and Iridium Diborides by Mechanochemistry: Synthesis, Structure, Thermal Stability and Mechanical Properties
Expected completion date	Dec 2014
Estimated size(pages)	300
Total	0.00 USD

Terms and Conditions

**American Association for the Advancement of Science TERMS AND CONDITIONS**

**SPRINGER LICENSE  
TERMS AND CONDITIONS**

Nov 06, 2014

---

---

This is a License Agreement between Zhilin Xie ("You") and Springer ("Springer") provided by Copyright Clearance Center ("CCC"). The license consists of your order details, the terms and conditions provided by Springer, and the payment terms and conditions.

**All payments must be made in full to CCC. For payment instructions, please see information listed at the bottom of this form.**

License Number	3503120347495
License date	Nov 06, 2014
Licensed content publisher	Springer
Licensed content publication	Journal of Thermal Analysis and Calorimetry
Licensed content title	Phase diagram investigation and thermodynamic study of Os-B system
Licensed content author	L. Stuparević
Licensed content date	Jan 1, 2004
Volume number	76
Issue number	3
Type of Use	Thesis/Dissertation
Portion	Figures
Author of this Springer article	No
Country of republication	other
Order reference number	None
Original figure numbers	Figure 7
Title of your thesis / dissertation	Rhenium, Osmium and Iridium Diborides by Mechanochemistry: Synthesis, Structure, Thermal Stability and Mechanical Properties
Expected completion date	Dec 2014
Estimated size(pages)	300
Total	0.00 USD
Terms and Conditions	

**ELSEVIER LICENSE  
TERMS AND CONDITIONS**

Nov 06, 2014

---

This is a License Agreement between Zhilin Xie ("You") and Elsevier ("Elsevier") provided by Copyright Clearance Center ("CCC"). The license consists of your order details, the terms and conditions provided by Elsevier, and the payment terms and conditions.

**All payments must be made in full to CCC. For payment instructions, please see information listed at the bottom of this form.**

Supplier	Elsevier Limited The Boulevard, Langford Lane Kidlington, Oxford, OX5 1GB, UK
Registered Company Number	1982084
Customer name	Zhilin Xie
Customer address	1713 Tealbriar Ave. OVIEDO, FL 32765
License number	3503130163445
License date	Nov 06, 2014
Licensed content publisher	Elsevier
Licensed content publication	Journal of the Less Common Metals
Licensed content title	Constitution diagrams of the binary systems Pd□B and Ir□B
Licensed content author	H Ipsier, P Rogl
Licensed content date	November–December 1981
Licensed content volume number	82
Licensed content issue number	n/a
Number of pages	1
Start Page	363
End Page	0
Type of Use	reuse in a thesis/dissertation
Intended publisher of new work	other
Portion	figures/tables/illustrations
Number of figures/tables/illustrations	2
Actual number of figures/tables/illustrations	2
Format	both print and electronic
Are you the author of this Elsevier article?	No
Will you be translating?	No
Title of your thesis/dissertation	Rhenium, Osmium and Iridium Diborides by Mechanochemistry: Synthesis, Structure, Thermal Stability and Mechanical Properties
Expected completion date	Dec 2014
Estimated size (number of pages)	300
Elsevier VAT number	GB 494 6272 12
Permissions price	0.00 USD
VAT/Local Sales Tax	0.00 USD / 0.00 GBP
Total	0.00 USD
Terms and Conditions	

**ELSEVIER LICENSE  
TERMS AND CONDITIONS**

Nov 06, 2014

---

This is a License Agreement between Zhilin Xie ("You") and Elsevier ("Elsevier") provided by Copyright Clearance Center ("CCC"). The license consists of your order details, the terms and conditions provided by Elsevier, and the payment terms and conditions.

**All payments must be made in full to CCC. For payment instructions, please see information listed at the bottom of this form.**

Supplier	Elsevier Limited The Boulevard, Langford Lane Kidlington, Oxford, OX5 1GB, UK
Registered Company Number	1982084
Customer name	Zhilin Xie
Customer address	1713 Tealbriar Ave. OVIEDO, FL 32765
License number	3503140779009
License date	Nov 06, 2014
Licensed content publisher	Elsevier
Licensed content publication	Journal of Physics and Chemistry of Solids
Licensed content title	Electronic structure, phase stability, and hardness of the osmium borides, carbides, nitrides, and oxides: First-principles calculations
Licensed content author	Miao Zhang, Mei Wang, Tian Cui, Yanming Ma, Yingli Niu, Guangtian Zou
Licensed content date	August 2008
Licensed content volume number	69
Licensed content issue number	8
Number of pages	7
Start Page	2096
End Page	2102
Type of Use	reuse in a thesis/dissertation
Intended publisher of new work	other
Portion	figures/tables/illustrations
Number of figures/tables/illustrations	1
Format	both print and electronic
Are you the author of this Elsevier article?	No
Will you be translating?	No
Title of your thesis/dissertation	Rhenium, Osmium and Iridium Diborides by Mechanochemistry: Synthesis, Structure, Thermal Stability and Mechanical Properties
Expected completion date	Dec 2014
Estimated size (number of pages)	300
Elsevier VAT number	GB 494 6272 12
Permissions price	0.00 USD
VAT/Local Sales Tax	0.00 USD / 0.00 GBP
Total	0.00 USD
Terms and Conditions	

**NATURE PUBLISHING GROUP LICENSE  
TERMS AND CONDITIONS**

Nov 06, 2014

---

This is a License Agreement between Zhilin Xie ("You") and Nature Publishing Group ("Nature Publishing Group") provided by Copyright Clearance Center ("CCC"). The license consists of your order details, the terms and conditions provided by Nature Publishing Group, and the payment terms and conditions.

**All payments must be made in full to CCC. For payment instructions, please see information listed at the bottom of this form.**

License Number	3503160428830
License date	Nov 06, 2014
Licensed content publisher	Nature Publishing Group
Licensed content publication	Nature Chemistry
Licensed content title	Mechanochemical synthesis: How grinding evolves
Licensed content author	Kenneth D. M. Harris
Licensed content date	Dec 18, 2012
Volume number	5
Issue number	1
Type of Use	reuse in a dissertation / thesis
Requestor type	academic/educational
Format	print and electronic
Portion	figures/tables/illustrations
Number of figures/tables/illustrations	1
High-res required	no
Figures	Figure 1 (a)
Author of this NPG article	no
Your reference number	None
Title of your thesis / dissertation	Rhenium, Osmium and Iridium Diborides by Mechanochemistry: Synthesis, Structure, Thermal Stability and Mechanical Properties
Expected completion date	Dec 2014
Estimated size (number of pages)	300
Total	0.00 USD
Terms and Conditions	

## High-pressure surface science and engineering

**Order detail ID:** 65925747  
**Order License Id:** 3503190054560  
**ISBN:** 978-0-7503-0881-6  
**Publication Type:** Book  
**Publisher:** TAYLOR & FRANCIS GROUP LLC - BOOKS  
**Author/Editor:** Gogotsi, IŮ. G. ; Domnich, Vladislav

**Permission Status:**  **Granted**  
**Permission type:** Republish or display content  
**Type of use:** Republish in a thesis/dissertation


[Hide details](#)

<b>Requestor type</b>	Academic institution
<b>Format</b>	Print, Electronic
<b>Portion</b>	chart/graph/table/figure
<b>Number of charts/graphs/tables/figures</b>	2
<b>Title or numeric reference of the portion(s)</b>	High Pressure Surface Science and Engineering
<b>Title of the article or chapter the portion is from</b>	Chapter 3:Continuum mechanical fundamentals of mechanochemistry
<b>Editor of portion(s)</b>	Vladislav Domnich and Yury Gogotsi
<b>Author of portion(s)</b>	Valery I . Levitas
<b>Volume of serial or monograph</b>	N/A
<b>Issue, if republishing an article from a serial</b>	N/A
<b>Page range of portion</b>	161-292
<b>Publication date of portion</b>	2003
<b>Rights for</b>	Main product
<b>Duration of use</b>	Life of current edition
<b>Creation of copies for the disabled</b>	no
<b>With minor editing privileges</b>	no
<b>For distribution to</b>	Worldwide
<b>In the following language(s)</b>	Original language of publication
<b>With incidental promotional use</b>	no
<b>Lifetime unit quantity of new product</b>	Up to 499
<b>Made available in the following markets</b>	Education
<b>The requesting person/organization</b>	Zhilin Xie
<b>Order reference number</b>	
<b>Author/Editor</b>	Zhilin Xie
<b>The standard identifier</b>	N/A
<b>The proposed price</b>	N/A
<b>Title</b>	Rhenium, Osmium and Iridium Diborides by Mechanochemistry: Synthesis, Structure, Thermal Stability and Mechanical Properties



## High-pressure surface science and engineering

**Order detail ID:** 65929486  
**Order License Id:** 3505980740402  
**ISBN:** 978-0-7503-0881-6  
**Publication Type:** Book  
**Publisher:** TAYLOR & FRANCIS GROUP LLC - BOOKS  
**Author/Editor:** Gogotsi, IŮ. G. ; Domnich, Vladislav

**Permission Status:**  **Granted**

**Permission type:** Republish or display content  
**Type of use:** Republish in a thesis/dissertation

Hide details

<b>Requestor type</b>	Academic institution
<b>Format</b>	Print, Electronic
<b>Portion</b>	page
<b>Number of pages requested</b>	3
<b>Title or numeric reference of the portion(s)</b>	Chapter 3. Continuum mechanical fundamentals of mechanochemistry
<b>Title of the article or chapter the portion is from</b>	N/A
<b>Editor of portion(s)</b>	Vladislav Domnich and Yury Gogotsi
<b>Author of portion(s)</b>	Valery I . Levitas
<b>Volume of serial or monograph</b>	N/A
<b>Issue, if republishing an article from a serial</b>	N/A
<b>Page range of portion</b>	170-172
<b>Publication date of portion</b>	2003
<b>Rights for</b>	Main product
<b>Duration of use</b>	Life of current edition
<b>Creation of copies for the disabled</b>	no
<b>With minor editing privileges</b>	no
<b>For distribution to</b>	Worldwide
<b>In the following language(s)</b>	Original language of publication
<b>With incidental promotional use</b>	no
<b>Lifetime unit quantity of new product</b>	Up to 499
<b>Made available in the following markets</b>	Education
<b>The requesting person/organization</b>	Zhilin Xie
<b>Order reference number</b>	
<b>Author/Editor</b>	Zhilin Xie
<b>The standard identifier</b>	N/A
<b>The proposed price</b>	N/A
<b>Title</b>	Rhenium, Osmium and Iridium Diborides by Mechanochemistry: Synthesis, Structure, Thermal Stability and Mechanical Properties
<b>Publisher</b>	University of Central Florida dissertation
<b>Expected publication date</b>	Jul 2015



## APPENDIX B: TRANSMISSION ELECTRON MICROGRAPHS

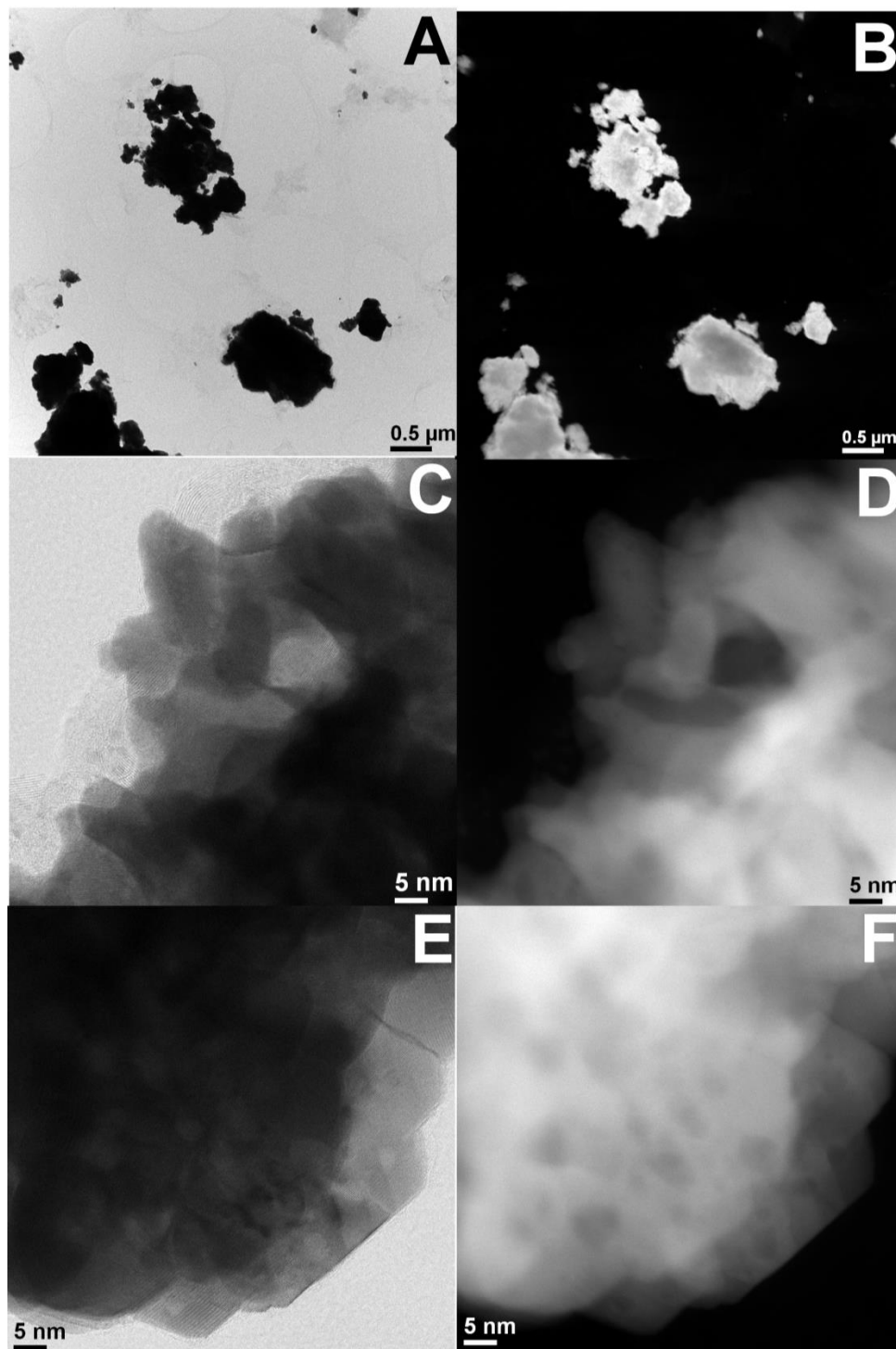


Figure 82: Bright field (A, C and E) and dark field (B, D and F) STEM images of pure Os metal.

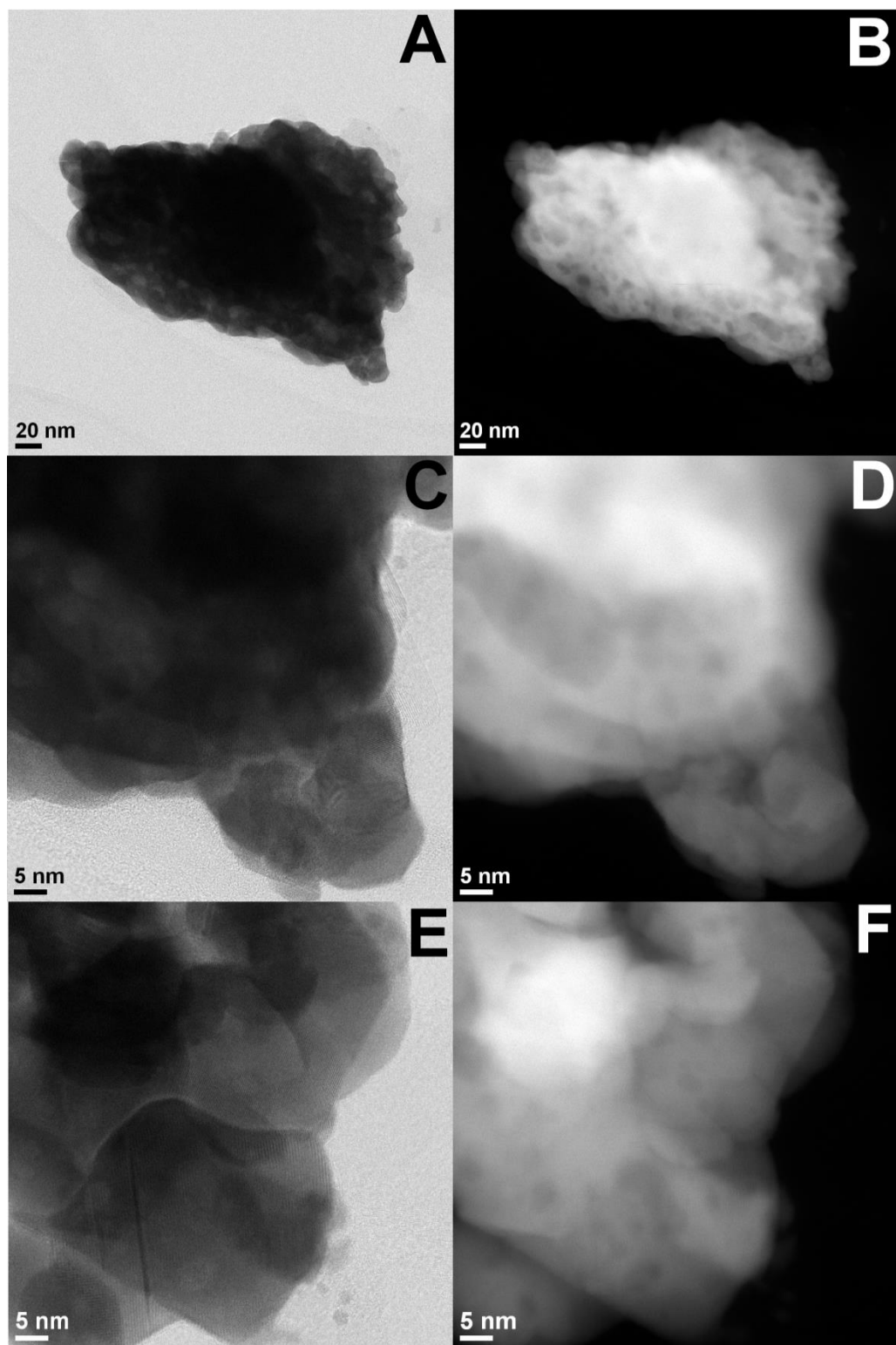


Figure 83: Bright field (A, C and E) and dark field (B, D and F) STEM images of pure Os metal.

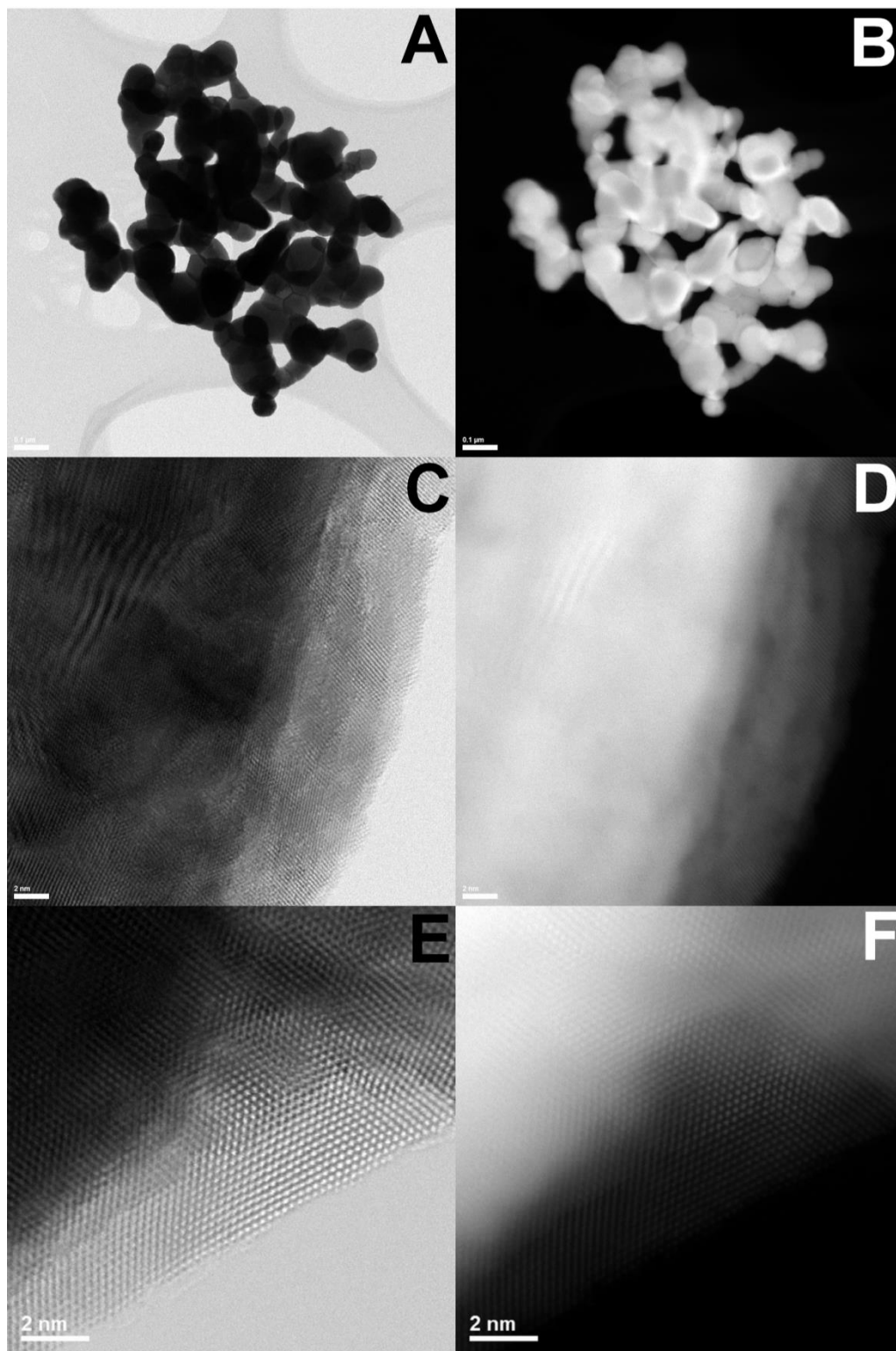


Figure 84: Bright field (A, C and E) and dark field (B, D and F) STEM images of pure Os metal.

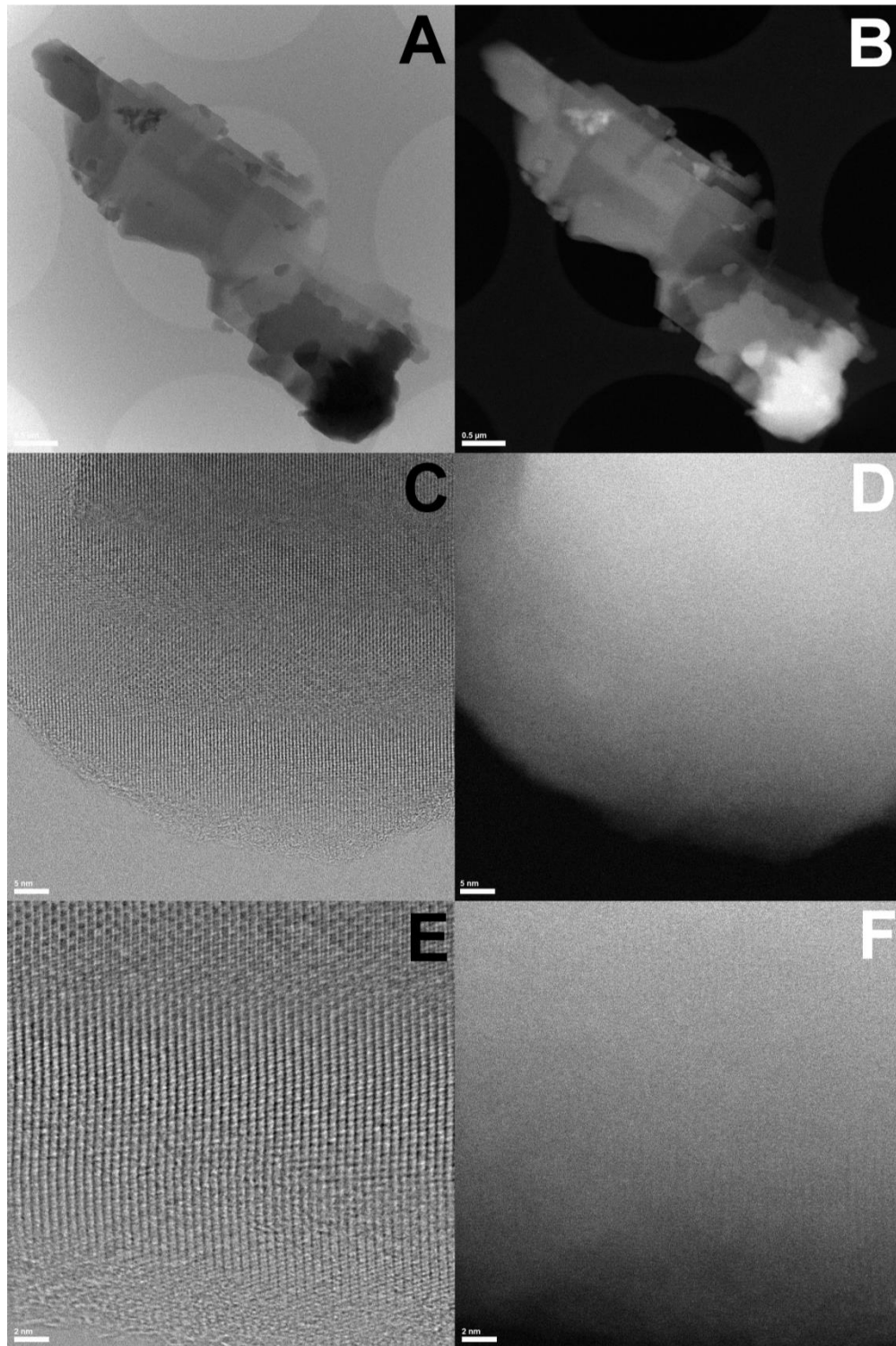


Figure 85: Bright field (A, C and E) and dark field (B, D and F) STEM images of amorphous and crystalline boron.

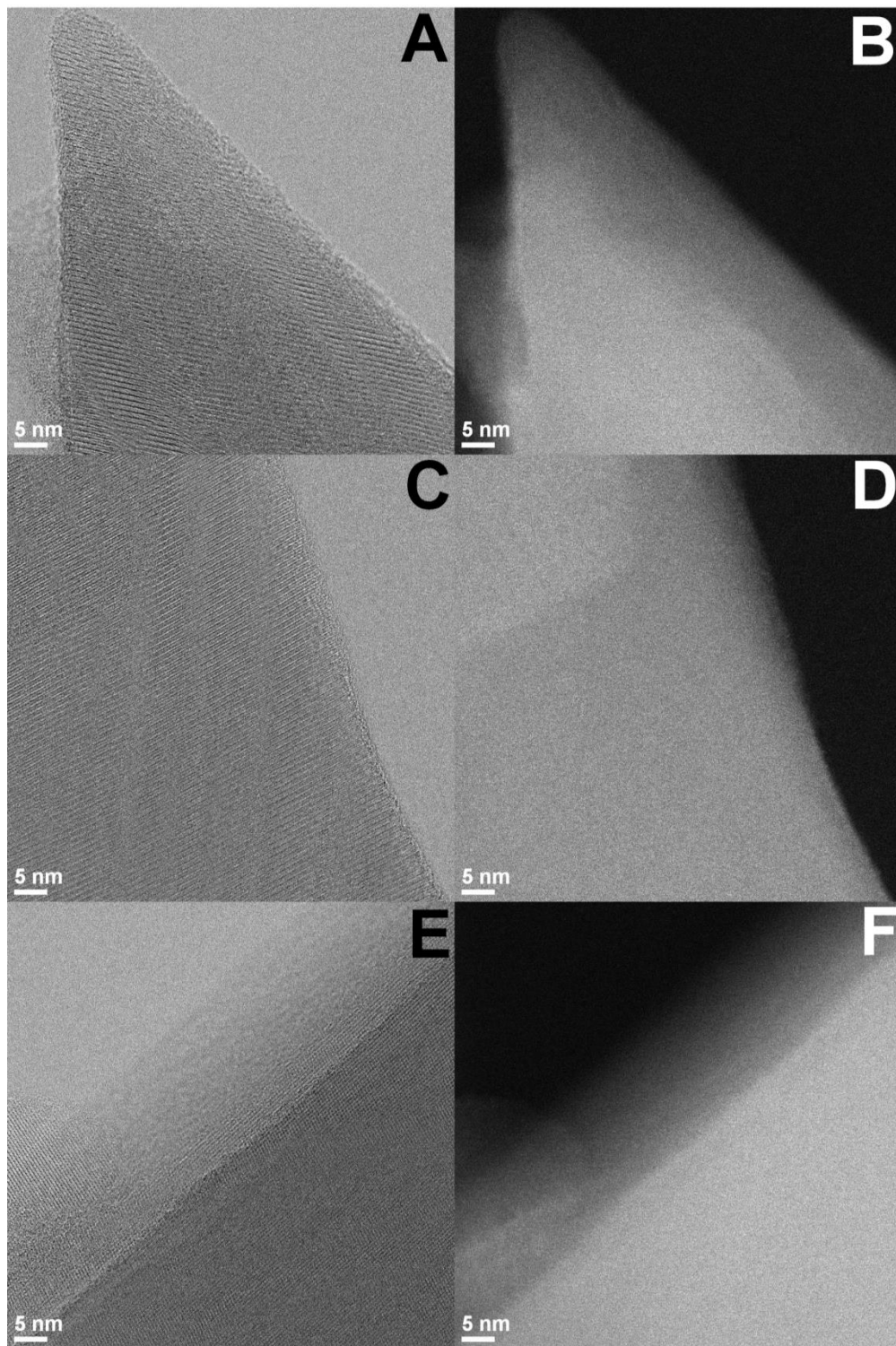


Figure 86: Bright field (A, C and E) and dark field (B, D and F) STEM images of crystalline  $^{11}\text{B}$ .



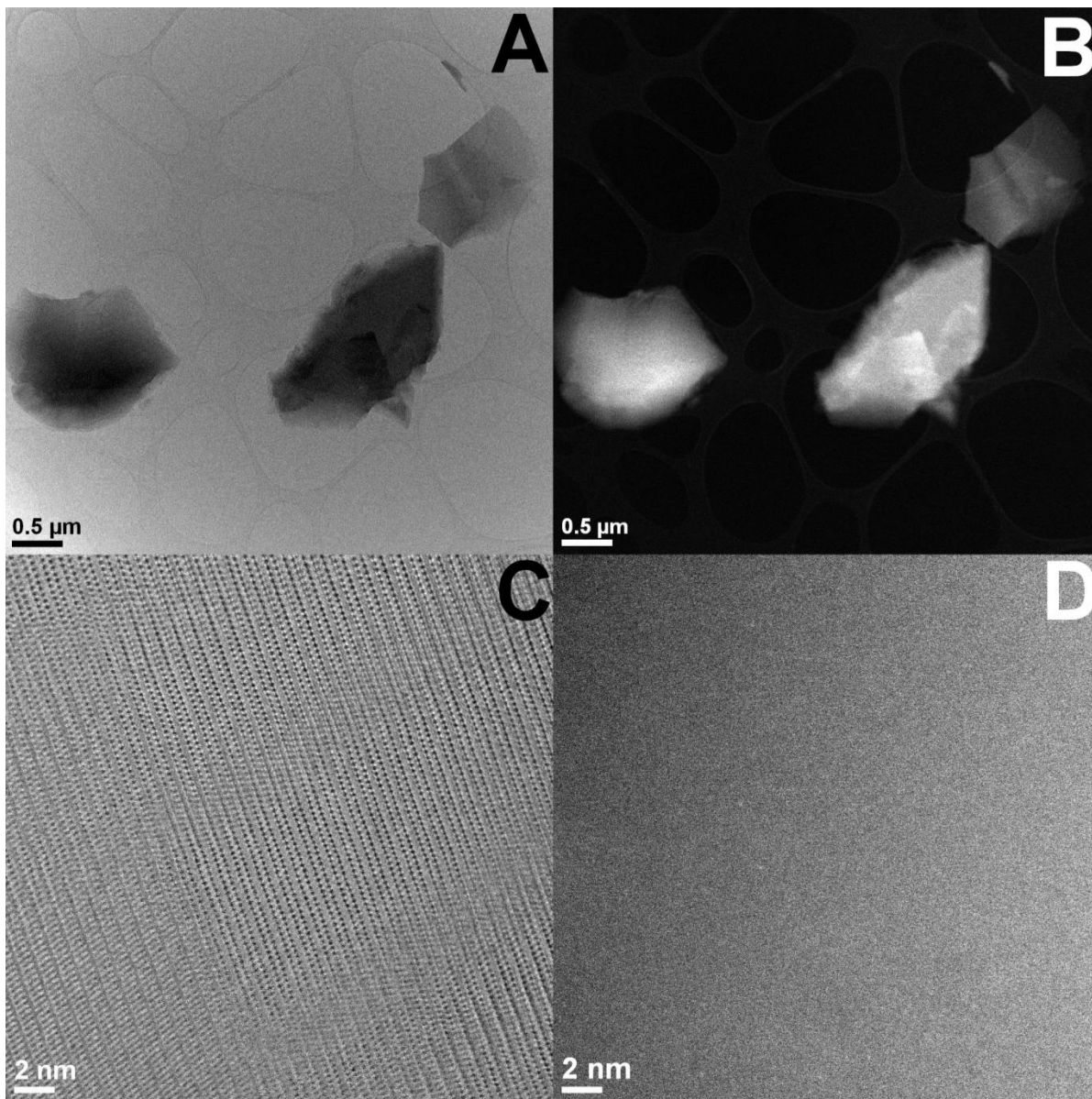


Figure 87: Bright field (A and C) and dark field (B and D) STEM images of crystalline  $^{11}\text{B}$ .

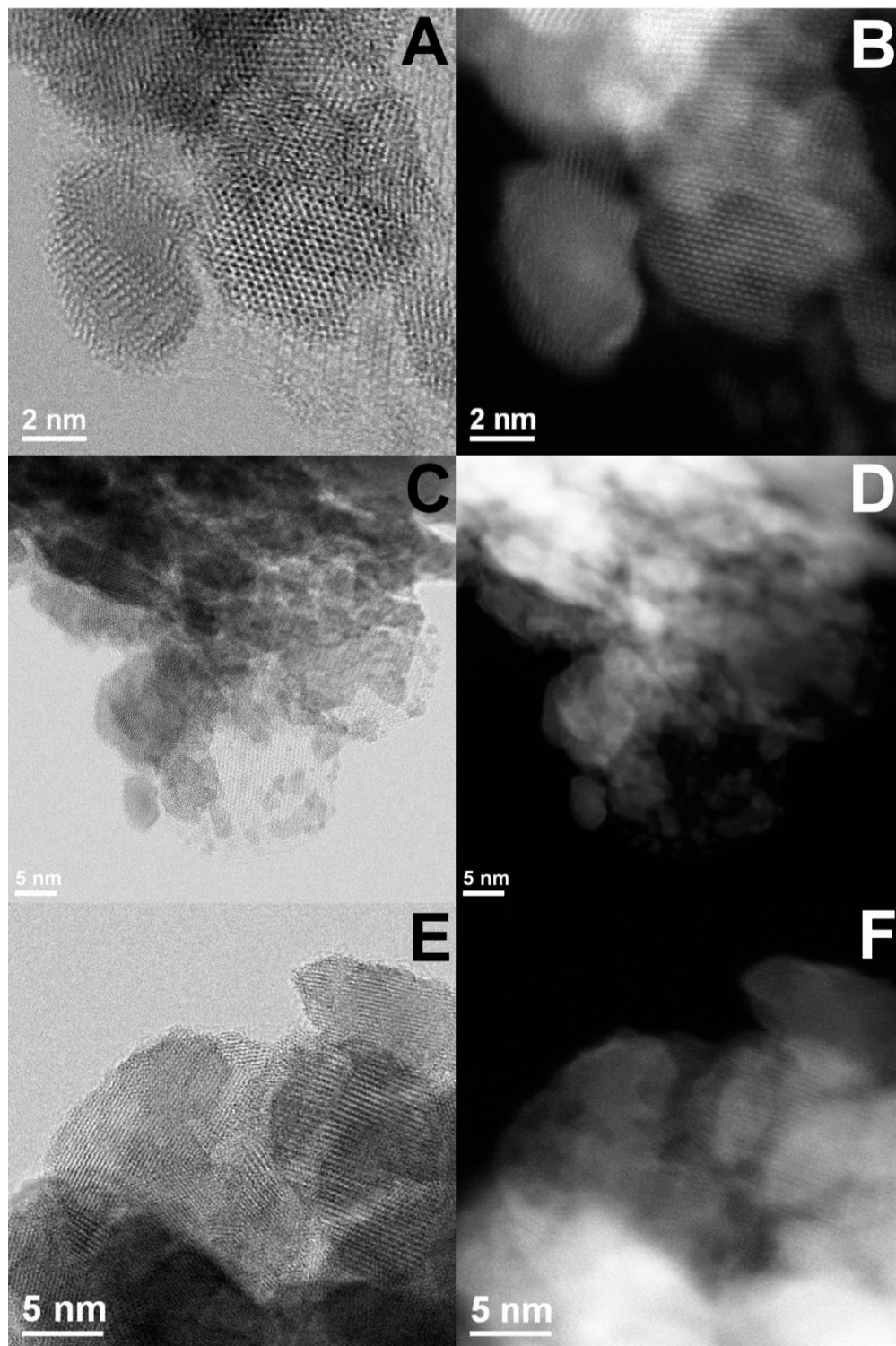


Figure 88: Bright field (A, C and E) and dark field (B, D and F) STEM images of hexagonal OsB<sub>2</sub>.

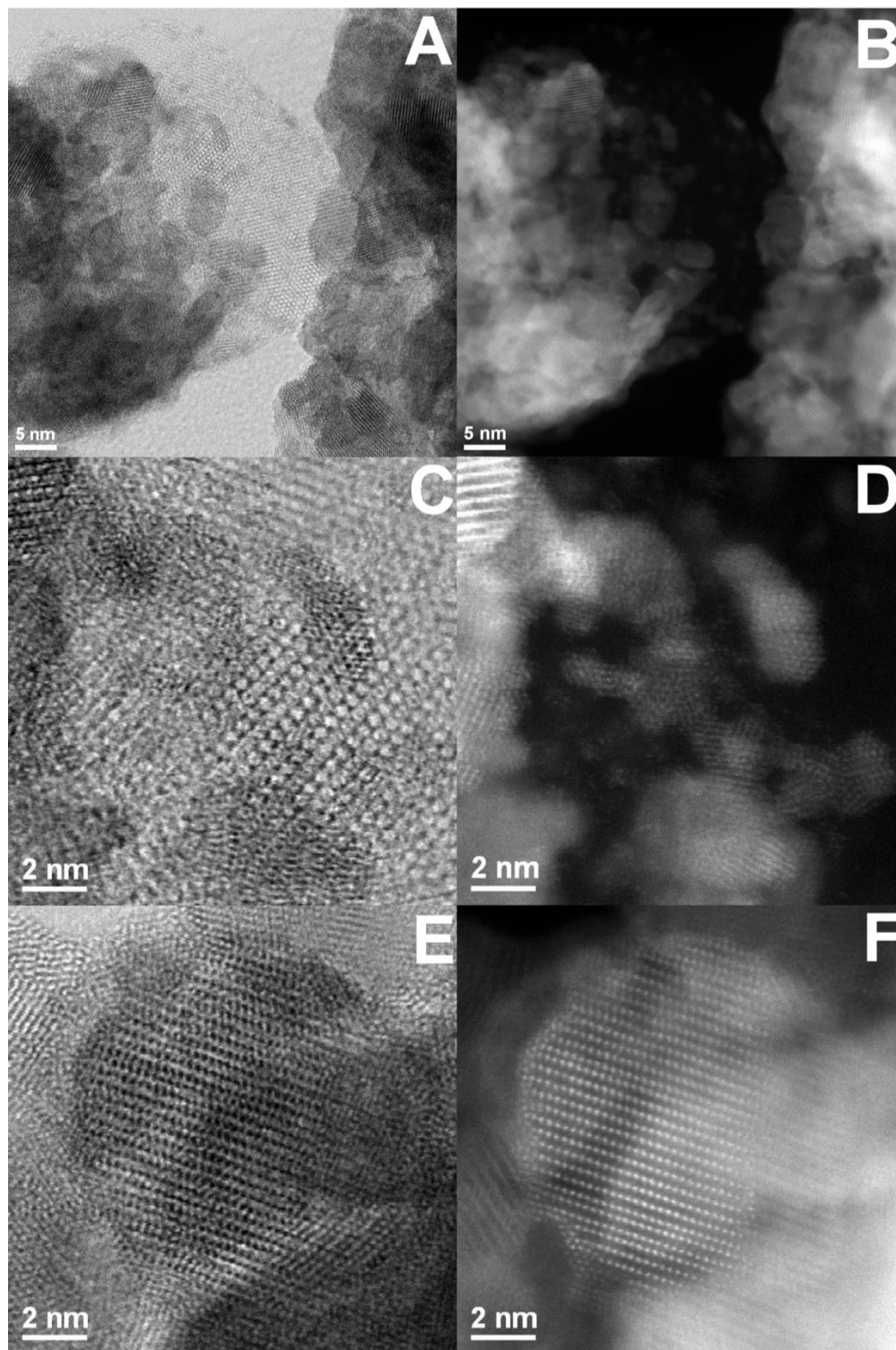


Figure 89: Bright field (A, C and E) and dark field (B, D and F) STEM images of hexagonal OsB<sub>2</sub>.





Figure 90: Bright field (A, C and E) and dark field (B, D and F) STEM images of hexagonal OsB<sub>2</sub>.

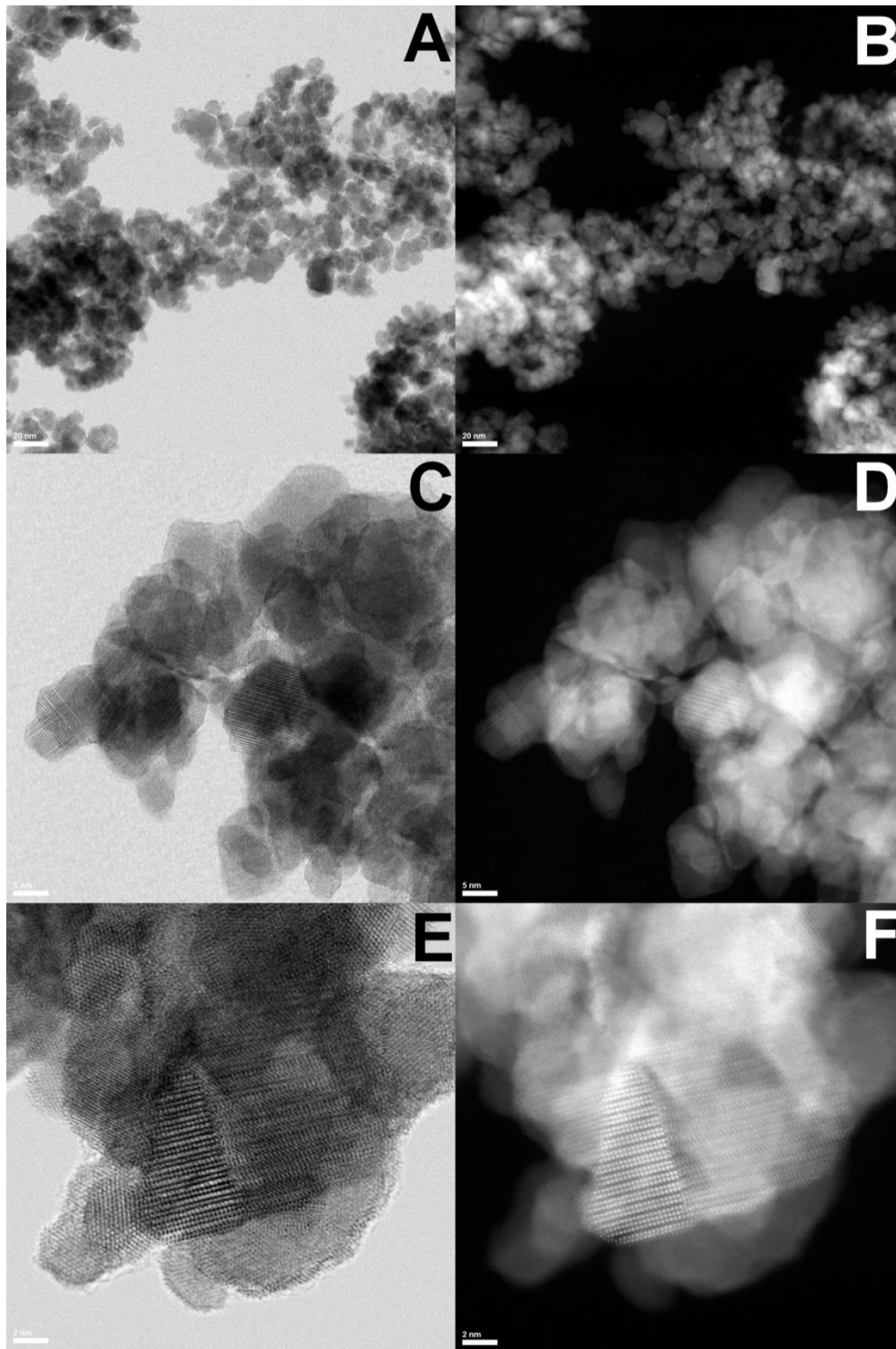


Figure 91: Bright field (A, C and E) and dark field (B, D and F) STEM images of  $\text{Os}_2\text{B}_3$ .

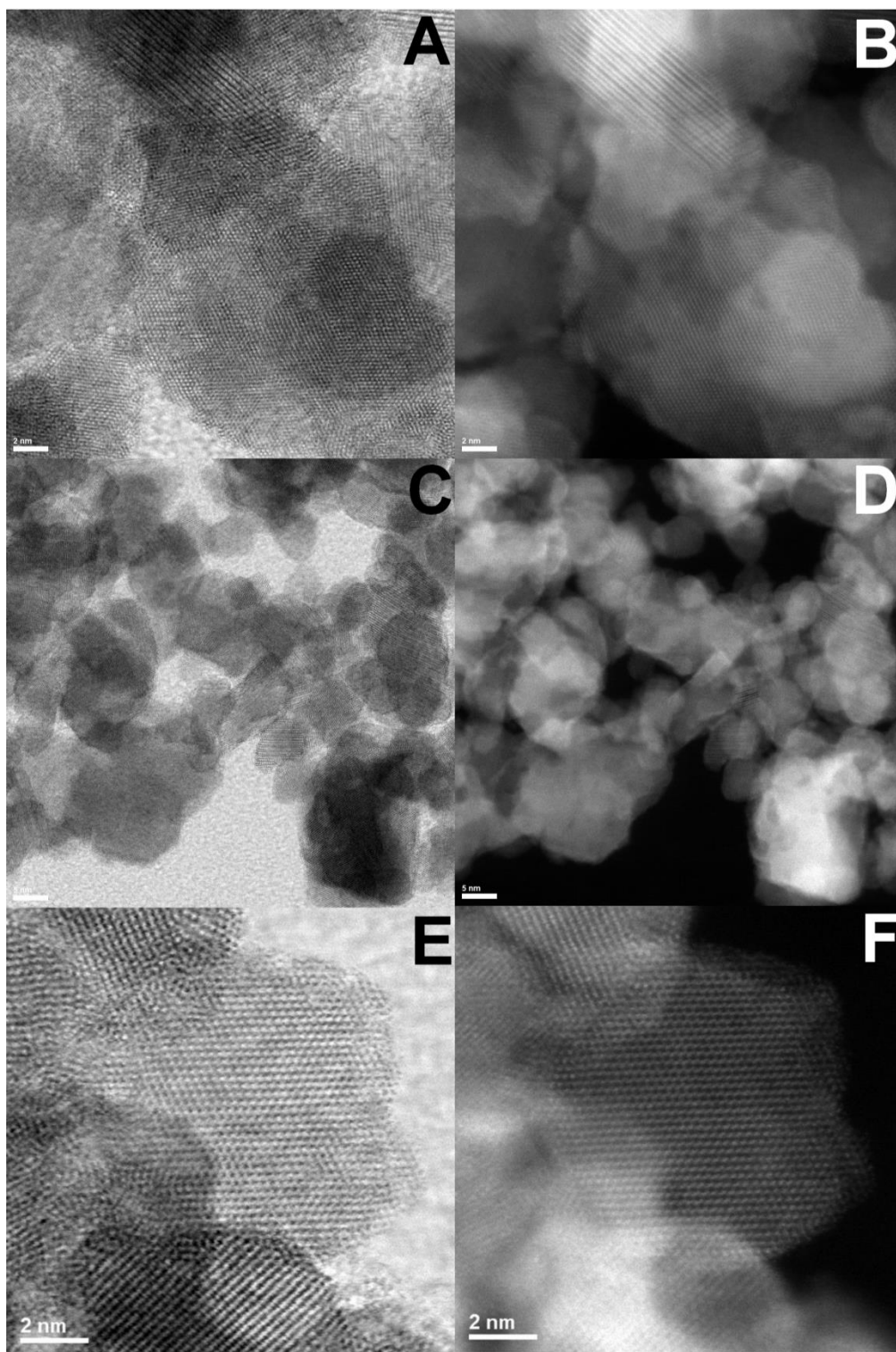


Figure 92: Bright field (A, C and E) and dark field (B, D and F) STEM images of  $\text{Os}_2\text{B}_3$ .

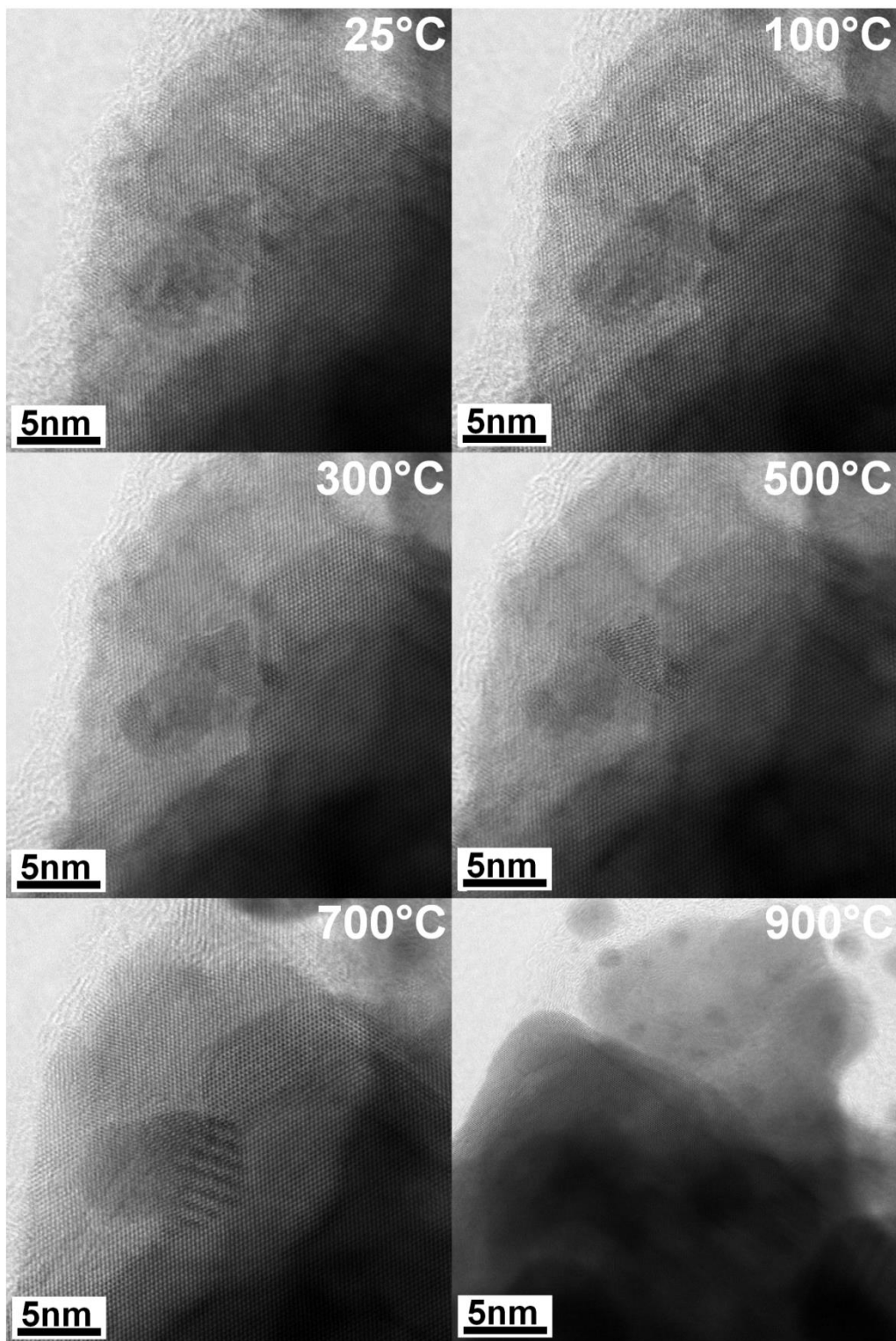


Figure 93: High temperature TEM images of *h*-OsB<sub>2</sub> particles at different temperature.

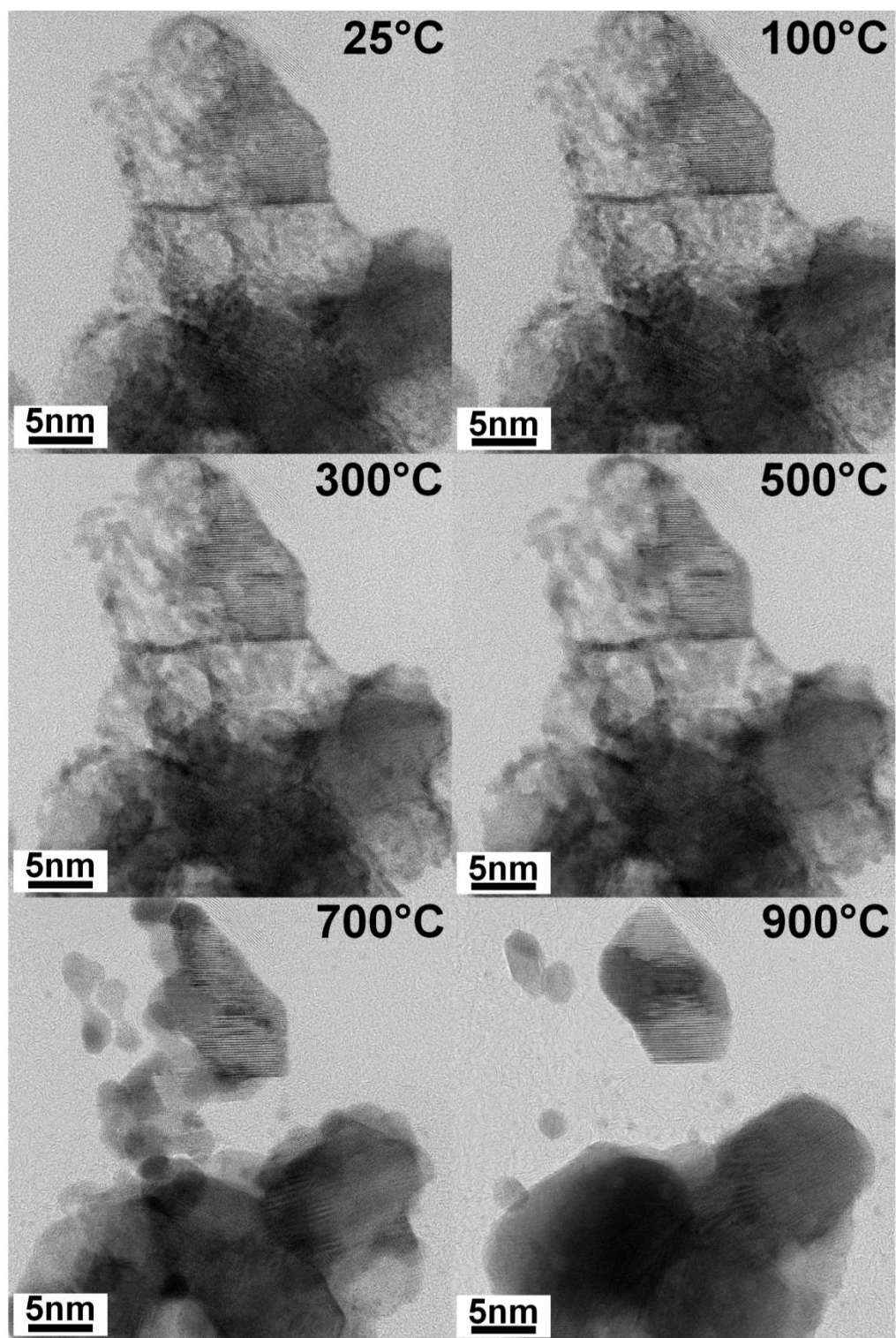


Figure 94: High temperature TEM images of *h*-OsB<sub>2</sub> particles at different temperature.



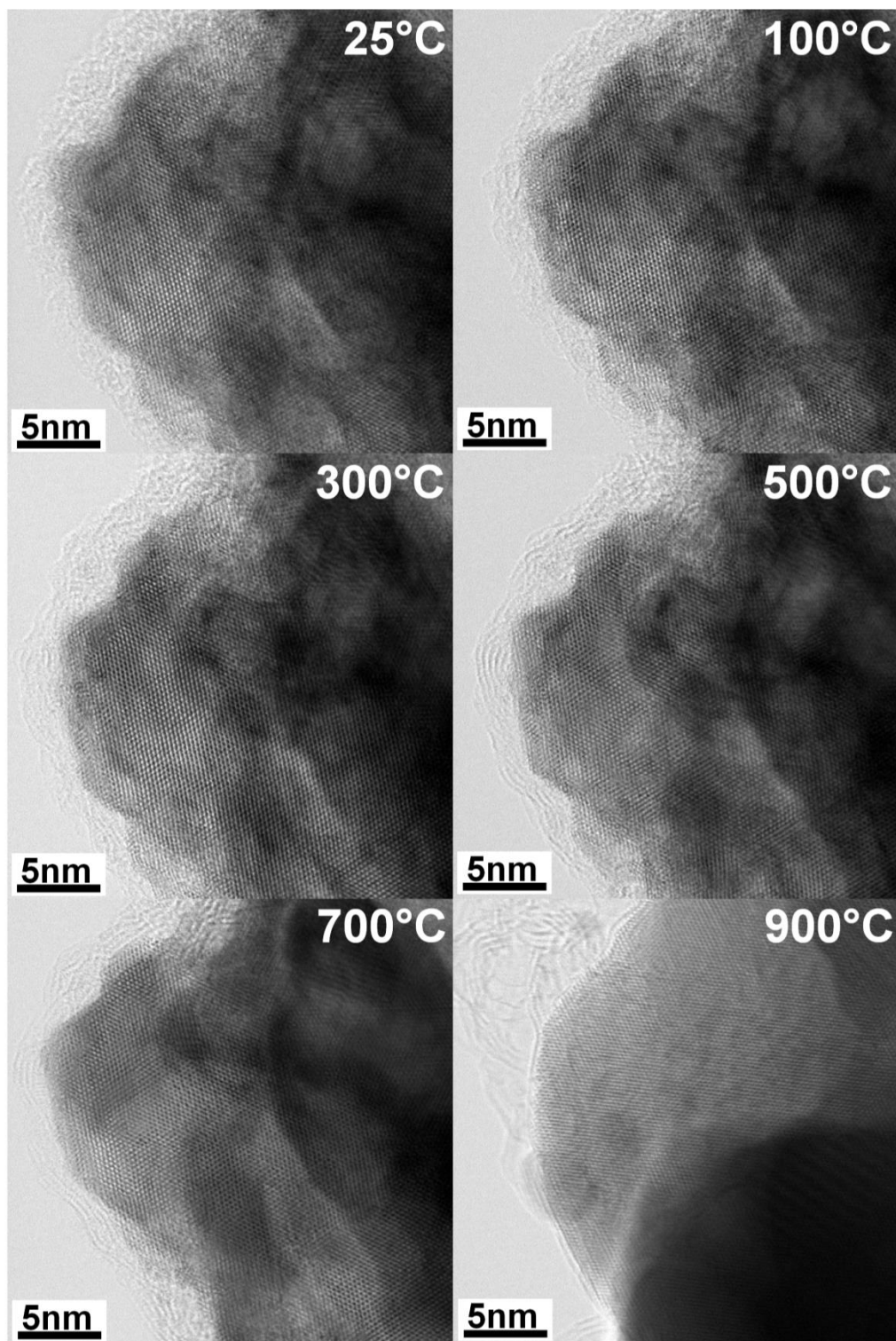


Figure 95: High temperature TEM images of *h*-OsB<sub>2</sub> particles at different temperature.

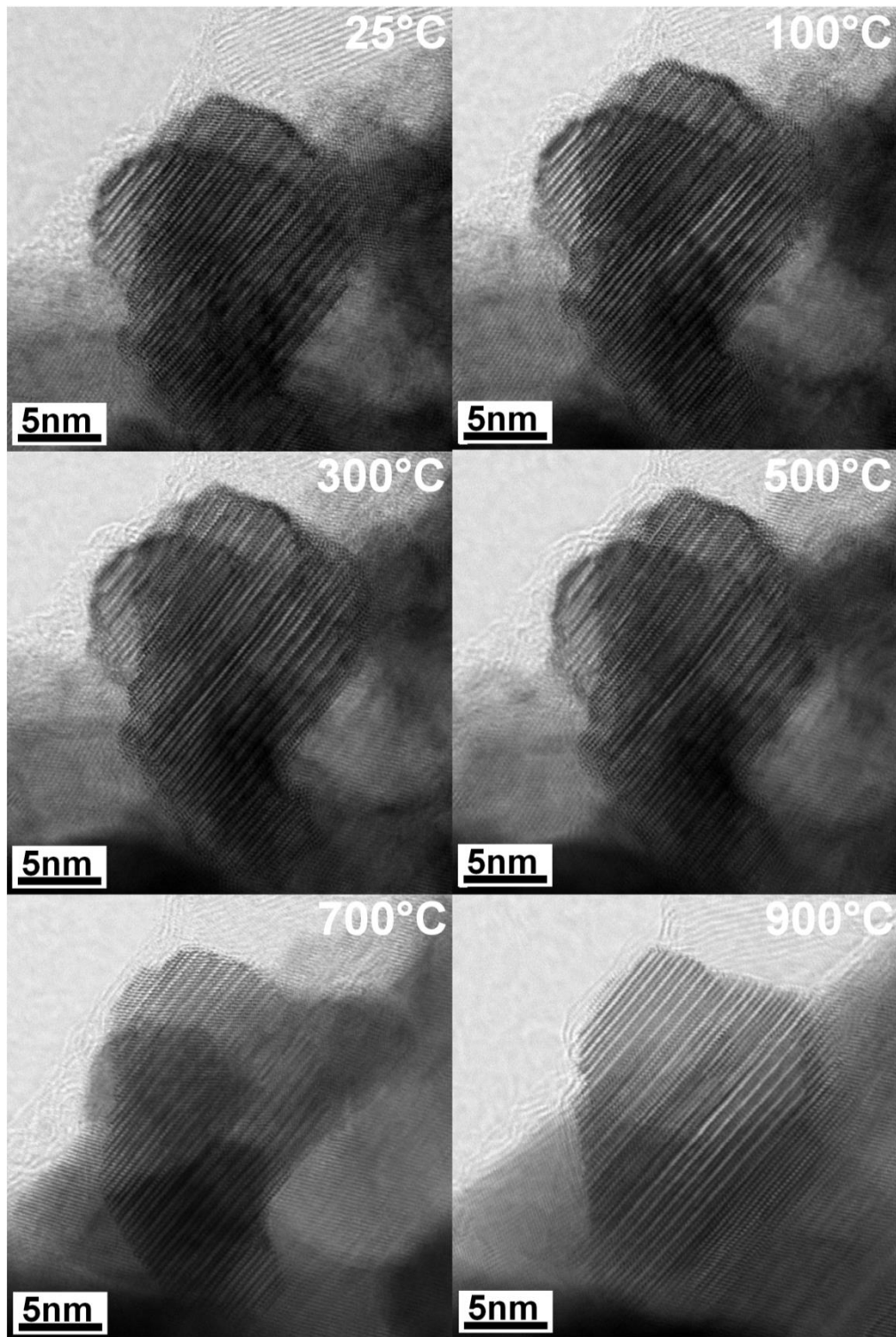


Figure 96: High temperature TEM images of *h*-OsB<sub>2</sub> particles at different temperature.

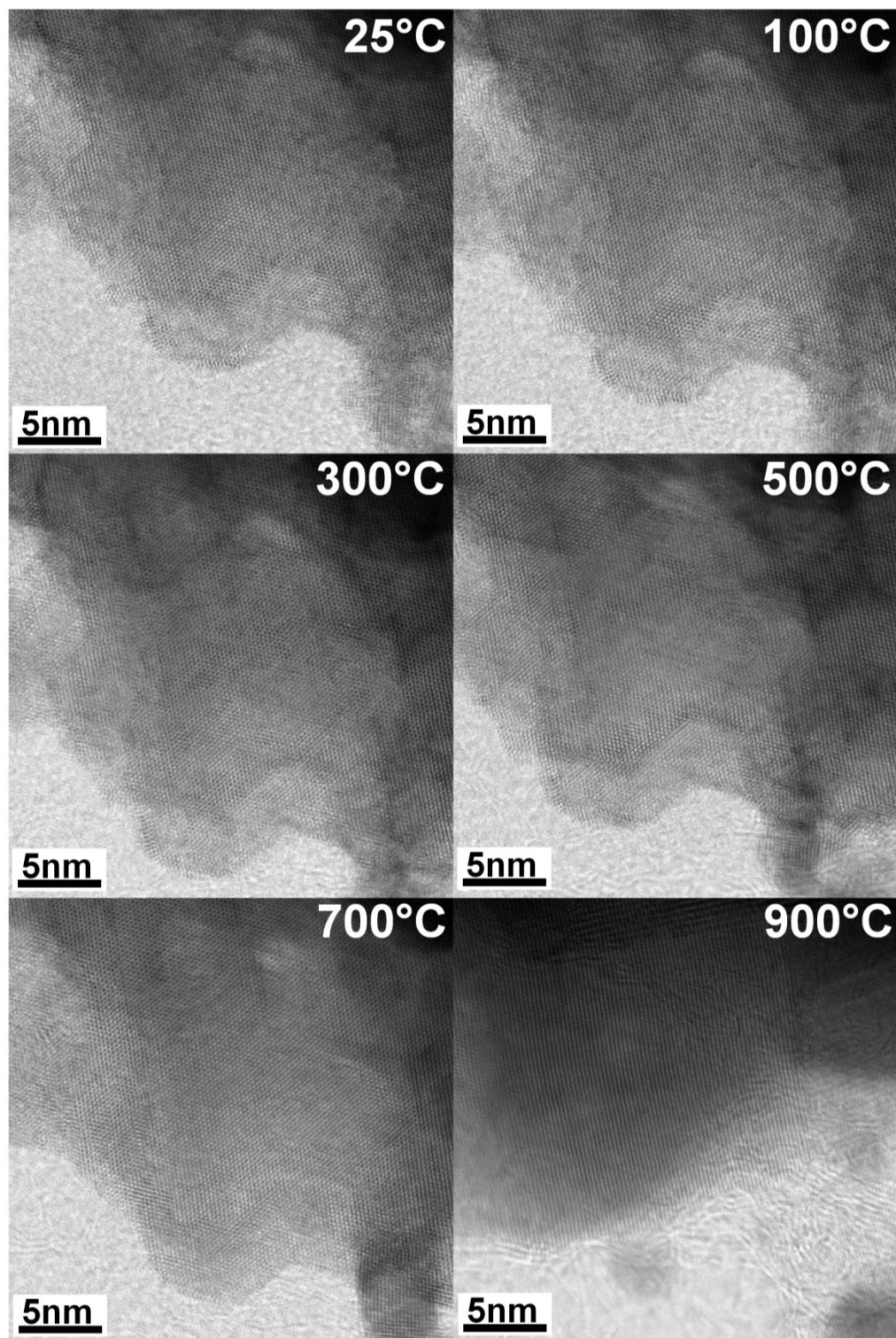


Figure 97: High temperature TEM images of *h*-OsB<sub>2</sub> particles at different temperature.



## LIST OF REFERENCES

- [1] A.L. Ivanovskii. Mechanical and electronic properties of diborides of transition 3d–5d metals from first principles: Toward search of novel ultra-incompressible and superhard materials, *Progress in Materials Science* 57 (2012) 184-228.
- [2] D.M. Teter. Computational alchemy: the search for new superhard materials, *MRS Bulletin* 23 (1998) 22-27.
- [3] J. Haines, J. Léger, G. Bocquillon. Synthesis and design of superhard materials, *Ann. Rev. Mater. Res.* 31 (2001) 1-23.
- [4] S. Veprek, M.J.G. Veprek-Heijman. Industrial applications of superhard nanocomposite coatings, *Surface and Coatings Technology* 202 (2008) 5063-5073.
- [5] V.L. Solozhenko, E. Gregoryanz. Synthesis of superhard materials, *Materials Today* 8 (2005) 44-51.
- [6] R. Riedel. Novel Ultrahard Materials, *Advanced Materials* 6 (1994) 549-560.

- [7] S. Veprek, A.S. Argon. Towards the understanding of mechanical properties of super- and ultrahard nanocomposites, *Journal of Vacuum Science & Technology B* 20 (2002) 650-664.
- [8] V.V. Brazhkin. High-pressure synthesized materials: treasures and hints, *High Pressure Research* 27 (2007) 333-351.
- [9] J. Haines, J.M. Léger, A. Atouf. Crystal Structure and Equation of State of Cotunnite-Type Zirconia, *Journal of the American Ceramic Society* 78 (1995) 445-448.
- [10] J.J. Gilman, R.W. Cumberland, R.B. Kaner. Design of hard crystals, *International Journal of Refractory Metals and Hard Materials* 24 (2006) 1-5.
- [11] J.J. Gilman. Chemical theory of dislocation mobility, *Materials Science and Engineering: A* 409 (2005) 7-12.
- [12] I.V. Aleksandrov, A.F. Goncharov, E.V. Yakovenko, S.M. Stishov. High Pressure Study of Diamond, Graphite and Related Materials. *High-Pressure Research: Application to Earth and Planetary Sciences*. American Geophysical Union, 2013. pp. 409-416.
- [13] R.B. Kaner, J.J. Gilman, S.H. Tolbert. Designing Superhard Materials, *Science* 308 (2005) 1268-1269.

- [14] I.V. Aleksandrov, A.F. Goncharov, A.N. Zisman, S.M. Stishov. Diamond at high pressures: Raman scattering of light, equations of state, and high-pressure scale, *Sov. Phys. JETP* 66 (1987) 384.
- [15] A.Y. LIU, M.L. COHEN. Prediction of New Low Compressibility Solids, *Science* 245 (1989) 841-842.
- [16] H. Xianfeng, W. Zhijian, X. Yuanhui, Z. Defeng, L. Xiaojuan, M. Jian. Trends in elasticity and electronic structure of 5d transition metal diborides: first-principles calculations, *Journal of Physics: Condensed Matter* 19 (2007) 196212.
- [17] H. Cynn, J.E. Klepeis, C.-S. Yoo, D.A. Young. Osmium has the Lowest Experimentally Determined Compressibility, *Physical Review Letters* 88 (2002) 135701.
- [18] H.J. McSkimin, W.L. Bond. Elastic Moduli of Diamond, *Physical Review* 105 (1957) 116-121.
- [19] H. Ledbetter. Monocrystal elastic constants and derived properties of the cubic and hexagonal elements. In: Chapter 7, Academic Press, New York, 2001.
- [20] R.E. Macfarlane, J.A. Rayne, C.K. Jones. Anomalous temperature dependence of shear modulus  $c_{44}$  for platinum, *Phys. Lett.* 18 (1965) 91.

- [21] J.M. Dickinson, P.E. Armstrong. Temperature Dependence of the Elastic Constants of Molybdenum, *Journal of Applied Physics* 38 (1967) 602-606.
- [22] Y. Hiki, A.V. Granato. Anharmonicity in Noble Metals; Higher Order Elastic Constants, *Physical Review* 144 (1966) 411-419.
- [23] N. Soga. Comparison of Measured and Predicted Bulk Moduli of Tantalum and Tungsten at High Temperatures, *Journal of Applied Physics* 37 (1966) 3416-3420.
- [24] J.J. Gilman. *Electronic basis of the strength of materials*, UK: Cambridge University Press, 2003.
- [25] L. Fast, J.M. Wills, B. Johansson, O. Eriksson. Elastic constants of hexagonal transition metals: Theory, *Physical Review B* 51 (1995) 17431-17438.
- [26] A.F. Young, C. Sanloup, E. Gregoryanz, S. Scandolo, R.J. Hemley, H.-k. Mao. Synthesis of Novel Transition Metal Nitrides  $\text{IrN}_2$  and  $\text{OsN}_2$ , *Physical Review Letters* 96 (2006) 155501.
- [27] Electronic, dynamical, and thermal properties of ultra-incompressible superhard rhenium diboride: a combined first-principles and neutron scattering study, *Phys. Rev.* 76 (2007) 184113.

- [28] Z. Chen, M. Gu, C.Q. Sun, X. Zhang, R. Liu. Ultrastiff carbides uncovered in first principles, *Applied Physics Letters* 91 (2007) 061905-061905-061903.
- [29] H.-Y. Chung, J.M. Yang, S.H. Tolbert, R.B. Kaner. Anisotropic mechanical properties of ultra-incompressible, hard osmium diboride, *Journal of Materials Research* 23 (2008) 1797-1801.
- [30] X.P. Du, Y.X. Wang. Investigation of osmium carbides with various stoichiometries: First-principles calculations, *Journal of Applied Physics* 107 (2010) -.
- [31] J.J. Gilman. Chemistry and physics of mechanical hardness, *Wiley series on processing of engineering materials* 1 (2009).
- [32] Q. Gu, G. Krauss, W. Steurer. Transition Metal Borides: Superhard versus Ultra-incompressible, *Advanced Materials* 20 (2008) 3620-3626.
- [33] I.G. Talmy, J.A. Zaykoski, M.M. Opeka, S. Dallek. Oxidation of  $ZrB_2$  ceramics modified with SiC and group IV–VI transition metal diborides. *Elec. Chem. Soc. Proc*, vol. 12, 2001. p.144-158.
- [34] M. Wang, Y. Li, T. Cui, Y. Ma, G. Zou. Origin of hardness in  $WB_4$  and its implications for  $ReB_4$ ,  $TaB_4$ ,  $MoB_4$ ,  $TcB_4$ , and  $OsB_4$ , *Applied Physics Letters* 93 (2008) -.

- [35] E. Wuchina, E. Opila, M. Opeka, W. Fahrenholtz, I. Talmy. UHTCs: Ultra-High Temperature Ceramic Materials for extreme environment applications, The Electrochemical Society Interface (Winter 2007) 30-36.
- [36] E. Zhao, J. Wang, Z. Wu. Structural stability and phase transition in OsC and RuC, Journal of computational chemistry 31 (2010) 2883-2888.
- [37] S. Ono, T. Kikegawa, Y. Ohishi. A high-pressure and high-temperature synthesis of platinum carbide, Solid State Communications 133 (2005) 55-59.
- [38] R. Licheri, R. Orrù, C. Musa, G. Cao. Synthesis, densification and characterization of TaB<sub>2</sub>-SiC composites, Ceramics International 36 (2010) 937-941.
- [39] E. Gregoryanz, C. Sanloup, M. Somayazulu, J. Badro, G. Fiquet, H.-k. Mao, R.J. Hemley. Synthesis and characterization of a binary noble metal nitride, Nat Mater 3 (2004) 294-297.
- [40] Y. Liang, B. Zhang. Mechanical and electronic properties of superhard ReB<sub>2</sub>, Physical Review B 76 (2007) 132101.
- [41] X. Zhang, G.E. Hilmas, W.G. Fahrenholtz. Synthesis, densification, and mechanical properties of TaB<sub>2</sub>, Materials Letters 62 (2008) 4251-4253.

- [42] J. Cai, E. Zhao, Z. Wu. First principles investigation on the structural, mechanical and electronic properties of OsC<sub>2</sub>, Computational Materials Science 46 (2009) 1098-1101.
- [43] W.J. Zhao, Y.X. Wang. Structural, mechanical, and electronic properties of TaB<sub>2</sub>, TaB, IrB<sub>2</sub> and IrB: First-principle calculations, Journal of Solid State Chemistry 182 (2009) 2880-2886.
- [44] B. Winkler, E.A. Juarez-Arellano, A. Friedrich, L. Bayarjargal, F. Schröder, J. Biehler, V. Milman, S.M. Clark, J. Yan. *In situ* synchrotron X-ray diffraction study of the formation of TaB<sub>2</sub> from the elements in a laser heated diamond anvil cell, Solid State Sciences 12 (2010) 2059-2064.
- [45] A. Latini, J.V. Rau, D. Ferro, R. Teghil, V.R. Albertini, S.M. Barinov. Superhard Rhenium Diboride Films: Preparation and Characterization, Chemistry of Materials 20 (2008) 4507-4511.
- [46] J.B. Levine, S.L. Nguyen, H.I. Rasool, J.A. Wright, S.E. Brown, R.B. Kaner. Preparation and Properties of Metallic, Superhard Rhenium Diboride Crystals, Journal of the American Chemical Society 130 (2008) 16953-16958.

- [47] Z. Zhao, M. Wang, L. Cui, J. He, D. Yu, Y. Tian. Semiconducting Superhard Ruthenium Monocarbide, *The Journal of Physical Chemistry C* 114 (2010) 9961-9964.
- [48] X. Li, X.P. Du, Y.X. Wang. Structural, Mechanical Stability, and Physical Properties of Iridium Carbides with Various Stoichiometries: First-Principles Investigations, *The Journal of Physical Chemistry C* 115 (2011) 6948-6953.
- [49] A. Knappschneider, C. Litterscheid, D. Dzivenko, J.A. Kurzman, R. Seshadri, N. Wagner, J. Beck, R. Riedel, B. Albert. Possible Superhardness of CrB<sub>4</sub>, *Inorganic Chemistry* 52 (2013) 540-542.
- [50] J.C. Crowhurst, A.F. Goncharov, B. Sadigh, C.L. Evans, P.G. Morrall, J.L. Ferreira, A.J. Nelson. Synthesis and Characterization of the Nitrides of Platinum and Iridium, *Science* 311 (2006) 1275-1278.
- [51] J. Haines, J.M. Léger. Phase transitions in ruthenium dioxide up to 40 GPa: Mechanism for the rutile-to-fluorite phase transformation and a model for the high-pressure behavior of stishovite SiO<sub>2</sub>, *Physical Review B* 48 (1993) 13344-13350.
- [52] H.-Y. Chung, M.B. Weinberger, J.B. Levine, A. Kavner, J.-M. Yang, S.H. Tolbert, R.B. Kaner. Synthesis of Ultra-Incompressible Superhard Rhenium Diboride at Ambient Pressure, *Science* 316 (2007) 436-439.



- [53] R.W. Cumberland, M.B. Weinberger, J.J. Gilman, S.M. Clark, S.H. Tolbert, R.B. Kaner. Osmium Diboride, An Ultra-Incompressible, Hard Material, *Journal of the American Chemical Society* 127 (2005) 7264-7265.
- [54] R. Mohammadi, A.T. Lech, M. Xie, B.E. Weaver, M.T. Yeung, S.H. Tolbert, R.B. Kaner. Tungsten tetraboride, an inexpensive superhard material, *Proceedings of the National Academy of Sciences* (2011).
- [55] M.B. Weinberger, J.B. Levine, H.-Y. Chung, R.W. Cumberland, H.I. Rasool, J.-M. Yang, R.B. Kaner, S.H. Tolbert. Incompressibility and Hardness of Solid Solution Transition Metal Diborides:  $\text{Os}_{1-x}\text{Ru}_x\text{B}_2$ , *Chemistry of Materials* 21 (2009) 1915-1921.
- [56] M. Frotscher, M. Hölzel, B. Albert. Crystal Structures of the Metal Diborides  $\text{ReB}_2$ ,  $\text{RuB}_2$ , and  $\text{OsB}_2$  from Neutron Powder Diffraction *Zeitschrift für anorganische und allgemeine Chemie* 636 (2010) 1783-1786.
- [57] A. Latini, J.V. Rau, R. Teghil, A. Generosi, V.R. Albertini. Superhard Properties of Rhodium and Iridium Boride Films, *ACS applied materials & interfaces* 2 (2010) 581-587.

- [58] S. Chiodo, H.J. Gotsis, N. Russo, E. Sicilia. OsB<sub>2</sub> and RuB<sub>2</sub>, ultra-incompressible, hard materials: First-principles electronic structure calculations, *Chemical Physics Letters* 425 (2006) 311-314.
- [59] S.J. La Placa, B. Post. The crystal structure of rhenium diboride, *Acta Crystallographica* 15 (1962) 97-99.
- [60] Y. Wang, J. Zhang, L.L. Daemen, Z. Lin, Y. Zhao, L. Wang. Thermal equation of state of rhenium diboride by high pressure-temperature synchrotron x-ray studies, *Physical Review B* 78 (2008) 224106.
- [61] X. Liu, W. Liu, Q. He, L.-W. Deng, H.-J. Wang, D.-w. He, B.-S. Li. Isotropic Thermal Expansivity and Anisotropic Compressibility of ReB<sub>2</sub>, *Chinese Physics Letters* 28 (2011) 036401.
- [62] Y. Wang, J. Zhang, L. Daemen, Z. Lin, Y. Zhao, L. Wang. Thermal equation of state of rhenium diboride by high pressure-temperature synchrotron x-ray studies, *Physical Review B* 78 (2008).
- [63] J. Pellicer-Porres, A. Segura, A. Muñoz, A. Polian, A. Congeduti. Bond length compressibility in hard ReB<sub>2</sub> investigated by X-ray absorption under high pressure, *Journal of Physics: Condensed Matter* 22 (2010) 045701.

- [64] M.R. Koehler, V. Keppens, B.C. Sales, R. Jin, D. Mandrus. Elastic moduli of superhard rhenium diboride, *Journal of Physics D: Applied Physics* 42 (2009) 095414.
- [65] S.N. Tkachev, J.B. Levine, A. Kisliuk, A.P. Sokolov, S. Guo, J.T. Eng, R.B. Kaner. Shear Modulus of Polycrystalline Rhenium Diboride Determined from Surface Brillouin Spectroscopy, *Advanced Materials* 21 (2009) 4284-4286.
- [66] N. Dubrovinskaia, L. Dubrovinsky, V.L. Solozhenko. Comment on "Synthesis of Ultra-Incompressible Superhard Rhenium Diboride at Ambient Pressure", *Science* 318 (2007) 1550.
- [67] H.-Y. Chung, M.B. Weinberger, J.B. Levine, R.W. Cumberland, A. Kavner, J.-M. Yang, S.H. Tolbert, R.B. Kaner. Response to Comment on "Synthesis of Ultra-Incompressible Superhard Rhenium Diboride at Ambient Pressure", *Science* 318 (2007) 1550.
- [68] S. Otani, M.M. Korsukova, T. Aizawa. High-temperature hardness of  $\text{ReB}_2$  single crystals, *Journal of Alloys and Compounds* 477 (2009) L28-L29.
- [69] J. Qin, D. He, J. Wang, L. Fang, L. Lei, Y. Li, J. Hu, Z. Kou, Y. Bi. Is Rhenium Diboride a Superhard Material?, *Advanced Materials* 20 (2008) 4780-4783.

- [70] J.B. Levine, J.B. Betts, J.D. Garrett, S.Q. Guo, J.T. Eng, A. Migliori, R.B. Kaner. Full elastic tensor of a crystal of the superhard compound  $\text{ReB}_2$ , *Acta Materialia* 58 (2010) 1530-1535.
- [71] A.M. Locci, R. Licheri, R. Orrù, G. Cao. Reactive Spark Plasma Sintering of rhenium diboride, *Ceramics International* 35 (2009) 397-400.
- [72] A.B. Lyashchenko, V.N. Paderno, V.B. Filippov, D.F. Borshchevskii. Growth and some properties of rhenium diboride single crystals, *SVerkhtVerd. Mater.* 79 (2006).
- [73] S. Otani, T. Aizawa, Y. Ishizawa. Preparation of  $\text{ReB}_2$  single crystals by the floating zone method, *Journal of Alloys and Compounds* 252 (1997) L19-L21.
- [74] B.L. Ivanov, M.S. Wellons, C.M. Lukehart. Confined-Plume Chemical Deposition: Rapid Synthesis of Crystalline Coatings of Known Hard or Superhard Materials on Inorganic or Organic Supports by Resonant IR Decomposition of Molecular Precursors, *Journal of the American Chemical Society* 131 (2009) 11744-11750.
- [75] G. Soto, M.G. Moreno-Armenta, A. Reyes-Serrato. Study on the formation of rhenium borides by density functional calculations, *Computational Materials Science* 44 (2008) 628-634.

- [76] V.S. Neshpor, Y.B. Paderno, G.V. Samsonov. Dokl. Akad. Nauk SSSR 118 (1958).
- [77] B. Aronsson, E. Stenberg, J. Aselius. Borides of Rhenium and the Platinum Metals, Acta Chemica Scandinavica 14 (1960).
- [78] G.V. Samsonov, I.Y. Kondratov. Cermet alloys of rhenium with yttrium hexaboride, Poroshkovaya Metallurgiya 8 (1969).
- [79] V. Pecharsky, L. Akselrud, V. Davydov. PDF#00-048-1739, L'viv Inst. of Theoretical Material Research (1996).
- [80] A.P. Tyutyunnik, T.V. Dyachkova, Y.G. Zaynulin, S.A. Gromilov. Structure of the monoclinic modification of  $\text{Re}_3\text{B}$ , J Struct Chem 55 (2014) 84-88.
- [81] E.A. Juarez-Arellano, B. Winkler, A. Friedrich, L. Bayarjargal, W. Morgenroth, M. Kunz, V. Milman. *In situ* study of the formation of rhenium borides from the elements at high-(P,T) conditions: Extreme incompressibility of  $\text{Re}_7\text{B}_3$  and formation of new phases, Solid State Sciences 25 (2013) 85-92.
- [82] K.I. Portnoi, V.M. Romashov. Phase diagram of the system rhenium-boron, Powder Metall Met Ceram 7 (1968) 112-114.
- [83] B. Wang, D.Y. Wang, Y.X. Wang. A new hard phase of  $\text{ReB}_4$  predicted from first principles, Journal of Alloys and Compounds 573 (2013) 20-26.

- [84] X.-J. Feng, L.-X. Zhao, T.-T. Cao, Y.-M. Lei, Y.-H. Luo. Theoretical prediction of structural and magnetic properties of small rhenium boride clusters  $\text{Re}_m\text{B}_n$  ( $m=1-3$ ,  $n=1-3m$ ), *Physica B: Condensed Matter* 403 (2008) 4323-4327.
- [85] W. Zhou, H. Wu, T. Yildirim. Electronic, dynamical, and thermal properties of ultra-incompressible superhard rhenium diboride: A combined first-principles and neutron scattering study, *Physical Review B* 76 (2007) 184113.
- [86] A. Vegas, L.A. Martinez-Cruz, A. Ramos-Gallardo, A. Romero. A study of cation arrays in  $\text{MB}_2$ ,  $\text{MB}_4$  and  $\text{MB}_6$  borides. Part I. Their relation to their parent metals, *Zeitschrift für Kristallographie*. 210 (1995) 574-580.
- [87] Y.X. Wang. Elastic and electronic properties of  $\text{TcB}_2$  and superhard  $\text{ReB}_2$ : First-principles calculations, *Applied Physics Letters* 91 (2007) -.
- [88] M.-M. Zhong, X.-Y. Kuang, Z.-H. Wang, P. Shao, L.-P. Ding, X.-F. Huang. Phase stability, physical properties of rhenium diboride under high pressure and the effect of metallic bonding on its hardness, *Journal of Alloys and Compounds* 581 (2013) 206-212.
- [89] Y.X. Wang. Elastic and electronic properties of  $\text{TcB}_2$  and superhard  $\text{ReB}_2$ : First-principles calculations, *Applied Physics Letters* 91 (2007) 101904.

- [90] E. Zhao, J. Wang, J. Meng, Z. Wu. Phase stability and mechanical properties of rhenium borides by first-principles calculations, *Journal of computational chemistry* 31 (2010) 1904-1910.
- [91] S. Okada, K. Kudou, T. Lundström. Preparations and Some Properties of  $W_2B$ ,  $\delta$ -WB and  $WB_2$  Crystals from High-Temperature Metal Solutions, *Japanese Journal of Applied Physics* 34 (1995) 226.
- [92] S. Okada, K. Kudou, I. Higashi, T. Lundström. Single crystals of TaB,  $Ta_5B_6$ ,  $Ta_3B_4$  and  $TaB_2$ , as obtained from high-temperature metal solutions, and their properties, *Journal of Crystal Growth* 128 (1993).
- [93] A. Kavner, M.M. Armentrout, E.S.G. Rainey, M. Xie, B.E. Weaver, S.H. Tolbert, R.B. Kaner. Thermoelastic properties of  $ReB_2$  at high pressures and temperatures and comparison with Pt, Os, and Re, *Journal of Applied Physics* 110 (2011) -.
- [94] A. Šimůnek. Anisotropy of hardness from first principles: The cases of  $ReB_2$  and  $OsB_2$ , *Physical Review B* 80 (2009) 060103.
- [95] A.L. Ivanovskii. Microhardness of compounds of rhenium with boron, carbon, and nitrogen, *Journal of Superhard Materials* 34 (2012) 75-80.
- [96] E.O. Hall. The Deformation and Ageing of Mild Steel: III Discussion of Results, *Proceedings of the Physical Society. Section B* 64 (1951) 747.

- [97] N.J. Petch. The cleavage strength of polycrystals, *Journal of the Iron and Steel Institute* 174 (1953) 25-28.
- [98] H.-Y. Chung, M.B. Weinberger, J.-M. Yang, S.H. Tolbert, R.B. Kaner. Correlation between hardness and elastic moduli of the ultraincompressible transition metal diborides  $\text{RuB}_2$ ,  $\text{OsB}_2$ , and  $\text{ReB}_2$ , *Applied Physics Letters* 92 (2008) -.
- [99] S. Aydin, M. Simsek. First-principles calculations of  $\text{MnB}_2$ ,  $\text{TcB}_2$ , and  $\text{ReB}_2$  within the  $\text{ReB}_2$ -type structure, *Physical Review B* 80 (2009).
- [100] X. Hao, Y. Xu, Z. Wu, D. Zhou, X. Liu, X. Cao, J. Meng. Low-compressibility and hard materials  $\text{ReB}_2$  and  $\text{WB}_2$ : Prediction from first-principles study, *Physical Review B* 74 (2006) 224112.
- [101] X. Zhu, D. Li, X. Cheng. Elasticity properties of the low-compressible material  $\text{ReB}_2$ , *Solid State Communications* 147 (2008) 301-304.
- [102] C. Zang, H. Sun, J.S. Tse, C. Chen. Indentation strength of ultraincompressible rhenium boride, carbide, and nitride from first-principles calculations, *Physical Review B* 86 (2012) 014108.
- [103] V. Tvergaard, J.W. Hutchinson. Microcracking in Ceramics Induced by Thermal Expansion or Elastic Anisotropy, *Journal of the American Ceramic Society* 71 (1988) 157-166.



- [104] Y. Suzuki, J.B. Levine, A. Migliori, J.D. Garrett, R.B. Kaner, V.R. Fanelli, J.B. Betts. Rhenium diboride's monocystal elastic constants, 308 to 5 K, The Journal of the Acoustical Society of America 127 (2010) 2797-2801.
- [105] L.K. Zhao, E.J. Zhao, Z.J. Wu. First-principles calculations of structural thermodynamic and mechanical properties of 5d transitional metal diborides, Acta phys. Sin 62 (2013) 046201.
- [106] R. Long, Y. Dai, H. Jin, B. Huang. Structural, Elastic, and Electronic Properties of  $\text{ReB}_2$ : A First-Principles Calculation, Research Letters in Physics 2008 (2008) 1-5.
- [107] R.F. Zhang, S. Veprek, A.S. Argon. Mechanical and electronic properties of hard rhenium diboride of low elastic compressibility studied by first-principles calculation, Applied Physics Letters 91 (2007) -.
- [108] M. Xie, B. Winkler, Z. Mao, R.B. Kaner, A. Kavner, S.H. Tolbert. Raman scattering from superhard rhenium diboride under high pressure, Applied Physics Letters 104 (2014) -.
- [109] F. Peng, Q. Liu, H. Fu, X. Yang. Electronic and thermodynamic properties of under high pressure and temperature, Solid State Communications 149 (2009) 56-59.

- [110] A. Kawano, Y. Mizuta, H. Takagiwa, T. Muranaka, J. Akimitsu. The Superconductivity in Re–B System, *Journal of the Physical Society of Japan* 72 (2003) 1724-1728.
- [111] S.V. Meschel, O.J. Kleppa. Standard enthalpies of formation of NbB<sub>2</sub>, MoB, and ReB<sub>2</sub> by high-temperature direct synthesis calorimetry, *MTA* 24 (1993) 947-950.
- [112] X.-Q. Chen, C.L. Fu, M. Krčmar, G.S. Painter. Electronic and Structural Origin of Ultraincompressibility of 5d Transition-Metal Diborides MB<sub>2</sub> (M=W, Re, Os), *Physical Review Letters* 100 (2008) 196403.
- [113] F. Ren, Y. Wang, V.C. Lo. Pressure induced structural phase transition of OsB<sub>2</sub>: First-principles calculations, *Journal of Solid State Chemistry* 183 (2010) 915-919.
- [114] C.P. Kempter, R.J. Fries. Crystallography of the Ru–B and Os–B Systems, *The Journal of Chemical Physics* 34 (1961) 1994-1995.
- [115] R.B. Roof, C.P. Kempter. New Orthorhombic Phase in the Ru–B and Os–B Systems, *The Journal of Chemical Physics* 37 (1962) 1473-1476.
- [116] B. Aronsson. The Crystal Structure of RuB<sub>2</sub>, OsB<sub>2</sub>, and IrB<sub>1.35</sub> and Some General Comments on the Crystal Chemistry of Borides in the Composition Range MeB - MeB<sub>3</sub>, *Acta Chemica Scandinavica* 17 (1963).

- [117] L. Stuparević, D. Živković. Phase diagram investigation and thermodynamic study of Os-B system, *Journal of Thermal Analysis and Calorimetry* 76 (2004) 975-983.
- [118] Y. Singh, A. Niazi, M.D. Vannette, R. Prozorov, D.C. Johnston. Superconducting and normal-state properties of the layered boride OsB<sub>2</sub>, *Physical Review B* 76 (2007) 214510.
- [119] Y. Singh, C. Martin, S.L. Bud'ko, A. Ellern, R. Prozorov, D.C. Johnston. Multigap superconductivity and Shubnikov–de Haas oscillations in single crystals of the layered boride OsB<sub>2</sub>, *Physical Review B* 82 (2010) 144532.
- [120] X. Hao, Y. Xu, F. Gao. Electronic and elastic properties of new semiconducting *oP*<sub>12</sub>-type RuB<sub>2</sub> and OsB<sub>2</sub>, *Journal of Physics: Condensed Matter* 23 (2011) 125501.
- [121] M. Hebbache, L. Stuparević, D. Živković. A new superhard material: Osmium diboride OsB<sub>2</sub>, *Solid State Communications* 139 (2006) 227-231.
- [122] Z.Y. Chen, H.J. Xiang, J. Yang, J.G. Hou, Q. Zhu. Structural and electronic properties of OsB<sub>2</sub>: A hard metallic material, *Physical Review B* 74 (2006) 012102.

- [123] Z.-W. Ji, C.-H. Hu, D.-H. Wang, Y. Zhong, J. Yang, W.-Q. Zhang, H.-Y. Zhou. Mechanical properties and chemical bonding of the Os–B system: A first-principles study, *Acta Materialia* 60 (2012) 4208-4217.
- [124] J. Yang, H. Sun, C. Chen. Is Osmium Diboride An Ultra-Hard Material?, *Journal of the American Chemical Society* 130 (2008) 7200-7201.
- [125] W.C. Oliver, G.M. Pharr. An improved technique for determining hardness and elastic modulus using load and displacement sensing indentation experiments, *Journal of Materials Research* 7 (1992) 1564-1583.
- [126] H. Gou, L. Hou, J. Zhang, H. Li, G. Sun, F. Gao. First-principles study of low compressibility osmium borides, *Applied Physics Letters* 88 (2006) -.
- [127] A. Kavner, M.B. Weinberger, A. Shahar, R.W. Cumberland, J.B. Levine, R.B. Kaner, S.H. Tolbert. Lattice strain of osmium diboride under high pressure and nonhydrostatic stress, *Journal of Applied Physics* 112 (2012) -.
- [128] Z.F. Hou. First-Principles Study of Elasticity and Electronic Structure of Incompressible Osmium Diboride, *arXiv:cond-mat/0601216v2* [cond-mat.mtrl-sci] (2008).
- [129] B.P.T. Fokwa, P.R.N. Misse, M. Gilleßen, R. Dronskowski. Sn-flux syntheses, characterizations and bonding analyses of OsB and TiB<sub>2</sub>, *Journal of Alloys and Compounds* 489 (2010) 339-342.

- [130] Y. Liang, J. Zhao, B. Zhang. Electronic structure and mechanical properties of osmium borides, carbides and nitrides from first principles, *Solid State Communications* 146 (2008) 450-453.
- [131] M. Zhang, M. Wang, T. Cui, Y. Ma, Y. Niu, G. Zou. Electronic structure, phase stability, and hardness of the osmium borides, carbides, nitrides, and oxides: First-principles calculations, *Journal of Physics and Chemistry of Solids* 69 (2008) 2096-2102.
- [132] Y. Li, Z. Zeng, H. Lin. Structural, elastic, electronic and dynamical properties of OsB and ReB: Density functional calculations, *Chemical Physics Letters* 492 (2010) 246-250.
- [133] H.-H. Chen, Z. Li, Y. Cheng, Y. Bi, L.-C. Cai. Thermodynamic properties of OsB under high temperature and high pressure, *Physica B: Condensed Matter* 406 (2011) 3338-3341.
- [134] M. Zhang, H. Yan, G. Zhang, H. Wang. Ultra-incompressible Orthorhombic Phase of Osmium Tetraboride ( $\text{OsB}_4$ ) Predicted from First Principles, *The Journal of Physical Chemistry C* 116 (2012) 4293-4297.
- [135] B. Aronsson, E. Stenberg, J. Aselius. Borides of Ruthenium, Osmium and Iridium, *Nature* 195 (1962) 377-378.

- [136] P. Rogl, H. Nowotny, F. Benesovsky. Ein Beitrag zur Strukturchemie der Iridiumboride, Monatshefte für Chemie 102 (1971) 678-686.
- [137] T. Lundström, L.-E. Tergenius. Refinement of the crystal structure of the non-stoichiometric boride IrB<sub>1.35</sub>, Acta Chemica Scandinavica 27 (1973) 3705-3711.
- [138] P. Rogl, H. Nowotny, F. Benesovsky. Komplexboride mit ReB<sub>2</sub>-Struktur, Monatshefte für Chemie 101 (1970) 27-31.
- [139] Y.K. Rao, G.R. Belton. In chemical metallurgy-A tribute to Carl Wagner, Edited by N.A. Gocken, Metall. Soc. of AIME Warrendale, Pa. (1981) 75-96.
- [140] Y.K. Rao. Stoichiometry and thermodynamics of metallurgical processes, Cambridge University Press, New York (1985).
- [141] Dragana Živković, L. Stuparevic. Calculation of the thermodynamic properties in the Ir-B system based on the known phase diagram, RMZ-Materials and Geoenvironment 52 (2005) 463-468.
- [142] H. Ipsier, P. Rogl. Constitution diagrams of the binary systems Pd-B and Ir-B, Journal of the Less Common Metals 82 (1981) 363.
- [143] H.F. Pang, Y.W. Ng, Y. Xia, A.S.C. Cheung. Electronic transitions of iridium monoboride, Chemical Physics Letters 501 (2011) 257-262.

- [144] J.V. Rau, A. Latini. New Hard and Superhard Materials: RhB<sub>1.1</sub> and IrB<sub>1.35</sub>, Chemistry of Materials 21 (2009) 1407-1409.
- [145] P. Lazar, X.-Q. Chen, R. Podloucky. First-principles modeling of hardness in transition-metal diborides, Physical Review B 80 (2009).
- [146] J. Haines, J.M. Leger, G. Bocquillon. Synthesis and design of superhard materials, Ann. Rev. Mater. Res. 31 (2001) 1-23.
- [147] P.A. Romans, M.P. Krug. Composition and crystallographic data for the highest boride of tungsten, Acta Crystallographica 20 (1966) 313-315.
- [148] H.P. Woods, F.E. Wawner, B.G. Fox. Tungsten Diboride: Preparation and Structure, Science 151 (1966) 75.
- [149] S. Otani, Y. Ishizawa. Preparation of WB<sub>2-x</sub> single crystals by the floating zone method, Journal of Crystal Growth 154 (1995) 81-84.
- [150] J.B. Levine, S.H. Tolbert, R.B. Kaner. Advancements in the Search for Superhard Ultra-Incompressible Metal Borides, Advanced Functional Materials 19 (2009) 3519-3533.
- [151] R.H. Wentorf. Cubic Form of Boron Nitride, The Journal of Chemical Physics 26 (1957) 956-956.

- [152] P. Rogl, H. Nowotny, F. Benesovsky. Ternary Complex Borides within the Systems (Mo,W)(Ru,Os)-B and W-Ir-B, *Monatsh. Chem.* 101 (1970) 850-854.
- [153] P. Rogl, E. Rudy. New complex borides with  $\text{ReB}_2$ - and  $\text{Mo}_2\text{IrB}_2$ -type structure, *Journal of Solid State Chemistry* 24 (1978) 175-181.
- [154] F. Lin, K. Wu, J. He, R. Sa, Q. Li, Y. Wei. Mixed-metal effects on ultra-incompressible metal diborides: Density functional computations, *Chemical Physics Letters* 494 (2010) 31-36.
- [155] S. Veprek, R.F. Zhang, A.S. Argon. Mechanical properties and hardness of boron and boron-rich solids, *Journal of Superhard Materials* 33 (2011) 409-420.
- [156] V.V. Brazhkin, A.G. Lyapin, R.J. Hemley. Harder than diamond: Dreams and reality, *Philosophical Magazine A* 82 (2002) 231-253.
- [157] J.M. Léger, P. Djemia, F. Ganot, J. Haines, A.S. Pereira, J.A.H. da Jornada. Hardness and elasticity in cubic ruthenium dioxide, *Applied Physics Letters* 79 (2001) 2169-2171.
- [158] T. Kenichi. Bulk modulus of osmium: High-pressure powder x-ray diffraction experiments under quasihydrostatic conditions, *Physical Review B* 70 (2004) 012101.



- [159] C. Pantea, I. Mihut, H. Ledbetter, J.B. Betts, Y. Zhao, L.L. Daemen, H. Cynn, A. Migliori. Bulk modulus of osmium, 4–300K, *Acta Materialia* 57 (2009) 544-548.
- [160] C. Pantea, I. Stroe, H. Ledbetter, J.B. Betts, Y. Zhao, L.L. Daemen, H. Cynn, A. Migliori. Elastic constants of osmium between 5 and 300 K, *Physical Review B* 80 (2009) 024112.
- [161] G. Kaupp. Waste-free synthesis and production all across chemistry with the benefit of self-assembled crystal packings, *Journal of Physical Organic Chemistry* 21 (2008) 630-643.
- [162] J.J. Gilman. Mechanochemistry, *Science* 274 (1996) 65.
- [163] L. Takacs. Quicksilver from cinnabar: The first documented mechanochemical reaction?, *JOM* 52 (2000) 12-13.
- [164] L. Takacs. M. Carey Lea, The father of mechanochemistry, *Bull. Hist. Chem.* 28 (2003).
- [165] M. Carey Lea. Disruption of the silver haloid molecule by mechanical force, *Am. J. Sci.* 43 (1892).
- [166] M. Carey Lea. On endothermic decompositions obtained by pressure; Part II, Transformations of energy by shearing stress, *Am. J. Sci.* 46 (1893).

- [167] M. Carey Lea. Transformations of mechanical into chemical energy; Part III, Action of shearing stress continued, *Am. J. Sci.* 47 (1894).
- [168] L. Takacs. The mechanochemical reduction of AgCl with metals, *Journal of Thermal Analysis and Calorimetry* 90 (2007) 81-84.
- [169] M. Faraday. *Chemical Manipulations; being Instructions to Students in Chemistry on the Methods of Performing Experiments of Demonstrations or of Research, with Accuracy and with Success*, London, 1827.
- [170] V.V. Boldyrev. Mechanochemistry and mechanical activation of solids, *Russ. Chem. Rev.* 75 (2006).
- [171] S.L. James, C.J. Adams, C. Bolm, D. Braga, P. Collier, T. Friscic, F. Grepioni, K.D.M. Harris, G. Hyett, W. Jones, A. Krebs, J. Mack, L. Maini, A.G. Orpen, I.P. Parkin, W.C. Shearouse, J.W. Steed, D.C. Waddell. Mechanochemistry: opportunities for new and cleaner synthesis, *Chemical Society Reviews* 41 (2012) 413-447.
- [172] D. Restrepo. *Mechanochemistry for Solid-State Syntheses and Catalysis*. Department of Chemistry, vol. Doctoral Dissertation: University of Central Florida, 2014. p.284.

- [173] Y. Todaka, P. McCormick, nbsp, Gerard, K. Tsuchiya, M. Umemoto. Synthesis of Fe-Cu Nanoparticles by Mechanochemical Processing Using a Ball Mill, MATERIALS TRANSACTIONS 43 (2002) 667-673.
- [174] J. Ding, T. Tsuzuki, P.G. McCormick. Ultrafine Alumina Particles Prepared by Mechanochemical/Thermal Processing, Journal of the American Ceramic Society 79 (1996) 2956-2958.
- [175] J. Eckert, J.C. Holzer, C.E. Krill, W.L. Johnson. Mechanically driven alloying and grain size changes in nanocrystalline Fe - Cu powders, Journal of Applied Physics 73 (1993) 2794-2802.
- [176] R.G. Blair, Chapter 10: Mechanical and Combined Chemical and Mechanical Treatment of Biomass, in Production of Biofuels and Chemicals with Ultrasound, Fang, Editor. In Press.
- [177] P. Baláž. Mechanochemistry in Nanoscience and Minerals Engineering, Springer-Verlag, Berlin Heidelberg, 2008.
- [178] C. Suryanarayana. Mechanical alloying and milling, Progress in Materials Science 46 (2001) 1-184.
- [179] T. Sritharan, F.Y.C. Boey, A. Srinivas. Synthesis of complex ceramics by mechanochemical activation, Journal of Materials Processing Technology 192–193 (2007) 255-258.

- [180] Z.Ž. Lazarević, N.Ž. Romčević, J.D. Bobić, M.J. Romčević, Z. Dohčević-Mitrović, B.D. Stojanović. Study on bi-layered ceramics powders prepared by the mechanochemical synthesis, *Journal of Alloys and Compounds* 486 (2009) 848-852.
- [181] H.-J. Kim, H.-J. Choi, J.-G. Lee. Mechanochemical Synthesis and Pressureless Sintering of  $TiB_2$ -AlN Composites, *Journal of the American Ceramic Society* 85 (2002) 1022-1024.
- [182] A.L. Black, J.M. Lenhardt, S.L. Craig. From molecular mechanochemistry to stress-responsive materials, *Journal of Materials Chemistry* 21 (2011) 1655-1663.
- [183] J.N. Brantley, K.M. Wiggins, C.W. Bielawski. Polymer mechanochemistry: the design and study of mechanophores, *Polymer International* 62 (2013) 2-12.
- [184] G.-W. Wang. Fullerene mechanochemistry, *Encyclopedia of nanoscience and nanotechnology* 3 (2004) 557-565.
- [185] X. Guo, D. Xiang, G. Duan, P. Mou. A review of mechanochemistry applications in waste management, *Waste management* 30 (2010) 4-10.
- [186] I. Halasz, S.A.J. Kimber, P.J. Beldon, A.M. Belenguer, F. Adams, V. Honkimäki, R.C. Nightingale, R.E. Dinnebier, T. Friščić. *In situ* and real-

- time monitoring of mechanochemical milling reactions using synchrotron X-ray diffraction, *Nat. Protocols* 8 (2013) 1718-1729.
- [187] I. Halasz, A. Puškarić, S.A.J. Kimber, P.J. Beldon, A.M. Belenguer, F. Adams, V. Honkimäki, R.E. Dinnebier, B. Patel, W. Jones, V. Štrukil, T. Friščić. Real-Time *In Situ* Powder X-ray Diffraction Monitoring of Mechanochemical Synthesis of Pharmaceutical Cocrystals, *Angewandte Chemie International Edition* 52 (2013) 11538-11541.
- [188] K.D.M. Harris. Mechanochemical synthesis: How grinding evolves, *Nat Chem* 5 (2013) 12-14.
- [189] M. Petruschke. *Tribochemistry*. von G. HEINICKE. Berlin: Akademie-Verlag 1984. Bestellnummer: 7631993(6746). 495 S., 329 Bilder, 106 Tabellen, 98,- M, *Acta Polymerica* 36 (1985) 400-401.
- [190] S. Kaloshkin, I. Tomilin, G. Andrianov, U. Baldokhin, E. Shelekhov. Phase transformations and hyperfine interactions in mechanically alloyed Fe-Cu solid solutions. *Materials Science Forum*, vol. 235: Trans Tech Publ, 1996. p.565-570.
- [191] V.V. Boldyrev, K. Tkáčová. Mechanochemistry of Solids: Past, Present, and Prospects, *Journal of Materials Synthesis and Processing* 8 (2000) 121-132.

- [192] S.M. Hick, C. Griebel, D.T. Restrepo, J.H. Truitt, E.J. Buker, C. Bylda, R.G. Blair. Mechanocatalysis for biomass-derived chemicals and fuels, *Green Chemistry* 12 (2010) 468-474.
- [193] J. Gilman. Mechanism of shear-induced metallization, *Czech J Phys* 45 (1995) 913-919.
- [194] V.I. Levitas. Continuum mechanical fundamentals of mechanochemistry. *High Pressure Surface Science and Engineering*. Taylor & Francis, 2003. pp. 161-292.
- [195] V.I. Levitas. High-pressure mechanochemistry: Conceptual multiscale theory and interpretation of experiments, *Physical Review B* 70 (2004) 184118.
- [196] V.I. Levitas. Strain-induced nucleation at a dislocation pile-up: a nanoscale model for high pressure mechanochemistry, *Physics Letters A* 327 (2004) 180-185.
- [197] V.I. Levitas, R. Ravelo. Virtual melting as a new mechanism of stress relaxation under high strain rate loading, *Proceedings of the National Academy of Sciences* 109 (2012) 13204-13207.

- [198] V.I. Levitas, V.F. Nesterenko, M.A. Meyers. Strain-induced structural changes and chemical reactions—I. Thermomechanical and kinetic models, *Acta Materialia* 46 (1998) 5929-5945.
- [199] V. Nesterenko, M. Meyers, H. Chen, J. LaSalvia. Controlled high - rate localized shear in porous reactive media, *Applied physics letters* 65 (1994) 3069-3071.
- [200] V. Nesterenko, M. Meyers, H. Chen, J. LaSalvia. The structure of controlled shear bands in dynamically deformed reactive mixtures, *Metall and Mat Trans A* 26 (1995) 2511-2519.
- [201] C. Ji, V.I. Levitas, H. Zhu, J. Chaudhuri, A. Marathe, Y. Ma. Shear-induced phase transition of nanocrystalline hexagonal boron nitride to wurtzitic structure at room temperature and lower pressure, *Proceedings of the National Academy of Sciences* 109 (2012) 19108-19112.
- [202] J. Pellicer-Porres, A. Segura, A. Munoz, A. Polian, A. Congeduti. Bond length compressibility in hard  $\text{ReB}_2$  investigated by X-ray absorption under high pressure, *Journal of physics. Condensed matter : an Institute of Physics journal* 22 (2010) 045701.
- [203] A.J. McAlister. *Binary Alloy Phase Diagram*, Materials Park, OH, 1990.

- [204] L. Takacs. Self-sustaining reactions induced by ball milling, *Progress in Materials Science* 47 (2002) 355-414.
- [205] W. Haessler, M. Herrmann, B. Birajdar, C. Rodig, M. Schubert, B. Holzapfel, O. Eibl, L. Schultz. Superconducting MgB<sub>2</sub> Tapes Prepared Using Mechanically Alloyed Nanocrystalline Precursor Powder, *Applied Superconductivity, IEEE Transactions on* 17 (2007) 2919-2921.
- [206] P. Millet, T. Hwang. Preparation of TiB<sub>2</sub> and ZrB<sub>2</sub>. influence of a mechanochemical treatment on the borothermic reduction of titania and zirconia, *J Mater Sci* 31 (1996) 351-355.
- [207] Y. Hwang, J.K. Lee. Preparation of TiB<sub>2</sub> powders by mechanical alloying, *Materials Letters* 54 (2002) 1-7.
- [208] D.D. Radev, D. Klisurski. Properties of TiB<sub>2</sub> powders obtained in a mechanochemical way, *Journal of Alloys and Compounds* 206 (1994) 39-41.
- [209] N. Setoudeh, N.J. Welham. Formation of zirconium diboride (ZrB<sub>2</sub>) by room temperature mechanochemical reaction between ZrO<sub>2</sub>, B<sub>2</sub>O<sub>3</sub> and Mg, *Journal of Alloys and Compounds* 420 (2006) 225-228.
- [210] R.A. Varin, C. Chiu. Synthesis of nanocrystalline magnesium diboride (MgB<sub>2</sub>) metallic superconductor by mechano-chemical reaction and post-annealing, *Journal of Alloys and Compounds* 407 (2006) 268-273.



- [211] G.E. Boyd, J.W. Cobble, W.T. Smith. Thermodynamic Properties of Technetium and Rhenium Compounds. III. Heats of Formation of Rhenium Heptoxide and Trioxide, and a Revised Potential Diagram for Rhenium1, *Journal of the American Chemical Society* 75 (1953) 5783-5784.
- [212] R.F. Zhang, D. Legut, R. Niewa, A.S. Argon, S. Veprek. Shear-induced structural transformation and plasticity in ultraincompressible ReB<sub>2</sub> limit its hardness, *Physical Review B* 82 (2010).
- [213] N. Orlovskaya, Z. Xie, M. Klimov, H. Heinrich, D. Restrepo, R. Blair, C. Suryanarayana. Mechanochemical synthesis of ReB<sub>2</sub> powder, *Journal of Materials Research* 26 (2011) 2772-2779.
- [214] M.A. Grinfeld. The stress driven instability in elastic crystals: Mathematical models and physical manifestations, *J Nonlinear Sci* 3 (1993) 35-83.
- [215] V.I. Levitas. Phase transitions in elastoplastic materials: Continuum thermomechanical theory and examples of control—part I, *Journal of the Mechanics and Physics of Solids* 45 (1997) 923-947.
- [216] B. Feng, V.I. Levitas, O.M. Zarechnyy. Plastic flows and phase transformations in materials under compression in diamond anvil cell: Effect of contact sliding, *Journal of Applied Physics* 114 (2013) -.

- [217] A.L. Kovarskii. High Pressure Chemistry and Physics of Polymers, CRC Press Inc., Boca Raton, FL, USA., 1994.
- [218] A.C. Larson, R.B. Von Dreele. General Structure Analysis System (GSAS), Los Alamos National Laboratory Report LAUR (1994) 86-748.
- [219] B.H. Toby. EXPGUI, a graphical user interface for GSAS, J. Appl. Cryst. 34 (2001) 210-213.
- [220] Blanks, Spear. PDF#030-0879, Penn State University, University Park, Pennsylvania, USA. (1978).
- [221] Z. Xie, M. Graule, N. Orlovskaya, E. Andrew Payzant, D.A. Cullen, R.G. Blair. Novel high pressure hexagonal OsB<sub>2</sub> by mechanochemistry, Journal of Solid State Chemistry 215 (2014) 16-21.
- [222] N. Orlovskaya, Z. Xie, R. Blair. Mechanochemical Synthesis of Hexagonal OsB<sub>2</sub>, U.S. Patent 14/157,216 (2014).
- [223] J.W. Arblaster. Densities of Osmium and Iridium, Platinum Metals Rev. 33 (1989) 14-16.
- [224] G.N. Glavee, K.J. Klabunde, C.M. Sorensen, G.C. Hadjapanayis. Borohydride reductions of metal ions. A new understanding of the chemistry leading to nanoscale particles of metals, borides, and metal borates, Langmuir 8 (1992) 771-773.

- [225] D.D. Jayaseelan, Y. Wang, G.E. Hilmas, W. Fahrenholtz, P. Brown, W.E. Lee. TEM investigation of hot pressed - 10 vol.%SiC–ZrB<sub>2</sub> composite, *Advances in Applied Ceramics* 110 (2011) 1-7.
- [226] A.K. Khanra, M.M. Godkhindi. Effect of Ni additives on pressureless sintering of SHS ZrB<sub>2</sub>, *Advances in Applied Ceramics* 104 (2005) 273-276.
- [227] R.S. Dohedoe, G.D. West, M.H. Lewis. Spark plasma sintering of ceramics: understanding temperature distribution enables more realistic comparison with conventional processing, *Advances in Applied Ceramics* 104 (2005) 110-116.
- [228] N. Orlovskaya, R. Stadelmann, M. Lugovy, V. Subbotin, G. Subhash, M. Neubert, C.G. Aneziris, T. Graule, J. Kuebler. Mechanical properties of ZrB<sub>2</sub>–SiC ceramic composites: room temperature instantaneous behaviour, *Advances in Applied Ceramics* 112 (2013) 9-16.
- [229] E. Padovano, C. Badini, S. Biamino, M. Pavese, W.S. Yang, P. Fino. Pressureless sintering of ZrB<sub>2</sub>–SiC composite laminates using boron and carbon as sintering aids, *Advances in Applied Ceramics* 112 (2013) 478-486.
- [230] B. Ganem, J.O. Osby. Synthetically useful reactions with metal boride and aluminide catalysts, *Chemical Reviews* 86 (1986) 763-780.

- [231] T. Mori. Chapter 238 - Higher Borides. in: Karl A. Gschneidner J-CGB, Vitalij KP, (Eds.). Handbook on the Physics and Chemistry of Rare Earths, vol. Volume 38. Elsevier, 2008. pp. 105-173.
- [232] J.K. Sonber, A.K. Suri. Synthesis and consolidation of zirconium diboride: review, *Advances in Applied Ceramics* 110 (2011) 321-334.
- [233] A.K. Khanra, L.C. Pathak, M.M. Godkhindi. Carbothermal synthesis of zirconium diboride ( $ZrB_2$ ) whiskers, *Advances in Applied Ceramics* 106 (2007) 155-160.
- [234] M. Jalaly, M. Sh. Bafghi, M. Tamizifar, F.J. Gotor. Mechanochemical synthesis of nanocrystalline  $ZrB_2$ -based powders by mechanically induced self-sustaining reaction method, *Advances in Applied Ceramics* 112 (2013) 383-388.
- [235] A.K. Khanra, L.C. Pathak, S.K. Mishra, M.M. Godkhindi. Sintering of ultrafine zirconium diboride powder prepared by modified SHS technique, *Advances in Applied Ceramics* 104 (2005) 282-284.
- [236] H. Wu, C. Xie, W. Zhang, J. Zhang. Fabrication and properties of 2D C/C- $ZrB_2$ -ZrC-SiC composites by hybrid precursor infiltration and pyrolysis, *Advances in Applied Ceramics* 112 (2013) 366-373.

- [237] S. Carencu, D. Portehault, C. Boissière, N. Mézailles, C. Sanchez. Nanoscaled Metal Borides and Phosphides: Recent Developments and Perspectives, *Chemical Reviews* 113 (2013) 7981-8065.
- [238] Z. Xie, R.G. Blair, N. Orlovskaya, D.A. Cullen, E. Andrew Payzant. Thermal stability of hexagonal OsB<sub>2</sub>: Negative thermal expansion, in preparation for submission (2014).
- [239] J.A. Dean, N.A. Lange. Lange's handbook of chemistry, McGraw-Hill, 1992.
- [240] L.V. Gurvich. Reference books and data banks on the thermodynamic properties of individual substances, *Pure and Applied Chemistry* 61 (1989) 1027–1031.
- [241] I. Glassman, R.A. Yetter. Chapter 9 - Combustion of Nonvolatile Fuels. in: Glassman I, Yetter RA, (Eds.). *Combustion (Fourth Edition)*. Academic Press, Burlington, 2008. pp. 495-550.
- [242] L.T. Akulova, M.V. Vlasova, I.V. Voropaeva, O.T. Horpyakov. Behaviour of molybdenum diboride in resistive thick film, *J Mater Sci* 27 (1992) 3293-3296.
- [243] R.G. Munro. Material Properties of Titanium Diboride, *J. Res. Natl. Inst. Stand. Technol.* 105 (2000) 709-720.

- [244] F. Thévenot. Boron carbide—A comprehensive review, *Journal of the European Ceramic Society* 6 (1990) 205-225.
- [245] B.A. Cook, J.S. Peters, J.L. Harringa, A.M. Russell. Enhanced wear resistance in AlMgB<sub>14</sub>-TiB<sub>2</sub> composites, *Wear* 271 (2011) 640-646.
- [246] A. Agarwal, N.B. Dahotre. Comparative wear in titanium diboride coatings on steel using high energy density processes, *Wear* 240 (2000) 144-151.
- [247] X. Fan, X. Xiao, L. Chen, J. Shao, L. Zhang, S. Li, H. Ge, Q. Wang. Superior Catalytic Effects of Transition Metal Boride Nanoparticles on the Reversible Hydrogen Storage Properties of Li-Mg-B-H System, *Particle & Particle Systems Characterization* 31 (2014) 195-200.
- [248] H. Ahmed, A.N. Broers. Lanthanum Hexaboride Electron Emitter, *Journal of Applied Physics* 43 (1972) 2185-2192.
- [249] J.D. Verhoeven, E.D. Gibson. Evaluation of a LaB<sub>6</sub> cathode electron gun, *Journal of Physics E: Scientific Instruments* 9 (1976) 65.
- [250] J.P. Viricelle, P. Goursat, D. Bahloul-Hourlier. Oxidation Behaviour of A Boron Carbide Based Material in Dry and Wet Oxygen, *Journal of Thermal Analysis and Calorimetry* 63 (2000) 507-515.

- [251] Z. Xie, R.G. Blair, N. Orlovskaya, D.A. Cullen, E. Andrew Payzant. Thermal stability of hexagonal OsB<sub>2</sub>, *Journal of Solid State Chemistry* 219 (2014) 210-219.
- [252] Z. Xie, R. Blair, N. Orlovskaya, E.A. Payzant. Hexagonal OsB<sub>2</sub> reduction upon heating in H<sub>2</sub> containing environment, *Advances in Applied Ceramics* In press (2014).
- [253] W.G. Fahrenholtz, G.E. Hilmas, I.G. Talmy, J.A. Zaykoski. Refractory Diborides of Zirconium and Hafnium, *Journal of the American Ceramic Society* 90 (2007) 1347-1364.
- [254] Z. Xie, N. Orlovskaya, D.A. Cullen. Characterization of hexagonal OsB<sub>2</sub>, in preparation for submission.
- [255] F.M. Gao, L.H. Gao. Microscopic models of hardness, *Journal of Superhard Materials* 32 (2010) 148-166.
- [256] S. Pathak, S.R. Kalidindi, C. Klemenz, N. Orlovskaya. Analyzing indentation stress–strain response of LaGaO<sub>3</sub> single crystals using spherical indenters, *Journal of the European Ceramic Society* 28 (2008) 2213-2220.
- [257] M. Sakai. The Meyer hardness: A measure for plasticity?, *Journal of Materials Research* 14 (1999) 3630-3639.

- [258] J. Malzbender. Comment on hardness definitions, *Journal of the European Ceramic Society* 23 (2003) 1355-1359.
- [259] J. Chen, S.J. Bull. A critical examination of the relationship between plastic deformation zone size and Young's modulus to hardness ratio in indentation testing, *J. Mater. Res.* 21 (2006) 2617-2627.
- [260] E. Eakins, D. Jayaseelan, W. Lee. Toward Oxidation-Resistant  $ZrB_2$ -SiC Ultra High Temperature Ceramics, *Metall and Mat Trans A* 42 (2011) 878-887.
- [261] B. Cristina, Y. Tsutomu. Review of the superconducting properties of  $MgB_2$ , *Superconductor Science and Technology* 14 (2001) R115.
- [262] A. Knappschneider, C. Litterscheid, J. Kurzman, R. Seshadri, B. Albert. Crystal Structure Refinement and Bonding Patterns of  $CrB_4$ : A Boron-Rich Boride with a Framework of Tetrahedrally Coordinated B Atoms, *Inorganic Chemistry* 50 (2011) 10540-10542.
- [263] D.Y. Wang, B. Wang, Y.X. Wang. New Crystal Structures of IrB and  $IrB_2$ : First-Principles Calculations, *The Journal of Physical Chemistry C* 116 (2012) 21961-21966.
- [264] B. Aronsson, S. Rundqvist. Borides, Silicides and Phosphides of the Platinum Metals, *Platinum Metals Rev.*, 5 (1961) 93-95.



- [265] G.F. Tavadze, A.S. Shteinberg. Production of advanced materials by methods of self-propagating high-temperature synthesis, Springer, 2013.
- [266] C. Suryanarayana, E. Ivanov, V.V. Boldyrev. The science and technology of mechanical alloying, *Materials Science and Engineering: A* 304–306 (2001) 151-158.